Measurement of Physiological Variables by Dynamic Gd-DTPA Enhanced MRI

Aleksandra Radjenovic

Submitted in accordance with the requirements for the degree of PhD

The University of Leeds

School of Medicine

Academic Unit of Medical Physics

September 2003

The candidate confirms that the work submitted is her own and that appropriate credit has been given where reference has been made to the work of others.

Acknowledgements

I wish to thank Dr John Ridgway and Professor Mike Smith for their assistance, patience and support. Luka arrived as I started work on this project and Anna joined us two years ago. Whilst Luka thinks it is fascinating that these big magnets can help us to look inside people's bodies without taking any parts off, Anna still has not expressed any opinion on my work (apart from occasionally resetting my computer). Alek is the fourth member of our team and without his support and love I would not have been able to complete this work. My parents provided an unending source of encouragement and I am deeply grateful to them.

I would like to thank Dr Barbara Dall who recruited the patients in the Breast Cancer Study and coordinated the collection of histology data and Dr Mark Gilthorpe who provided helpful statistical advice. Patient recruitment in two rheumatoid arthritis studies was carried out by Dr Richard Reece and Dr Philip Conaghan. I would also like to thank the team of radiographers from the LGI for carrying out clinical imaging. Many thanks to Dr Jim Meaney for his friendship and for sharing with me his enthusiasm for gadolinium.

This work is dedicated to the memory of Nikola Tesla, who also lived in foreign lands and dreamt in my obscure language and to my teacher Fadila Muhamedagić who instilled in me the love of learning.

Abstract

Abnormal angiogenesis is characterised by the alteration of physiological variables such as capillary permeability and fractional volume of the extravascular extracellular space. The aim of the work presented in this thesis was to investigate the feasibility of non-invasive measurement of these physiological variables through quantitative analysis of dynamic Gd-DTPA enhanced MRI (DEMRI) acquired using standard imaging hardware within a clinical setting.

A method for quantitative analysis of DEMRI (QDEMRI) was developed and implemented on a standard personal computer platform using a set of programs written in the C programming language. The method includes pharmacokinetic modelling of Gd-DTPA kinetics based on the modification of existing approaches and moving-window algorithms for the measurement of black-box quantifiers of DEMRI.

The measurements were performed in two angiogenesis dependent diseases: breast cancer and rheumatoid arthritis (RA). In a study involving QDEMRI analysis of 59 primary invasive breast carcinomas, a significant relationship between capillary permeability-related QDEMRI variables and tumour grade was found. In a randomised controlled study of early RA in metacarpophalangeal joints, a significant reduction in the QDEMRI variable which reflects fractional volume of the extravascular extracellular space was found three months after the start of therapy in 20 patients treated with methotrexate and intra-articular methylprednisolone injections, whereas it remained constant in a control group of 17 patients who were treated with slow-acting methotrexate only. A significant reduction in the permeability-related QDEMRI variable was detected in 17 patients treated with leflunomide four months after the start of treatment whilst it remained unchanged in 17 patients treated with methotrexate in a randomised controlled study of established RA of the knee joint.

The results obtained in this work indicate that the proposed QDEMRI method can be used in its present form to monitor treatment-induced changes in angiogenesis dependent diseases. Further work is needed to render these measurements fully independent of DEMRI acquisition settings and allow the evaluation of individual lesions.

Table of contents

List of figures

List of tables

Abbreviations

BB ..... black-box

DEMRI ..... dynamic contrast enhanced MRI

DMARD ..... disease modifying anti-rheumatic drug

EES ..... extracellular extravascular space

FOV ..... field of view

Gd-DTPA ..... gadolinium diethylene triamine pentacetic acid

GE ..... gradient echo

IACS ..... intra-articular corticosteroids

IRE ..... initial rate of enhancement

LEF ..... leflunomide

MCPJ ..... metacarpophalangeal joint

ME ..... maximal enhancement

MMCM ..... macro-molecular contrast medium

MRI ..... magnetic resonance imaging

MTX ..... methotrexate

MVD ..... microvessel density

NMR ..... nuclear magnetic resonance

PK ..... pharmacokinetic

PS ..... permeability surface area product

PV ..... plasma volume

QDEMRI ..... quantitative analysis of DEMRI

RA ..... rheumatoid arthritis

RF ..... radio frequency

SI ..... signal intensity

SNR ..... signal to noise ratio

TE.....echo time

TR..... repetition time

VCAM-1 .....vascular cell adhesion molecule 1

VEGF ..... vascular endothelial growth factor

VPF .....vascular permeability factor

WOS .....wash-out slope

Chapter 1. Introduction

The research presented in this thesis was carried out at the time when two strands of scientific endeavour which were originated in 1970s reached maturity and converged. The first one is magnetic resonance imaging (MRI) and the second is the study of angiogenesis – the process of formation of new blood vessels.

The research into angiogenesis produced mounting evidence that alterations in microcirculation (blood circulation at a capillary level) play an important, if not central role, in the pathogenesis of many neoplastic and non-neoplastic diseases [1]. At the same time, MRI reached the stage when the prospect of quantitation of physiological variables which reflect the microcirculation became feasible [2]. This convergence became of even greater interest as the study of angiogenesis moved from in-vitro and animal model investigations onto human trials and the need for non-invasive monitoring of tissue microvasculature became more acute. In addition to Doppler sonography and positron emission tomography (PET), MRI has been identified as a potential tool for non-invasive assessment of angiogenesis and monitoring of therapies in angiogenesis-dependent diseases [3].

The objective of this work was the development of a method for the measurement of physiological variables that characterise tissue microcirculation (capillary permeability and the volume of the extracellular fluid) through quantitative analysis of dynamic contrast enhanced MRI (DEMRI). This method was applied to the assessment of microcirculation in two angiogenesis dependent diseases: breast cancer and rheumatoid arthritis (RA).

In this chapter an overview of angiogenesis is presented with the aim of elucidating the importance of the measurement of these physiological variables (Section 1.1). The main features of MRI (and DEMRI in particular) that make it a potentially useful tool for non-invasive monitoring of angiogenesis dependent diseases are also presented in this chapter (Section 1.2).

In addition to the computation of descriptive quantifiers of DEMRI, the methodology used for quantitative analysis of DEMRI in this thesis included pharmacokinetic modelling of MRI contrast agent kinetics. Pharmacokinetic modelling of DEMRI in neoplastic disease has been widely studied. However, it has not yet been applied to the quantitative assessment of disease activity in clinical studies of rheumatoid arthritis. In order to justify the application of this method in RA and underline the parallels between changes in microcirculation that occur in neoplastic disease and RA, the role of angiogenesis in RA is described in a separate section (Section 7.1).

The final part of this chapter contains a description of the research project and the explanation of the contents of the subsequent chapters of this thesis.

1.1. Alterations of microcirculation in angiogenesis dependent disorders

Angiogenesis is a process central to many normal physiological functions such as embryogenesis [4, 5], wound healing [6] and the female reproductive cycle [7]. It is regulated by a complex interaction of positive (angiogenesis stimulating) and negative (angiogenesis inhibiting) factors. A delicate equilibrium between angiogenesis stimulators and inhibitors depends on numerous cellular and biochemical events [8].

Disruption of control mechanisms that govern angiogenesis results in pathological neovascularisation in both malignant and non-malignant diseases. Pathological angiogenesis can demonstrate itself as both excessive and insufficient angiogenesis. In malignant diseases, tumour growth and metastasis are driven by excessive angiogenesis [9]. Excessive angiogenesis is present in non-malignant diseases such as diabetic retinopathy [10], glaucoma [11], hemangioma [12] and rheumatoid arthritis [13]. Insufficient angiogenesis is associated with chronic myocardial ischaemia [14]. Pathological angiogenesis is regulated by the interaction between positive and negative angiogenic factors arising from both the pathological cells [15] and host tissues [16]. Therapeutic interventions capable of restoring angiogenic equilibrium by targeting key cellular and biochemical processes may lead to the control of angiogenesis-dependent diseases [17, 18].

Angiogenic cascade

Endothelial cells that form blood vessels produce angiogenic growth factors in response to injury or disease. These proteins subsequently bind to receptors on existing blood vessels and activate the production of enzymes which create holes in the basement membrane of blood vessels. Endothelial cells begin to proliferate and migrate through these holes with the aid of adhesion molecules and integrins. At the same time, enzymes such as

metalloproteinases dissolve the tissues in the vicinity of the new blood vessel and aid its further growth. The newly formed blood vessels connect into loops enabling blood to flow [19, 20].

Angiogenesis related changes in microcirculation

The principal site of nutrient delivery to tissues are blood capillaries. Their diameter is approximately 0.1 mm and they normally consist of a single layer of endothelial cells surrounded by a thin basement membrane. The bi-directional transport of materials across the capillary wall occurs via three principal routes: simple convection, osmotic and pinocytic transfer [21, 22]. Microcirculation is dictated by the metabolic activity of the tissues. In normal tissues, the properties of microvasculature are matched with the metabolic demand. Pathological angiogenesis occurs in response to an increase in metabolic demand in neoplastic and inflammatory disease but can often become decoupled from the metabolic demand and persist even when the metabolic demand of the tissue is met. Resulting pathological neovasculature has markedly different characteristics when compared to normal, host tissue capillary network: there is often an increase in microvascular density resulting from the growth of new capillary networks, vasodilatation of existing vessels, increased capillary permeability and increased volume of the extravascular extracellular space (EES).

Studies of microvascular properties of animal and human tumours have demonstrated a marked alteration of vascular and extravascular spaces in tumours as well as capillary permeability compared to the normal tissues [23]. A large degree of heterogeneity has been found between different types of tumours and also within individual tumours with regard to their microcirculatory properties.

Early morphological studies of tumour microvascular architecture in human brain tumours have revealed markedly widened intra-endothelial cell junctions in capillary walls [24]. An

increased number of endothelial cells forming the vessels with associated increase in the number of cellular junctions was also noted [25]. Areas with a markedly elevated number (and increased size) of capillary fenestrations were associated with accumulation of interstitial fluid (brain oedema). Radioactive isotope measurement of capillary permeability in transplantable rat tumours and intact intestine using ^{125}I labelled macromolecules revealed 2-5 times higher values of permeability surface area product within the tumour microvasculature when compared with the permeability of normal intestine [26]. A measurement of the extracellular fluid volume in transplantable rat tumour models by using a combination of ^{125}I labelled albumin and ^{51}Cr-EDTA also confirmed significant physiological differences between tumours and normal tissue [26]. The tumour extravascular extracellular volume ranged from 0.35 to 0.5 ml/g whereas muscle extravascular extracellular volume was markedly lower (0.13 ml/g).

Neovascular microcirculation has in recent years been a subject of intensive research with the aim of understanding the pathways of drug delivery [27]. Hyperpermeability of tumour blood vessels as well as the increase in extracellular fluid pressure have been demonstrated in-vivo in animal models using intra-vital fluorescence in a rabbit ear, hamster cheek-pouch, and mouse dorsal skin chamber and cranial window [28, 29]. The results of animal studies have been scaled-up using theoretical modelling in an attempt to translate these findings into clinically relevant information.

Surrogate markers of angiogenesis

Two surrogate markers of angiogenesis feature prominently in the clinical studies of angiogenesis. These surrogate markers are microvessel density (MVD) and vascular endothelial growth factor (VEGF) also known as vascular permeability factor (VPF). Since the validity of MRI-derived measures of microcirculation is often judged by their agreement

and relationship to these established measures, a brief description of MVD and VEGF/VPF is presented in this section.

One of the most widely used methods for quantitative assessment of angiogenesis in clinical studies is the measurement of microvessel density (MVD) as proposed by Weidner in the early 1990s [30]. Tissue samples were stained with panendothelial marker (factor VIII-related antigen). The areas presenting with highest concentration of blood vessels ("hot-spots") were identified and the number of vessels was counted using light microscopy. The results of this seminal paper demonstrated a linear relationship between the probability of metastasis and "hot-spot" MVD in 49 patients with invasive breast cancer. Since the publication of Weidner's initial report, this technique was applied in numerous studies looking at the prognostic value of MVD in breast cancer as well as other solid tumours. Gasparini presented a review of the studies where the clinical outcome in breast cancer (relapse free survival and overall survival) was compared with measurements of MVD [31]. In a majority of studies MVD was found to be a significant independent prognostic factor in breast cancer. MVD was also found to be a significant prognostic factor in other types of cancer, including prostate [32] and cervix [33] cancers. However, in some in studies, no significant relationship between MVD and clinical outcome was found. This disparity can only partially be explained by the variations in methodology including the use of different immunohistochemical markers (e.g. anti-CD31 or anti-CD34) or different vessel counting techniques (manual or automated).

VEGF (or vascular permeability factor) is a potent mitogen for endothelial cells [34]. VEGF is necessary for angiogenesis [35, 36] and it also directly regulates blood vessel permeability [37-39]. Secretion of VEGF by tumour cells is triggered by a range of stimuli, including hypoxia and the action of certain cytokines. In a majority of published studies, where VEGF levels in breast cancer were compared with clinical outcome, VEGF was found to be a significant and independent prognostic marker [31]. This finding, however, is not

unequivocal. Obermair, for example, reported no significant relationship between VEGF levels in breast cancer and clinical outcome [40]. Although there is sporadic evidence that serum VEGF (c.f. tumour VEGF) also has clinical prognostic value [41], the data currently available does not provide conclusive evidence of its utility in the assessment of angiogenesis in cancer.

1.2. Role of MRI in the non-invasive assessment of microcirculation

The main features of MRI which make it a potentially useful tool for monitoring microcirculation are its non-invasiveness, superior soft tissue contrast, high spatial and temporal resolution and the availability of safe and efficient contrast agents. In this section, each of these features will be described and the principles of quantitative analysis of DEMRI will be outlined. A more detailed description of some aspects of MRI theory which are relevant to the work presented in this thesis is presented in Chapter 2. A comprehensive treatment of physical basis and technical aspects of MRI can be found in standard textbooks such as [42] and [43], respectively. A detailed coverage of current clinical applications of MRI is presented in [44] and a review of advanced MRI applications is given in [45].

MRI is based on spatially encoded nuclear magnetic resonance (NMR) signal. The phenomenon of NMR was first described in 1946 by Bloch [46] and Purcell [47]. NMR involves selective absorption and re-emission of the electromagnetic energy in the radio-frequency (RF) range by a sample of nuclei with non-zero magnetic moments subjected to a strong static magnetic field. The fact that NMR involves energy transition in the RF (non-ionising) range accounts for its non-invasive nature and contributes to suitability for bio-medical applications. A comprehensive review of safety aspects of NMR is given in [48].

An NMR signal can be derived from the nuclei of the isotopes such as ^{1}H, ^{13}C, ^{19}F and ^{31}P (all of which possess a non-zero nuclear magnetic moment). Magnetic resonance spectroscopy (MRS) is concerned with the study of the NMR signal derived from these nuclei [49]. Due to its superior biological abundance in living tissues and high strength of its nuclear magnetic moment, the ^{1}H (hydrogen proton) is used in MRI. The following very brief description will therefore be restricted to proton (^{1}H) NMR and its aim is solely to illustrate the source of often quoted "superior MRI soft tissue contrast".

When placed inside a strong static magnetic field, a collection of ^{1}H protons forms a net magnetic moment. Following an excitation by an RF field with a characteristic resonant (Larmor) frequency, a measurable, time varying NMR signal is induced in a receiver RF coil. The resonant nature of this phenomenon is a consequence of the quantum nature of energy transitions. The dynamic behaviour of the system of protons in response to the controlled perturbation and energy transition determines the properties of the time-varying NMR signal. NMR signal is characterised by three intrinsic NMR parameters: proton density (ρ), spin-lattice or longitudinal relaxation time (T1) and spin-spin or transverse relaxation time (T2).

In living tissues, NMR signal is derived from mobile hydrogen-containing molecules. The primary tissue properties reflect not only the number of ^{1}H protons inside mobile hydrogen-containing molecules (through proton density ρ), but also characterise the mobility of these molecules (through relaxation times T1 and T2). Therefore, NMR tissue properties reflect tissue characteristics at the molecular level and provide a powerful tool for assessing not only the anatomical features of tissues but also their biochemical and pathological status. The range of values that these parameters can assume in both normal and pathological tissues is greater then that of the parameters used in other imaging modalities [50]. Furthermore, the dependence of NMR signal intensity on T1 and T2 is exponential, which further increases

the dynamic range of NMR and accounts for superior sensitivity of spatially encoded NMR (MRI) for imaging living tissues.

The first application of NMR to the diagnosis of cancer (or indeed the first attempt to utilise NMR in medical diagnosis in general) was published by Damadian [51] in 1971. He proposed that benign and malignant tissues could be differentiated on the basis of differences in spin-lattice and spin-spin relaxation times (T1 and T2) as determined in vitro with NMR spectrometers.

The arrival of MRI was marked by the publication of Lauterbur's seminal paper in 1973 [52]. The paper presented the first two-dimensional MR image obtained with the application of linear gradients for spatial localisation. The first image of the human body was published in 1977 by Damadian [53]. In the same year, a detailed image of the wrist was published by Hinshaw [54].

Over the last three decades, numerous scientific and technological advances in the field of hardware and software design have transformed MRI from an exotic, expensive imaging modality, with crude spatial resolution and prohibitively long scanning time, to a widely used clinical diagnostic and investigational tool.

Some of the most notable early methodological advancements include the introduction of Fourier imaging by Kumar [55], the development of the spin warp imaging technique by Edelstein [56] as well as the foundation of the principles of echo-planar imaging (EPI) by Mansfield [57].

Major technological developments include the design of highly homogenous wide bore superconducting magnets for clinical applications with typical magnetic field strength of 1 or 1.5 Tesla, the development of powerful gradient systems with gradient strength in excess of 20 mT/m and rise times shorter than 200 μs, as well as an improvement in the performance

of the RF coils. All these developments have lead to the improvements in signal to noise ratio (SNR) and increased spatial and temporal resolution in modern MRI systems [58].

As a result of these technological and methodological advancements, and driven by the need to eliminate image degradation by motion artefacts (both physiological and gross body motion), several rapid imaging techniques were developed in the early 1990s. They include fast gradient echo [59], fast spin echo [60] and the commercial implementation of EPI [57]. Rapid acquisition techniques have dramatically reduced MRI acquisition times. An important result of the availability of rapid imaging techniques is the possibility of dynamic scanning with temporal resolution of the order of 1 second or even as low as 0.1 second on high performance systems [45].

Another landmark in the development of MRI was the design of effective and safe contrast agents which improved the capacity of MRI to depict lesion morphology in situations where the inherent tissue contrast is not sufficient to enable accurate delineation of pathological tissue. The first MRI contrast agent approved for clinical applications was gadopentetate dimeglumine (Gd-DTPA). In 1984, the results of the first volunteer and patient studies involving intra-venous administration of Gd-DTPA were published [61, 62].

Gd-DTPA is a paramagnetic extracellular contrast agent that selectively alters MRI signal intensity (SI) throughout its distribution volume (blood plasma and extravascular extracellular fluid). The effect that Gd-DTPA exerts on MRI signal intensity results from the paramagnetic properties of the Gd^{3+} ion and its spatial relationship to the chelate (DTPA molecule) [63], whereas its pharmacokinetics is defined by the in vivo behaviour of the chelate [64]. Physiological variables that determine tissue microcirculation have a direct influence on the resulting local bulk tissue concentration of Gd-DTPA following intravenous administration [65]. In conventional (static) MRI applications, Gd-DTPA is used to delineate

tissue morphology since Gd-DTPA selectively enhances highly perfused and permeable tissues with a high extracellular volume.

Furthermore, the availability of the fast imaging sequences opened the possibility of monitoring contrast kinetics dynamically, with high temporal and spatial resolution, thus providing not only morphological, but also functional information.

The current methodological challenge is the development of strategies for quantitative analysis of DEMRI and the extraction of sequence- and platform-independent measures of the functional status of the microvasculature.

1.3. Quantitative analysis of DEMRI

MRI has in recent years revolutionised diagnostic radiology in virtually every organ system of the body [44]. Perhaps because of its seemingly inexhaustible versatility, which led to its widespread use in conventional qualitative radiology, not enough impetus existed for the development of methods for quantitative analysis of MRI.

Signal intensity (SI) in MRI, expressed in arbitrary units, is dependent not only on the fundamental tissue properties but also on the imaging system field strength, the design of acquisition sequence, the geometry and performance of the RF coils, the receiver gain setting and the method used for mapping the detected signal onto a grey level (display) scale. A direct comparison of MRI signal intensity obtained using different acquisition sequences is therefore difficult.

Interestingly, the very first application of NMR in medical diagnosis, presented an attempt to provide a quantitative measure of fundamental tissue properties, namely relaxation times T1 and T2 [51]. However, Damadian's claims that malignant tissue was uniquely defined by its

T1 and T2 values were quickly disputed by Hollis and others [66, 67]. The availability of fast imaging techniques and the recognition of the potential of DEMRI to provide functional information resulted in a renewed interest in quantitative MRI.

Methods for quantitative analysis of DEMRI can be divided into two fundamentally different groups: 'black-box' and pharmacokinetic methods.

In 'black-box' methods the effect of Gd-DTPA is quantified in terms of heuristic, descriptive parameters describing the time course of enhancement. These 'black-box' parameters include Maximal Enhancement (ME), Initial Rate of Enhancement (IRE) and Time to Peak (TTP). This method of analysis arguably does not utilise optimally the available data as information from only parts of the SI/time curves are used and the definitions of IRE, ME and TTP are based on arbitrarily chosen thresholds. It is not possible to correlate findings obtained by different pulse sequences or to compare parameters measured in different centres. In quantifying the extent of Gd-DTPA-induced contrast enhancement, no presumptions are made about the underlying physical or physiological processes. These parameters are certainly related to the physiological variables that govern tissue microcirculation but the form of this relationship is not known. Parameters such as IRE and ME might reflect an undefined combination of separate physiological factors.

In contrast to descriptive black-box analysis, pharmacokinetic methods for quantitative analysis of DEMRI provide a framework that can be used to link the physics of MRI signal acquisition and the underlying patho-physiology that governs Gd-DTPA kinetics [68-71]. Pharmacokinetic (or compartmental) modelling of Gd-DTPA kinetics allows quantification of physiologically relevant variables such as the volume of the extravascular extracellular space and capillary permeability. The development of methods for quantification of DEMRI based on pharmacokinetic (compartmental) modelling has largely centred on cancer applications and assessment of blood brain barrier integrity. Within the context of

pharmacokinetic modelling it is theoretically possible to separate the influence of physical and physiological parameters on the observed changes in SI following controlled peripheral administration of contrast agents and thus enable the interpretation of measured DEMRI signal in terms of physiological variables that characterise pathological microcirculation.

1.4. Project outline

The primary methodological aim of this project was the formulation of a method suitable for quantitative analysis of DEMRI studies acquired in a clinical setting. The development of the method involved a modification of the existing approaches for pharmacokinetic modelling of Gd-DTPA enhanced DEMRI [68, 69, 71] with the aim of extracting maximal information within the constraints imposed by the need to perform image acquisition within a clinical setting, as part of a comprehensive clinical protocol.

This method for quantitative analysis of DEMRI (QDEMRI analysis) was applied in three clinical studies in order to assess its potential to extract physiologically relevant quantifiers of microcirculation.

The first study involved the application of QDEMRI analysis in breast cancer (the Breast Cancer Study). In the second clinical study, QDEMRI analysis was applied in the assessment of rheumatoid arthritis in the metacarpophalangeal (MCP) joints (MCPJ). This study will be referred to as the Hand RA Study. The third study involved the application of QDEMRI analysis in rheumatoid knee joints (the Knee RA Study).

Implicit functional validation of this method was performed by investigating the relationship between the measured QDEMRI variables related to capillary permeability and histologically determined tumour grade in the Breast Cancer Study.

In the Hand RA Study, QDEMRI analysis was performed in a randomised study of the therapeutic effect of two established anti-rheumatic therapies with known differences in the timing of action: intra-articular corticosteroid (IACS) methylprednisolone and methotrexate (MTX). QDEMRI analysis of MCPJs was undertaken at baseline (immediately before the initiation of treatment) and at three and twelve months after the baseline assessment. Due to the known effect of intra-articular steroids on the rapid reduction of tissue oedema, and consequently the volume of the extracellular space in the synovial tissue, this study provided a framework for implicit functional validation of QDEMRI variable related to the volume of the extracellular space.

In the third study (Knee RA Study), QDEMRI was undertaken as a part of a randomised multicentre study to investigate the treatment effectiveness of a novel anti-rheumatic drug, leflunomide (LEF), compared to the effectiveness of an established anti-rheumatic drug MTX. The measurements were performed at baseline and at four months after the start of treatment with the aim of investigating the potential of QDEMRI variables to measure possible subclinical differences in treatment effectiveness between these two therapeutic agents.

The results of the QDEMRI analysis include the measurements of three pharmacokinetic variables: A, k_{21} and Ak_{21}. Throughout the text these variables will be referred to as pharmacokinetic (PK) variables. As will be explained in Chapter 3, these variables are proportional to the physiological variables: the volume of the extravascular extracellular fluid EES (A, Ak_{21}) and capillary permeability (k_{21}, Ak_{21}). In addition to the measurement of PK variables, two black-box (BB) variables were measured in all three studies. These BB variables are: maximal enhancement (ME) and initial rate of enhancement (IRE). In the Breast Cancer study, one additional BB variable, washout slope (WOS) was measured as well. The illustration of BB variables is presented in Chapter 4.

In the Hand RA and Knee RA studies, QDEMRI analysis was performed on a voxel-by-voxel basis, in contrast to the Breast Cancer Study, where PK and BB parameters were derived from discrete regions of interest (ROIs). This is why the results of the Hand RA and Knee RA studies include two additional parameters: the total voxel counts obtained in BB and PK analysis (N-BB and N-PK). A summary of all measured variables, including their symbols and units is presented in Appendix A.

A relationship between MRI signal intensity and local tissue concentration of Gd-DTPA is described in Section 2.4. A general description of compartmental modelling is presented in Section 2.5. An overview of principal models for pharmacokinetic analysis is presented in Chapter 3.

A development of the model used for the extraction of PK variables is presented in Chapter 4. This section also includes the results of the Monte Carlo modelling which was undertaken to guide the practical implementation of the method which is described in Chapter 5.

The results of the Breast Cancer Study are presented in Chapter 6 and Chapter 7 contains the results of two RA studies. Finally, Chapter 8 includes a summary and the interpretation of the findings of this project.

Chapter 2. Theory of Gd-DTPA enhanced MRI

DEMRI can adequately monitor the temporal variation of Gd-DTPA concentration only if the Gd-DTPA induced change in SI is sufficiently high, if the relationship between DEMRI signal intensity and underlying Gd-DTPA concentration is known over the range of tissue concentrations expected in clinical examinations and if the DEMRI signal can be collected with an adequate temporal resolution. Once the link between DEMRI signal intensity and Gd-DTPA concentration in the tissue sample C = Ct(t) is established, the resulting Ct(t) can be analysed within the framework of pharmacokinetic modelling to extract physiologically relevant pharmacokinetic variables that determine Gd-DTPA kinetics at a capillary level. The understanding of this mechanism of enhancement and its dependence on physical factors related to the DEMRI acquisition properties as well as systemic physiological factors (such as the temporal behaviour of Gd-DTPA in blood plasma) is necessary for the quantitation and interpretation of the observed DEMRI signal extracted from a lesion.

Therefore, the first step in the assessment of Gd-DTPA kinetics through the analysis of DEMRI is the formulation of the link between the MRI signal intensity and underlying bulk tissue concentration of Gd-DTPA. Signal intensity (SI) in magnetic resonance imaging (MRI) is a complex function of multiple factors including three unique intrinsic properties of tissues

(proton density (ρ), and relaxation times T1 and T2). Whereas other inherent tissue properties such as physiological flow, diffusion, susceptibility, chemical shift and magnetisation transfer also have an influence on SI, the SI enhancement utilised in this work is primarily defined by the alteration of relaxation times in the presence of a paramagnetic contrast agent Gd-DTPA. In this chapter, a link between Gd-DTPA concentration in tissues and resulting relaxation times is described (Section 2.4.1) and the resulting dependence of the MRI signal intensity of the spoiled gradient-echo sequences is derived (Section 2.4.2). For a detailed treatment of the MRI theory, the reader is referred to books by Abragam, Bradley et al and Haacke et al [42, 43, 45]. A comprehensive review of clinical applications of MRI is presented by Stark et al [44].

This chapter also includes the general description of pharmacokinetic modelling (Section 2.5) and an illustration of the application of this method for the assessment of Gd-DTPA kinetics (Section 2.5.2). The observed temporal variation of Gd-DTPA concentration in a tissue sample C = Ct(t) is described in terms of pharmacokinetic parameters that define the rate of extravasation (which is related to the capillary permeability) and the locally available distribution volume of the Gd-DTPA (the volume of the EES). The principles of pharmacokinetics and compartmental modelling are discussed in detail in a book by Wagner [72].

2.1. Origin of MR signal

A hydrogen (^{1}H) proton has an intrinsic angular momentum (spin) $\vec{I}$ which gives rise to the proton magnetic moment $\vec{\mu} = \gamma\hbar\vec{I}$, where γ represents gyromagnetic ratio and $\hbar$ represents Planck's constant h/2π (γ = 42.6 MHz/T for a ^{1}H proton). When placed inside a strong static magnetic field $\vec{B}_0 = \vec{k}B_0$ (where $\vec{k}$ represents the unit vector of the axis along which $\vec{B}_0$ is applied), proton magnetic moments exhibit precessional motion with a characteristic

Larmor precessional frequency $\omega_o = \gamma B_0$ ($\vec{\omega}_o = -\gamma \vec{B}_0$). They can assume only discrete energy states (Zeeman energy levels) which are determined by their spin quantum number I. In a large collection of protons in thermal equilibrium, a preferential adoption of the lower energy state results in the formation of a net magnetic moment $\vec{M} = \vec{k}M_0$ (equilibrium magnetisation) which is aligned parallel to the axis of the static field $\vec{B}_0$ and represents a vector sum of individual proton magnetic moments $\vec{\mu}$. If $\vec{M}$ is represented as a vector sum of the longitudinal magnetisation $\vec{M}_z$ (the component parallel to the axis of the field $\vec{B}_0$) and transverse magnetisation $\vec{M}_{tr}$ (the component perpendicular to the axis of the field $\vec{B}_0$), in thermal equilibrium $\vec{M} = \vec{M}_z + \vec{M}_{tr} = \vec{M}_z = \vec{k}M_0$, since $\vec{M}_{tr} = 0$.

The measurement of the amplitude of the equilibrium magnetisation, although theoretically possible [42], would be of little interest since it depends only on proton density (ρ) and the average strength of the individual proton magnetic moments. If, however, the system of ^1H protons is subjected to the second, oscillating magnetic field $\vec{B}_1$ perpendicular to the axis of $\vec{B}_0$, the energy is absorbed by the sample. $\vec{B}_1$ oscillates with the frequency equal to the Larmor frequency of precession, which belongs to the RF range of the electromagnetic spectrum, hence $\vec{B}_1$ is also called an RF field). The resonant nature of this perturbation stems from the quantum behaviour of individual magnetic moments. Energy absorption is possible only if the supplied energy corresponds to the difference between adjacent Zeeman energy levels, which is given by $\Delta E = \gamma \hbar B_0 = \hbar \omega_0$, i.e. the energy of transition is defined by the Larmor frequency ω_0. Macroscopically, as a result of the excitation by an RF field $\vec{B}_1$, a transient, time varying component of $\vec{M}$ will be created in the plane perpendicular to the axis of the static field $\vec{B}_0$ (i.e. transverse magnetisation $\vec{M}_{tr} \neq 0$). Time varying $\vec{M}_{tr}$ is capable of inducing a voltage in a receiver coil (Faraday's law of induction). At the same time, longitudinal magnetisation $\vec{M}_z$ will be depleted ($|\vec{M}_z| < M_0$) or completely destroyed ($|\vec{M}_z| = 0$), depending on the strength and the duration of the applied RF field $\vec{B}_1$ [43].

2.2. Relaxation mechanisms

Following excitation, the system will gradually regain its equilibrium, through the interaction of individual magnetic moments with the surrounding lattice and through the interaction between the neighbouring protons.

The behaviour of the system of protons in a liquid sample following energy absorption can be described by a set of phenomenological Bloch equations [46]. These equations describe the process of the restoration of longitudinal magnetisation (longitudinal relaxation) and the decay of transverse magnetisation (transverse relaxation) as a function of two exponential constants T1 and T2, respectively. The modified Bloch equation (expressing Bloch equations in a closed vector form), which incorporates the influence of an oscillating RF magnetic field $\vec{B}_1$, assuming $\left|\vec{B}_0\right| >> \left|\vec{B}_1\right|$ is presented in Eq. 2-1 [43].

$$\frac{d\vec{M}}{dt} = \gamma\vec{M} \times (\vec{k}B_0 + \vec{B}_1) - \frac{\vec{M}_{tr}}{T2} - \vec{k}\frac{M_z - M_0}{T1} \qquad \text{Eq. 2-1}$$

Spin-lattice or longitudinal relaxation time T1 characterises the exponential time constant of the process of restoring the equilibrium magnetisation following the excitation by an RF pulse. This process essentially involves energy dissipation, the transfer of absorbed energy to the surrounding lattice. Again, on a quantum level, this energy transition can only be achieved through energy transitions between adjacent Zeeman energy levels. The rate of longitudinal relaxation (and consequently T1) depends on the local availability of molecules with molecular tumbling rate which corresponds to the Larmor frequency.

Spin-spin or transverse relaxation time T2 is an exponential time constant of the process of progressive loss of phase coherence of the transverse magnetisation. This process is caused by the interaction between neighbouring magnetic moments and, unlike longitudinal relaxation, does not involve energy transitions. In practice, the process of dephasing is

accelerated by the presence of local magnetic field inhomogeneities and therefore transverse relaxation follows a faster exponential decay, defined by an effective transverse relaxation time $T2^* < T2$.

Whereas relaxation time constants T1, T2 and T2* influence the temporal behaviour of the NMR signal following excitation, proton density (ρ) determines the overall amplitude of the detected signal (through its influence on M_0).

By using a set of appropriate boundary conditions, theoretically predicted $\vec{M}_{tr}$ and $\vec{M}_z$ at any time point following excitation can be derived from the expression presented in Eq. 2-1. If the application of $\vec{B}_1$ (where $B_1 = |B_1| e^{-i\varpi_0 t}$ in complex notation) results in the nutation of $\vec{M}$ through 90° (i.e. the flip angle $\varphi = 90°$) and if the relaxation during the application of $\vec{B}_1$ is ignored, boundary conditions $M_x(0) = 0$, $M_y(0) = M_0$ and $M_z(0) = 0$ apply, and the solution to the system of Bloch equations yields the following expressions for M_x, M_y and M_z:

$$\left.\begin{aligned} \frac{dM_x}{dt} &= \omega_0 M_y - \frac{M_x}{T2} \\ \frac{dM_y}{dt} &= -\omega_0 M_x - \frac{M_y}{T2} \\ \frac{dM_z}{dt} &= -\frac{M_z - M_0}{T1} \end{aligned}\right\} \quad \left\{\begin{aligned} M_x &= M_0 \sin(\varpi_0 t) e^{-\frac{t}{T2}} \\ M_y &= M_0 \cos(\varpi_0 t) e^{-\frac{t}{T2}} \\ M_z &= M_0 (1 - e^{-\frac{t}{T1}}) \end{aligned}\right. \qquad \text{Eq. 2-2}$$

The vector $\vec{M}_{tr}$ has a time varying amplitude $M_{tr} = M_0 e^{-\frac{t}{T2}}$. Similarly, if a sample is repeatedly excited by the application of RF pulses with a repetition time TR and a flip angle φ, the solution of the Bloch equation will give an expression for $\vec{M}_z$ after n successive excitations (Eq. 2-3).

$$M_z(nTR) = M_0\left[(1-e^{-\frac{TR}{T1}})\frac{1-\cos^n\varphi\cdot e^{-\frac{nTR}{T1}}}{1-\cos\varphi\cdot e^{-\frac{TR}{T1}}}+\cos^n\varphi\cdot e^{-\frac{nTR}{T1}}\right] \qquad \text{Eq. 2-3}$$

Steady state longitudinal magnetisation and the amplitude of transverse magnetisation at time TE (echo time) following the application of an RF pulse (and assuming that $\vec{M}_{tr}=0$ prior to the application of each RF pulse), is given by expression in Eq. 2-4.

$$M_z(TR) = M_0\frac{(1-e^{-\frac{TR}{T1}})}{1-\cos\varphi\cdot e^{-\frac{TR}{T1}}}$$

$$M_{tr}(TE) = M_0\frac{(1-e^{-\frac{TR}{T1}})}{1-\cos\varphi\cdot e^{-\frac{TR}{T1}}}\sin\varphi\cdot e^{-\frac{TE}{T2^*}} \qquad \text{Eq. 2-4}$$

This excitation scheme is the basis of the spoiled gradient echo (GE) sequence, which is often used in DEMRI studies. The relationship between the measured signal intensity in MRI (which is proportional to $M_{tr}(TE)$ in the equation Eq. 2-4) on relaxation times T1 and T2* is dependent upon the choice of acquisition parameters TR, TE and φ. The choice of imaging parameters therefore determines the sensitivity of the signal to changes in T1 and T2* (T1 or T2* weighting) and will be discussed further in Section 2.4, in the context of Gd-DTPA enhanced MRI.

2.3. MR image formation

A very brief treatment of the process of image formation is presented in this section with the aim of illustrating the spatial and temporal aspects of MR image formation which have a direct bearing on the capacity of DEMRI to allow the assessment of dynamic physiological processes. The method for spatial encoding of NMR described here was based on the

method of Fourier zeugmatography proposed by Kumar et al [55] and modified by Edelstein et al ("spin-warp" technique, [56]).

The signal derived from a volume element (voxel) dxdydz following an excitation by and RF pulse is proportional to the time varying transverse magnetisation $\overrightarrow{M}_{tr} = \overrightarrow{M}_{tr}(x,y,z)$, where x, y and z represent the spatial coordinates of the voxel. This vector can be represented in a complex form and characterised by time-varying amplitude and phase, and the signal detected in a quadrature receiver coil is also a complex quantity (S). The signal emanating from the entire sample volume is then given as a sum (or a volume integral) of the contributions from all voxels in the volume (Eq. 2-5). In equation Eq. 2-5, S and M_{tr} correspond to the complex representations of the measured signal and longitudinal magnetisation, respectively and ξ represents a constant of proportionality determined by the receiver circuit settings (and assuming spatially invariant $\xi=\xi(x, y, z) = \text{const.}$).

$$S = \xi \iiint M_{tr}(x,y,z)dxdydz \qquad \text{Eq. 2-5}$$

If the spatial modulation of the phase of M_{tr} is performed by introducing a controlled time- and space-variant phase shift θ, where θ is given as:

$$\theta = k_x x + k_y y + k_z z \qquad \text{Eq. 2-6}$$

and where k_x, k_y and k_z represent spatial frequency (k-space) coordinates expressed in rad/m, the measured signal S can be expressed as:

$$S(k_x, k_y, k_z) = \xi \iiint M_{tr}(x, y, z) \cdot e^{j(k_x x + k_y y + k_z z)} dx dy dz \qquad \text{Eq. 2-7}$$

i.e. S represents a 3D Fourier transformation of the spatial distribution of $M_{tr}(x, y, z)$. Therefore, the application of an inverse 3D Fourier transform on a signal sampled in k-space domain $S(k_x, k_y, k_z)$ yields an image of $M_{tr}(x, y, z)$ in a spatial domain – an MR image.

In practice, spatial modulation of θ is achieved by selectively altering the magnitude of the static field B_0 throughout the sample volume through the application of linear magnetic field gradients in three orthogonal directions G_x, G_y and G_z. The magnitude of the effective magnetic field B experienced by a voxel located at (x, y, z) in the presence of linear gradients is given as:

$$B = B_0 + xG_x + yG_y + zG_z \qquad \text{Eq. 2-8}$$

The resultant Larmor frequency at any location in the sample is given as:

$$\omega = \omega_0 + \gamma x G_x + \gamma y G_y + \gamma z G_z \qquad \text{Eq. 2-9}$$

The fast frequency component ω_0 is removed from the signal by demodulation [43] and the expression for θ (Eq. 2-6) becomes:

$$\theta = k_x x + k_y y + k_z z = \gamma \int \left(x G_x(t) + y G_y(t) + z G_z(t) \right) dt \qquad \text{Eq. 2-10}$$

The signal sampling in the k-space domain is performed in discrete steps by adjusting the timing and the amplitude of linear gradients and thus selecting different coordinates k_x, k_y and k_z. This process is referred to as frequency (k_x) and phase (k_y and k_z) encoding.

The MR image (containing amplitude and phase information) is obtained by performing an inverse 3D Discrete Fourier Transform (DFT) on a complex matrix $S(k_x, k_y, k_z)$.

The process of image formation is illustrated below, using as an example a two-dimensional spoiled GE sequence, where M_{tr} is described by the equation Eq. 2-4. The timing of the excitation (RF) pulses and the linear gradients (pulse sequence diagram) is illustrated in Figure 2-1.

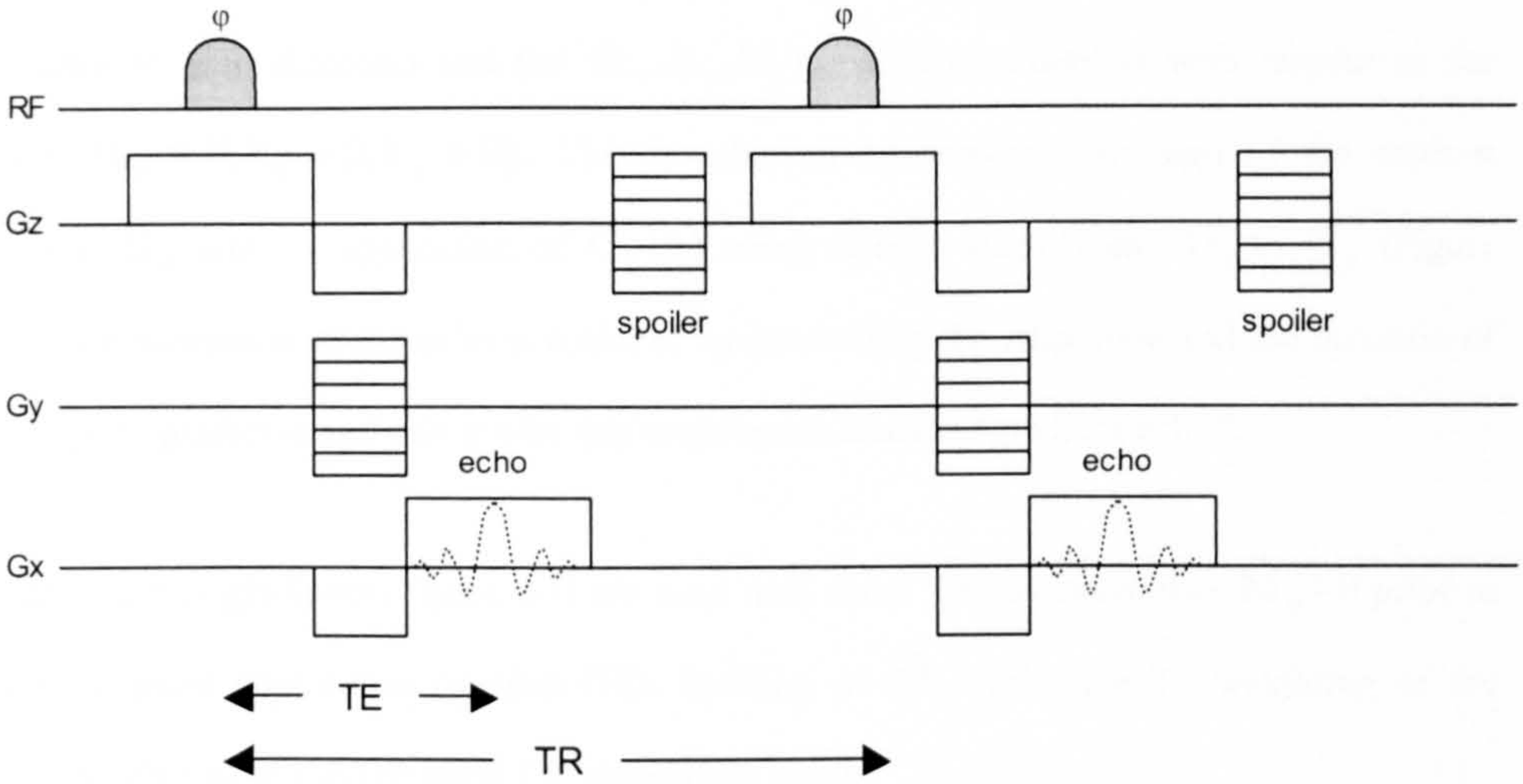

Figure 2-1 Pulse sequence diagram for a spoiled GE sequence

A slice selective excitation by an RF pulse is achieved by the application of G_z during the excitation, thus ensuring that a single slice (x, y, z = const) is excited. The selected slice has a finite thickness determined by the strength of the G_z gradient and the bandwidth of the applied RF pulse. Next, the phase encoding G_y gradient is switched on with amplitude $G_y(n)$ and duration T_y, thus creating a phase shift of $\gamma G_y(n) T_y y$ and selecting a single line of the two-dimensional k-space matrix (k_x, $k_y = \gamma G_y(n) T_y$). During the signal readout, G_x is switched on and this gradient creates a phase shift of $\gamma G_x t_m x$, where t_m represent discrete time points during the signal sampling, ensuring that a single line of k-space matrix is traversed ($k_x = \gamma G_x t_m$, $k_y = \gamma G_y(n) T_y$). As m varies from 1 to Nx, Nx

elements of a single line of k-space are collected during the signal readout (this process is referred to as frequency encoding). In each repetition cycle (TR) one line of k-space is acquired. To sample an entire 2D matrix (Nx x Ny) elements, this procedure is repeated Ny times, where Ny represents the number of phase-encoding steps. In each successive phase-encoding step, a different amplitude of $G_y = G_y(n)$ is selected, and thus Ny lines of k-space, characterised by $(k_x,\ k_y = \gamma G_y(n) T_y)$ are sampled with n = 1 to Ny. The total imaging time required for the reconstruction of a single 2D slice is given by TR x Ny. In the practical implementation of this method of spatial encoding, k-space matrix contains 2^n elements in each direction and the (k_x, k_y, k_z) matrix symmetrical with respect to the origin $(k_x = 0, k_y = 0, k_z = 0)$. This is achieved by reversing the sign of the readout gradient G_x and the application of $G_y(n)$ using discrete steps from $-G_y$ to G_y (Figure 2-1). The formation of the echo is achieved by controlling the amplitude and the duration of the applied gradients and this is why this sequence is labelled "gradient echo".

Finally, spoiler gradients (Figure 2-1) are used with short TR to ensure that $\vec{M}_{tr} = 0$ prior to each RF pulse application (spoiled GE). Spoiling of $\vec{M}_{tr}$ enhances T1 weighting of the signal by eliminating the residual T2* dependent signal.

To sample a 3D matrix containing Nx × Ny × Nz elements, the signal needs to be read out Ny × Nz times, requiring often prohibitively long acquisition time of TR × Ny × Nz. However, due to the Hermitian symmetry of the k-space, partial filling of matrix elements can be used, thus reducing the overall imaging time. Furthermore, fast imaging techniques allow the acquisition of multiple lines of k-space during a single TR interval (segmented k-space) or even the sampling of an entire 2D matrix within a single TR as in single-shot EPI.

The relationship between signal to noise ratio, image contrast, temporal and spatial resolution in MRI can be illustrated using this 2D sequence as an example, although the general principles apply to any MRI sequence [43].

The volume of the image voxel (with slice thickness δz) is $\delta V = \delta x \times \delta y \times \delta z$, where δx and δy are related to the field of view (FOV) in each direction (Lx and Ly, respectively) by the expression:

$$\delta V = \delta x \times \delta y \times \delta z = \frac{Lx}{Nx} \times \frac{Ly}{Ny} \times \delta z \qquad \text{Eq. 2-11}$$

The time required to acquire a single slice is determined by the product TR × Ny, i.e. the temporal resolution is TR × Ny. Signal to noise ratio (SNR) is also a function of spatial and temporal acquisition settings. SNR is defied as the ratio of the signal intensity and the square root of the noise variance, and for a sample element δV SNR is given as:

$$SNR = \frac{S}{N} \propto \frac{M_{tr} \times \delta V}{\sqrt{\frac{\upsilon_s}{Nx \times Ny}}} = \frac{M_{tr} \times \delta V}{\frac{1}{\sqrt{Nx \times Ny \times \tau_s}}} = M_{tr} \frac{\frac{Lx}{Nx} \times \frac{Ly}{Ny} \times \delta z}{\frac{1}{\sqrt{Ny \times Ts}}} \qquad \text{Eq. 2-12}$$

where Ts represents total sampling time and τ_s represents dwell time or the sampling interval used in analogue to digital conversion (ADC) of the signal in the frequency encoding direction (sampling bandwidth υ_s is defined as $1/\tau_s$, and $Ts = Nx \times \tau_s$).

$$SNR \propto M_{tr} \delta V \sqrt{Ny \times Ts}$$

$$SNR \propto M_{tr} \frac{Lx}{Nx} \frac{Ly}{Ny} \delta z \sqrt{Nx \times Ny \times \tau_s} = M_{tr} \frac{Lx \times Ly}{\sqrt{Nx \times Ny}} \delta z \sqrt{\tau_s} \qquad \text{Eq. 2-13}$$

Whilst at constant FOV the temporal resolution can be increased by reducing Ny, this will result in the loss of spatial resolution (Eq. 2-11). Temporal resolution can also be reduced if TR is reduced. However, the SNR is proportional to M_{tr} (Eq. 2-13) which in turn depends on TR (Eq. 2-4) and very short TR values will result in a low SNR. Higher SNR can be achieved by using longer TR with concurrent loss of T1 weighting. Furthermore, imaging larger voxels (by increasing FOV) will lead to an increase in SNR accompanied by the loss of

spatial resolution. Conversely, increasing the matrix size will lead to the reduction of voxel volume and cause SNR loss according to (Eq. 2-13). Therefore, the increase in spatial resolution which is necessary for the detection of small lesions or assessment of lesion heterogeneity has to be balanced against the concomitant SNR loss. And finally, increasing tissue coverage by imaging multiple slices increases the temporal resolution by the factor Ns (number of slices) in 2D imaging. If higher values of TR are used, multiple slice imaging within a single TR interval is possible. However, this also has consequences on the contrast behaviour of the signal.

Therefore, the relationship between temporal and spatial properties in MR imaging as well as image contrast and SNR is very complex: the requirements for large tissue coverage and high spatial resolution must be balanced against the overall imaging time which is a direct function of the number of voxels sampled. Furthermore, signal to noise ratio (SNR) and the contrast properties in MR imaging, also depend on the chosen acquisition sequence parameters.

This relationship plays an important part in conventional, static imaging, where the achieved image quality (SNR and contrast properties), spatial resolution and tissue coverage must be balanced against the overall duration of the examination and problems related to gross patient motion. However, in abdominal imaging and DEMRI applications, the balance between these opposing requirements is particularly delicate, since the time-scale of the physiological motion and the rate of dynamic processes imposes much more severe constraints on the acceptable duration of the image acquisition.

The exact choice of the imaging sequence, acquisition parameters and other parameters such as field of view, matrix size, slice thickness and orientation, depends on the information being sought. MRI provides great flexibility in this respect and by careful tailoring of the imaging protocols it is possible to acquire images suitable for assessing a wide range of conditions.

However, in certain pathological states, intrinsic tissue properties do not provide sufficient contrast between the lesion and surrounding tissue. In such situations, optimisation of sequence parameters can provide only marginal improvements in the visualisation of the lesion, especially if the lesion size is small and partial volume effects further diminish the contrast.

Application of exogenous contrast agents can, however, create sufficient contrast between the lesion and the adjacent tissue if the microvascular properties of the lesion differ significantly from its surroundings thus further improving sensitivity and specificity of MRI. In the following sections, the mechanisms by which exogenous paramagnetic contrast agent Gd-DTPA alters primary tissue parameters and resulting signal intensity will be described.

2.4. Gd-DTPA induced changes in MRI signal intensity

The phenomenon of enhancement of proton relaxation in aqueous solutions through the interaction of magnetic moments of protons and large paramagnetic ions was fist described by Solomon and Bloembergen [73, 74].

The magnitude of this relaxation effect depends primarily on the number of unpaired electrons in the valence shell of the paramagnetic species. The gadolinium ion (Gd^{3+}) belongs to the lanthanide metal group and is an effective relaxation agent primarily due to its large number of unpaired electrons (Table 2-1).

	Valence shell configuration	Number of unpaired electrons	Net magnetic moment (magnetons)	Electron spin relaxation time (ms)
Gd^{3+}	4f7	7	7.6	10^{-5} - 10^{-6}

Table 2-1 Gd3+ properties

The proton relaxation enhancement, however, could not be utilised in MR applications before the effective means of chelating paramagnetic ions to suitable molecules (such as DTPA) became available. This was necessary because of the considerable toxicity of ions such as Gd^{3+}. Chelating agents prevent trapping of these toxic ions in tissues and ensure complete excretion of toxic ions from the body [75].

2.4.1. Effects of Gd-DTPA on relaxation times

Linear relationships between the change in proton relaxation rates and Gd-DTPA concentration were found in aqueous solutions of Gd-DTPA and also experimentally demonstrated for solutions in biological fluids as well as tissues [76, 77].

The relationship between tissue relaxation rates and local tissue concentration of the contrast agent is given in Eq. 2-14.

$$\frac{1}{T1_C} = \frac{1}{T1_0} + \alpha C$$
$$\frac{1}{T2_C} = \frac{1}{T2_0} + \beta C \qquad \text{Eq. 2-14}$$

Equations describing the shortening of relaxation times in the presence of Gd-DTPA

In Eq. 2-14 subscript C denotes relaxation times in the presence of Gd-DTPA at a bulk tissue concentration of C expressed in mM = mmol/l, and subscript 0 denotes native relaxation times (for C = 0). Parameters α and β are contrast agent relaxivity constants (expressed in $(mMs)^{-1}$).

In gradient echo (GE) sequences (and fast imaging sequences derived from GE) effective transverse relaxation rate is related to the native transverse relaxation rate according to the following expression:

$$\frac{1}{T2^*} = \frac{1}{T2} + \gamma \frac{\Delta B_0}{2} \qquad \text{Eq. 2-15}$$

where γ stands for gyromagnetic ratio and ΔBo represents local field inhomogeneity. Shortening of the effective transverse relaxation time T2* is related to local bulk tissue concentration of Gd^{3+} and is described by the expression Eq. 2-16, where β' represents T2* relaxivity constant.

$$\frac{1}{T2^*_C} = \frac{1}{T2^*_0} + \beta' C \qquad \text{Eq. 2-16}$$

The shortening of relaxation times in the presence of Gd-DTPA is illustrated in Figure 2-2. Native T1 of the tissue was assumed to be 1000 ms and effective transverse relaxation time T2* was 100 ms. Relaxivity constants for T1 and T2* are α = 4.5 $(mMs)^{-1}$ and $\beta = \beta' = 5.5$ $(mMs)^{-1}$ respectively [78]. The range of Gd-DTPA concentrations is presented on the horizontal axis (using a logarithmic scale). Although both relaxation times are reduced in the presence of Gd-DTPA, the relative effect on T1 is much more pronounced, given the higher initial value of T1 ($T1_0$).

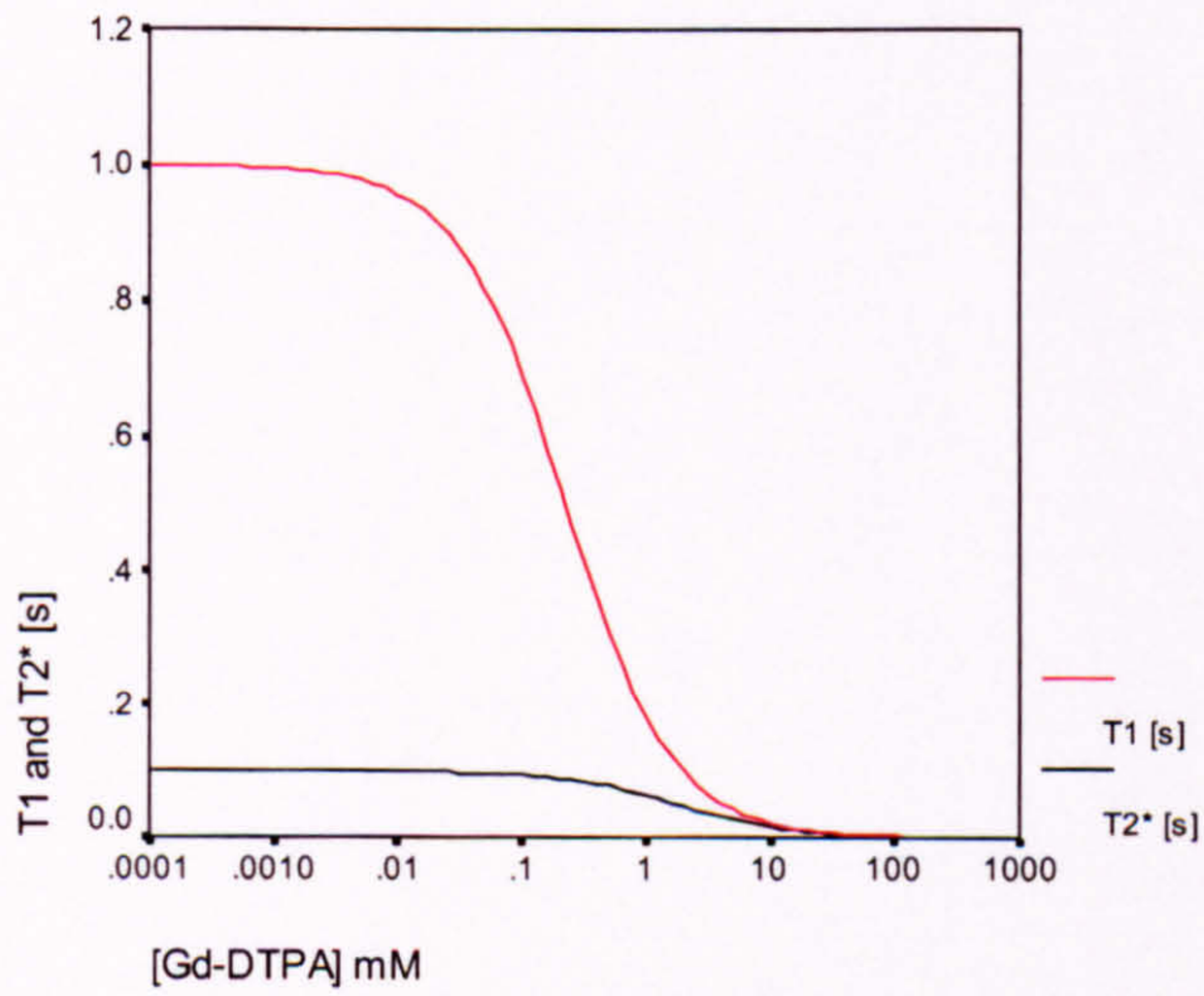

Figure 2-2 Shortening of the relaxation times in the presence of Gd-DTPA

In the following section, the influence of the shortening of relaxation times in the presence of Gd-DTPA on the measured signal intensity is described.

2.4.2. Effect of Gd-DTPA on signal intensity in MRI

Signal intensity in spoiled gradient echo (GE) sequences is given in Eq. 2-17 [43]. This expression reflects the dynamic behaviour of M_{tr}, as described in Eq. 2-4. In addition to intrinsic tissue properties, SI is defined by sequence parameters TR, TE and flip angle (φ). Consequently, the contrast between the tissue of interest and the surrounding tissues will depend on the differences in inherent parameters as well as the selection of the imaging parameters. As can be seen from the expression Eq. 2-17 below, SI will be increased in response to T1 shortening brought about by the introduction of Gd-DTPA. However, concomitant shortening of T2* will lead to the signal loss.

$$S = k\rho \frac{1 - e^{-\frac{TR}{T1}}}{1 - \cos\varphi \cdot e^{-\frac{TR}{T1}}} e^{-\frac{TE}{T2^*}} \sin\varphi \qquad \text{Eq. 2-17}$$

Spoiled GE sequence signal intensity

In DEMRI, SI is measured prior to the administration of the contrast and this signal represents baseline SI (S_0 at C = 0) and at discrete time intervals following the administration of contrast (S_C) whereupon relaxation rates experience shortening according to the equations Eq. 2-14 and Eq. 2-16, as illustrated in Figure 2-2. The resulting changes in Gd-DTPA concentration in the tissue sample will give rise to a corresponding change in measured SI. The normalised SI, i.e. the ratio of the SI measured in the presence of Gd-DTPA at concentration C and baseline SI is therefore a function of Gd-DTPA concentration (Eq. 2-18).

$$\frac{S_C}{S_0} = f(C) \qquad \text{Eq. 2-18}$$

The normalised SI is plotted against Gd-DTPA concentration (displayed on a logarithmic scale) in Figure 2-3. Whereas at low Gd-DTPA concentrations, normalised SI rises in response to the increased concentration of Gd-DTPA, it is apparent that at high Gd-DTPA concentrations signal loss, rather than signal increase occurs as can be seen from Figure 2-3 where normalised SI drops below unity at the high end of the Gd-DTPA concentration axis.

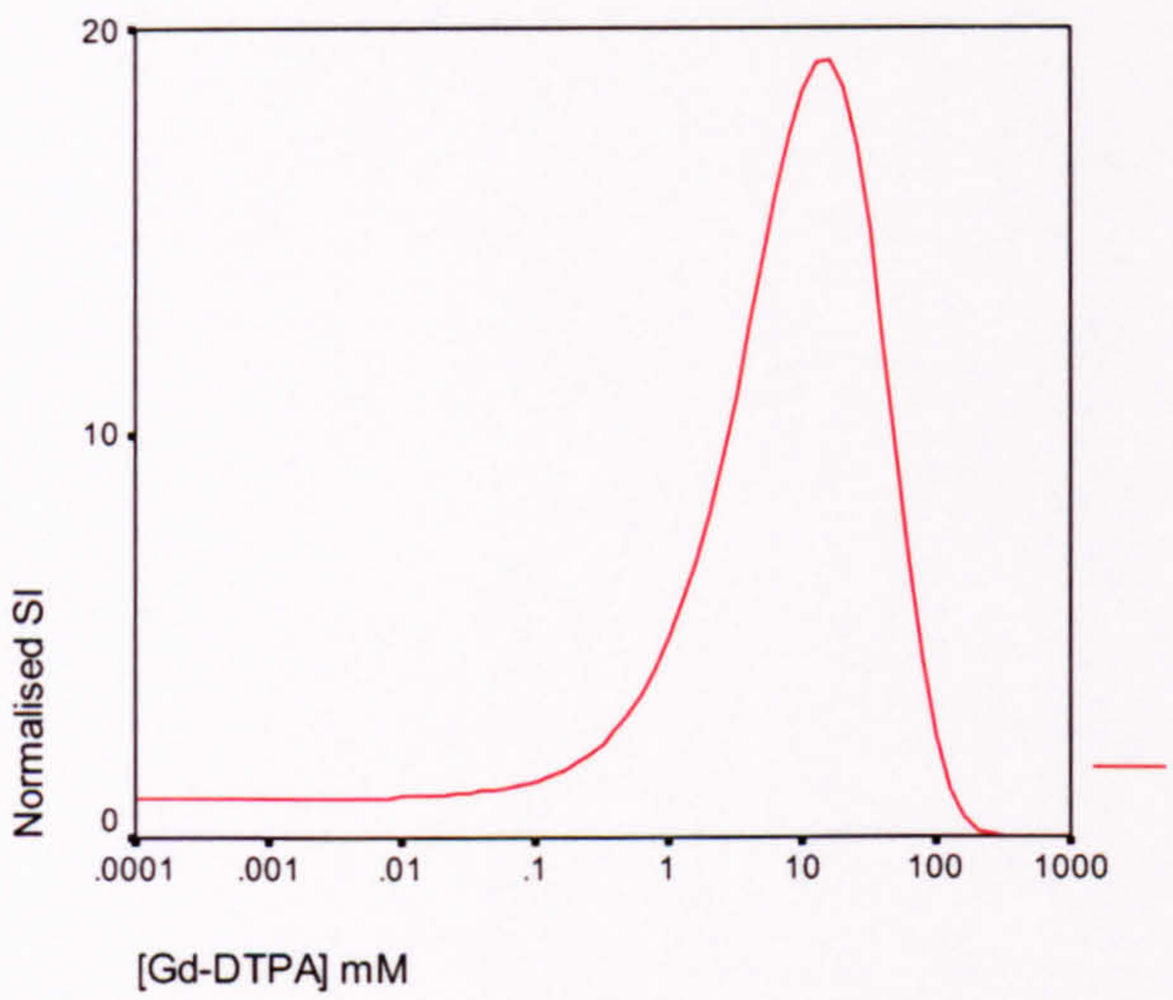

Figure 2-3 Illustration of normalised SI change with varying Gd-DTPA concentrations

The graph in Figure 2-3 represents the relative change of SI over baseline for a spoiled T1 weighted GE sequence with TR/TE/φ = 13/4.6/60°, $T1_0$ = 1000 ms, $T2_0^*$ = 100 ms and relaxivity constants α = 4.5 $(mMs)^{-1}$ and $\beta = \beta'$ = 5.5 $(mMs)^{-1}$, respectively, as in Figure 2-2. With increasing Gd-DTPA concentration, normalised SI measured using this particular acquisition sequence theoretically rises up to a value of 19 at the concentration of 16 mM. Any further increase in Gd-DTPA concentration leads to progressive decrease of normalised SI. This means that at very high Gd-DTPA concentrations, normalised SI is not uniquely determined by the underlying Gd-DTPA concentration in the tissue sample. However, at

higher Gd-DTPA concentrations actual T2* relaxivity constant β' may be considerably higher than $\beta = 5.5\ (mMs)^{-1}$ [79] and the progressive signal loss may occur at lower Gd-DTPA concentrations than those illustrated in Figure 2-3.

In clinical applications, only a narrow range of concentrations presented in Figure 2-2 and Figure 2-3 is achieved following Gd-DTPA administration at a standard dose of 0.1 mmol/kg body weight. Gd-DTPA concentrations as high as 3 mM are achieved only during the first pass in the blood pool [80]. Well perfused tissues typically reach a concentration of well below 0.9 mM which represents a theoretical upper limit for equilibrium Gd-DTPA concentration in the blood pool, liver, kidney and spleen combined, in the absence of peripheral extravasation [79]. At low concentrations the influence of T2* effects is minimal and normalised SI is proportional to the Gd-DTPA concentration in the sample. However, the exact relationship between the normalised SI and Gd-DTPA is dictated by the pre-contrast value of T1 ($T1_0$) as illustrated in Figure 2-4.

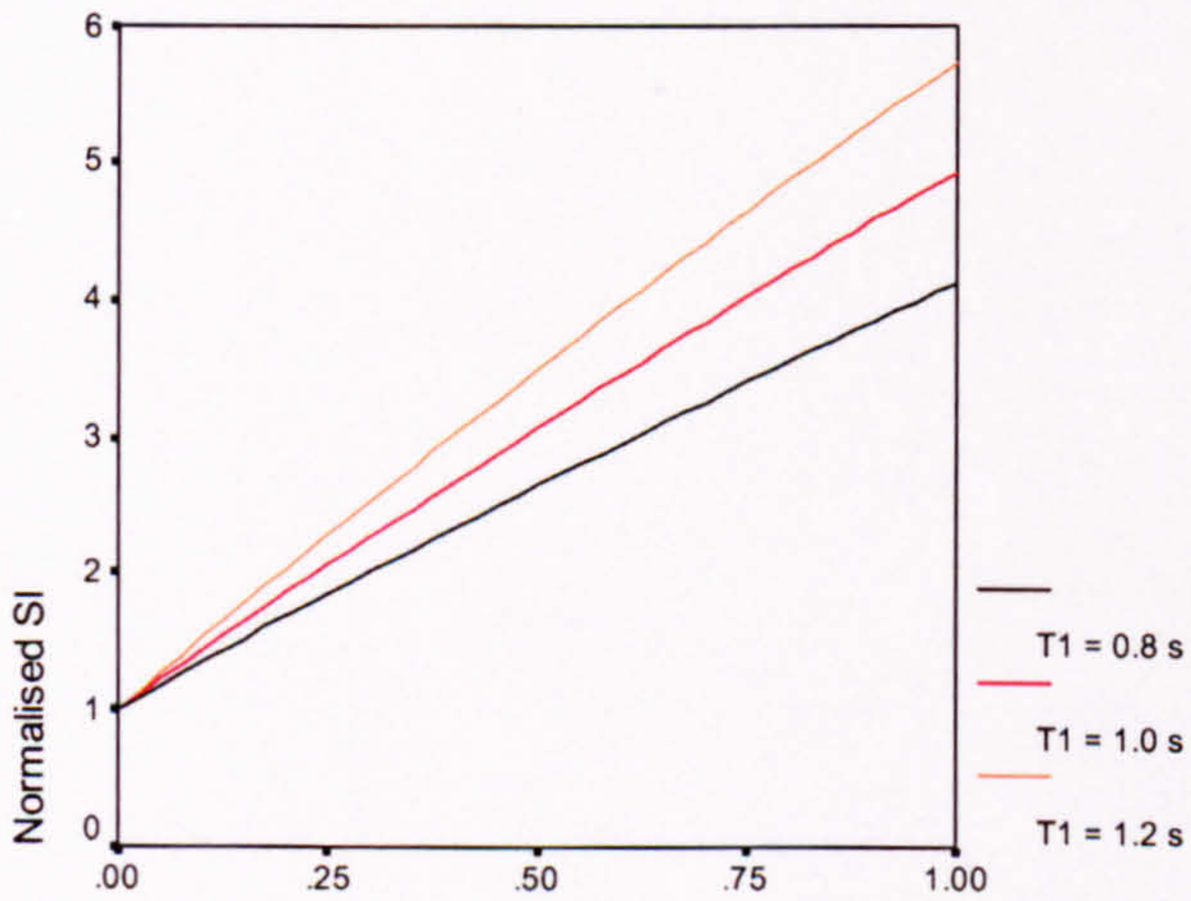

Figure 2-4 Dependence of normalised SI on pre-contrast T1

The link between normalised SI, pre-contrast $T1_0$ and Gd-DTPA concentration can be derived analytically (Eq. 2-19) from the expression for an arbitrary spoiled GE sequence

presented in Eq. 2-17. Therefore, the normalised DEMRI SI at any point following the administration of contrast (S_C/S_0) depends on the Gd-DTPA concentration in the tissue sample and the exact form of this relationship depends on the pre-contrast value of $T1_0$ as well as the DEMRI acquisition settings. If the pre-contrast T1 ($T1_0$) is known, normalised DEMRI SI can be converted into C = Ct(t) by using appropriate lookup tables or by solving equation Eq. 2-18 for every measured S_C/S_0 ratio, using Taylor expansion of the exponential terms.

$$\frac{S_C}{S_0} = \frac{\dfrac{1-e^{-TR\left(\frac{1}{T1_0}+\alpha C\right)}}{1-\cos\varphi\cdot e^{-TR\left(\frac{1}{T1_0}+\alpha C\right)}} e^{-TE\left(\frac{1}{T2_0^*}+\beta' C\right)}}{\dfrac{1-e^{-\frac{TR}{T1_0}}}{1-\cos\varphi\cdot e^{-\frac{TR}{T1_0}}} e^{-\frac{TE}{T2_0^*}}} \qquad \text{Eq. 2-19}$$

However, as can be seen from Figure 2-4, at low concentrations of Gd-DTPA, the relationship between S_C/S_0 and C can be approximated by a linear function of the form described by Eq. 2-20 (the derivation is presented in Appendix B). The range of Gd-DTPA concentrations over which this approximation adequately represents the functional relationship between normalised SI and C = Ct(t), depends on the chosen TR, TE and φ, in addition to the values of relaxivity constants α and β which are generally assumed to be well represented by in-vitro values measured in aqueous solutions at 21°C [78].

$$\frac{S_C}{S_0} \approx 1 + a \cdot C$$

$$a = \frac{e^{-\frac{TR}{T1_0}}}{1 - e^{-\frac{TR}{T1_0}}} \cdot TR\alpha$$

Eq. 2-20

A linear approximation of the normalised SI as a function of Gd-DTPA concentration

For very short TR ($TR << T1_0$) factor of proportionality a which links normalised signal intensity (relative signal enhancement) and local tissue concentration of Gd-DTPA could be further approximated by $\alpha T1_0$ (see Eq. 2-21). This means that under these conditions and at low Gd-DTPA concentrations, the relative signal change at a given Gd-DTPA tissue concentration will be primarily dictated by the native $T1_0$ of the tissue and in-vivo relaxivity constant α.

$$a = \frac{e^{-\frac{TR}{T1_0}}}{1 - e^{-\frac{TR}{T1_0}}} \cdot TR\alpha \approx \frac{1 - \frac{TR}{T1_0}}{\frac{TR}{T1_0}} \cdot TR\alpha = \left(\frac{T1_0}{TR} - 1\right) \cdot TR\alpha \approx T1_0 \cdot \alpha$$

Eq. 2-21

$$\text{for} \quad \frac{TR}{T1_0} << 1$$

On the other hand, if TR is large compared to $T1_0$ or an approximation over a wider range of concentrations is sought (i.e. up to 3 mM or higher), a more complex functional relationship (e.g. quadratic) between S_C/S_0 and C may be required.

Once the relationship between normalised DEMRI signal intensity and underlying bulk tissue concentration of Gd-DTPA is established (Eq. 2-20), temporal variation of DEMRI can be used to assess the local pharmacokinetics of Gd-DTPA and thus provide a measure of the microcirculatory properties of the tissue sample. To link the observed temporal changes DEMRI to the local microvascular properties of the tissues, pharmacokinetic

modelling is applied. The theoretical basis of pharmacokinetic modelling and its application to the measurement of the kinetics of Gd-DTPA following intravenous injection are presented in Section 2.5

2.5. Theory of the pharmacokinetic modelling of Gd-DTPA kinetics

A compartmental model is the mathematical description of the pharmacokinetic process, which incorporates both structural and physiological a priori knowledge about the system under investigation [72, 81]. This approach is widely used in pharmacology and nuclear medicine in those situations where the physiological processes under consideration are exceedingly complex or not known in sufficient detail.

The first step in building a compartmental model is to identify a subdivision of a system (a pool) where drug, contrast medium or tracer (indicator) can be identified either physically or chemically. A portion of a pool, which has unique, distinguishable and uniform kinetics, can be regarded as a viable compartment.

The requirement of uniform kinetics within the compartment is usually translated into an assumption of instantaneous mixing of the indicator within the compartment. This requirement is necessary in order to justify the transition between, by and large, inexact "real" processes and exact mathematical formalisms. Relevant physiological information can be concealed by the range of peripheral biological, chemical and physical processes which contribute to the dispersion of the indicator on passing through the system. However, in many applications the influence of these effects is such that the assumption of instantaneous mixing holds and compartmental modelling yields meaningful physiological information.

The relationship between individual compartments is defined and described by the corresponding transfer rate constants. Input functions can be obtained either by direct measurements or approximated by a mathematical assumption, thus taking the form of an idealised mathematical function. The two most frequently used input functions are bolus injection and constant rate infusion.

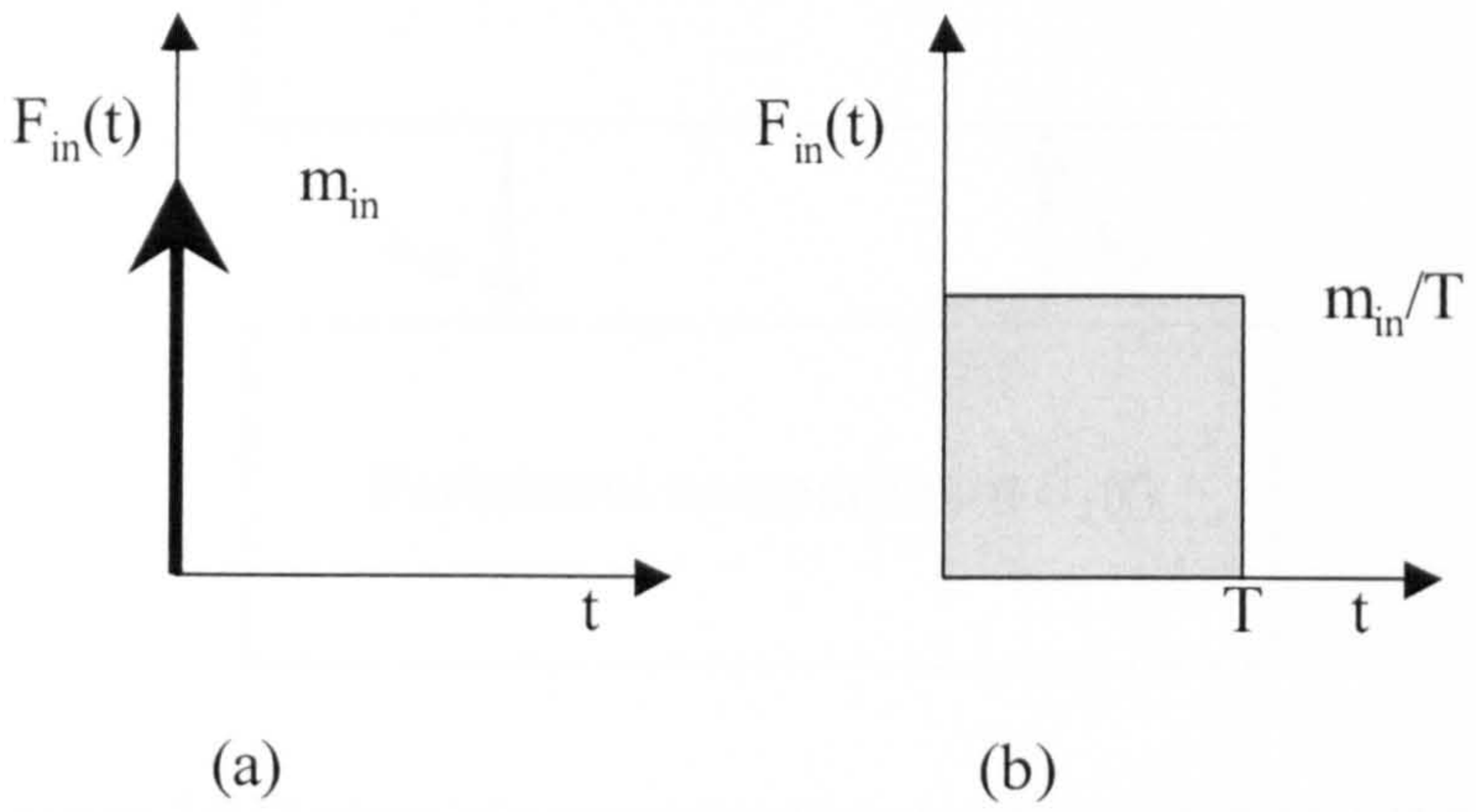

Figure 2-5 Standard input functions: (a) Bolus injection $m_{in}\delta(t)$ and (b) Constant rate infusion $\frac{m_{in}}{T}\left(u(t)-u(t-T)\right)$

A number of well-established configurations are widely used in modelling common physiological processes [72]. It is possible to model the same process with the compartmental models of varying complexity. If applied correctly, compartmental analysis increases the amount of information extracted from the pharmacological data. It can provide explicit expressions for the indicator concentrations in any of the body's kinetic compartments.

2.5.1. Description of an open two-compartment model

In this section, a general description of the modelling process will be given for the open two-compartment model. This derivation, based on the definition of mass balance equations for the exchange of the indicator between the compartments is presented here because it

provides a general framework for modelling indicator transport, regardless of the number of compartments, the nature of their interconnections and the form of the input function (or multiple input functions).

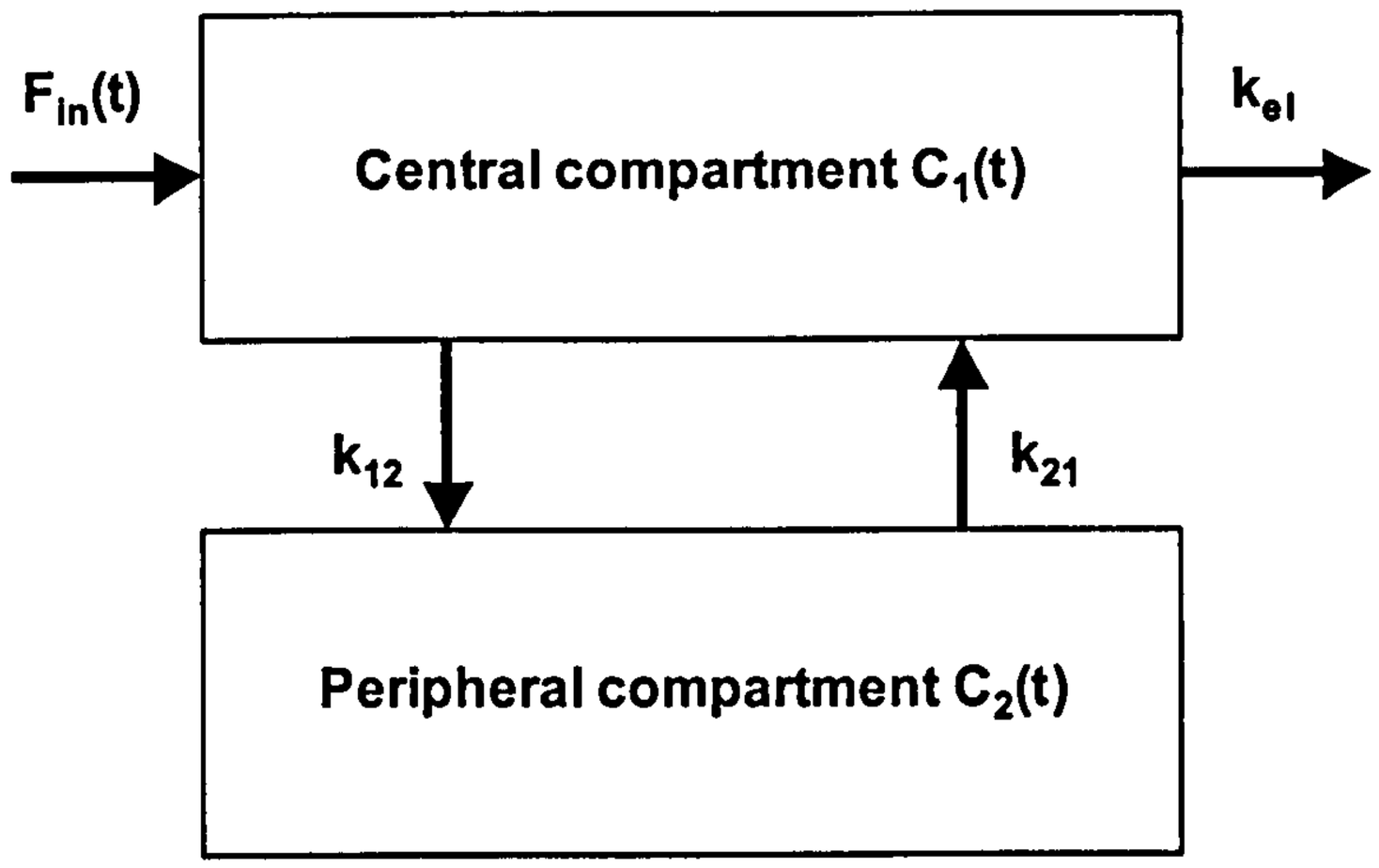

Figure 2-6 Diagram of a generalised two-compartment model with central and peripheral compartments, transfer rate constants and input function.

The central compartment usually encompasses those regions of the body in which the amount of the indicator present always remains in equilibrium with the concentration of the indicator in arterial plasma. This compartment includes plasma and those tissues or parts of tissues in which indicator concentrations rapidly reach equilibrium with plasma. These tissues are generally well perfused i.e. they have high blood flow per unit mass. Whether the particular tissue can be included in the central compartment depends largely upon the bio-distribution characteristics of the indicator (e.g. molecular weight, solubility). For example, the brain can be regarded as the part of the central compartment for substances which freely cross blood-brain barrier. Both the intracellular and extracellular regions of muscles and subcutaneous tissues, which are poorly perfused, are outside the central compartment when extracellular tracers are used.

In this two-compartment model it is assumed that the indicator is injected into and eliminated from the central compartment. The indicator which has been absorbed but not eliminated from the system is assumed to be in either the central or peripheral compartment at any given time (mass conservation). The fractional transfer rate of the indicators between these two compartments is described by the constants k_{12} and k_{21}. Fractional elimination rate constant k_{el} describes the fractional rate of elimination of the indicator from the central compartment.

The general input function is designated as Fin = Fin(t) and could be either constant rate infusion, single bolus or any combination of these (Figure 2-5). Mass balance equations governing the transfer of the indicator within this system are given below. Subscripts 1 and 2 denote values pertaining to the central and peripheral compartment respectively.

$$\frac{dm_1}{dt} = F_{in}(t) - (k_{12} + k_{el})m_1 + k_{21}m_2$$

$$\frac{dm_2}{dt} = k_{12}m_1 - k_{21}m_2 \qquad \text{Eq. 2-22}$$

Mass balance equations for the open two-compartment model

In these equations symbols m_1 and m_2 denote functions $m_1(t)$ and $m_2(t)$. Or in matrix notation:

$$\begin{bmatrix} \frac{dm_1}{dt} \\ \frac{dm_2}{dt} \end{bmatrix} = \begin{bmatrix} -(k_{12} + k_{el}) & k_{21} \\ k_{12} & -k_{21} \end{bmatrix} \begin{bmatrix} m_1 \\ m_2 \end{bmatrix} + \begin{bmatrix} F_{in}(t) \\ 0 \end{bmatrix} \qquad \text{Eq. 2-23}$$

Mass balance equations for the open two-compartment model in the matrix form

This system of differential equations can be rewritten in terms of the indicator concentration within the central and peripheral compartments by substituting:

$$m_1 = C_1 V_1$$
$$m_2 = C_2 V_2$$

Eq. 2-24

with C_1 and C_2 representing functions describing temporal variation of indicator concentration in the central and peripheral compartment, respectively. Mass transfer equations then yield:

$$\frac{dC_1}{dt} = \frac{F_{in}(t)}{V_1} - (k_{12} + k_{el})C_1 + k_{21}\frac{V_2}{V_1}C_2$$
$$\frac{dC_2}{dt} = k_{12}\frac{V_1}{V_2}C_1 - k_{21}C_2$$

Eq. 2-25

Mass balance equations for the two compartment model expressed in terms of indicator concentration

Or in matrix notation:

$$\begin{bmatrix} \frac{dC_1}{dt} \\ \frac{dC_2}{dt} \end{bmatrix} = \begin{bmatrix} -(k_{12} + k_{el}) & \frac{V_2}{V_1}k_{21} \\ \frac{V_1}{V_2}k_{12} & -k_{21} \end{bmatrix} \begin{bmatrix} C_1 \\ C_2 \end{bmatrix} + \begin{bmatrix} \frac{F_{in}(t)}{V_1} \\ 0 \end{bmatrix}$$

Eq. 2-26

This set of simultaneous differential equations is most conveniently solved in the Laplace domain:

$$\begin{bmatrix} sC_1(s) - C_1(0) \\ sC_2(s) - C_2(0) \end{bmatrix} = \begin{bmatrix} -(k_{12} + k_{el}) & \frac{V_2}{V_1}k_{21} \\ \frac{V_1}{V_2}k_{12} & -k_{21} \end{bmatrix} \begin{bmatrix} C_1(s) \\ C_2(s) \end{bmatrix} + \begin{bmatrix} \frac{F_{in}(s)}{V_1} \\ 0 \end{bmatrix}$$

Eq. 2-27

Linear system of equations in the Laplace domain

$C_1(0)$ and $C_2(0)$ represent the initial concentrations of the indicator in compartment 1 and 2 respectively. Laplace transforms of standard input functions are given as:

$$F_{in}(t) = m_{in}\delta(t) \rightarrow F_{in}(s) = m_{in} \qquad \text{Eq. 2-28}$$

Bolus Input

$$F_{in}(t) = \frac{m_{in}}{T}\left(u(t) - u(t-T)\right) \rightarrow F_{in}(s) = \frac{m_{in}}{Ts}\left(1 - e^{-sT}\right) \qquad \text{Eq. 2-29}$$

Constant Rate Infusion Input

By substituting Fin(s) with an appropriate expression and subsequently solving the system of linear equations (Eq. 2-27), expressions for $C_1(s)$ and $C_2(s)$ can be obtained. After performing inverse Laplace transform on those two functions, time-domain functions $C_1(t)$ and $C_2(t)$ governing the temporal change of indicator concentrations in central and peripheral compartment are derived.

However, even in a relatively simple compartment model configuration (such as this one) exceedingly complex solutions for the temporal variation of $C_1(t)$ and $C_2(t)$ are obtained after the application of inverse Laplace transform. Let's consider the solutions of the linear equations in the Laplace domain (Eq. 2-27) for the simplest form of the input function, i.e. idealised bolus with an illustration presented in Figure 2-5 and Laplace transform given in Eq. 2-28. Initial concentrations are assumed to be $C_1(0) = C_2(0) = 0$. The solutions are presented in Eq. 2-30 below.

$$C_1(s) = \frac{\frac{m_{in}}{V_1}(s + k_{21})}{s^2 + s(k_{12} + k_{21} + k_{el}) + k_{el}k_{21}}$$

$$C_2(s) = \frac{k_{12}\frac{m_{in}}{V_2}}{s^2 + s(k_{12} + k_{21} + k_{el}) + k_{el}k_{21}} \qquad \text{Eq. 2-30}$$

Compartmental concentrations in the Laplace domain

Temporal variation of C_2 is obtained by performing an inverse Laplace transform of the expression $C_2(s)$, yielding an expression presented in below.

$$C_2(t) = \frac{k_{12}\frac{m_{in}}{V_2}}{\sqrt{x}}\left(e^{(\frac{1}{2}\sqrt{x}-y)t} - e^{(-\frac{1}{2}\sqrt{x}+y)t}\right)$$

where:

Eq. 2-31

$$x = k_{12}^2 + 2k_{12}(k_{21}+k_{el}) + (k_{21}-k_{el})^2$$

and

$$y = k_{21} + k_{el} + k_{12}$$

Temporal variation of indicator concentration in the peripheral compartment

The solutions of the system of differential equations can, however, be simplified if it can be assumed that transfer velocities are the same in both directions at the interface between the central and peripheral compartment ($k_{12}V_1 = k_{21}V_2$) and that the volume of the peripheral compartment (V_2) is considerably smaller than the volume of the central compartment (V_1). Thus:

for $k_{12}V_1 = k_{21}V_2$ and $V_1 >> V_2$

$$k_{12} = k_{21}\frac{V_2}{V_1} << k_{21}$$

Eq. 2-32

yielding:

$$k_{21} + k_{el} + k_{12} \approx k_{21} + k_{el}$$

When these simplifications are introduced into the system presented in Eq. 2-30, the following system of equations is obtained:

$$C_1(s) = \frac{\frac{m_{in}}{V_1}(s + k_{21})}{s^2 + s(k_{21} + k_{el}) + k_{el}k_{21}} = \frac{\frac{m_{in}}{V_1}}{(s + k_{el})}$$

$$C_2(s) = \frac{k_{21}\frac{m_{in}}{V_1}}{s^2 + s(k_{21} + k_{el}) + k_{el}k_{21}} = \frac{k_{21}\frac{m_{in}}{V_1}}{(s + k_{21})(s + k_{el})}$$

Eq. 2-33

Compartmental concentrations in Laplace domain (simplified)

And finally, the application of inverse Laplace transform to $C_1(s)$ and $C_2(s)$ presented in Eq. 2-33 yields the formulation of the model-predicted temporal variation of tracer concentration in the peripheral compartment, in response to a bolus input (Eq. 2-34). The expression presented in Eq. 2-34 is evidently considerably simpler than the one presented in Eq. 2-31, and provided that the approximations outlined in Eq. 2-32 are justified, it can allow a more straightforward interpretation of the experimental data. This expression yields physiologically interpretable (non-negative) values of concentration C2(t) for $k_{21} > k_{el}$.

$$C_2(t) = \frac{k_{21}\frac{m_{in}}{V_1}}{k_{21} - k_{el}}\left(e^{-k_{el}t} - e^{-k_{21}t}\right)$$

Eq. 2-34

Temporal variation of indicator concentration in the peripheral compartment (simplified)

In a generalised model comprising n compartments, functions $C_n(t)$ will be multivariable functions of input parameters and linear fractional rate constants and will take the form of complex multi-exponential functions. Extraction of these parameters can be performed by means of non-linear least squares fitting algorithms, using pairs of model-predicted and measured values of $C_n(t)$ at discrete time intervals t_k.

To summarise, a general form of the mass balance equations system for an n-compartment model is represented by the following matrix equation:

$$\begin{bmatrix} \frac{dm_1}{dt} \\ \frac{dm_2}{dt} \\ \frac{dm_3}{dt} \\ . \\ \frac{dm_{n-1}}{dt} \\ \frac{dm_n}{dt} \end{bmatrix} = \begin{bmatrix} -O_1 & k_{21} & k_{31} & \cdot & k_{(n-1)1} & k_{n1} \\ k_{12} & -O_2 & k_{13} & \cdot & k_{(n-1)2} & k_{n2} \\ k_{13} & k_{23} & -O_3 & \cdot & k_{(n-1)3} & k_{n3} \\ . & . & . & . & . & . \\ k_{1(n-1)} & k_{2(n-1)} & \cdot & \cdot & -O_{n-1} & k_{(n-1)1} \\ k_{1n} & k_{2n} & \cdot & \cdot & k_{(n-1)n} & -O_n \end{bmatrix} \begin{bmatrix} m_1 \\ m_2 \\ m_3 \\ . \\ m_{n-1} \\ m_n \end{bmatrix} + \begin{bmatrix} F_{in}(t) \\ 0 \\ 0 \\ . \\ 0 \\ 0 \end{bmatrix} \qquad \text{Eq. 2-35}$$

Generalised mass balance equations for a compartmental model consisting of n compartments

Diagonal terms O_i represent the total sum of outflux transfer rate constants from the compartment i including the one which governs the transfer of the indicator out of the system (Eq. 2-36). In an open two-compartment model described above, $O_1 = k_{12} + k_{el}$ and $O_2 = k_{21}$.

$$O_i = \sum_{j=1}^{n} k_{ij} + k_{out}^{i} \qquad \text{Eq. 2-36}$$

Fractional transfer rate constants k_{ij} $(i, j = 1 .. n, i \neq j)$ represent the transfer of the indicator from compartment i to compartment j. In an open two-compartment model, only two fractional transfer rate constants (k_{12} and k_{21}) feature in the mathematical model description.

The generalised mathematical model described above (Eq. 2-35) allows handling of the models of theoretically unlimited complexity. However, it must be emphasised that the value of the compartmental model is primarily determined by the relevant physiological information it provides and not necessarily by its complexity [72]. It is therefore necessary to find the minimal set of compartments and their interconnections which resembles physiological processes under investigation to a satisfactory degree.

The success of the non-linear fitting algorithms used for the extraction of pharmacokinetic parameters in practical implementation of the modelling will depend critically on the configuration of the chosen model [82]. The form of the derived relationship between the concentrations of the indicator in model compartments can be simplified by a judicious introduction of approximations, based on relative ratios between individual parameters, as illustrated through the comparison between expressions Eq. 2-31 and Eq. 2-34.

2.5.2. Description of Gd-DTPA pharmacokinetics

After intravenous injection Gd-DTPA is rapidly distributed throughout the plasma volume and diffused (extravasated) into the extracellular space. Its plasma concentration reaches its maximum soon after administration and then decays following a bi-exponential curve. The early distribution phase has a mean half-life of 0.20 ± 0.13 hours and is followed by the elimination phase with the mean half-life of 1.56 ± 0.13 hours [64]. There is evidence that no metabolic trapping of Gd-DTPA occurs within the body and that it is completely eliminated in an unchanged form by renal excretion [64, 75]. Being a highly hydrophilic molecule, Gd-DTPA is unable to cross-cellular membranes. It has been shown that the variation of Gd-DTPA plasma concentration following a peripheral venous injection can be approximated by the monoexponential function over the period of time that is shorter than the mean half-life of the early distribution phase (12 minutes) [83]. This means that under those conditions the whole plasma volume can be represented by a single well-mixed compartment (central compartment). If the extra-vascular extra-cellular space of the lesion is represented as a second (peripheral) compartment in the formulation of an open two-compartment presented in Figure 2-6 and if the input (Gd-DTPA injection) is represented by an idealised delta function, i. e. bolus injection $m_{in}\delta(t)$, the following simplified compartmental description of Gd-DTPA kinetics is obtained (Figure 2-7).

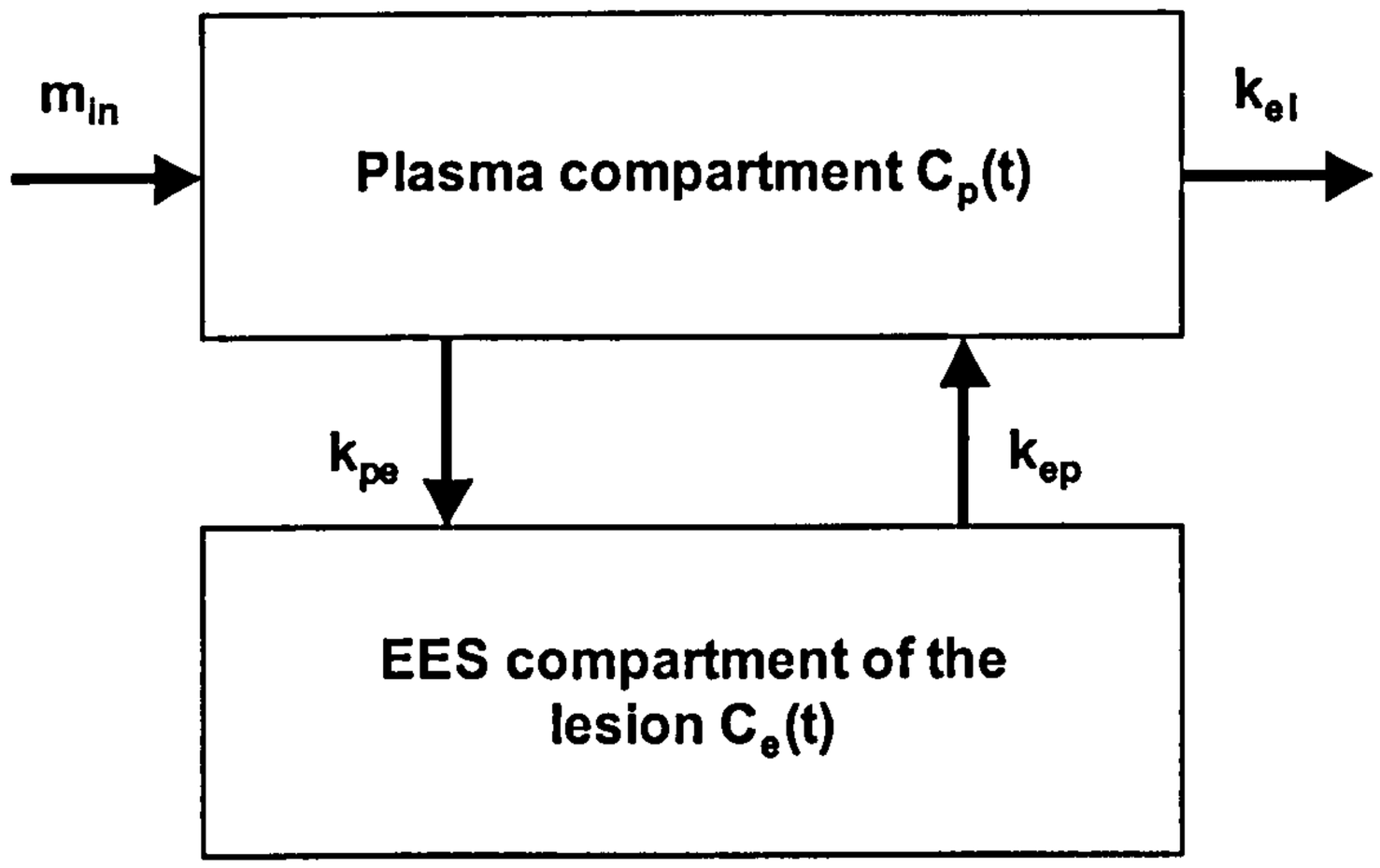

Figure 2-7 Diagram of the two-compartment model of Gd-DTPA kinetics

In this model, fractional transfer rates k_{ep} and k_{pe} describe the process of Gd-DTPA exchange across the capillary wall and are thus related to capillary permeability. Fractional elimination constant k_{el} represents the rate of Gd-DTPA elimination from plasma (glomerular filtration through the kidneys). The approximations used in Eq. 2-32 can be applied since the volume of the lesion EES is considerably smaller than plasma volume and it is reasonable to assume that there is no active accumulation of fluid in either of the compartments (i.e. the transfer velocities are the same in both directions). The resulting concentration of Gd-DTPA in the EES compartment Ce(t) can thus be represented by the expression presented in Eq. 2-37.

$$C_e(t) = \frac{k_{ep}\frac{m_{in}}{V_p}}{k_{ep} - k_{el}}\left(e^{-k_{el}t} - e^{-k_{ep}t}\right) \qquad \text{Eq. 2-37}$$

Temporal variation of Gd-DTPA concentration in the EES compartment of the lesion

The concentration of Gd-DTPA in the tissue sample where the fraction of the volume occupied by EES is v_e and where fractional volume of plasma can be assumed to be negligible is represented by Eq. 2-38.

$$C_t(t) = v_e C_e(t) = v_e \frac{k_{ep}\frac{m_{in}}{V_p}}{k_{ep} - k_{el}}\left(e^{-k_{el}t} - e^{-k_{ep}t}\right) \qquad \text{Eq. 2-38}$$

Temporal variation of Gd-DTPA concentration in the tissue sample

As the relationship between normalised SI and underlying bulk tissue concentration of Gd-DTPA can be assumed to be linear (Eq. 2-20), the expression presented in (Eq. 2-38) can be used to link the observed temporal change in normalised DEMRI variation and pharmacokinetic variables v_e, k_{el} and k_{ep}:

$$\frac{S_C}{S_0} \approx 1 + a \cdot C_t(t) = 1 + a \cdot v_e C_e(t) = 1 + a \cdot v_e \frac{k_{ep}\frac{m_{in}}{V_p}}{k_{ep} - k_{el}}\left(e^{-k_{el}t} - e^{-k_{ep}t}\right) \qquad \text{Eq. 2-39}$$

Temporal variation of normalised DEMRI signal intensity as a function of Gd-DTPA concentration in the tissue sample

where parameter **a** is a function of TR, relaxivity α and pre-contrast $T1_0$, as detailed in Section 2.4.2 and Eq. 2-20.

This expression for model-predicted temporal variation of normalised DEMRI can be used for the extraction of variables which describe Gd-DTPA kinetics and reflect the physiology of the microcirculation for a simple, generic two-compartment model and an idealised bolus injection of Gd-DTPA. Variable v_e reflects the fractional volume of the EES, whereas variable k_{ep} is related to the capillary permeability. Fractional elimination constant k_{el} is related to the systemic (rather than capillary) circulation and kidney function. Variables v_e, k_{ep} and k_{el} can be extracted from the measured DEMRI obtained at discrete time points t_k if other parameters that feature in the expression Eq. 2-39 (m_{in}, $T1_0$, TR, α, Vp) can be either measured or approximated by constant, known values. Several variations of the methodology presented in this chapter have been proposed in the literature and they are reviewed in the following chapter.

Chapter 3. Literature review

The first reports of pharmacokinetic analysis of Gd-DTPA enhanced dynamic MRI (DEMRI) were published in 1990 and 1991 by three independent European research groups (Copenhagen [71], London [69] and Heidelberg [68]). They have postulated the basis of this approach and applied this technique to the assessment of blood-brain barrier (BBB) breakdown in multiple sclerosis [69, 71] and brain tumours [68, 71]. In all these methods Gd-DTPA was used as an MRI contrast agent but the results are applicable to all extracellular contrast agents of similar molecular weight. Gd-DTPA kinetics is represented by the compartment models with linear exchange processes between the blood plasma and extracellular extravascular space (EES) of the lesion.

The potential of this technique for the assessment of microcirculatory properties of the tissues in a variety of other pathological states was quickly recognised. All subsequent models reported in the literature present the variations of these principal models [68, 69, 71] without radically changing the underlying methodology. Pharmacokinetic analysis of Gd-DTPA was applied to the assessment of breast cancer [83-85], cervical cancer [86], colorectal cancer [87] and heart disease [88-90].

All three methods rely on a common set of assumptions regarding the properties of principal compartments and their interactions. Both whole-body plasma compartment and EES compartment of the lesion are assumed to be well mixed and characterised by a uniform (spatially-invariant) concentration of contrast agent at any time point following a peripheral administration. The concentration in plasma is represented as a mono-, bi- or tri-exponential function. Although these functional forms arise from different compartmental representations of Gd-DTPA kinetics in plasma (one, two and three compartments respectively), the compartment representing EES of the lesion is assumed to interact with a single plasma compartment (blood-plasma compartment).

The transfer of contrast agent between compartments is assumed to be linear and time-invariant. A negligible interaction between EES compartment and the rest of the EES space is also assumed. Furthermore, relaxivity of contrast agent is assumed to be constant and well-represented by the in-vitro value and fast exchange model of ^1H protons is assumed throughout, allowing a representation of effective longitudinal relaxation of the lesion by a single longitudinal relaxation constant T1. The validity of assumptions regarding the in-vivo relaxivity [91] and the exact mechanism of water exchange [92] is still a subject of investigation.

Although three principal approaches rely on a common set of assumptions, they differ in the way the final formulation of the model-predicted tissue response curve is represented as a function of physiological parameters and in the way these parameters are labelled and interpreted. The main differences in the practical implementation of these models are related to the treatment of the temporal variation of the Gd-DTPA concentration in plasma, the choice of input function (mode of injection) and the measurement of native (pre-contrast) longitudinal relaxation time T1. A summary of the underlying methodology underpinning three principal approaches will be given in this chapter, generalised transport equations will be presented and the equivalence of mathematical representation of derived measured of

Gd-DTPA transport in tissues will be demonstrated. A list of parameter labels used in these models will be presented together with their relationship to the common set of labels proposed in a recent review [2].

3.1. Generalised model of Gd-DTPA kinetics

General description of Gd-DTPA behaviour in tissues can be derived from the modified transport equations described by Kety [93], originally developed to measure kinetics of inert gasses in tissues. General formulation relates to the most complicated physiological situation of capillary transport limited by both local flow and permeability. A detailed derivation is given in [2] and the list of quantities, symbols and units is presented in Table 3-1.

Symbol	Name	Units
Ct	tissue concentration of Gd-DTPA	mM
Cp	plasma concentration of Gd-DTPA	mM
ρ	tissue density	g ml^{-1}
E	extraction ratio	
F	flow of blood per unit mass of tissue	ml $(min\ g)^{-1}$
EF	extraction ratio flow product per unit mass of tissue	ml $(min\ g)^{-1}$
$EF\rho$	extraction ratio flow product per unit volume of tissue	min^{-1}
P	permeability	cm min^{-1}
S	surface area per unit mass of tissue	$cm^2\ g^{-1}$
PS	permeability surface area product per unit mass of tissue	ml $(min\ g)^{-1}$
$PS\rho$	permeability surface area product per unit volume of tissue	min^{-1}
v_e (f_{ex})	fractional volume of the EES (volume of the EES per unit volume of the tissue)	
Hct	hematocrit (a fraction of total blood volume occupied by formed blood elements)	

Table 3-1 Symbols for quantities used in the formulation of generalised transport equation Eq. 3-1

The differential equation relating the temporal change of the concentration of Gd-DTPA in the tissue Ct(t) to the concentration of Gd-DTPA in plasma Cp(t) is given below (Eq. 3-1). This transport is a function of extraction ratio flow product per unit volume of the tissue (EFρ), hematocrit (Hct) and the fractional volume of the EES (v_e).

$$\frac{dC_t(t)}{dt} = EF\rho \cdot (1 - Hct) \cdot (Cp - \frac{C_t}{v_e}) \qquad \text{Eq. 3-1}$$

Extraction ratio (E) is a function of flow (F), permeability surface area product (PS) and hematocrit (equation Eq. 3-2).

$$E = 1 - e^{-\left(\frac{PS}{F(1-Hct)}\right)} \qquad \text{Eq. 3-2}$$

The generalised transport equation (Eq. 3-1) can be further simplified by separating the linear coefficient governing the transfer of Gd-DTPA from plasma into the EES of the lesion (K^{trans}) and the constant describing the transfer of Gd-DTPA from EES back to plasma (k_{ep}) yielding a compact expression (Eq. 3-3). Symbols K^{trans}, k_{ep} were proposed in the review by Tofts [2] in an attempt to simplify the annotation used in the reported work and enable direct comparison of the results obtained in studies carried out by different research groups.

$$\frac{dC_t(t)}{dt} = K^{trans} \cdot C_p - k_{ep} \cdot C_t \qquad \text{Eq. 3-3}$$

The following descriptions of transfer rate constants K^{trans} and k_{ep} can be derived from equations Eq. 3-1 and Eq. 3-3:

$$K^{trans} = EF\rho \cdot (1 - Hct) \qquad \text{Eq. 3-4}$$

and

$$k_{ep} = \frac{EF\rho \cdot (1 - Hct)}{v_e} = \frac{K^{trans}}{v_e} \qquad \text{Eq. 3-5}$$

In this most general case of Gd-DTPA transport, transfer constants K^{trans} and k_{ep} reflect local arterial blood flow, capillary permeability (through extraction ratio which is a function of permeability surface area product PS and flow) and v_e. In this generalised model of Gd-DTPA kinetics, Ct(t) is assumed to be influenced exclusively by the EES fraction of Gd-DTPA and the influence of intra-vascular Gd-DTPA is ignored by assuming negligibly small fractional volume of intra-vascular plasma within the lesion. Furthermore, equal permeability across the vascular wall in both directions (plasma to EES and EES to plasma) is assumed.

In situations where either flow or permeability is the dominant physiological factor, i.e. when F>>PS (low permeability) or F<<PS (high permeability) expressions relating K^{trans} and k_{ep} to the physiological variables F, PS and v_e can be further simplified by transforming the expression for extraction ratio E (Eq. 3-2) according to the value of PS/F ratio.

F>>PS (low permeability or "PS limited" transport)

$$E = 1 - e^{-\left(\frac{PS}{F(1-Hct)}\right)} \approx \frac{PS}{F(1-Hct)} \qquad \text{Eq. 3-6}$$

F<<PS (high permeability or "flow limited" transport)

$$E = 1 - e^{-\left(\frac{PS}{F(1-Hct)}\right)} \approx 1 \qquad \text{Eq. 3-7}$$

Resulting expressions for transfer constants K^{trans} and k_{ep} are given in Table 3-2.

	K^{trans}	k_{ep}
Mixed flow and PS limited	$EF\rho(1-Hct)$	$\frac{EF\rho(1-Hct)}{v_e}$
PS limited	$PS\rho$	$\frac{PS\rho}{v_e}$
Flow limited	$F\rho(1-Hct)$	$\frac{F\rho(1-Hct)}{v_e}$

Table 3-2 K^{trans} and k_{ep} under different flow and permeability conditions

Factor 1-Hct is associated with F (blood flow) whenever it appears in the expressions for K^{trans} and k_{ep} to exclude the influence of formed blood elements and F(1-Hct) thus represents the flow of blood plasma, rather than total blood flow.

3.2. Model 1 (after Larsson [71])

In this model, direct arterial samples of Gd-DTPA were obtained from brachial artery and concentration of Gd-DTPA in plasma Cp(t) was measured by neutron activation. Plasma concentration was then modelled as a tri-exponential function (equation Eq. 3-8). Parameters a_i and m_i are obtained in each individual examination by fitting the Cp(t) obtained from blood samples to the equation Eq. 3-8.

$$C_p(t) = D \cdot \sum_{i=1}^{3} a_i \cdot e^{-m_i \cdot t} \qquad \text{Eq. 3-8}$$

This model allowed extraction of $K^{trans} / v_e = k_{ep}$ from measured dynamic signal intensities S(t), baseline S(0) and the initial rate of signal enhancement $\dot{S}(0)$ without the measurement of initial T1 ($T1_0$). A linear relationship between S(t) and Gd-DTPA concentration was assumed.

$$S(t) = S(0) + \frac{\dot{S}(0)}{\sum_{i=1}^{3} a_i} D \cdot \sum_{i=1}^{3} a_i \frac{e^{-\left(\frac{K^{trans}}{v_e}\right)\cdot t} - e^{-m_i \cdot t}}{m_i - \frac{K^{trans}}{v_e}} \qquad \text{Eq. 3-9}$$

Larsson et al also suggested a more complex version of this method, where initial $T1_0$ was measured and temporal variation of longitudinal relaxation rate R(t) rather than signal intensity S(t) was used for the measurement of K^{trans} / v_e (k_{ep}).

$$R(t) = R(0) + \frac{\dot{R}(0)}{\sum_{i=1}^{3} a_i} D \cdot \sum_{i=1}^{3} a_i \frac{e^{-\left(\frac{K^{trans}}{v_e}\right)\cdot t} - e^{-m_i \cdot t}}{m_i - \frac{K^{trans}}{v_e}} \qquad \text{Eq. 3-10}$$

Parameter K^{trans} was interpreted as EFρ(1-Hct) (extraction ratio flow product) i.e. mixed PS and flow conditions were assumed. If PS<<F this quantity is identical to that used by Tofts because under these conditions PSρ = EFρ(1-Hct). In mixed PS and flow-limited conditions K^{trans} represents "apparent capillary permeability".

The approach presented in Eq. 3-10 is the most rigorous of the three methods described in this section in that it includes individual measurement of $T1_0$ and Cp(t), both of which have a direct influence on the accuracy of extracted physiological variables. However, this approach is difficult to implement rigorously, especially in routine clinical practice. Measurement of Cp(t) in situations where representative blood vessel cannot be included in the field of view without considerable loss of spatial resolution requires interleaved acquisition to obtain Cp(t) measurements. This in turn affects the maximal achievable temporal resolution for the sampling of Ct(t). Furthermore, accurate sampling of Cp(t) following a bolus injection requires sampling interval of not more than 5 seconds [94]. At this temporal resolution, SNR will have to be compromised in all clinical applications where more than single slice coverage of the lesion under investigation is required. One solution for

this problem was suggested by Andersen et al [80] who proposed sequential collection of blood samples with ^{99m}Tc-DTPA as a tracer. This approach has an obvious advantage in that it does not compromise optimal acquisition settings for sampling of Ct(t). However, it is difficult to implement in clinical practice since it increases the complexity and invasiveness of the MRI examination.

According to the theory of Gd-DTPA induced contrast enhancement, temporal variation of SI will be related to the pre-contrast T1 relaxation time of the tissue (Eq. 2-20). Ideally, fast measurement of T1 would enable the most accurate measurement of the variation of the local bulk tissue concentration of Gd-DTPA. The changes in T1 relaxation rate (1/T1 = R1) would then be related to the local Gd-DTPA concentration according to the following expression:

$$\frac{1}{T1_C}(t) = \frac{1}{T1_0} + \alpha C(t)$$

$$R1(t) = R1_0(t) + \alpha C(t) \qquad \text{Eq. 3-11}$$

$$C(t) = \frac{1}{\alpha}\Delta R1(t)$$

The problems related to the influence of T2* effects in GE based sequences and the dependence of measurements on selected acquisition sequence parameters would be circumvented if this method was used for monitoring of Ct(t). However, reliable dynamic measurement of the T1 would require the reduction of the temporal resolution if the same amount of tissue is scanned with high spatial resolution and SNR. A compromise solution can be reached if pre-contrast T1 value ($T1_0$) is used in expressions Eq. 2-20 and C(t) is then derived from the observed changes of normalised SI.

Measurement of $T1_0$ also increases the complexity of the measurement. Accurate $T1_0$ measurement, and especially $T1_0$ mapping on pixel-by-pixel basis, requires the application of multiple pulse sequences, duration of which can often exceed the duration of the DEMRI

acquisition. Furthermore, quantitative mapping of $T1_0$ is not possible on all MRI systems designed for clinical use.

3.3. Model 2 (after Tofts [69])

In this model, temporal variation of Gd-DTPA concentration in tissue was expressed as in equation Eq. 3-12 given below.

$$C_t(t) = D \cdot K^{trans} \cdot \sum_{i=1}^{2} a_i^T \frac{e^{-\left(\frac{K^{trans}}{v_e}\right)\cdot t} - e^{-m_i \cdot t}}{m_i - \frac{K^{trans}}{v_e}} \qquad \text{Eq. 3-12}$$

Plasma concentration of Gd-DTPA was represented by a bi-exponential fit to the data reported by Weinmann [64] (equation Eq. 3-13). This dataset was obtained by measuring discrete venous blood samples from healthy volunteers.

$$C_p(t) = D \cdot \sum_{i=1}^{2} a_i^T \cdot e^{-m_i \cdot t} \qquad \text{Eq. 3-13}$$

In equations Eq. 3-12 and Eq. 3-13 D represents the dose of Gd-DTPA (mmol/kg body weight) and constants obtained by fitting of the Weinmann's data have the following values: $a_1^T = 3.99$ kg l^{-1}, $a_2^T = 4.78$ kg l^{-1}, $m_1 = 0.114$ min^{-1} and $m_2 = 0.0111$ min^{-1}. Other quantities are explained in Table 3-1 and equations Eq. 3-4 and Eq. 3-5.

Assuming that the in-vitro determined value of T1 relaxivity α remains unchanged in tissue and that native (pre-contrast) $T1_0$ is known, this model allows the extraction of K^{trans} and v_e directly from the measured signal intensity curves. Transfer rate constant k_{ep} can then be calculated indirectly according to Eq. 3-5.

The relationship between local plasma flow and permeability was assumed to be F>>PS i.e. the model is assumed to operate in the conditions of low PS (PS limited, see Table 3-2) and parameter K^{trans} was interpreted as permeability surface area product per unit volume of the tissue ($PS\sigma$) or "permeability" for short. In a subsequent report [84], where this model was applied to the assessment of Gd-DTPA enhancement in breast tumours, it was noted that mixed flow and PS conditions may better reflect the microcirculation in these fast enhancing lesions and K^{trans} was referred to as "apparent permeability" thus acknowledging possible influence of local flow to the measured values of K^{trans}.

This model has been one of the most frequently used in this field. It has the advantage over the Larsson's approach in that it does not require accurate sampling of arterial input function but proposes a theoretical representation of Cp(t). The theoretical model of Cp(t) is, however, based on a set of measurements on human subjects [64] and this certainly improves the validity of this approach. The data used for the formulation of Cp(t) was, however, acquired with low temporal resolution and Toft's representation of Cp(t) does not accurately represent Cp(t) in lesions which lie in the vicinity of major blood vessels. More recent data detailing the form of arterial input function [80] could be used to increase the accuracy of Cp(t) in those situations. $T1_0$ can be measured or assumed (as is the case with the other two models). The main criticism of this model is that it oversimplifies the Cp(t) and consequently Ct(t) by assuming that the injected bolus behaves as an idealised impulse (delta) function. Furthermore, bi-exponential representation of Cp(t) as suggested by Tofts may not be required for short DEMRI acquisitions.

3.4. Model 3 (after Brix [68])

In this model, normalised SI was represented as a linear function of bulk-tissue concentration. Gd-DTPA was administered as a long constant rate infusion (of duration T)

and represented mathematically as a block function (Figure 2-5). In the original notation compartment concentrations were labelled as C_1 (plasma compartment) and C_2 (EES compartment of the lesion) and fractional transfer rate k_{ep} was labelled as k_{21}. The variation of Cp(t) was assumed to be well-represented by a mono-exponential function and the expression for the bulk-tissue concentration of Gd-DTPA (based on mass balance equations) was derived as:

$$\frac{S_C}{S_0} = 1 + f_{ex} C_2(t) = 1 + A\left(u(e^{-k_{el}\tau} - 1)e^{-k_{el}\tau} - v(e^{-k_{21}\tau} - 1)e^{-k_{21}\tau}\right)$$

where:

$$\tau = \begin{cases} t & t \in [0, T] \\ T & t \in [T, \infty) \end{cases} \qquad \text{Eq. 3-14}$$

and:

$$u = \frac{k_{21}}{k_{el}(k_{21} - k_{el})} \qquad v = \frac{1}{k_{21} - k_{el}}$$

Model-predicted temporal variation of normalised SI

In this approach, DEMRI curves are characterised by three parameters: A, k_{21} and k_{el}. Whereas k_{21} is related to capillary permeability, parameter A is not given any physiological interpretation and in contrast to the other two models, where either individually measured or assumed normal value of Gd-DTPA clearance from the blood plasma is used, k_{el} is allowed to vary freely.

To enable a direct comparison of this model with the ones of Larsson and Tofts, the expression for tissue concentration of Gd-DTPA in response to a bolus injection was derived from this model [70]. Brix's notation was substituted by the notation used in the formulation of the generalised model of Gd-DTPA kinetics, i.e. C_1 = Cp, C_2 = Ce, k_{21} =

k_{ep}, V_1 = Vp. The expression for tissue concentration in response to a bolus injection is then derived as:

$$C_t(t) = f_{ex} \cdot C_e(t) = f_{ex} \cdot \frac{m_{in}}{V_p} \cdot k_{ep} \cdot \frac{e^{-k_{el}t} - e^{-k_{ep}t}}{k_{ep} - k_{el}}$$

$$= \frac{D}{\delta} \cdot K^{trans} \cdot \frac{e^{-k_{el}t} - e^{-k_{ep}t}}{k_{ep} - k_{el}} \qquad \text{Eq. 3-15}$$

This expression is identical to the one derived in the general description of open two-compartment model of Gd-DTPA kinetics presented in Eq. 2-38 and it enables a direct comparison between the kinetic variables used in Brix's approach and those used by Larsson and Tofts. When Eq. 3-15 is compared with Eq. 3-12, it becomes apparent that Brix's k_{ep} (or k_{21} in his notation) corresponds to the ratio of K^{trans} as defined by Tofts and v_e (or f_{ex} in Brix's original notation).

The main advantage of this method is that it provides flexibility with respect to the mathematical representation of the input function. Rather than modelling a bolus injection as an idealised delta function of infinitely short duration, a more realistic input function configuration is possible. The treatment of the input function actually depends on the form of physical administration (the nature of the Gd-DTPA intravenous injection) as well as the formal mathematical representation of the chosen input function. Brix and co-workers used a long constant-rate injection (with T>60 seconds). They claim that a long infusion provides a more controlled input function when compared to short bolus injection. One report [94], based on simulations of arterial input functions based on experimental data presented by [80], suggests that long infusion may even have negative effect on the accuracy of parameters extracted by pharmacokinetic modelling. Furthermore, it has been demonstrated that short injection has advantageous properties in that it ensures faster and more pronounced enhancement of signal intensity for a constant dose of Gd-DTPA [95].

The principal weakness of this model is that it over-generalises Cp(t). The model only provides a general shape of the Cp(t) function and even allows fraction elimination rate k_{el} to vary freely. Negative values of k_{el} were also reported although they are clearly physiologically meaningless and reduce the validity of the model. No attempt has been made to extract a physiologically meaningful variable (such as f_{ex}) from the value of parameter A, which is a complex function of sequence parameters, relaxivity, native $T1_0$ and f_{ex}. Parameter A can therefore be used only within the narrow setting of individual studies defined strictly by the acquisition sequence. Parameter k_{21} is a ratio between K^{trans} and v_e (or f_{ex} in Brix's notation). It represents a fractional elimination rate of Gd-DTPA between extracellular space and plasma. This parameter is independent on the acquisition settings and injection representation. It is directly related to K^{trans} which is a measure of permeability, but without the measurement of f_{ex}, this parameter cannot be directly related to the measurements obtained by using other models.

3.5. Correlation of QDEMRI variables with histopathology

Although three principal approaches for pharmacokinetic analysis of Gd-DTPA enhanced DEMRI have initially been applied to the assessment of brain lesions (brain tumours [68, 71] and multiple sclerosis [69, 71]), they have subsequently been used in the evaluation of a variety of tumours, with the research into Gd-DTPA pharmacokinetics in breast tumours being particularly prominent.

A comprehensive comparison between the results obtained using all three methods has not been reported in the literature although the mathematical equivalence of the three principal approaches was described [2, 70] as discussed in the previous sections. Berkowitz et al performed a validation of the Tofts' approach in a study where the measurement of

permeability in chemically induced blood-retinal barrier lesions in an animal model was obtained [96]. The measurements of permeability surface area product per unit volume of the tissue (PSρ) were in agreement with the measurements obtained using classical physiological methods. A comparison of Larsson's and Tofts' measurement of PSρ of the defective blood-brain barrier in multiple sclerosis indicated a good agreement between the results obtained using these two models [97]. However, the range of permeability in multiple sclerosis (up to 0.072 min^{-1}) is significantly lower than in a majority of cancerous lesions, and the equivalence of these two approaches in the assessment of pathologies with higher permeability has not been fully investigated. Mussurakis et al [98] performed a comparison of Tofts' and Brix's methods in a study of primary breast lesions. In this study, both methods yielded equivalent discriminatory power for the differentiation between benign and malignant breast lesions.

Pharmacokinetic analysis was applied in several other clinical studies of DEMRI in breast lesions where the primary aim of the quantitative analysis was the differentiation between benign and malignant tumours. Significantly higher permeability-related quantifiers of DEMRI were reported in invasive breast carcinomas than in benign lesions, although a variable degree of overlap between these groups of lesions was also noted in all published studies, regardless of the choice of the method used for PK analysis [98-104].

Quantitative analysis of DEMRI in breast cancer lesions based on black-box quantifiers of signal enhancement is still widely performed. Black-box analysis techniques involve the computation of the amplitude of enhancement at pre-specified time points, so-called enhancement ratios (ER) normalised to fatty tissue [105] or baseline pre-contrast SI [106], as well as the time [107] and the pattern [108] of contrast arrival. Furthermore, a macroscopic, qualitative evaluation of the shape of the enhancement curve is used for the classification of the lesions [109]. Other BB variables, such as maximal enhancement (ME), steepest-slope or

initial rate of enhancement (IRE), wash-out slope (WOS), and descriptive parameters derived from heuristic models such as that proposed by Orel [110], are also reported in the literature.

A comparison between BB and PK quantifiers of DEMRI has been only sporadically reported the literature and the results of these comparisons are equivocal. Müller-Schimpfle et al [111], for example, found that the application of PK modelling did not result in the improvement in the discrimination between benign and malignant breast lesions when compared to BB assessment. Hulka [101] and Mussurakis [98], on the other hand, reported that their PK variables allowed a more specific classification of breast cancer lesions than BB measurements (such as ER, ME and wash-out slope WOS). Whilst Müller-Schimpfle used Brix's model for the extraction of PK parameters, Hulka applied Larsson's method and Mussurakis used both Brix and Tofts methods (and found them to be equivalent). Temporal resolution of DEMRI in Müller-Schimpfle study was low (1 minute) whereas Hulka and Mussurakis used DEMRI sets acquired with a markedly higher temporal resolution of 12 and 6 seconds, respectively. Therefore, the different conclusions reached in these studies regarding the comparative utility of PK and BB methods are at least partly attributable to the differences in the DEMRI acquisition protocols.

It is virtually impossible to draw direct conclusions about the validity of individual approaches for both PK and BB analysis from the data currently presented in the literature due to the enormous diversity of the acquisition, sampling (i.e. ROI selection) and analysis methods. For example, acquisition protocols for DEMRI in breast tumours range from so-called semi-dynamic (with temporal resolution of more than 1 minute) with large tissue coverage to dynamic (with higher temporal resolution) and usually targeted selective unilateral tissue coverage. It is evident, however, that DEMRI patterns do differ significantly between benign and malignant lesions and in particular that permeability-related PK variables (regardless of the method used for PK analysis) do demonstrate a higher degree of permeability in malignant lesions.

The recognition that neovascularisation plays an important part in determining tumour aggressiveness [112] prompted investigations into the relationship between DEMRI findings and surrogate markers of angiogenesis such as microvessel density (MVD) and VEGF in breast cancer, as well as other types of cancer (see Chapter 1). Several studies have reported a significant relationship between these surrogate markers of angiogenesis and DEMRI in breast lesions using PK and BB analysis methods, whilst others identified no measurable link between them. The results of the representative studies are summarised in Table 3-3.

Study	Pathology	Summary of the findings
Knopp [99]	Breast lesions	• correlation between MVD and k_{21} in VEGF positive lesions • correlation between VEGF and k_{21}
Hulka [101] [100]	Breast lesions	• no correlation between EF and MVD
Ikeda [104]	Breast lesions	• correlation between K^{trans} and MVD
Hawighorst [113]	Cervical cancer	• correlation between A, ME and MVD • k_{21} and IRE prognostic factors
Hawighorst [86]	Cervical cancer	• correlation between A, k_{21} and MVD • k_{21} predicts lymphatic involvement
Mayr [115]	Cervical cancer	• correlation between A and k_{21} and MVD • negative correlation between k_{21} and VEGF
George [114]	Colorectal cancer	• correlation between K^{trans} and serum VEGF
Stomper [116]	Breast lesions	• correlation between MVD and ME • no correlation between MVD and IRE
Buadu [117]	Breast lesions	• correlation between MVD and IRE
Buckley [118]	Breast lesions	• correlation between MVD and IRE

Table 3-3 Reported correlations between surrogate angiogenesis markers and DEMRI

The most detailed study of the relationship between pharmacokinetic variables (A and k_{21}) and both MVD and VEGF in breast tumours was reported by Knopp [99]. In this study Brix's model has been used for pharmacokinetic analysis. Significantly higher values of k_{21} were measured in the malignant lesions when compared to the benign ones. In malignant

tumours, k_{21} was significantly higher in VEGF positive lesions than in the VEGF negative ones. Interestingly, k_{21} was strongly correlated with MVD only in VEGF negative lesions. In VEGF positive lesions (where higher k_{21} values were detected) there was no correlation between k_{21} and MVD.

Hulka [100, 101] reported no significant correlation between MVD and extraction-flow product (EF) in benign and malignant breast cancer (Larsson's approach). However, they found that cancers had higher EF than benign lesions and that ME was inferior in discriminating between benign and malignant lesions than EF. In another study of breast lesions Ikeda [104] demonstrated significant relationship between K^{trans} and MVD. A modified Tofts' method was used in this study. Mayr et al used Brix's method for the evaluation of cervical cancer and found that MVD correlated significantly with measured values of A and k_{21}. They also reported that k_{21} was inversely proportional to VEGF expression but they were unable to explain this seemingly contradictory finding.

Hawighorst [113] reported a significant correlation between the parameter A and MVD as well as ME and MVD in a study of primary uterine cervical cancer. In this study, VEGF and MVD were not correlated with survival whereas parameters k_{21} and IRE were shown to be significant prognostic factors (Brix's model). None of the measured DEMRI parameters correlated with VEGF. Black-box parameters were shown to give equivalent information. In their earlier study [86], they reported significant correlations between A and MVD as well as k_{21} and MVD in a mixed cohort of primary and recurrent cervical tumours. Parameter k_{21} (although correlated with MVD) was superior to MVD in detecting lymphatic involvement.

In a study reported by George [114] serum VEGF measurements were significantly correlated with K^{trans} (Tofts' model) in colorectal cancers. Pre-treatment K^{trans} values were predictive of treatment response. The lesions with higher pre-treatment K^{trans} had a better response to chemoradiotherapy.

Representative of the findings obtained in studies where black-box parameters were used in the assessment of breast tumours are the reports by Stomper [116], Buadu [117] and Buckley [118]. Stomper reported no correlation between ME in benign and malignant breast lesions whereas Buadu and Buckley reported significant correlation between IRE and MVD [117, 118]. Buckley reported that none of the PK variables demonstrated a significant correlation with MVD but pointed out that a natural logarithm of permeability-related PK variable correlated significantly with MVD.

A large degree of heterogeneity was observed in all these clinical studies and although some of them show measurable links between DEMRI findings and histopathological measures of microcirculation, the nature of these links is still not clear. Most authors agree, however, that DEMRI findings are indeed dependent upon the angiogenic status of the lesions. However, other contributing factors determine the overall DEMRI signal behaviour and the relationship between derived quantifiers of DEMRI and surrogate markers of angiogenesis. One of the recognised sources of variability arises from different methods used for MVD measurements. Furthermore, discrete MVD measurements are compared with PK and BB DEMRI variables derived from discrete ROIs with often uncertain spatial agreement between two tissue samples.

In conclusion, there is ample evidence that DEMRI findings obtained through a wide variety of methods vary significantly between benign and malignant lesions. As far as the pharmacokinetic modelling of Gd-DTPA is concerned, there is no convincing evidence that the principal approaches discussed in this chapter differ significantly in terms of their capacity to differentiate between benign and malignant lesions or to reflect isolated surrogate measures of angiogenesis.

These pharmacokinetic methods were shown to allow a comparable measurement of physiological variables such as the volume of the EES and apparent capillary permeability.

However, the methods used for quantitative analysis of DEMRI do differ in terms of their complexity and suitability for applications within a clinical setting as will be discussed in the following chapter.

Chapter 4. Development of the method for QDEMRI analysis

In this chapter, a development of the method used for QDEMRI analysis in the clinical applications (the breast cancer and RA) is described. The method includes the pharmacokinetic analysis of DEMRI (Section 4.1) as well as the computation of black-box variables (Section 4.3).

The theory of DEMRI dependence on the underlying physiological properties of the microcirculatory bed and the data currently reported in the literature suggest that temporal resolution as well as the sensitivity of the measured signal to changes in Gd-DTPA concentration define the capacity of DEMRI to measure physiological variables. Furthermore, tissue coverage and achieved spatial resolution are often important factors in defining the utility of DEMRI examinations performed within a clinical setting. Due to the nature of the MRI signal measurement and spatial encoding (Section 2.3), the temporal and spatial characteristics as well as the SNR and contrast properties of the DEMRI are not independent. Therefore, the requirements for a large tissue coverage and high spatial resolution impose constraints on the achievable temporal resolution, SNR and contrast properties of the DEMRI datasets. The design of the methods for the quantitative analysis of

DEMRI is therefore influenced by the nature of the experimental setting and the desired clinical objectives.

The analysis of the principal models for pharmacokinetic analysis of Gd-DTPA enhancement presented in Chapter 3 suggests that these methods are mathematically very similar and that the extracted pharmacokinetic variables obtained using these three methods are inter-related [70]. Furthermore, currently available evidence obtained in clinical applications of these methods does not provide conclusive evidence that any one of these methods is superior to the others. From the theoretical point of view, Larsson's approach is the most comprehensive one since it enables the correction for two most important covariates which influence the accuracy of DEMRI measurements of physiological variables, namely $T1_0$ mapping as well as individual sampling of Cp(t) (through the measurement of Gd-DTPA concentration in sequentially obtained blood-samples or parallel DEMRI sampling of vessels which supply the lesion of interest). However, rigorous implementation of this approach is difficult (if not impossible) on a majority of clinical MRI systems and it may compromise the maximum achievable spatial and temporal resolution, tissue coverage and T1 sensitivity of the signal extracted from the lesion of interest. Due to the complex inter-relationship between SNR, spatial and temporal resolution (Section 2.3), the acquisition of good quality signal for the sampling of Cp(t) can lead to the reduced quality of the DEMRI signal collected from the lesion of interest.

The selection of the acquisition settings for DEMRI in three clinical studies which are the subject of this thesis was constrained by a set of strict pre-set clinical requirements. A complete bi-lateral coverage of both breasts was required in the study of breast cancer since one of the principal clinical objectives was the detection of possible multifocality. In the RA studies, a representative multi-slice coverage of inflamed joints was required to allow the assessment of highly amorphous and heterogeneous synovial tissue. In all these studies, DEMRI was required to yield images of diagnostic quality, suitable for qualitative assessment

by radiologists. Furthermore, the duration of the DEMRI acquisition was required to be short (5 minutes or less) in order to minimise problems related to gross patient motion and patient discomfort. The duration of the DEMRI acquisition in the RA was also limited because of the need to minimise the impact of Gd-DTPA leakage into the synovial fluid and thus enable the measurement of synovial volume immediately after the completion of the DEMRI acquisition. Limiting the duration of the DEMRI was also deemed important with regard to reducing the total duration of the MRI examination.

The development of an effective method for pharmacokinetic modelling of Gd-DTPA enhancement for in the clinical applications which are the subject of this thesis focused on an adaptation of two models (Brix's and Tofts') which incorporate a theoretical representation of Cp(t) and thus do not impose additional constraints on the DEMRI acquisition within the tissue of interest. The comparison of the two approaches for theoretical representation of Cp(t), input function and contrast elimination is presented in Section 4.1 followed by the formulation of the mathematical representation of the pharmacokinetic model used in this thesis.

The model was then examined using a series of Monte Carlo simulations in order to investigate the influence of DEMRI sampling characteristics on the capacity of the proposed model to measure physiological variables (Section 4.2). The algorithm for the extraction of black-box variables is presented in Section 4.3. This algorithm was designed to allow automated, user-independent measurement of BB variables. The same algorithm was utilised in the design of the method for automated detection of the onset of enhancement and the calculation of the initial solutions for the non-linear least squares fitting of the simulated DEMRI datasets to the proposed theoretical model function.

4.1. Model definition

Treatment of plasma concentration Cp(t)

The treatment of Cp(t) was based on the theoretical representation of Cp(t) as proposed by Tofts et al and Brix et al (Section 3.3 and Section 3.4). In particular, a theoretical description of Cp(t) was sought which adequately represents Gd-DTPA plasma kinetics during a short DEMRI acquisition.

To enable a direct comparison between these two representations of Cp(t), Brix's model formulation in response to a bolus injection is considered here rather than a constant rate infusion, since Tofts' method also assumes a bolus input. According to Brix's model, Cp(t) is represented as a mono-exponential function (Eq. 4-1).

$$C_p(t) = \frac{m_{in}}{V_p} e^{-k_{el}t} \qquad \text{Eq. 4-1}$$

Total plasma volume is represented by Vp [l] and initial plasma concentration Cp(0) [mmol/l = mM] according to this model is given as:

$$C_p(0) = \frac{m_{in}}{V_p} = \frac{D \times BW}{\delta \times BW} \qquad \text{Eq. 4-2}$$

where D [mmol/kg] represents the injected dose per kilogram body weight (BW [kg]) and δ [l/kg] represents the fraction of BW occupied by body plasma.

The standard administration dose of Gd-DTPA is 0.1 mmol/kg. For a subject with a body weight of 70 kg, a total of 14 ml of contrast is injected (with a standard concentration of 0.5 M). Uniform levels of Gd-DTPA concentration in plasma (in different subjects) are achieved if the assumption of a constant ratio between body weight and total plasma volume holds.

The calculation of plasma volume from body weight is adequate for persons of average body weight. If the subject is at either end of the spectrum for weight (excessively obese or excessively cachectic), then plasma volume should be calculated from body surface area [119]. The ratio of plasma volume and body weight (δ) ranges between 0.04 l/kg to 0.05 l/kg with an average of 0.045 l/kg [119], i.e. an average $\delta = 0.045$ l/kg. The plasma volume can be calculated as 55% of total blood volume which in turn represents 8% of the total body weight yielding an average of 0.044 l of plasma per kg body weight [120], a figure which is in agreement to that reported in [119].

If the injected Gd-DTPA mixes uniformly and instantaneously within the entire plasma volume, the initial concentration of Gd-DTPA in plasma will be 2.22 mM, corresponding to a dilution of the injected Gd-DTPA in a volume of $Vp = \delta \times BW = 3.15$ litres for a subject with a body weight of BW = 70 kg and $\delta = 0.045$ l/kg (Eq. 4-3).

$$C_p(0) = \frac{m_{in}}{V_p} = \frac{0.1 \times BW}{0.045 \times BW} = 2.22\text{mM} \qquad \text{Eq. 4-3}$$

However, Tofts' representation of Cp(t) yields the following value of Cp(0):

$$C_p(0) = D\sum_{i=1}^{2} a_i^T = 0.877\text{mM} \qquad \text{Eq. 4-4}$$

This concentration reflects a larger effective Gd-DTPA distribution volume of approximately 0.114 [l/kg] × BW [kg], or 7.98 litres for a subject with a body weight of BW = 70 kg.

This enlargement of Gd-DTPA distribution volume is a result of the rapid extravasation of Gd-DTPA on its passage through the blood vessels following peripheral administration. The administered dose is therefore diluted throughout the plasma volume and the portion of the total body interstitial fluid. This process of peripheral extravasation is accounted for in the Tofts' model, where Cp(t) is represented as a bi-exponential function.

Brix's formulation of Gd-DTPA concentration in the lesion EES compartment also features the value of Vp (Eq. 3-15) but it is in effect combined with other parameters (including the fractional volume of the extracellular fluid f_{ex}) to form their parameter A (Eq. 3-14) or A/τ in Hoffman's version of the same model [83], where τ represents the duration of the infusion. Consequently, they were unable to offer any physiological interpretation for their parameter A (Eq. 3-14). According to the analysis of Cp(0) presented above, their central compartment should comprise not only blood plasma but also a fraction of the peripheral EES space which rapidly equilibrates with blood plasma, thus forming a larger initial distribution volume of Gd-DTPA.

A direct comparison between the bi-exponential plasma model suggested by Tofts (Eq. 3-13) and the simplified mono-exponential representation of plasma clearance (Eq. 4-5) was performed. In the simplified mono-exponential representation, a single fractional elimination constant (k_{el} = 0.058 min^{-1}) reported by Weinmann et al [64] was used together with the initial plasma concentration Cp(0) of 0.877 mM as described above (Eq. 4-4).

$$C_p(t) = 0.877e^{-k_{el}t} \qquad \text{Eq. 4-5}$$

The result suggests that a mono-exponential fit may adequately replace a more complex, bi-exponential representation for scanning duration of less than 5 minutes. The difference in Cp(t) computed using these two models at 5 minutes post-injection is 3% (0.02 mM) with an overall mean difference of 1% ± 1%. (See Figure 4-1). However, at 10 minutes post-injection this difference is considerably larger (11%) and bi-exponential representation of Cp(t) may be required.

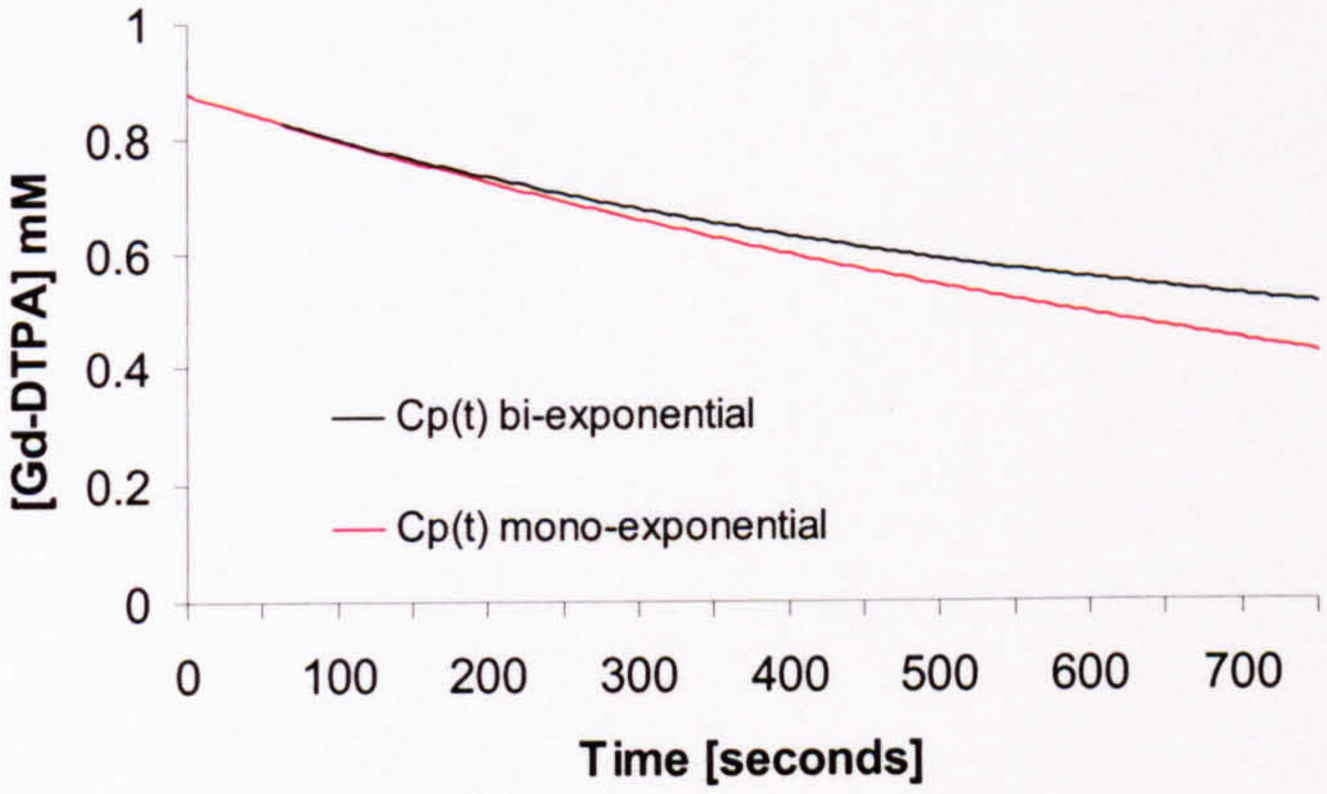

Figure 4-1 Mono-exponential approximation of Cp(t)

The fractional elimination rate k_{el} was allowed to vary freely in the Brix's method. As discussed in Section 3.4, this parameter can assume physiologically uninterpretable values, especially if the observation of Ct(t) through DEMRI is truncated shortly after the equilibrium between Gd-DTPA concentration in plasma and EES of the lesion is reached. Buckley et al also used mono-exponential representation of Cp(t) over the sampling period of 5 minutes in a variation of the Brix's method [121], following the same argument that over this time period a mono-exponential representation of Cp(0) is sufficient. He, however, allowed k_{el} to vary freely, but later noted that due to the symmetry of the function Ct(t) with respect to k_{el} and k_{21}, the estimation of k_{el} can cause unpredictable errors in the estimation of the permeability-related parameter k_{21} [122].

In this work, it was therefore decided to fix parameter k_{el} to the mean value measured in healthy volunteers (as did Tofts). However, as explained above, a mono-exponential function was shown to be adequate approximation of a more complex bi-exponential representation of Cp(t), for DEMRI studies with the duration of less than 5 minutes.

Treatment of the input function

Another important difference between Brix's and Tofts' methods stems from the differences in the chosen method of Gd-DTPA administration and the mathematical representation of the input function. The relationship between these two models was discussed in Section 3.4 where Brix's zero-order constant infusion input function was reduced to an idealised bolus in order to enable a direct comparison with the Tofts' representation.

However, the influence of the representation of the input function can be examined by performing the opposite transformation, i.e. assuming a constant rate infusion input function (with the duration of the infusion T, as used by Brix), which in the limit as T approaches zero is reduced to a delta function which corresponds to an idealised bolus (as used by Tofts). Furthermore, an approximation of the input function as a constant rate infusion allows a more realistic representation of the plasma and tissue response to a peripheral administration in the initial period following injection and especially at sites distal from the major supply arteries. A bolus injection is usually administered over a period of approximately 10 seconds. The data reported by Andersen et al and Fritz-Hansen et al [80, 88] demonstrate that the resulting Cp(t) curve has an approximate width of 20 seconds (time to peak). Therefore, a short constant rate infusion may be a more realistic representation of the bolus injection than an idealised delta function.

According to the arguments outlined above, the final formulation of the Cp(t) is therefore assumed to follow the expression given in Eq. 4-6, with a fixed $k_{el} = 0.058$ min^{-1} and a constant rate infusion input of duration T seconds. The expression is derived by substituting the representation of constant rate infusion in the Laplace domain (Eq. 2-29) in the system of linear equations presented in Eq. 2-27 and applying approximations described in Eq. 2-32.

$$C_p(t) = \frac{m_{in}}{V_p T k_{el}}(e^{k_{el}\tau} - 1)e^{-k_{el}t} = \frac{0.877}{T k_{el}}(e^{k_{el}\tau} - 1)e^{-k_{el}t}$$

where:

Eq. 4-6

$$\tau = \begin{cases} t & t \in [0, T] \\ T & t \in [T, \infty) \end{cases}$$

As discussed above, this expression actually describes the variation of Gd-DTPA in blood plasma and a portion of the EES which rapidly equilibrates with blood plasma. This function is illustrated in Figure 4-2 for a constant rate infusion of T = 20 seconds duration.

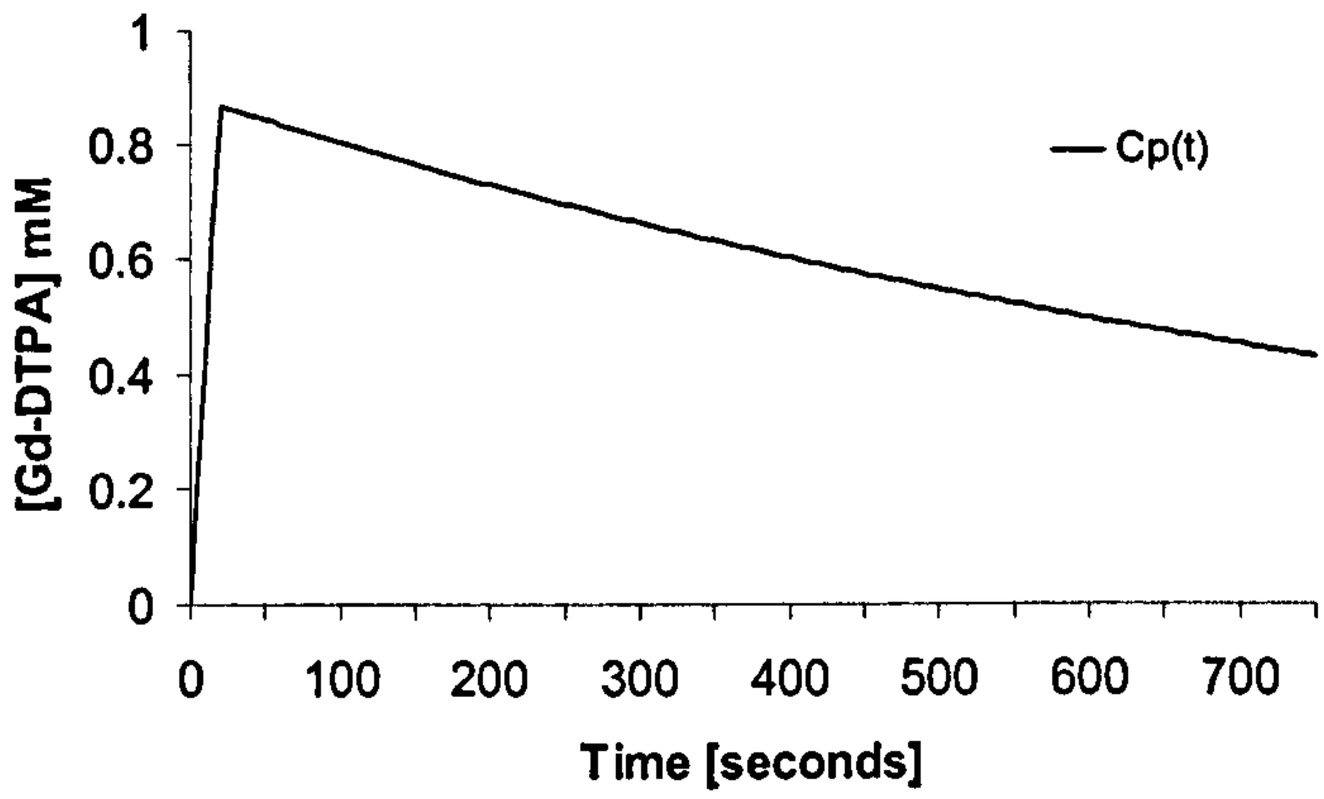

Figure 4-2 Cp(t) model

The concentration of the Gd-DTPA in the EES space of the lesion (Ce(t) = $C_2(t)$) in response to a constant rate infusion with duration T and Cp(t) of the form presented in Eq. 4-6 is derived and presented in Eq. 4-7 below, with fixed k_{el} = 0.058 min^{-1}. Again, this function is derived from a system of equations Eq. 2-29 in response to a constant rate infusion.

$$C_e(t) = C_2(t) = \frac{m_{in}}{V_p T}\left(u(e^{-k_{el}\tau} - 1)e^{-k_{el}\tau} - v(e^{-k_{21}\tau} - 1)e^{-k_{21}\tau}\right) =$$

$$= \frac{0.877}{T}\left(u(e^{-k_{el}\tau} - 1)e^{-k_{el}\tau} - v(e^{-k_{21}\tau} - 1)e^{-k_{21}\tau}\right)$$

where:

$$\tau = \begin{cases} t & t \in [0, T] \\ T & t \in [T, \infty) \end{cases}$$

Eq. 4-7

and:

$$u = \frac{k_{21}}{k_{el}(k_{21} - k_{el})} \qquad v = \frac{1}{k_{21} - k_{el}}$$

Model-predicted temporal variation of Gd-DTPA concentration in the peripheral compartment

The resulting model-predicted temporal variation of normalised DEMRI SI (f(t)), is then derived by combining the expressions presented in Eq. 2-20 and Eq. 4-7. The symbols u, v and τ are defined in Eq. 4-7.

$$f(t) = \frac{S_C}{S_0} = 1 + a\, C_t(t) = 1 + f_{ex} C_2(t) =$$

$$= 1 + a\, f_{ex} \frac{0.877}{T}\left(u(e^{-k_{el}\tau} - 1)e^{-k_{el}\tau} - v(e^{-k_{21}\tau} - 1)e^{-k_{21}\tau}\right) =$$

$$= 1 + A\left(u(e^{-k_{el}\tau} - 1)e^{-k_{el}\tau} - v(e^{-k_{21}\tau} - 1)e^{-k_{21}\tau}\right)$$

Eq. 4-8

where:

$$A = a\, f_{ex} \frac{0.877}{T}$$

Model-predicted temporal variation of normalised SI

This function is mathematically identical to the one proposed by Brix (Eq. 3-14). However, by using a modified Tofts' representation of Cp(t), the variable A is linked explicitly with the underlying fractional volume of the EES of the lesion (f_{ex} or v_e). Furthermore, the

fractional elimination rate k_{el} is excluded from the set of model parameters and replaced by a constant value.

Only two variables (k_{21} and f_{ex}) are allowed to vary freely. Each SI curve derived from the DEMRI set from either a discrete ROI or a single voxel is therefore characterized by a pair of pharmacokinetic parameters (f_{ex}, k_{21}). These parameters are extracted from the measured values of normalized SI ($s(t_k)$) at discrete time intervals t_k by means of non-linear least squares fitting (Levenberg-Marquardt, [123]). Non-linear least squares methods are applied to find the values of the parameters f_{ex} and k_{21} for which the sum of the squared variations of the model-predicted values $f(t_k)$ from the measured normalised signal intensity curves $s(t_k)$ is minimised. The problem can be described in terms of minimisation of the non-linear, multivariable objective function Chi Square (χ^2) given as:

$$\chi^2 = \sum_{k=0}^{n-1} \frac{(f(t_k, fex, k_{21}) - s(t_k))^2}{\sigma_k^2} \qquad \text{Eq. 4-9}$$

In Eq. 4-9 σ_k represents the values of standard deviations of the measurements $s(t_k)$ and n represents the total number of points in each SI curve.

To assess the behaviour of this model under different SNR and sampling conditions (sampling interval and sampling duration) and determine the influence of the length of infusion (T) on the accuracy and precision of the extracted physiological parameters, a series of Monte Carlo simulations was performed.

4.2. Monte Carlo simulations

Monte Carlo methods refer to a family of computational methods for simulation of natural processes which contain a naturally random component with the application of computer-

generated, pseudo-random numbers [124]. The development of Monte Carlo methods is closely related to the development of modern computers. It is used extensively in computational physics to solve previously intractable problems in field theory and thermodynamics.

In this work, a pseudo-random number generator was used to simulate MRI signal subjected to different levels of Gaussian noise. Signal intensity curves, derived from a range of simulated values of variables f_{ex} and k_{21} and under different assumed experimental conditions (sampling duration, sampling frequency, duration of the infusion) were subjected to varied levels of Gaussian noise, generated using a random number generator [123]. This random number generator is based on the one proposed by Park and Miller with Bays-Durham correction [125]. For every predefined pair of variables f_{ex} and k_{21}, under constant experimental conditions and constant noise level, 1000 curves were generated and analysed. The ability of non-linear fitting algorithms to extract true values of k_{21} and f_{ex} under different experimental conditions and noise levels was quantified in terms of the relationship between the pre-set values and the population of fitted values.

This method for the estimation of uncertainties of the measured values of k_{21} and f_{ex} was also used as a tool for the assessment of sampling and contrast administration requirements.

4.2.1. Core simulation

The model-predicted function describing the normalised SI variation as a function of f_{ex} and k_{21} (f(t), Eq. 4-8) was computed in the core simulation with the following set of assumed parameters: repetition time TR = 13 ms, flip-angle $\varphi = 60°$, T1 relaxivity $\alpha = 4.5$ (mMs)-1, pre-contrast $T1_0 = 900$ ms, infusion duration T = 20 seconds, sampling interval Delta T = 10 seconds, sampling duration 300 seconds. The range of f_{ex} was 0.1 – 0.9 and the range of k_{21} was 0.01 – 0.09 s^{-1}. This range of simulated values encompasses the entire range of f_{ex},

k_{21} and K^{trans} values reported in the literature (with resulting K^{trans} ranging from 0.06 min^{-1} to 4.86 min^{-1}). The pre-contrast $T1_0$ = 900 ms was chosen since it corresponds to the upper end of the range of T1 values in skeletal muscle at 1.5 T [50] and also approximates the mean T1 value of breast cancer [126, 127]. Furthermore, when the in-vivo measurements of T1 in synovitis, which were performed by Hull et all [128] using a 0.04 T MRI system, are converted to corresponding values at 1.5 T, an estimate of synovial T1 of 958 ms is obtained. The conversion of these T1 values to values T1 at 1.5 T was performed by applying the empirically derived constant for magnetic field dependence of T1 in breast carcinomas, reported in a review by Bottomley et al [127].

In the core simulation, it was assumed that the time of the onset of enhancement in tissue is known (T_{onset}) and that it coincides with the onset of enhancement in plasma. Furthermore, initial solutions required for the non-linear least squares fitting were equal to the known, pre-set values of f_{ex} and k_{21}. Monte Carlo simulations were performed using software written in the C programming language (Appendix E) with random number generators, straight line and non-linear least squares fitting routines adopted from a book by Press et al [123].

The examined range of k_{21} was represented by a set of nine discrete values, ranging from 0.01 s^{-1} to 0.09 s^{-1}, in steps of 0.01 s^{-1}. Similarly, nine discrete f_{ex} values were selected to represent f_{ex} values ranging from 0.1 to 0.9, in steps of 0.1. The two-dimensional matrix was thus formed, consisting of 81 elements. This matrix can be regarded as a test phantom comprising equal proportions of samples characterised by 81 distinct f_{ex} and k_{21} combinations.

For each pair of pre-set values of f_{ex} and k_{21} (f_{ex}, k_{21}) a series of 1000 curves with Gaussian noise was generated and subjected to non-linear least squares fitting to the proposed model function. The results obtained by fitting individual curves were stored in an array. For a matrix of consisting of 81 (f_{ex}, k_{21}) elements, a total of 81000 SI curves were

simulated, and 81000 pairs of fitted values of f_{ex} and k_{21} were obtained. Illustrations of core simulation curves generated under 1% and 10% Gaussian noise levels (with corresponding SNR of 100 and 10, respectively) and pre-set values of f_{ex} = 0.5 and k_{21} = 0.05 s^{-1} are given in Figure 4-3 and Figure 4-4. Simulated noiseless curves s(t) are depicted with red lines with superimposed noisy curves (s_n(t)).

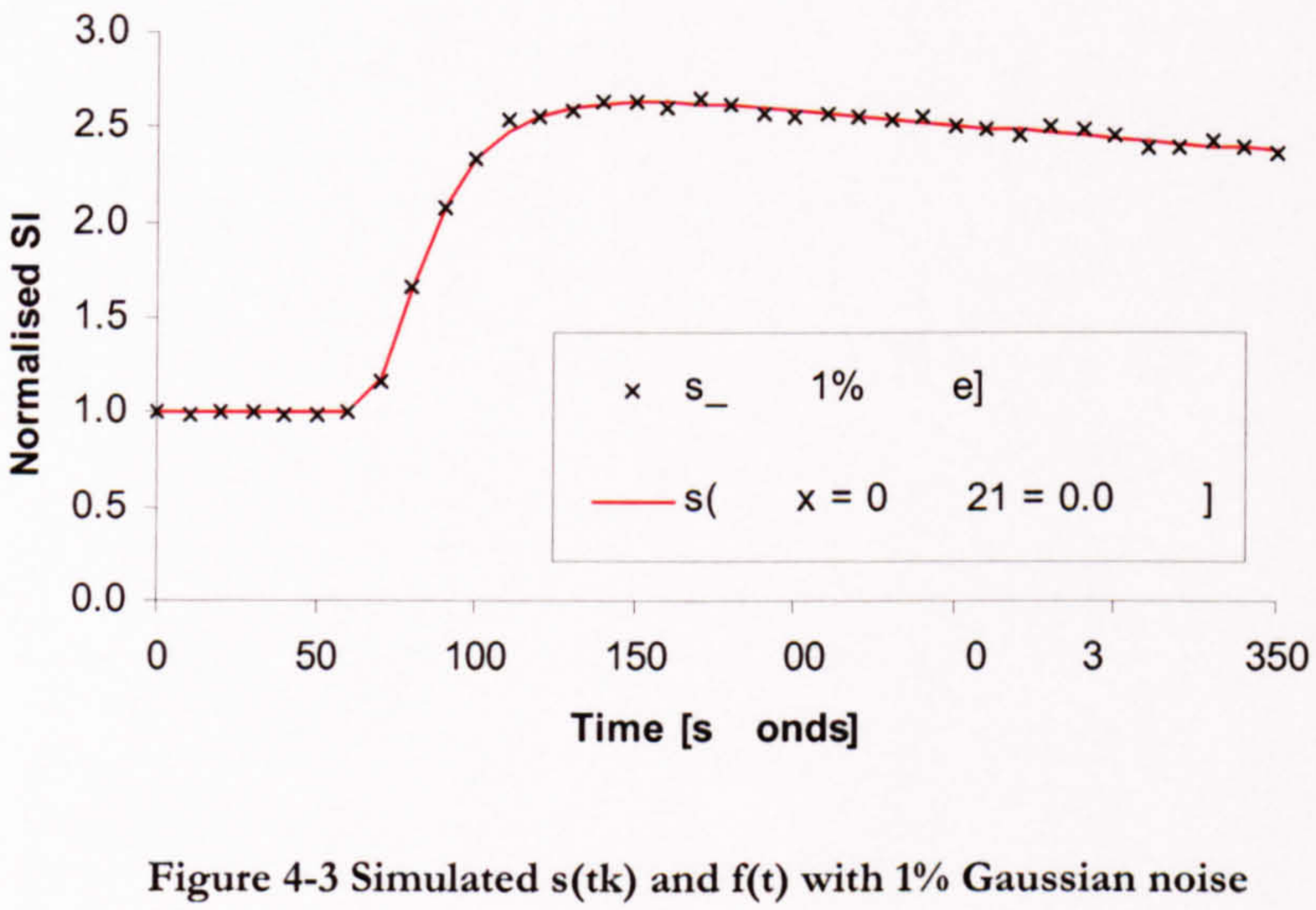

Figure 4-3 Simulated s(tk) and f(t) with 1% Gaussian noise

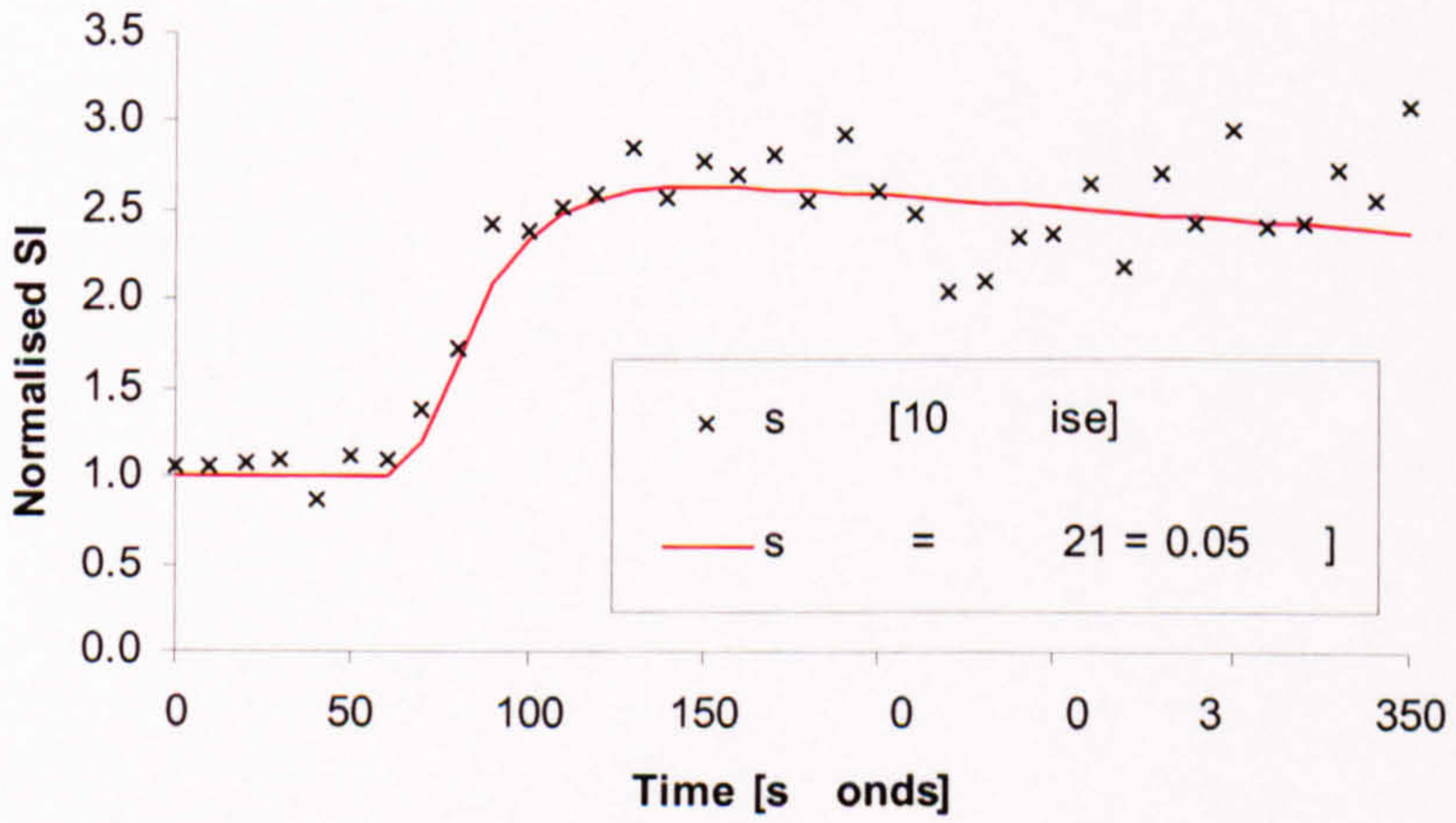

Figure 4-4 Simulated s(tk) and f(t) with 10% Gaussian noise

The curve presented in Figure 4-3, for example, belongs to a set of 1000 curves generated and analysed within this particular matrix element (f_{ex} =0.5, k_{21} =0.05 s^{-1}), in this Monte Carlo simulation run (which comprised the simulation of 81000 curves in total).

On completion of the Monte Carlo simulation run, the relationship between the population of results obtained by fitting the simulated curves to the model-predicted function and pre-set values of f_{ex} and k_{21} was examined.

All the results collected for a given f_{ex} and k_{21} pair were summarised in terms of the achieved accuracy (the difference between the mean of the fitted values and the pre-set values) and precision (the level of dispersion of the fitted values).

The accuracy of the fitting procedure for each of the resulting 81 matrix elements was computed as a difference between the mean fitted value and the nominal value expressed as a percentage of the nominal value. The accuracy of f_{ex} estimation is denoted as $A\_f_{ex}(f_{ex}, k_{21})$ and the accuracy of k_{21} estimation is labelled $A\_k_{21}(f_{ex}, k_{21})$. Both values are two-dimensional functions of the nominal, pre-set values of f_{ex} and k_{21}, and are presented as percentages.

$$A\_f_{ex}(f_{ex}, k_{21}) = 100(f_{ex}\_fit - f_{ex})/f_{ex}\ [\%]$$

$$A\_k_{21}(f_{ex}, k_{21}) = 100(k_{21}\_fit - k_{21})/k_{21}\ [\%]$$

In these calculations, f_{ex}_fit and k_{21}_fit represent the mean fitted value of f_{ex} and k_{21} (respectively), obtained in a series of n = 1000 Monte Carlo runs. For example, the fitting of a series of 1000 curves obtained in a matrix element (f_{ex} =0.5, k_{21} =0.05 s^{-1}) at 1% noise level (one of which is illustrated in Figure 4-3) yielded an average f_{ex}_fit of 0.49997 with a standard deviation of 0.00176 and an average k_{21}_fit of 0.05005 s^{-1} with a standard deviation of 0.00101 s^{-1}. The accuracy of the fitting in this matrix element (f_{ex} =0.5,

k_{21} =0.05 s^{-1}) is thus calculated as $A\_f_{ex}(f_{ex}, k_{21})$ = -0.006% and $A\_k_{21}(f_{ex}, k_{21})$ = 2.013%.

Precision of the fitting procedure (the degree of dispersion of the fitted parameters) was expressed as the coefficient of variation (CV). Precision of f_{ex} estimation is denoted as $P\_f_{ex}(f_{ex}, k_{21})$ and precision of k_{21} estimation is labelled $P\_k_{21}(f_{ex}, k_{21})$.

$$P\_f_{ex}(f_{ex}, k_{21}) = 100SD(f_{ex}\_fit)/f_{ex}\_fit\ [\%]$$

$$P\_k_{21}(f_{ex}, k_{21}) = 100SD(k_{21}\_fit)/k_{21}\_fit\ [\%]$$

Using the same example as before (i.e. 1000 simulations in a matrix element (f_{ex} =0.5, k_{21} =0.05 s^{-1}) at 1% noise level), the precision of f_{ex} estimates in this matrix element is calculated as $P\_f_{ex}(f_{ex}, k_{21})$ = 0.352% and $P\_k_{21}(f_{ex}, k_{21})$ = 2.012%. A diagram of the simulation procedure is presented in Figure 4-5.

The overall precision and accuracy (A_f_{ex}, A_k_{21}, P_f_{ex}, P_k_{21}) achieved in one complete simulation run over the entire range of f_{ex} and k_{21} (involving the analysis of a full set of 81000 curves) is expressed as the average of all matrix cell values (Eq. 4-10).

$$A\_f_{ex} = \sum_{f_{ex}}\sum_{k_{21}} A\_f_{ex}(f_{ex}, k_{21}) \qquad P\_f_{ex} = \sum_{f_{ex}}\sum_{k_{21}} P\_f_{ex}(f_{ex}, k_{21})$$

$$A\_k_{21} = \sum_{f_{ex}}\sum_{k_{21}} A\_k_{21}(f_{ex}, k_{21}) \qquad P\_k_{21} = \sum_{f_{ex}}\sum_{k_{21}} P\_k_{21}(f_{ex}, k_{21}) \qquad \text{Eq. 4-10}$$

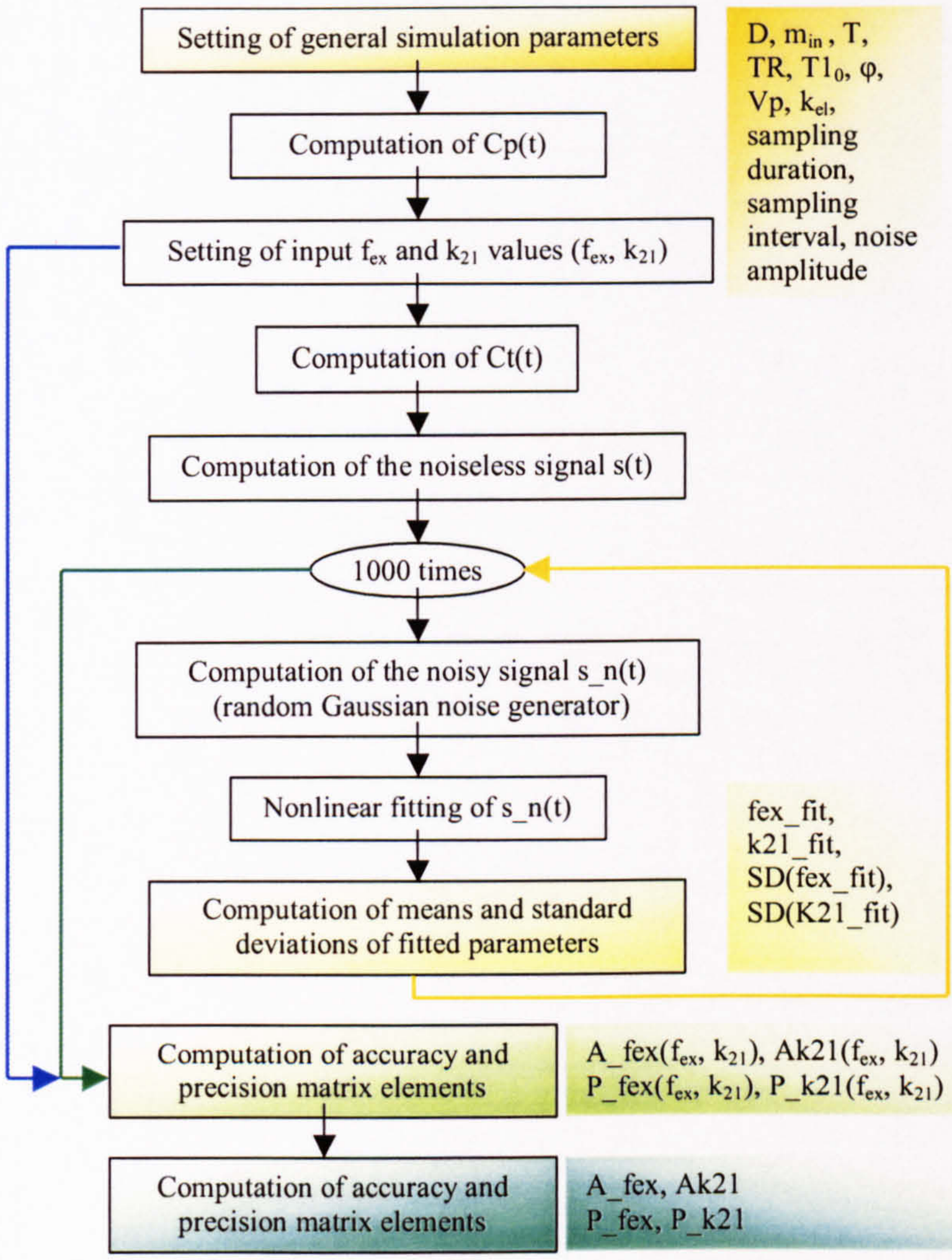

Figure 4-5 Monte Carlo simulation flow-chart

4.2.2. Constrained minimisation

All parameters were subjected to the constraint of non-negativity. In addition to this constraint, k_{21} was required to be at least two times larger than the fractional elimination rate constant k_{el} in order to avoid problems associated with the symmetry of the expression for Ct(t) with respect to k_{21} and kel [122]. A modification of the fitting algorithm was also implemented to restrict the fitted values of k_{21} to below a threshold of 0.125

(experimentally determined) due to the tendency of the algorithm to find local minima at extremely high k_{21} values in a proportion of curves simulated under high noise levels.

Nois		Unconstrained	Constrained
Acc	f fex	0.01 (0.03)	0.01 (0.03)
Acc	f k21	0.05 (0.11)	0.51 (0.33)
Prec	fex	0.51 (0.33)	0.05 (0.11)
Prec	k21	2.66 (1.42)	2.66 (1.42)

Nois		Unconstrained	Constrained
Acc	f fex	0.58 (1.00)	0.58 (1.00)
Acc	f k21	8.08 (14.53)	5.24 (3.56)
Prec	fex	5.27 (3.58)	3.01 (3.91)
Prec	k21	34.90 (30.35)	24.73 (10.40)

Table 4-1 Results of the constrained minimisation in the core simulation at 1% and 10% noise levels

The results of the simulations performed at two different noise levels (1% and 10%) are listed in Table 4-1, where table elements represent the overall achieved accuracy and precision (mean and one standard deviation), expressed as a percentage of the nominal (pre-set) values, as defined in the previous section. As can be seen from Table 4-1, parameter f_{ex} can be estimated with high accuracy (less than 1% of the nominal value) at both noise levels and irrespective of the application of the k_{21} constraint as described above. Parameter k_{21}, however, displays significantly larger level of bias (8% reduced to 5% when the constraint is employed) and considerable level of dispersion (35% and 25% for unconstrained and constrained algorithms, respectively). The influence of the k_{21} constraint becomes apparent only at high noise levels, with the measurements performed at 1% noise remaining unchanged.

To illustrate the performance of the constrained algorithm for different elements of (f_{ex}, k_{21}) matrix, two-dimensional maps of P_f_{ex} and P_k_{21} are presented in Figure 4-6.

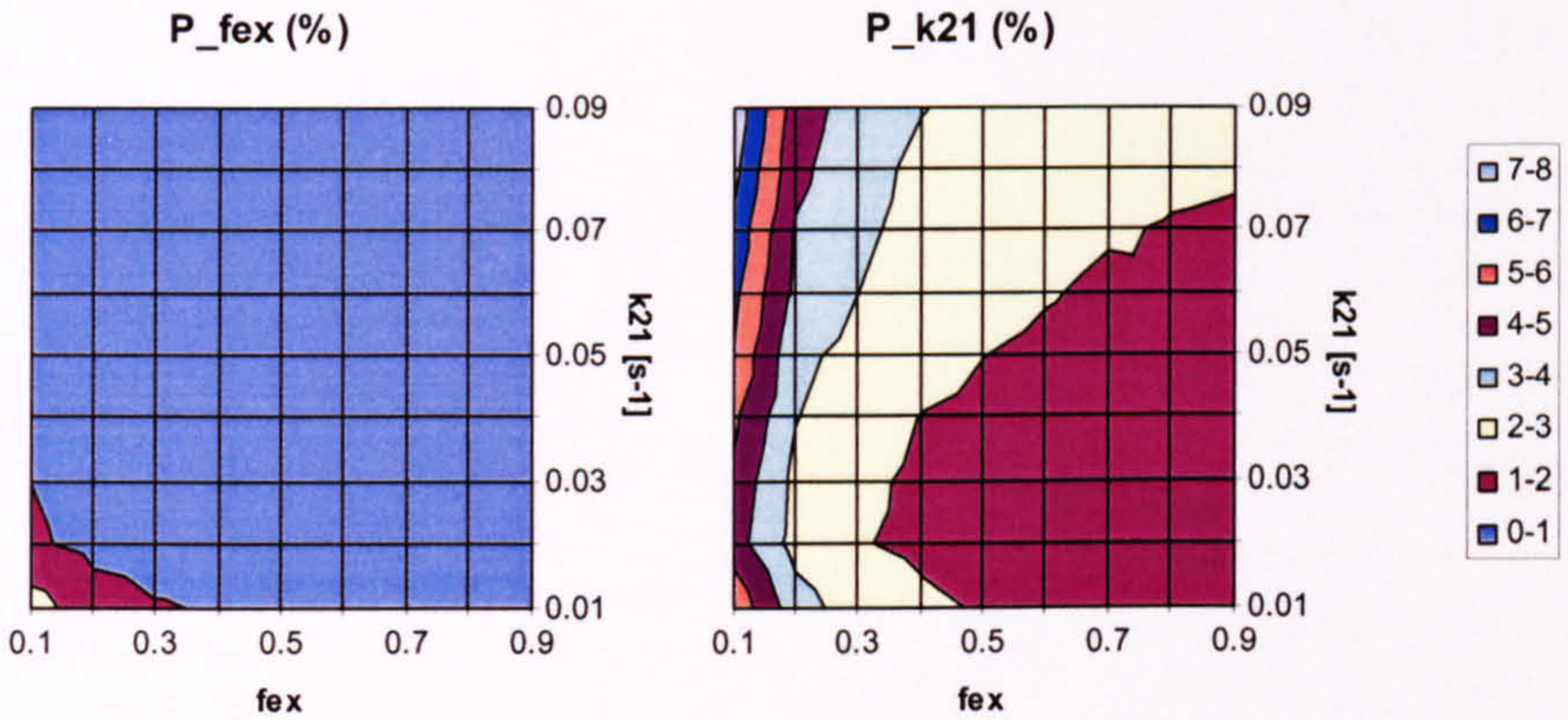

Figure 4-6 Precision of f_{ex} and k_{21} estimates under 1% noise level

In this two-dimensional surface-plot representation, the matrix elements with coordinates (f_{ex} , k_{21}) are located at the intersections of vertical and horizontal gridlines. The measured values of precision of the estimates achieved in individual matrix elements are expressed as percentages and colour coded using an identical colour-coding scheme (displayed in the legend). The precision of f_{ex} estimation is within 1% (coded in light blue) for all matrix elements apart from the ones in the bottom left-hand corner (where both f_{ex} and k_{21} are at the extreme lower end of the examined range). The precision of k_{21} estimates, however, varies considerably and deteriorates with decreasing f_{ex} and increasing k_{21}. In the upper half of the examined range of f_{ex} the precision of k_{21} estimates is between 1% and 3% of the nominal value at this noise level (the areas coded dark red and yellow).

4.2.3. Influence of SNR on model performance

The results presented in Table 4-1 illustrate the importance of noise levels on the performance of the algorithm. To examine more closely the nature of this influence, a core simulation was performed (with the application of the k_{21} constraint) under ten noise levels, ranging from 1% to 10%. The results are presented in Figure 4-7.

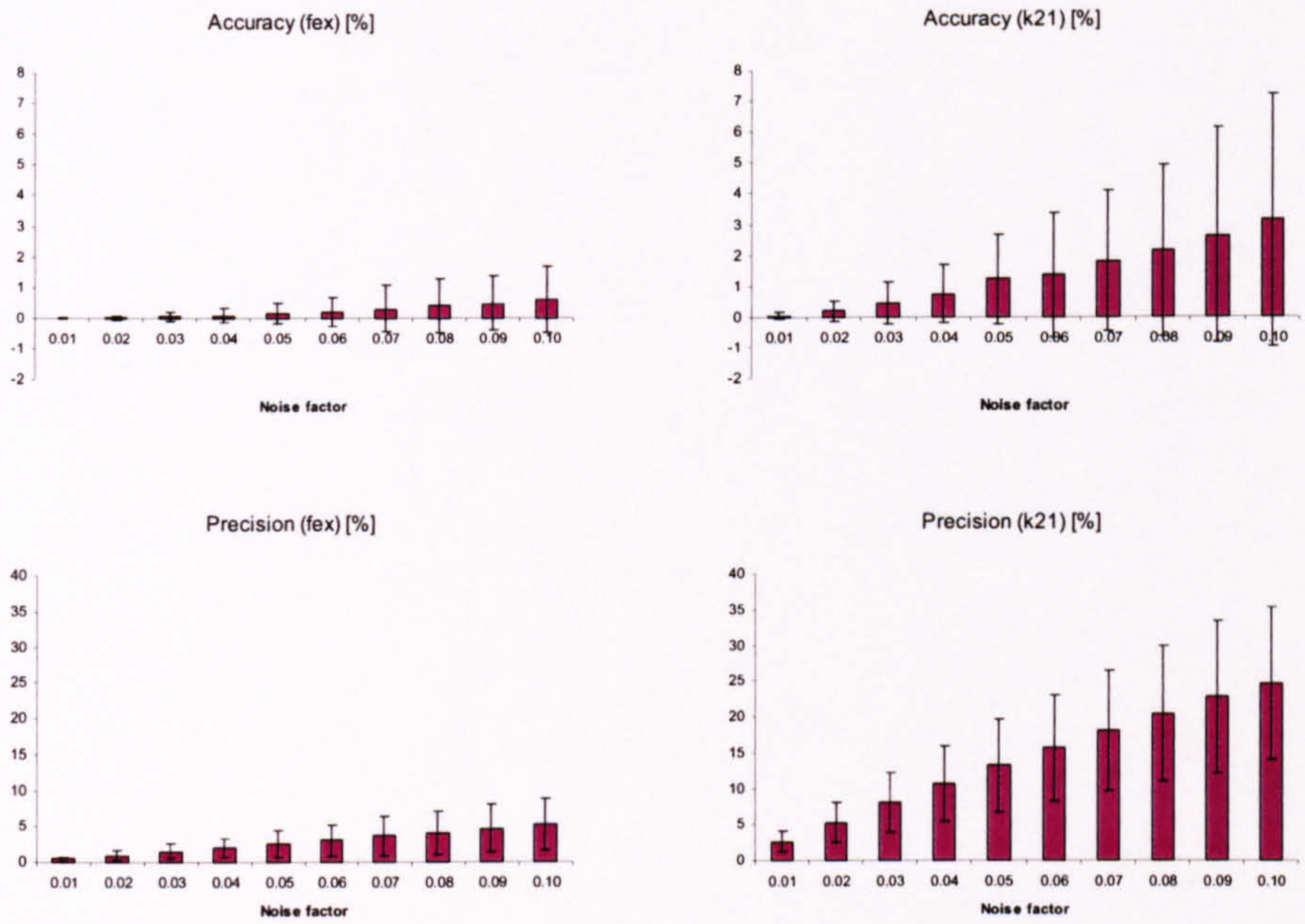

Figure 4-7 Accuracy and precision of f_{ex} and k_{21} estimates under varying noise levels

The values on horizontal axes represent noise factors, i.e. noise factor of 0.01 (1% noise) corresponds to a SNR setting of 100. Error bars represent 1 SD limits. At all noise levels, parameter f_{ex} displays very stable behaviour. However, the ability of the minimisation algorithm to reliably extract k_{21} from noisy datasets deteriorates rapidly with decreasing SNR.

4.2.4. Influence of temporal resolution on model performance

The influence of the temporal resolution (Delta T) on the performance of the fitting routine was assessed by modifying the core simulation and collecting f(t) samples (s(tk)) with Delta T = 1 second, 5 seconds and 20 seconds (with a fixed overall sampling duration of 300 seconds). The results were compared with the core simulation (Delta T = 10 seconds) and the summary of the measurements is presented in Table 4-2.

1% Noise	Delta T = 1s	Delta T = 5s	Delta T =10s	Delta T = 20s
Accuracy of fex	0.00 (0.01)	0.00 (0.02)	0.01 (0.03)	0.01 (0.04)
Precision of fex	0.16 (0.10)	0.36 (0.22)	0.51 (0.33)	0.73 (0.47)
Accuracy of k21	0.00 (0.02)	0.02 (0.07)	0.05 (0.11)	0.09 (0.16)
Precision of k21	0.84 (0.44)	1.88 (1.00)	2.66 (1.42)	3.70 (1.94)

10% Noise	Delta T = 1s	Delta T = 5s	Delta T =10s	Delta T = 20s
Accuracy of fex	0.06 (0.13)	0.34 (0.82)	0.58 (1.00)	1.11 (1.43)
Precision of fex	1.59 (1.02)	3.67 (2.69)	5.24 (3.56)	7.58 (4.85)
Accuracy of k21	0.52 (0.72)	1.78 (2.29)	3.01 (3.91)	4.67 (7.45)
Precision of k21	8.40 (4.32)	18.22 (8.29)	24.73 (10.40)	32.62 (13.45)

Table 4-2 Results of the simulations performed with different sampling intervals (Delta T)

As can be seen from Table 4-2, the accuracy and precision of fitted parameters deteriorates with increasing Delta T at any given noise level. This relationship, however, is not linear. Doubling sampling frequency by reducing Delta T from 10 seconds to 5 seconds, results in the improvement in P_k_{21} from 25% to 18% at the 10% noise level. The parameter f_{ex}, again displays only a moderate degree of dependence on Delta T and can be fitted reliably even at the 10% noise level and low temporal resolution (Delta T = 20 seconds).

4.2.5. Trade-off between SNR and sampling interval

The results of simulations performed at noise levels of 1.41 and 0.7% in addition to the original 1% and 14.1% and 7% in addition to original 10%, revealed that doubling of sampling frequency has approximately the same effect as the loss of SNR by a factor of $\sqrt{2}$ (i.e. increase in the noise level by the same factor). The results obtained at Delta T =10 at 10% noise level are equivalent to those obtained at Delta T = 5 at 7% noise level. In other words, sampling at higher frequencies (higher temporal resolution) accompanied by the concomitant reduction of SNR to $\sqrt{2}$ SNR does not improve the accuracy of the fitted parameters.

	Delta T = 5s 1.41% noise	Delta T = 10s 1% noise	Delta T = 20s 0.7% noise
Accuracy of fex	0.01 (0.02)	0.01 (0.03)	0.01 (0.02)
Precision of fex	0.50 (0.32)	0.51 (0.33)	0.51 (0.33)
Accuracy of k21	0.04 (0.11)	0.05 (0.11)	0.05 (0.10)
Precision of k21	2.67 (1.42)	2.66 (1.42)	2.62 (1.36)

	Delta T = 5s 14.1% noise	Delta T = 10s 10% noise	Delta T = 20s 7% noise
Accuracy of fex	0.64 (1.26)	0.58 (1.00)	0.60 (0.91)
Precision of fex	5.24 (3.70)	5.24 (3.56)	5.31 (3.54)
Accuracy of k21	2.96 (3.90)	3.01 (3.91)	2.84 (3.96)
Precision of k21	24.84 (10.86)	24.73 (10.40)	24.55 (10.71)

Table 4-3 Trade-off between sampling duration and noise level

Similarly, sampling at a lower temporal resolution (long Delta T) does not adversely affect the performance of the model if the SNR is increased by at least factor of $\sqrt{2}$.

4.2.6. Influence of infusion duration

The simulations were performed using variable duration of infusion, ranging from T = 1 second (which approximates an idealised bolus input) to T = 120 seconds. The results are summarised in Table 4-4.

Noise 1%	T = 1s	T = 5s	T = 10s	T = 20s
Accuracy of fex	0.01 (0.02)	0.01 (0.02)	0.01 (0.02)	0.01 (0.03)
Precision of fex	0.49 (0.31)	0.49 (0.31)	0.50 (0.32)	0.51 (0.33)
Accuracy of k21	0.04 (0.10)	0.04 (0.10)	0.04 (0.10)	0.05 (0.11)
Precision of k21	2.55 (1.33)	2.53 (1.31)	2.58 (1.35)	2.66 (1.42)

Noise 1%	T = 30s	T = 60s	T = 120s
Accuracy of fex	0.01 (0.03)	0.01 (0.03)	0.01 (0.04)
Precision of fex	0.52 (0.34)	0.55 (0.38)	0.67 (0.52)
Accuracy of k21	0.06 (0.12)	0.09 (0.17)	0.15 (0.27)
Precision of k21	2.77 (1.50)	3.14 (1.76)	4.06 (2.41)

Noise 10%	T = 1s	T = 5s	T = 10s	T = 20s
Accuracy of fex	0.54 (0.93)	0.55 (0.96)	0.56 (0.96)	0.58 (1.00)
Precision of fex	5.07 (3.41)	5.12 (3.46)	5.14 (3.47)	5.24 (3.56)
Accuracy of k21	2.83 (3.96)	2.74 (3.91)	2.88 (3.98)	3.01 (3.91)
Precision of k21	24.05 (10.47)	23.87 (10.43)	24.21 (10.47)	24.73 (10.4)

Noise 10%	T = 30s	T = 60s	T = 120s
Accuracy of fex	0.62 (1.04)	0.71 (1.09)	0.92 (1.05)
Precision of fex	5.35 (3.68)	5.70 (3.88)	6.66 (4.31)
Accuracy of k21	3.19 (4.02)	3.83 (4.87)	5.63 (7.51)
Precision of k21	25.48 (10.64)	27.87 (11.7)	33.15 (13.03)

Table 4-4 Influence of infusion duration on model performance

The results presented in Table 4-4 suggest that shorter infusion duration allows mode reliable estimation of k_{21} and f_{ex}. These results confirm the findings reported by Tofts and Henderson [94, 95] although they show only a mild overall influence of the infusion duration T. The duration of infusion has direct bearing on the overall duration of DEMRI acquisition and, according to the results presented here, longer infusion times do not improve the model performance. On the other hand, the assumption that the experimental data are derived from samples with an effective T of 5 seconds (or lower) is unrealistic in tissues distal from the major supply vessels and the site of contrast injection [80, 88]. The results presented in Table

4-4 indicate that the variation in the algorithm performance over the range of T between 10 seconds and 30 seconds is negligible.

To assess the potential errors caused by modelling the input function as a bolus whilst the actual input function is a constant-rate infusion with T = 20 seconds, another simulation was performed by using data samples calculated by assuming T = 20 seconds but modelled using a function with T = 1 seconds (idealised bolus). If the start of enhancement coincides with the start of bolus, fitted values of k_{21} are underestimated by 34% at both noise levels. The values obtained by "bolus" modelling will coincide with the parameters fitted by assuming T of 20 seconds only if the bolus is assumed to occur at the centre of the infusion.

4.2.7. Influence of sampling duration

To assess the influence of sampling duration on the performance of the model, a core simulation was performed with sampling duration of 150 seconds (one half of the original 300 seconds) and 600 seconds (double the original 300 seconds).

Noise 1%	Duration 150s	Duration 300s	Duration 600s
Accuracy of fex	0.06 (0.18)	0.01 (0.03)	0.00 (0.01)
Precision of fex	1.30 (1.54)	0.51 (0.33)	0.31 (0.15)
Accuracy of k21	0.05 (0.17)	0.05 (0.11)	0.06 (0.10)
Precision of k21	3.81 (2.37)	2.66 (1.42)	2.39 (1.39)

Noise 10%	Duration 150s	Duration 300s	Duration 600s
Accuracy of fex	1.67 (1.59)	0.58 (1.00)	0.14 (0.19)
Precision of fex	11.06 (7.38)	5.24 (3.56)	3.05 (1.45)
Accuracy of k21	5.32 (7.11)	3.01 (3.91)	2.61 (3.66)
Precision of k21	32.23 (13.68)	24.73 (10.40)	22.13 (10.04)

Table 4-5 Influence of sampling duration on model performance

The results presented in Table 4-5 suggest that increase in sampling duration yields a relatively minor improvement in the performance of the fitting algorithm. However, very short sampling duration (150 seconds) results in increased errors in both f_{ex} and k_{21}. The findings presented in Table 4-5 have an important bearing on the practical implementation of DEMRI because they demonstrate that the doubling of the examination duration from 5 min to 10 min does not confer any benefit regarding the quantitative analysis of DEMRI.

4.2.8. Influence of time offset between s(t) and Cp(t)

The results presented so far have been obtained under the assumption that a true onset of the enhancement (T_{onset}) is known and that the time scale used for fitting the sample data coincides with the time axis used to generate the concentration curves. However, the true start of the enhancement can occur at any point within the sampling interval. To simulate the effect of the uncertainty of the time offset between the measured samples of s(t) and the Cp(t), a series of simulations was performed with a variable time offset between the Cp(t) and Ct(t). The simulated error in T_{onset} (δ) was varied from –10 seconds to +10 seconds in steps of 1 second.

$$T_{onset}' = T_{onset} + \delta,\ \delta = -10, -9, .. -1, 0, 1, .. 9, 10$$

For example, with a sampling interval of Delta T = 10 seconds, $T_{onset}' = T_{onset} - 10$, the assumed start of enhancement (T_{onset}') occurs 10 seconds ahead of the true onset (T_{onset}). As can be seen from Figure 4-8, high accuracy of f_{ex} and k_{21} fitting can only be achieved if the T_{onset} is known or detected accurately.

Furthermore, if the errors in the measurement of T_{onset} are symmetrically distributed either side of T_{onset}, the errors in f_{ex} and k_{21} will be partially cancelled. If the probability distribution of δ is uniform, overall accuracy of f_{ex} and k_{21} with 1% noise in s_n(t) will be

0.10±0.67 (%) and 5.65±11.16 (%) respectively. Overall accuracy is computed over the entire set of 21 simulations (with different delta values ranging from –10 to +10 seconds). Figure 4-8 also illustrate the fact that the effect of T_{onset} uncertainty on the fitted values of f_{ex} and k_{21} is markedly different. Underestimation of T_{onset} ($\delta<0$) results in the underestimation of f_{ex} and overestimation k_{21}. When $\delta>0$, the sign of errors are reversed.

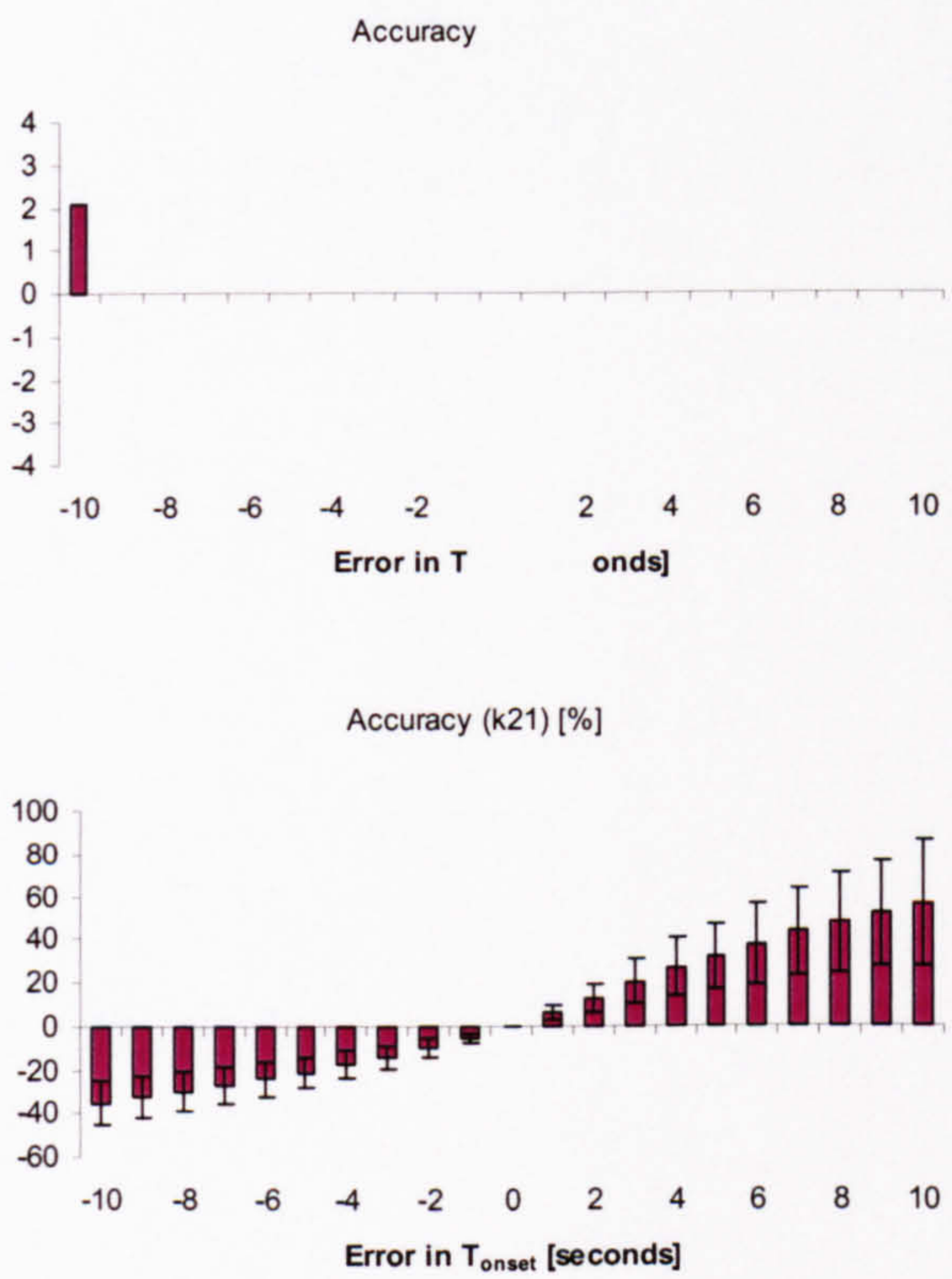

Figure 4-8 Distribution of errors in f_{ex} and k_{21} estimation as a function of the errors in T_{onset} at 1% noise level

This set of simulations was repeated at the higher noise level (10%). At this noise level, the overall accuracy of f_{ex} and k_{21} are 0.67±11.27 (%) and 6.06±10.20(%) respectively (again, uniform distribution of δ is assumed). A similar pattern of errors in f_{ex} and k_{21} was detected (Figure 4-9). The accuracy of fitted values of k_{21} is predominantly determined by the uncertainty of T_{onset} and changes only marginally in response to the 10-fold increase in

noise level. At the higher noise level of 10% f_{ex} has a small positive bias when $\delta = 0$ (when true T_{onset} is assumed), and the smallest errors occur when $\delta = 3$ seconds.

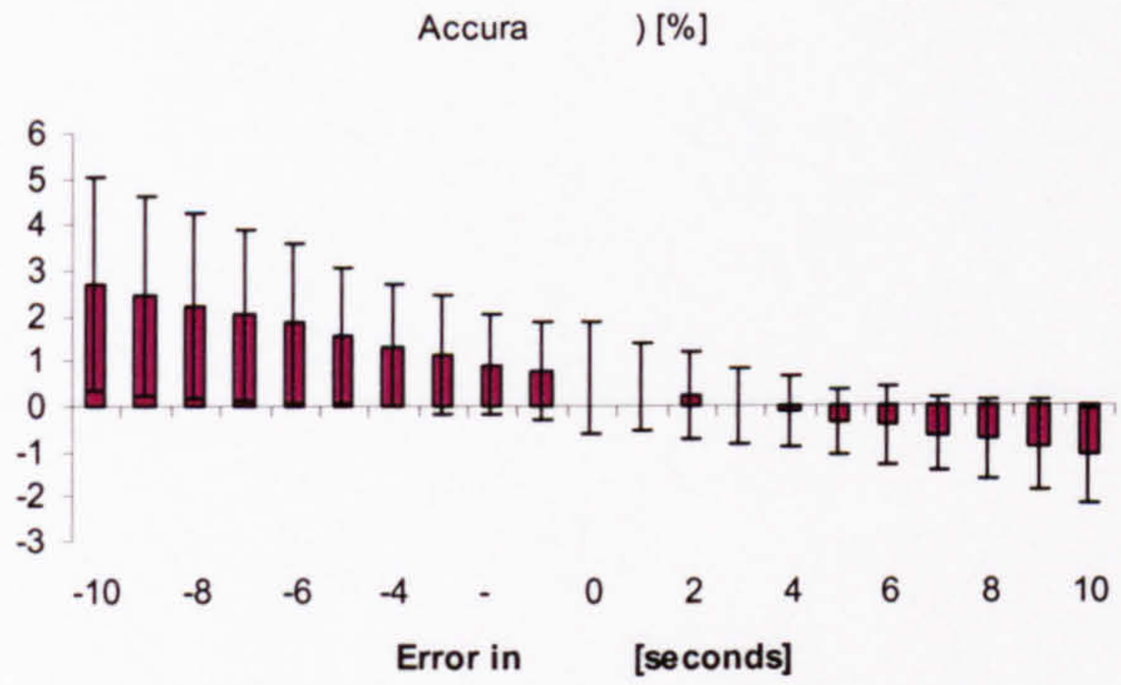

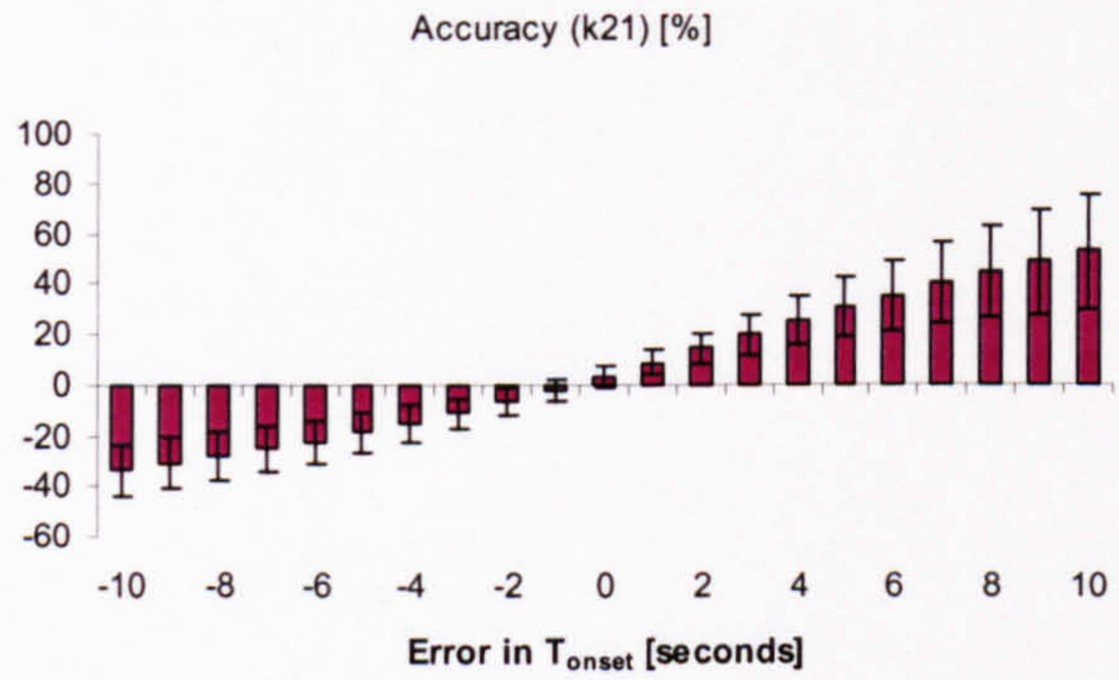

Figure 4-9 Distribution of errors in f_{ex} and k_{21} estimation as a function of the errors in T_{onset} at 10% noise level

These results demonstrate that the detection of the onset of enhancement has a very strong influence on the performance of the fitting algorithm and the achieved levels of accuracy and precision. The errors incurred by incorrect measurement of T_{onset} are substantial even at low noise levels. The parameter k_{21} is more susceptible to this source of error than f_{ex}. Furthermore, the true influence of the temporal resolution (Delta T) on the performance of the fitting algorithm (and consequently, the ability to accurately measure f_{ex} and k_{21}) is a direct consequence of the magnitude of the uncertainty of T_{onset}. As can be seen from Table

4-2, in the absence of T_{onset} uncertainty ($\delta = 0$), sampling time has only a mild influence on the performance of the fitting algorithm.

However, by noting that errors in f_{ex} and k_{21} in particular rise sharply with $|\delta|$ (modulus of δ), and that the maximal value of $|\delta|$ is directly related to the temporal sampling resolution (Delta T), the true influence of sampling time on the ability to measure f_{ex} and k_{21} is revealed.

The algorithm used for the detection of T_{onset} in s_n(t) was based on the measurement of the black-box variable IRE (initial rate of enhancement). The description of the algorithms used for the measurement of black-box variables is therefore presented in the following section. It includes the description of the algorithms used for the measurement of IRE and maximal enhancement (ME).

4.3. Algorithms for measurement of black-box variables

In this section, the algorithms for the measurement of black-box (BB) variables ME and IRE are presented. The relationship of these heuristic variables to the underlying pharmacokinetic variables f_{ex} and k_{21} is explored by computing theoretical, model-based equivalents of ME and IRE. The method for the detection of the onset of enhancement (T_{onset}) based on the measurements of IRE is also described in this section.

According to the mathematical representation of the model (Eq. 4-7 and Eq. 4-8), the maximal rate of change in Ce(t) and consequently Ct(t) and f(t) will be reached at the end of infusion (t = T). The function presented in Eq. 4-8 has a discontinuity at t = T but the maximal rate of change can be computed as the slope of the tangent to the f(t) curve at t = T. An accurate detection of this tangent will lead to the accurate detection of T_{onset}. From the equation Eq. 4-8, the following expression is obtained for the derivative of f(t) at t = T:

$$IRE \propto \left.\frac{df(t)}{dt}\right|_{t=T} = a\left.\frac{dC_t(t)}{dt}\right|_{t=T}$$

$$= a\, f_{ex}\, \frac{0.877}{T}\frac{k_{21}}{k_{21}-k_{el}}\left(e^{-k_{el}T} - e^{-k_{21}T}\right) \qquad \text{Eq. 4-11}$$

Maximal enhancement (f_{max}) is reached when the first derivative of f(t) equals zero (Eq. 4-12).

$$\frac{df(t)}{dt} = 0 \Rightarrow e^{-k_{el}t} - e^{-k_{21}t} = 0 \qquad \text{Eq. 4-12}$$

The resulting expression for the t_{max} (the time when the maximal enhancement is reached) is given below (Eq. 4-13).

$$t_{max} = \frac{1}{k_{21}-k_{el}}\ln\left(\frac{e^{k_{21}T}-1}{e^{k_{el}T}-1}\right) \qquad \text{Eq. 4-13}$$

It is now possible to obtain the expression for model-based equivalent of ME as a function of pharmacokinetic parameters (Eq. 4-14).

$$ME \propto f_{max} = 1 + a\, C_t(t_{max}) =$$

$$= 1 + A\left(\frac{k_{21}}{k_{el}(k_{21}-k_{el})}(e^{k_{21}T}-1)e^{-k_{21}t_{max}} - \frac{1}{(k_{21}-k_{el})}(e^{k_{el}T}-1)e^{-k_{el}t_{max}}\right) \qquad \text{Eq. 4-14}$$

$$\text{where } A = a\, f_{ex}\, \frac{0.877}{T}$$

This relationship between model-based equivalents of BB variables ME and IRE and PK variables k_{21} and f_{ex} is illustrated in Figure 4-10 and Figure 4-11.

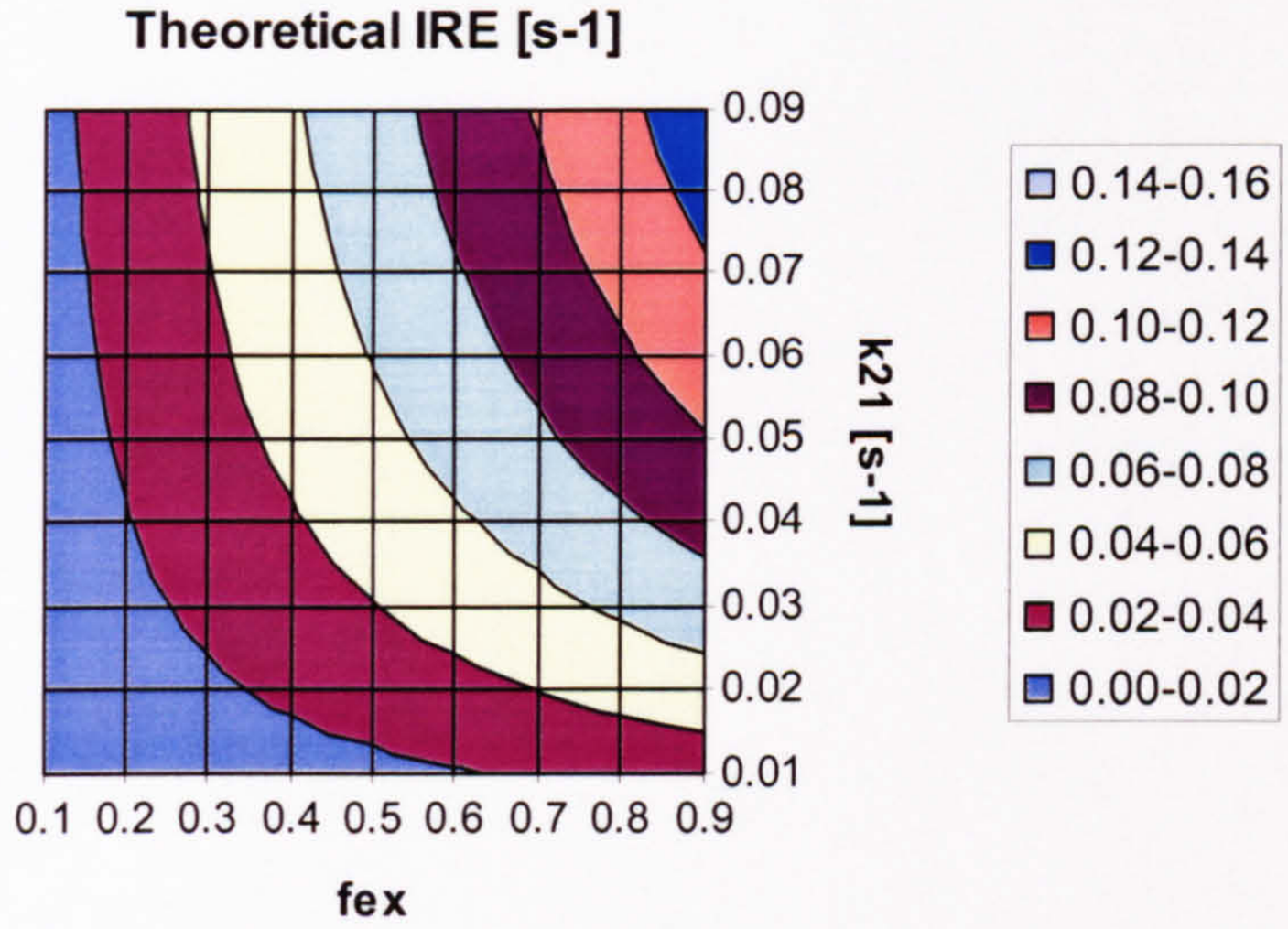

Figure 4-10 Influence of f_{ex} and k_{21} on IRE

The initial rate of enhancement is strongly influenced by both PK variables. The highest values of IRE occur when both f_{ex} and k_{21} reach the upper end of the range (the area shaded in blue, Figure 4-10).

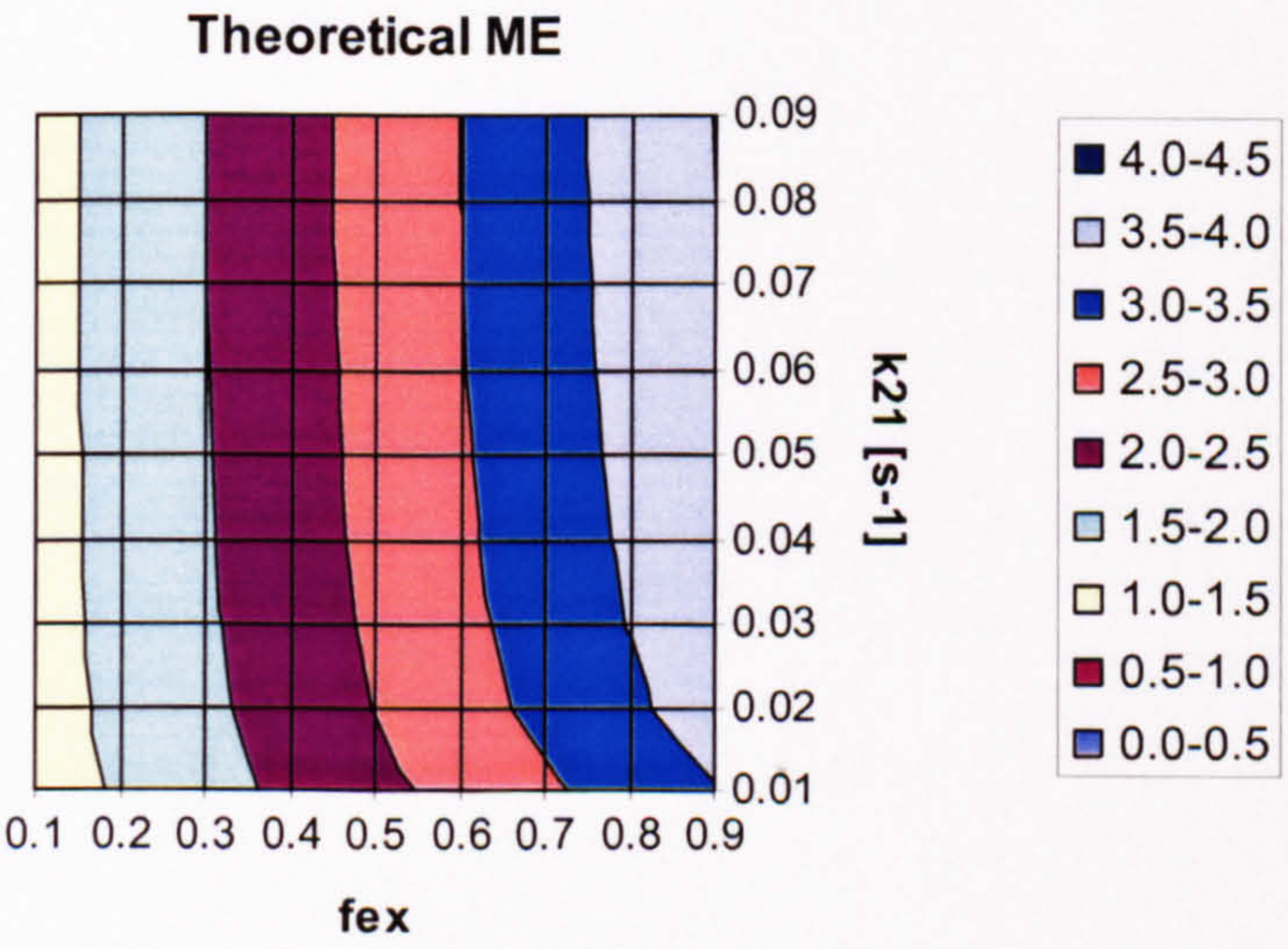

Figure 4-11 Influence of f_{ex} and k_{21} on ME

Maximal enhancement (ME), however, is predominantly determined by the value of f_{ex}, with only a mild influence of k_{21}, as illustrated in Figure 4-11.

To enable an automated measurement of BB variables, moving window algorithms were developed and implemented in the C programming language. The application of the moving-window calculation of IRE and ME was designed to minimise the influence of random noise fluctuations which are particularly prominent in voxel-by-voxel sampling where inherent SNR of the SI/time curves is likely to be low. These algorithms were also designed to eliminate the need for visual inspection of individual curves and subjective selection of time points where ME and IRE are measured. Furthermore, an automated measurement of IRE allowed the identification of T_{onset} which is an essential pre-requisite for automated non-linear modelling of DEMRI and the calculation of PK variables, as discussed in Section 4.2.8. The description of the algorithms is based on the data presented in Section 4.2.1 (core simulation, Figure 4-3 and Figure 4-4).

An algorithm for the measurement of ME involved the application of moving window averaging of groups of n = 5 consecutive points. The chosen number of points encompassed a temporal window of 40 seconds, at a pre-set sampling interval of Delta T = 10 seconds. The algorithm stored the values of ME obtained in individual windows in an array, and following the inspection of an entire SI/time curve (including N – n + 1 windows), the maximal value was identified and stored.

To enable the automated measurement of IRE, an algorithm employing moving-window least squares fitting of the straight line through a series of consecutive points on the normalised SI/time curve was developed. The routine for least squares fitting of the straight line was adopted from a book by Press et al [123]. This method is illustrated below in Figure 4-12, where straight lines fitted using five windows comprising five consecutive points are superimposed on the normalised SI/time curve. The five illustrated windows start at 40, 50,

60, 70 and 80 seconds. The line subtending the maximal angle to the horizontal axis (the line representing the segment where maximal rate of enhancement is detected) is highlighted in red. The simulated curve is identical to the one presented in Figure 4-4 (subjected to a 10% Gaussian noise level). Only the initial part of the curve is illustrated here (with t ranging from 0 to 150 seconds).

The maximal number of windows (groups of consecutive points) is determined by the total number of measurements in the DEMRI series (N) and the window size (n). In this example, $N = 36$, $n = 5$ and the maximal number of windows is $N - n + 1 = 31$. However, the number of windows can be reduced by specifying the start and the end point for the temporal range where IRE is expected to occur, thus reducing the total processing time.

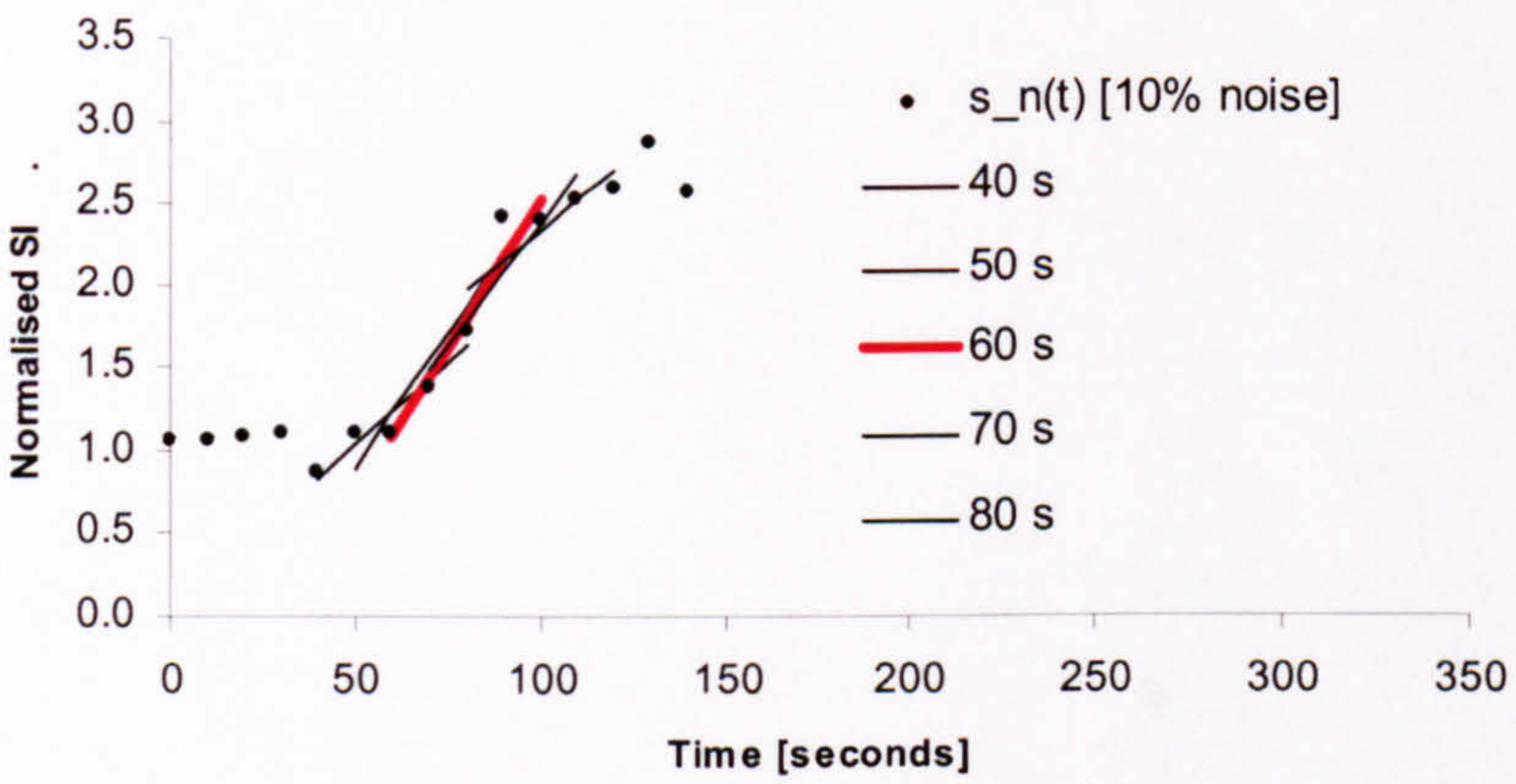

Figure 4-12 Moving window algorithm for the measurement of IRE

Figure 4-13 illustrates the resulting values of the slopes of the straight lines fitted through 16 consecutive windows (with window start ranging from 0 to 150 seconds) under 1% and 10% noise levels.

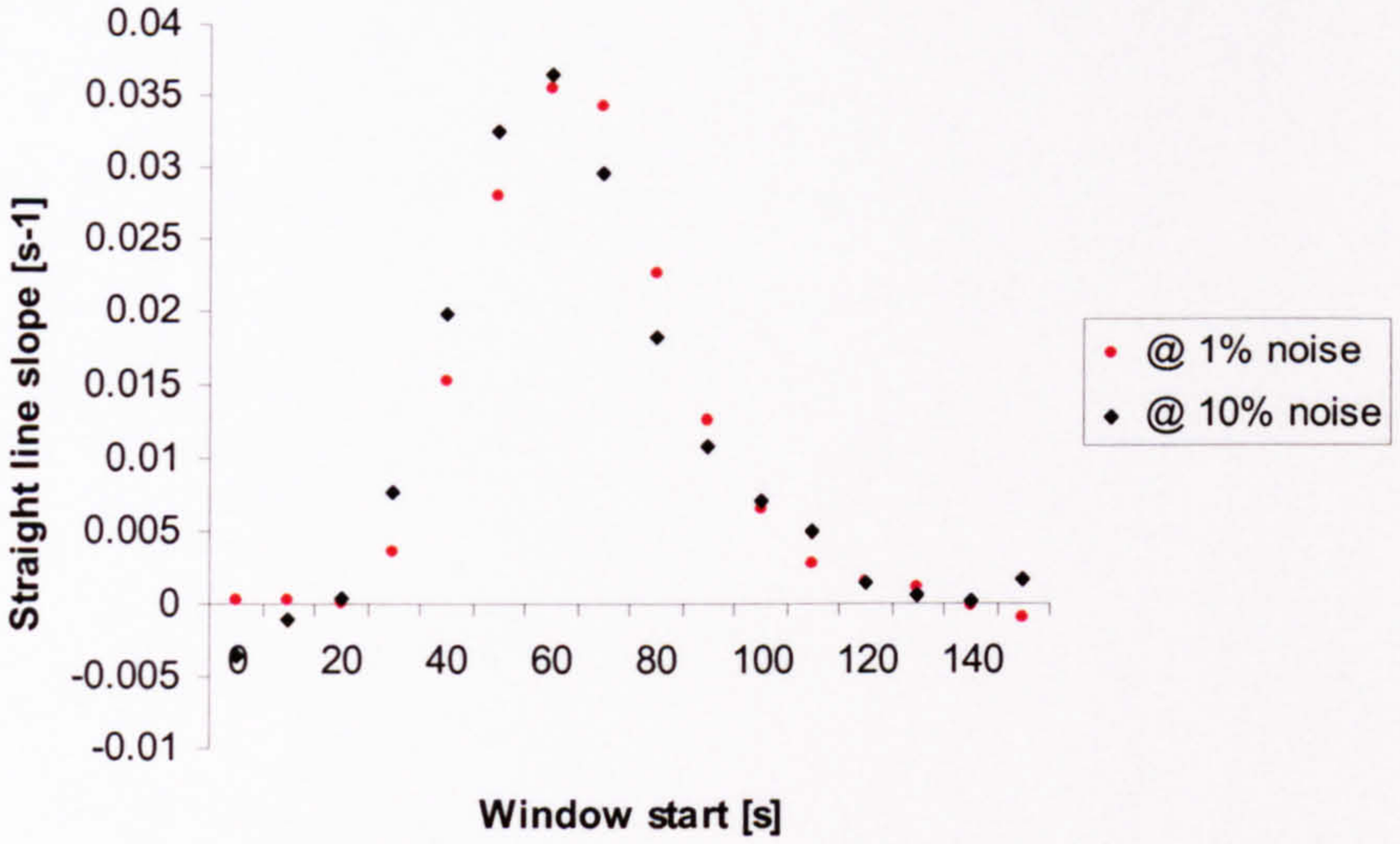

Figure 4-13 Identification of T_{onset} and IRE

The algorithm for the detection of T_{onset} and the measurement of IRE stores these values into an array, identifies the maximal slope and the location of the window where this maximal value is measured. In this example, the pre-set value of the onset of enhancement (60 seconds) is correctly identified under both noise levels.

The relationship between theoretical values of BB variables and the measurements obtained in a series of simulations at the 10% noise level (core simulation settings, as described in Section 4.2.1) is illustrated below in figures Figure 4-14 to Figure 4-17. The measurement of IRE by straight line fitting results in consistently lower values of IRE than the theoretically derived tangent calculated using Eq. 4-11 (Figure 4-14 and Figure 4-15).

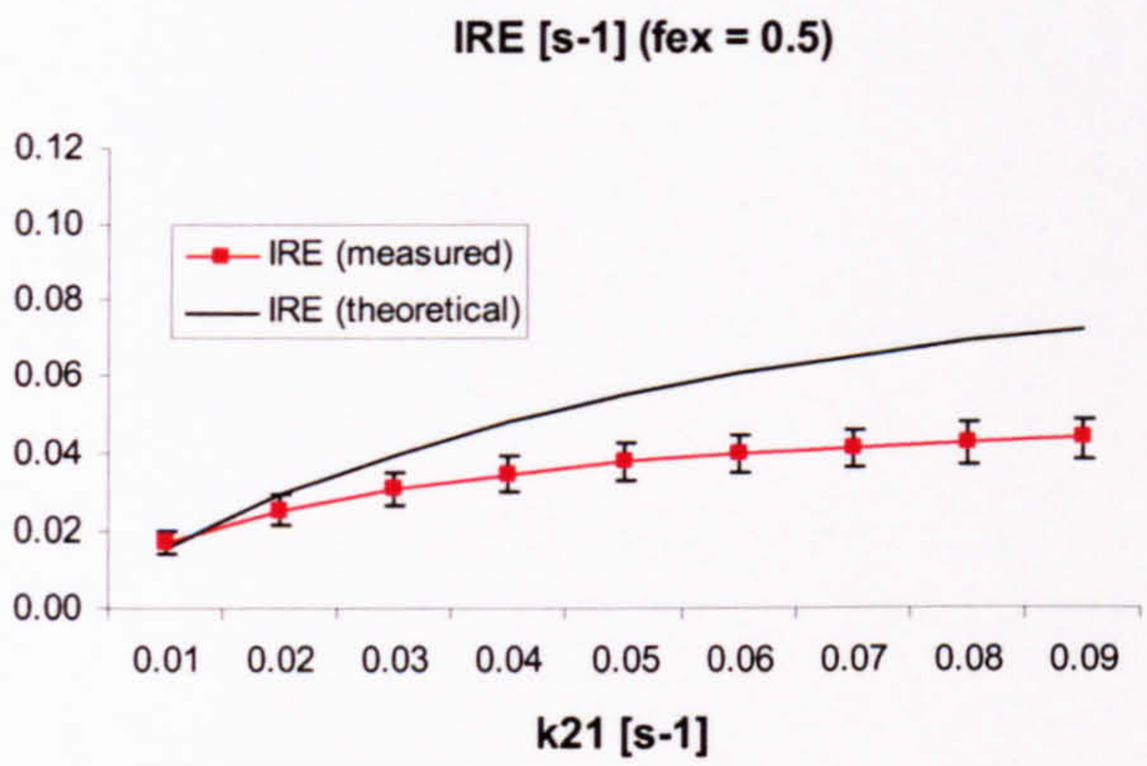

Figure 4-14 Relationship between IRE and k_{21} for fixed f_{ex} = 0.5

The error bars represent 1 SD limits of the measurements obtained in Monte Carlo simulations. Although the proportionality between the measured IRE and PK variables is preserved, the sensitivity of the measured IRE to underlying values of k_{21} and f_{ex} is markedly reduced when compared to the relationship between theoretical IRE and PK variables. For example, a nine-fold difference in k_{21} results in only two-fold difference in IRE. The sensitivity of IRE to changes in f_{ex} is significantly higher, with nine-fold difference in f_{ex} resulting in seven-fold difference in IRE.

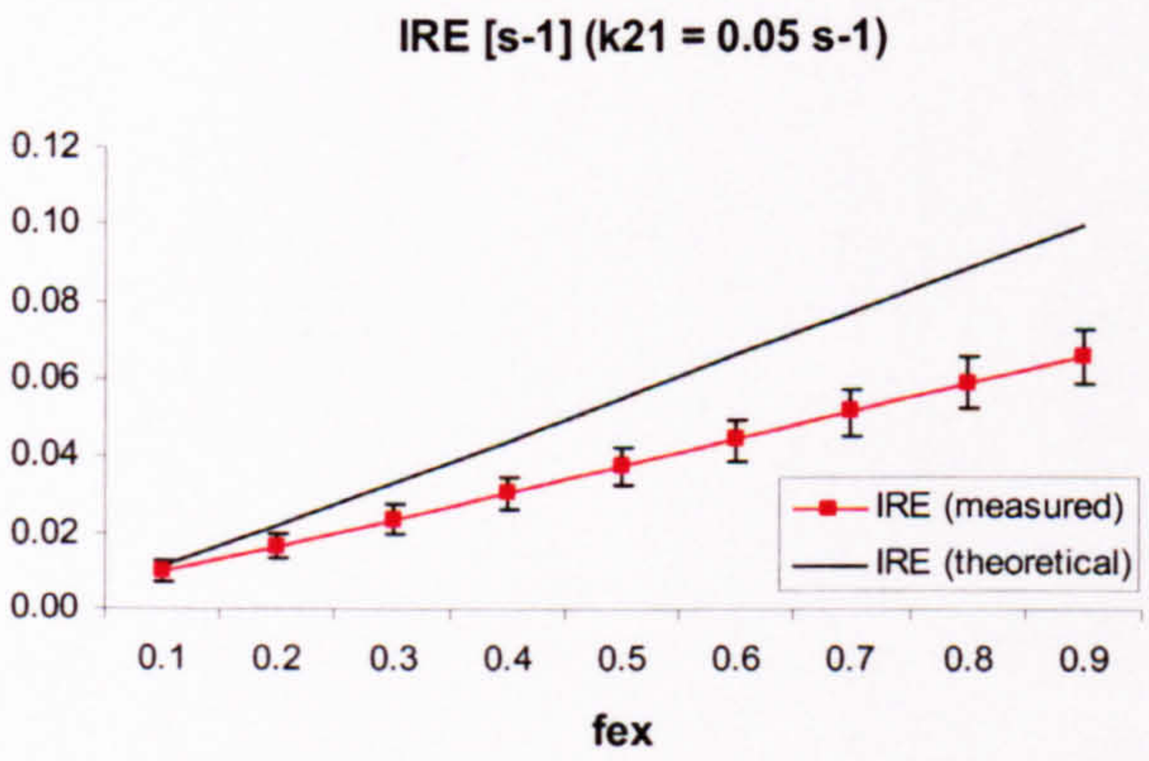

Figure 4-15 Relationship between IRE and f_{ex} for fixed k_{21} = 0.05 s^{-1}

The measurements of ME, however, remain almost independent of k_{21} as illustrated in Figure 4-16.

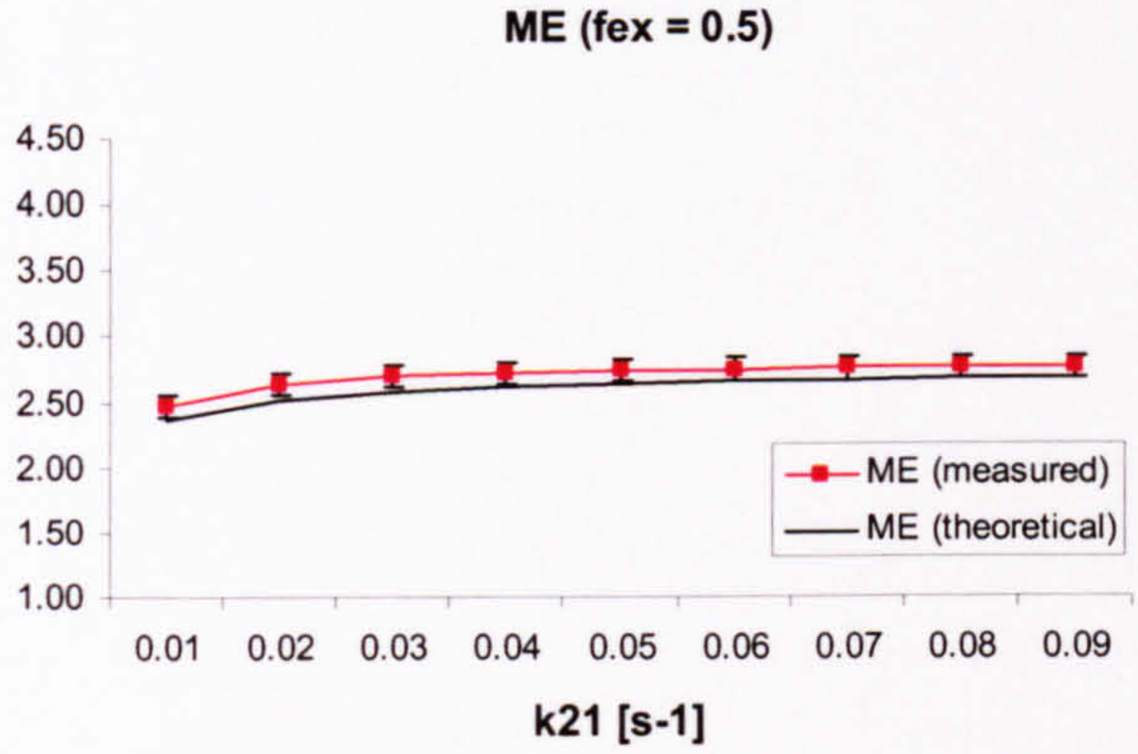

Figure 4-16 Relationship between ME and k_{21} for fixed f_{ex} = 0.5

In contrast to its relationship to k_{21}, ME is highly sensitive to changes in f_{ex}, with the preserved degree of proportionality and sensitivity to f_{ex} in the measured values of ME.

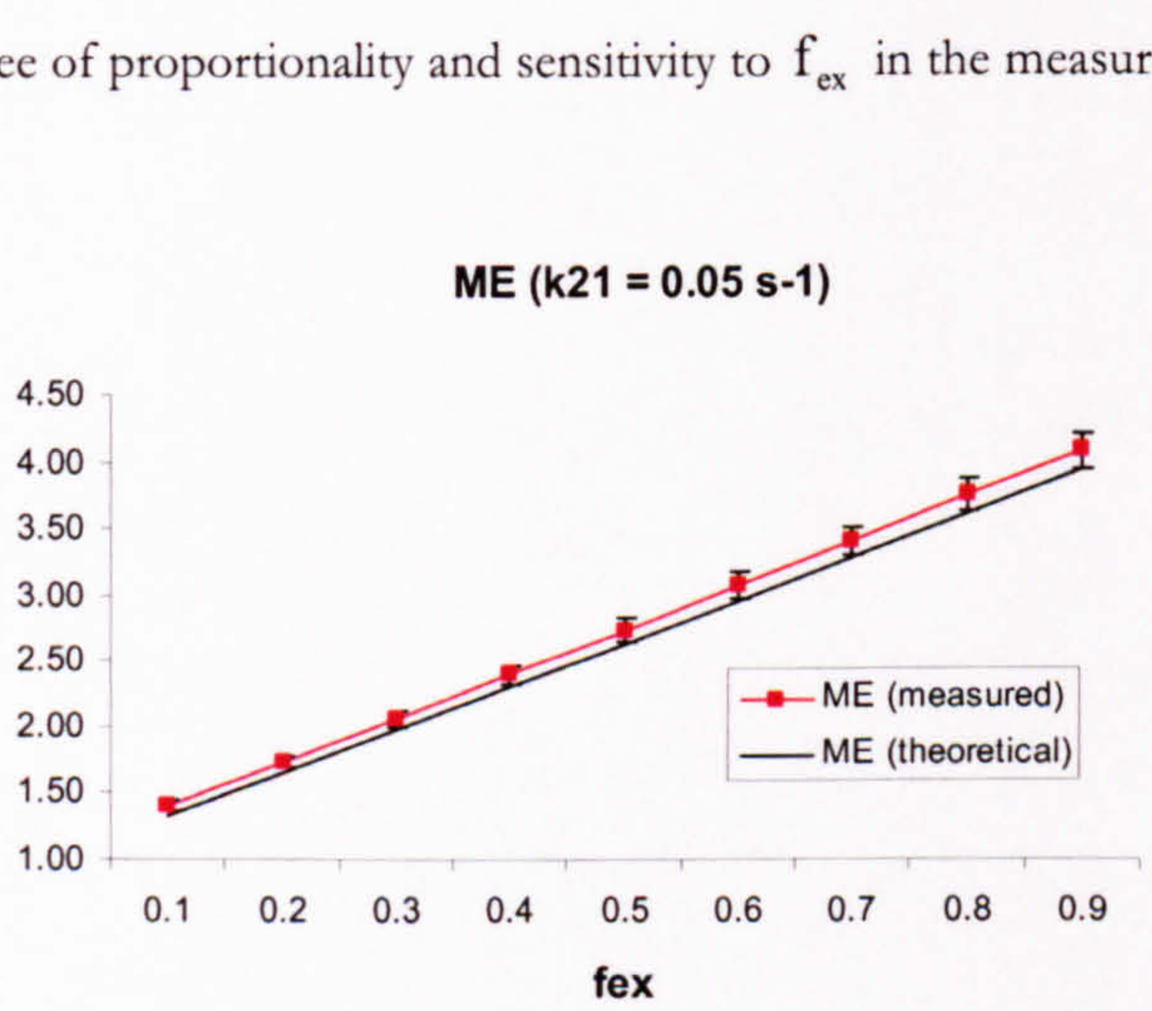

Figure 4-17 Relationship between ME and f_{ex} for fixed k_{21} = 0.05 s^{-1}

Furthermore, as indicated by one standard deviation (SD) error bars in Figure 4-14 to Figure 4-17, the measurements of IRE are subject to a higher level of dispersion than the

corresponding measurements of ME with an average coefficient of variation over the entire range of k_{21} and f_{ex} of 3% for ME and 15.6% for IRE.

The application of this algorithm allowed an automated detection of T_{onset} with average T_{onset} over the entire range of f_{ex} and k_{21} being 65.4 seconds with SD of 9.4 seconds compared to the pre-set value of 60 seconds. However, the application of the same algorithm at a 1% noise level, yields an average T_{onset} of 63.4 seconds with a standard deviation of only 1.3 seconds, which further illustrates the importance of SNR in the quantification of DEMRI.

The influence of the uncertainty in the measurement of T_{onset} is illustrated by comparing the results obtained in simulations with a 1% noise level and a known value of T_{onset} (pre-set in the core simulation) and the results obtained by the measurement of T_{onset} from simulated curves using the above-described algorithm (Table 4-6). Whereas the influence of the uncertainty in T_{onset} has virtually no effect on estimated values of f_{ex}, the effect on the estimates of k_{21} is pronounced even at this low noise level.

	Known Tonset	Measured Tonset
Accuracy of fex	0.01 (0.03)	-0.94 (1.62)
Precision of fex	0.51 (0.33)	0.64 (0.56)
Accuracy of k21	0.05 (0.11)	11.79 (15.52)
Precision of k21	2.66 (1.42)	7.11 (6.71)

Table 4-6 Influence of the uncertainty in T_{onset} on the measurement of PK at 1% noise level

The influence of the increasing noise level on the ability of this algorithm to estimate PK variables f_{ex} and k_{21} is illustrated in Table 4-7, below.

	1% Noise	5% Noise	10% Noise
Accuracy of fex	-0.94 (1.62)	-0.99 (1.79)	-0.77 (1.70)
Precision of fex	0.64 (0.56)	2.82 (2.16)	5.39 (3.78)
Accuracy of k21	11.79 (15.52)	22.7 (21.98)	35.27 (31.89)
Precision of k21	7.11 (6.71)	29.92 (12.55)	44.12 (14.66)

Table 4-7 Influence of noise on the measurement of PK variables with uncertain T_{onset}

4.3.1. Allocation of initial solutions for non-linear minimisation

In all of the simulations presented so far, the non-linear minimisation was performed by supplying pre-set values of PK variables f_{ex} and k_{21} as initial (starting) solutions. In the practical implementation of this algorithm, these values need to be supplied to the algorithm at the start of iterative minimisation. The clinical applications of DEMRI, which are the subject of this thesis, require extensive coverage of diffuse, highly inhomogeneous tissue. Such DEMRI datasets present a difficult environment for complex, iterative non-linear fitting. Given that the typical dataset would yield tens of thousands of SI curves with a significant noise component, the optimal allocation of initial solutions is critical to the success of the DEMRI analysis.

Whilst user defined initial solutions could be acceptable in the analysis of a small number of ROIs, pixel-to-pixel analysis of the datasets acquired in the clinical applications described in this study require a fully automated approach. The allocation of fixed initial values may not be suitable for this type of analysis due to a large degree of inhomogeneity and the resulting wide range of enhancement patterns within the pathology under investigation as well as the surrounding parenchyma.

In this project, an automated method for generation of initial solutions for non-linear least squares fitting of the measured DEMRI SI/time curves to the model-predicted function was developed. The calculation of the initial solutions was based on the measurements of BB variables ME and IRE. By examining the relationship between model-based equivalents of BB variables ME and IRE (Figure 4-10 and Figure 4-11), and the analytical expressions which provide a direct link between BB and underlying PK variables, it was noted that the ratio of the IRE and the maximal amplitude of enhancement (ME – 1) depends solely on the value of k_{21}.

If the expressions given in Eq. 4-11 and Eq. 4-13 are combined to form the ratio IRE/(ME-1), the following expression is obtained:

$$\frac{IRE}{ME-1} = \frac{k_{21}(e^{-k_{el}T} - e^{-k_{21}T})}{\left(\frac{k_{21}}{k_{el}}(e^{k_{21}T}-1)e^{k_{21}t_{max}} - (e^{k_{el}T}-1)e^{k_{el}t_{max}}\right)} \qquad \text{Eq. 4-15}$$

This ratio is determined solely by variable k_{21} (when k_{el} is fixed, as described in Section 4.1) and it can be used to estimate k_{21} based on the measured values of ME and IRE. Whilst both BB variables have a degree of dependence on both f_{ex} and k_{21}, the ratio between IRE and the amplitude of enhancement ME-1 can be explicitly linked to the value of the fractional transfer rate k_{21}. The surface plot of the ratio defined in Eq. 4-15 is presented in Figure 4-18 illustrating the dependence of this ratio on k_{21} and its independence of f_{ex}.

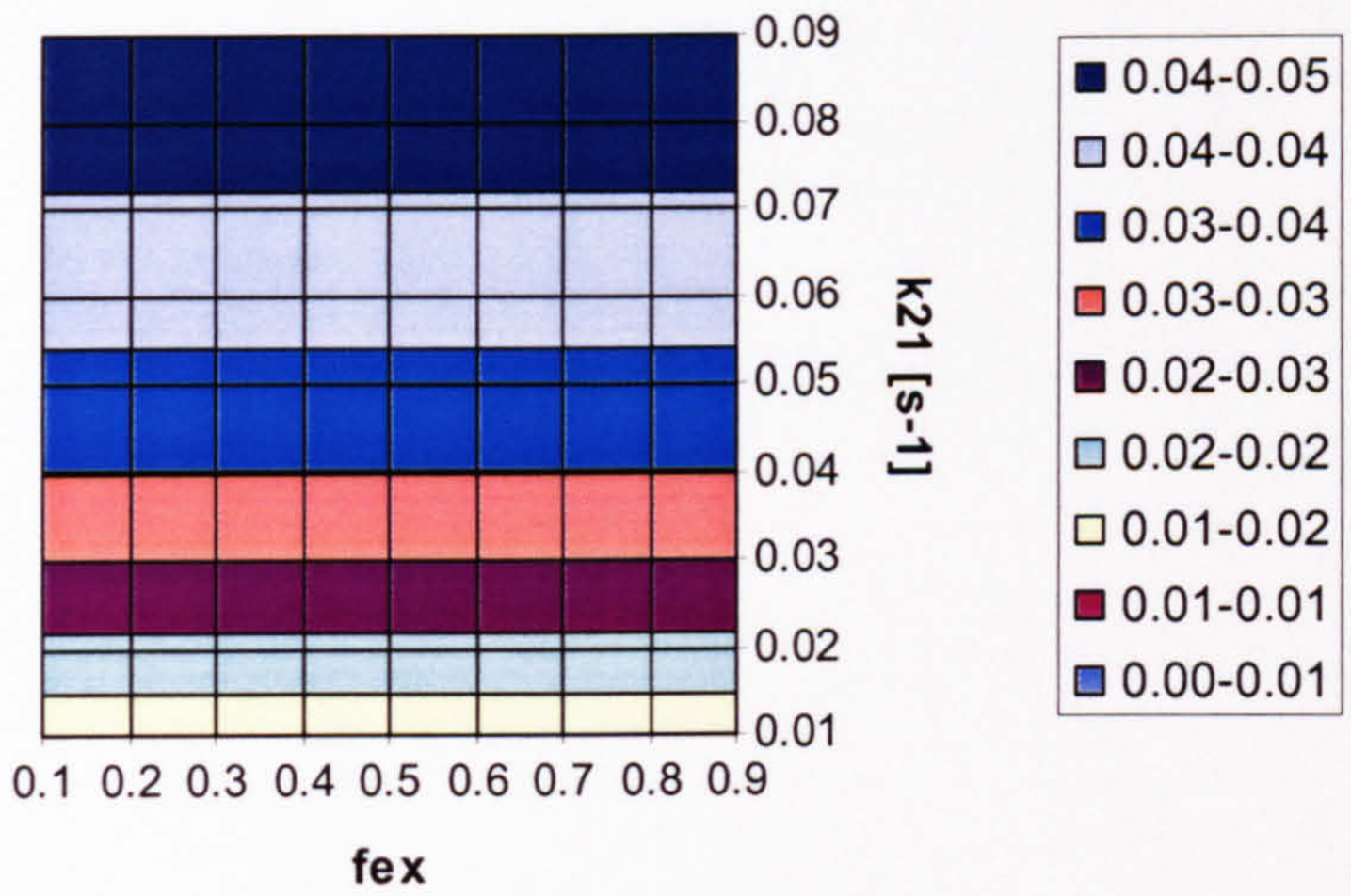

Figure 4-18 Influence of f_{ex} and k_{21} on IRE/(ME-1)

Following the estimation of k_{21} from the ratio presented in Eq. 4-15, an estimate of f_{ex} can be derived from the expression for ME (Eq. 4-13). When the initial solutions calculated using this method were supplied to the non-linear fitting algorithm (in a simulation performed at 5% noise level), the following results were obtained:

	Pre-set Initial Solutions	Calculated Initial Solutions
Accuracy of fex	-0.99 (1.79)	-1.03 (1.76)
Precision of fex	2.82 (2.16)	2.89 (2.26)
Accuracy of k21	22.7 (21.98)	22.31 (22.15)
Precision of k21	29.92 (12.55)	29.62 (12.62)

Table 4-8 Comparison between the estimates of PK variables obtained with pre-set and calculated initial solutions

As the results presented in Table 4-8 demonstrate, the performance of the fitting routines remained essentially unchanged when these calculated initial solutions were supplied instead of the known, pre-set values. These simulations were performed at 5% noise level.

The method for QDEMRI analysis described in this chapter was applied to the study of Gd-DTPA enhancement in primary breast cancer and in rheumatoid arthritis of the MCP joints and knees. The measurements of pre-contrast T1 ($T1_0$) were not available in these studies and the pharmacokinetic modelling resulted in the computation of two independent pharmacokinetic variables, A and k_{21}. Variable A is directly proportional to the local value of f_{ex} but it also depends on tissue pre-contrast T1, T1 relaxivity α, the applied repetition time TR and the initial plasma concentration Cp(0) according to the following expression:

$$A = a\, f_{ex} \frac{Cp(0)}{T} = a\, f_{ex} \frac{0.877}{T} = \frac{e^{-\frac{TR}{T1_0}}}{1 - e^{-\frac{TR}{T1_0}}} TR\alpha\, f_{ex} \frac{Cp(0)}{T} \qquad \text{Eq. 4-16}$$

Furthermore, to obtain the measurement corresponding to the transfer rate constant ($K^{trans} = f_{ex} \cdot k_{21}$), the product of two measured PK variables A and k_{21} (Ak_{21}) was also recorded. By assuming an average value of Cp(0) = 0.877 mM, in-vitro relaxivity α and a representative $T1_0$ value, variable A can be used to estimate the underlying fraction of the EES (f_{ex}). Similarly, variable Ak_{21} can be used to provide an estimate of K^{trans}, which is related to permeability surface area product. The fractional transfer constant k_{21} does not depend on any other systemic or MR data acquisition variable. In addition to these three PK variables, the method includes the measurement of BB variables ME and IRE in all three studies.

Chapter 5. Implementation of QDEMRI for clinical applications

In this chapter, a description of the practical implementation of the method for QDEMRI analysis, which was introduced in Chapter 4, is presented. The chapter includes the description of the image acquisition protocols (Section 5.1), as well as the explanation of the pre-processing procedures including the selection of ROIs and the selection of sub-volumes for voxel-by-voxel processing (Section 5.2). Image viewing, ROI selection and image segmentation were performed using an image processing package Analyze™ (Biomedical Imaging Resource; Mayo Foundation, Rochester, MN). All QDEMRI processing was performed on a standard PC platform (running under Windows NT and Windows 2000 operating systems), using a set of programs written in the C programming language. The routines for straight-line fitting and non-linear minimisation were adopted from a book by Press et al [123].

5.1. DEMRI acquisition

All imaging was performed on a 1.5 T MRI scanner (Gyroscan ACS NT, Philips Medical Systems, Best, The Netherlands). The MR signal detection was performed with a quadrature

knee coil in the Knee RA Study, a linear circular 11 cm diameter surface coil in the Hand RA Study and a standard bilateral breast coil in the Breast Cancer Study.

The selection of the imaging volumes was performed following the acquisition of survey scans in three orthogonal directions. In the Breast Cancer Study, the complete coverage of both breasts was ensured. Imaging volume selection was particularly important in the RA Studies, since the selection of optimal anatomical landmarks allowed adequate volume repositioning in the follow-up scans.

5.1.1. Breast Cancer Study DEMRI acquisition protocol

A 2D multislice, T1-weighted gradient echo sequence was used (TR/TE/φ = 213/4.6/90°, FOV = 300mm, RFOV = 100%, 25 slices, 4mm slice thickness, 12 dynamic scans at 32.5 seconds intervals, 154 × 256 image matrix, reconstructed to 256 × 256 matrix). Total imaging time was 390 seconds. The patients were positioned prone with both breasts inside the breast coil. The imaging was performed in the transverse plane, with the imaging volume encompassing both breasts in all three dimensions.

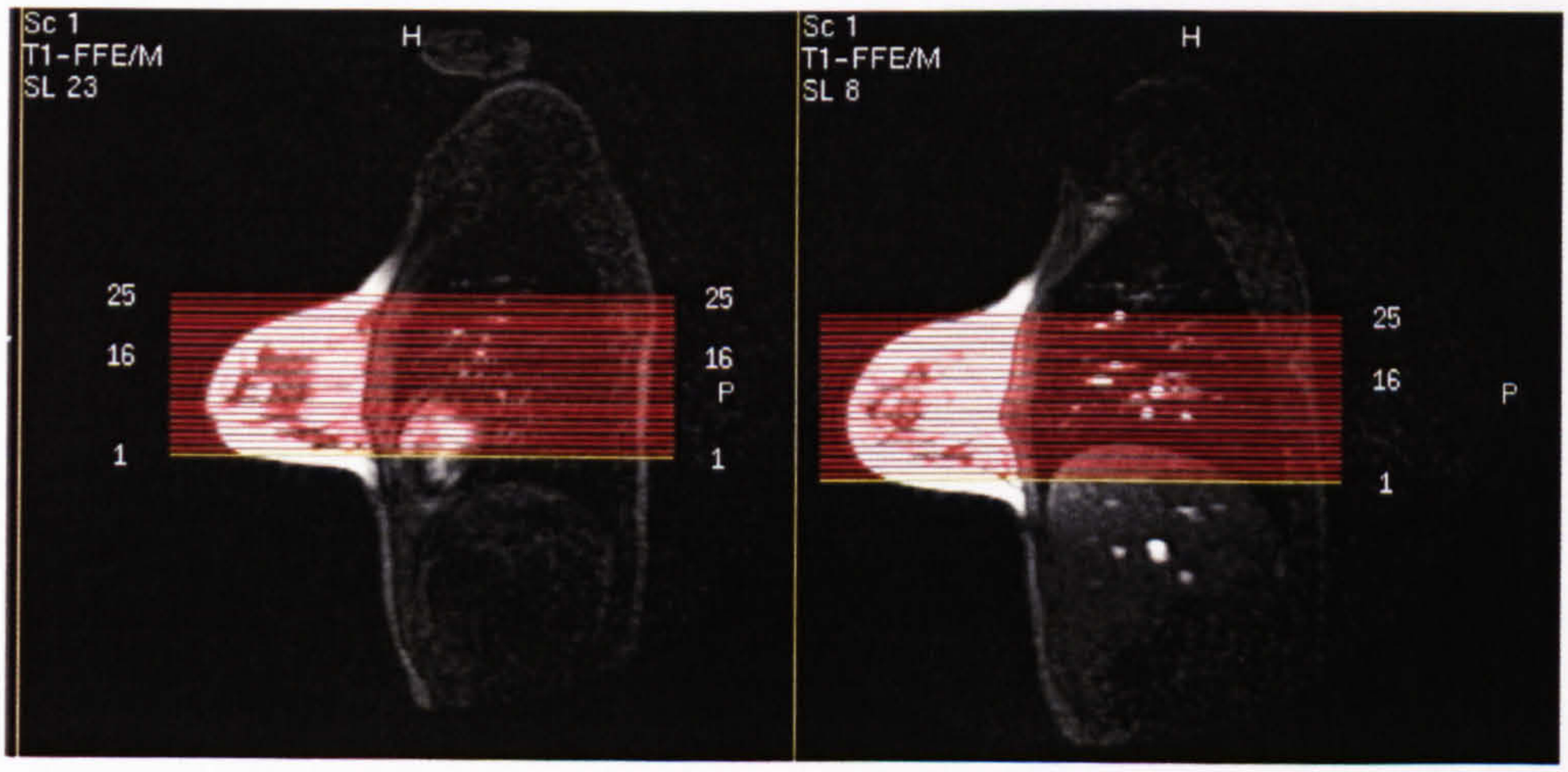

Figure 5-1 Positioning of the imaging volume in the Breast Cancer Study

An illustration of the positioning of the imaged volume is presented in Figure 5-1. where coloured lines indicate the position of transverse slices superimposed on sagittal cross sections through right and left breast.

5.1.2. Hand RA Study DEMRI acquisition protocol

DEMRI of the dominant hand was performed using a 3D T1 weighted spoiled gradient echo sequence (TR/TE/φ = 14/3.8/40°, FOV = 100mm, RFOV = 50%, 6 slices, 3mm slice thickness, 20 dynamic scans at 7.1 seconds intervals with 170 × 256 image matrix, reconstructed to 256 × 256). The total scanning time was 142 seconds. The imaging volume encompassed four (2nd to 5th) MCPJs. The patients were positioned prone with their arm extended in front of their head and the circular coil placed on the dorsum of the hand.

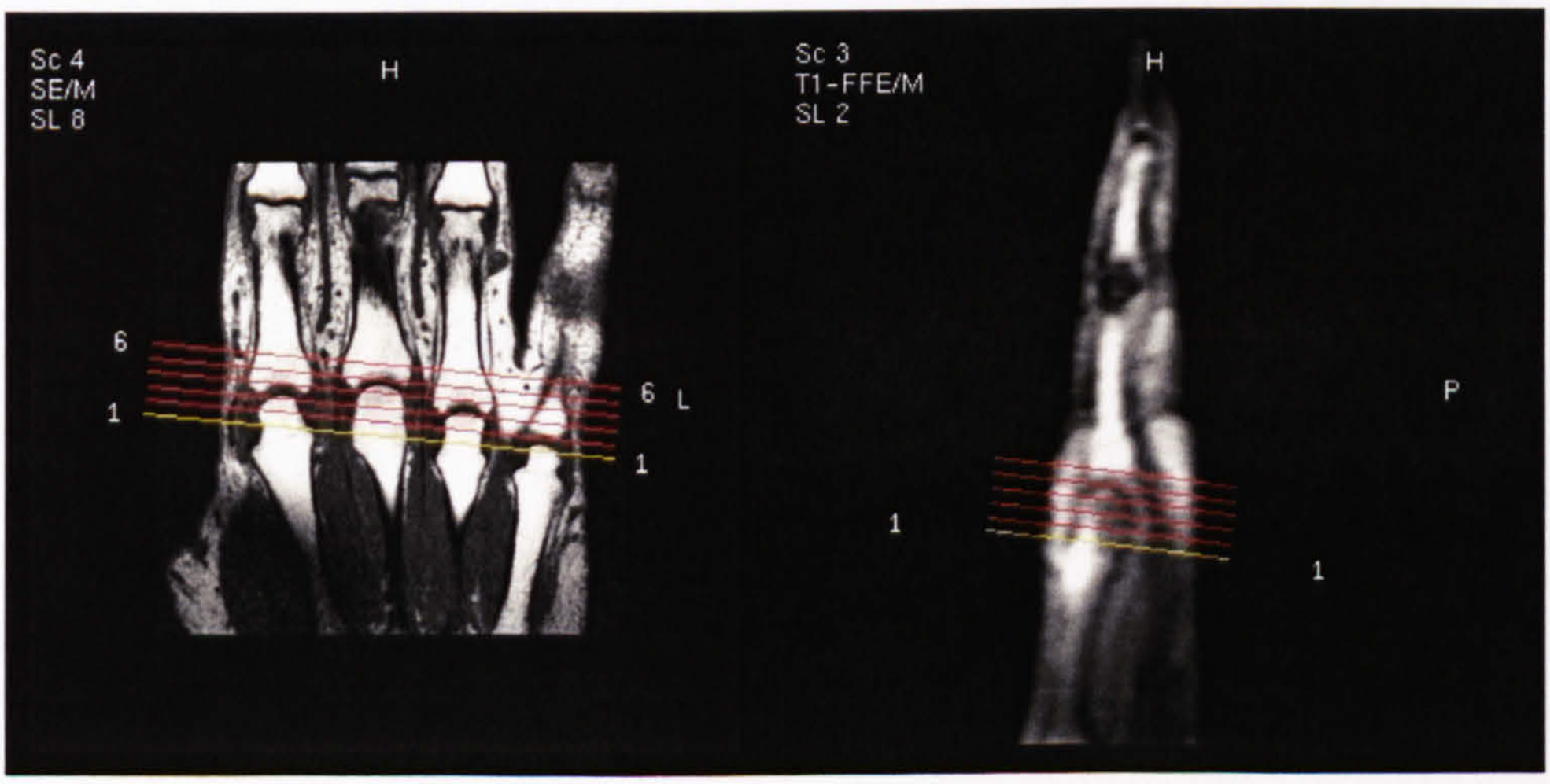

Figure 5-2 Positioning of the imaging volume in the Hand RA Study

An illustration of the positioning of the imaging volume is presented in Figure 5-2, where coloured lines indicate the positions of transverse slices superimposed on a coronal and sagittal cross section. The imaging volume encompassed four (2nd to 5th) MCPJs and was positioned using a set of precise anatomical landmarks to ensure adequate coverage of the

MCP joint capsules at baseline and follow-up scans. The angulation of the imaging volume was defined by the central plane cutting through the middle of the 2nd and 4th MCPJs spaces as defined by coronal images.

5.1.3. Knee RA Study DEMRI acquisition protocol

DEMRI scans of the knee were acquired by using a 2D multislice, T1-weighted spoiled gradient echo sequence (TR/TE/φ = 13/5.0/60°, FOV = 250mm, RFOV = 60%, 5 slices, 5mm slice thickness with 5mm gap, 40 dynamic scans at 8 seconds intervals with 205 × 256 image matrix, reconstructed to 256 × 256). The total scanning time was 320 seconds. The patients were positioned supine with the signal knee positioned inside knee coil. An illustration of the positioning of the imaging volume is presented in Figure 5-3 where the coloured lines indicate the position of the sagittal slices superimposed on coronal and transverse cross sections.

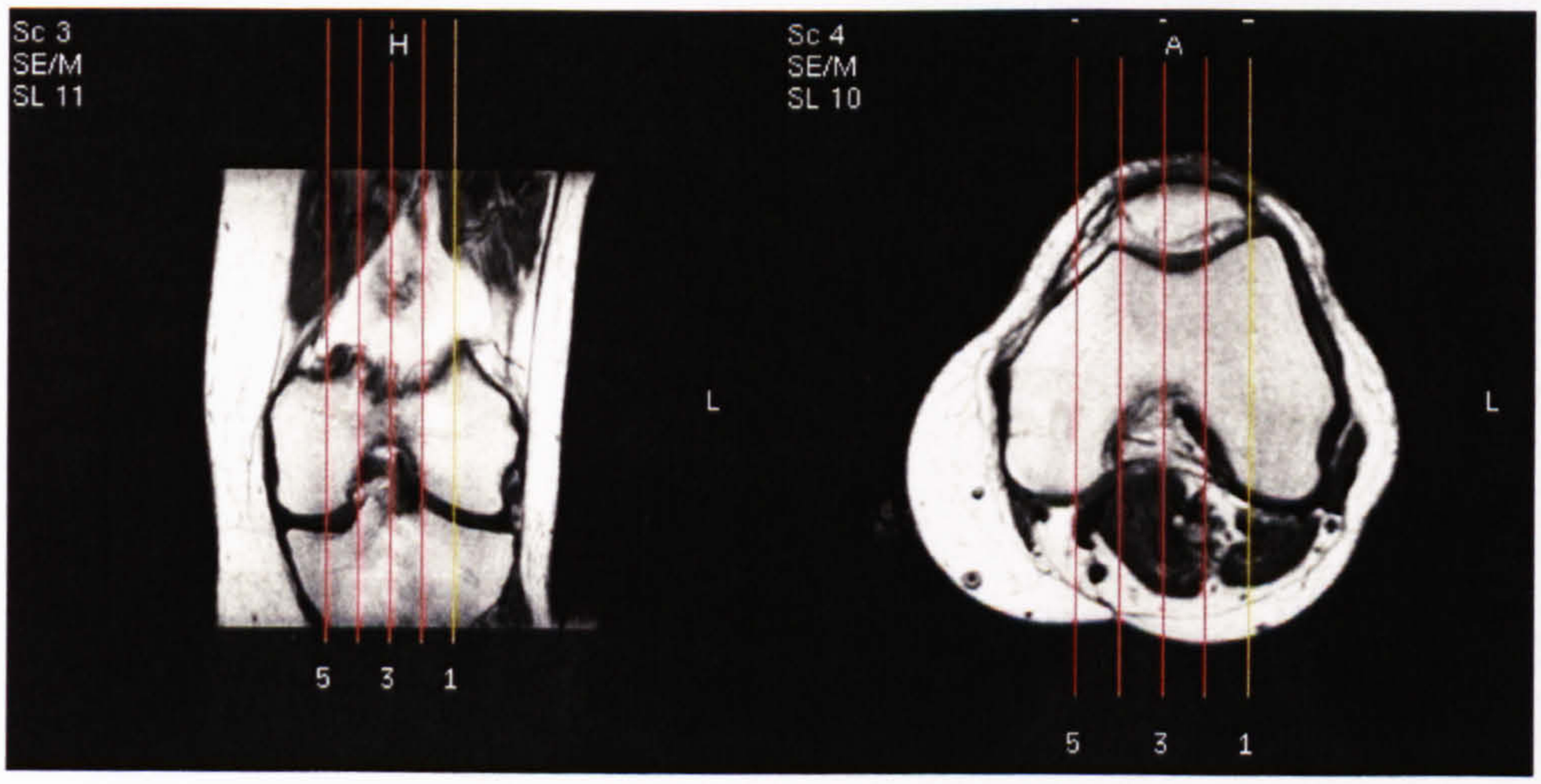

Figure 5-3 Positioning of the imaging volume in the Knee RA Study

The imaging volume was positioned using a set of precise anatomical landmarks: five sagittal slices were selected centred on the middle of the interchondylar notch and orthogonal to the planes tangential to the femoral chondyles, both posteriorly and inferiorly.

5.1.4. Gd-DTPA injection

A standard dose of 0.1 mmol per kilogram body weight of gadopentetate dimeglumine Gd-DTPA (Magnevist®, Schering, Berlin, Germany) was used. The Gd-DTPA injection was followed by a 10 ml saline flush. The injection was administered manually with a constant injection rate over a period of Tinf = Delta T in the RA studies (i.e. 7.1 and 8 seconds in the Hand RA and Knee RA studies, respectively) in order to facilitate the synchronisation between the injection and the acquisition. In the Breast Cancer Study, Tinf was set to Tinf = Delta T/2, due to the low temporal resolution (Delta T = 32.5 seconds). In all studies, effective duration of the infusion (T) which was used for the modelling of SI, was approximated by 2×Tinf (i.e. double the actual injection duration). This approximation was based on the data reported by Andersen et al and Fritz-Hansen et al [80, 88] for short peripheral injections. Furthermore, the analysis presented in Section 4.2.6 indicates that the effects of the variation in T over this range of values exert a minimal influence on the performance of the fitting algorithm. Effective injection duration was T = 14.2 seconds in the Hand RA Study, T = 16 seconds in the Knee RA Study and T = 32.5 seconds in the Breast Cancer Study.

5.2. DEMRI pre-processing

5.2.1. Breast Cancer Study

An illustration of the pre-contrast and post contrast images (acquired 4 minutes after the baseline scan) in the Breast Cancer Study is presented in Figure 5-4 and Figure 5-5, respectively. These images represent all 25 transverse anatomical slices acquired at t = 0 and t = 4.02 minutes. Individual DEMRI datasets in this study included 300 images (25 slices × 12 dynamic frames) yielding files containing almost 20 million voxels (or 37.5 Mbytes of data, since a 2-byte representation of grey-level SI was used).

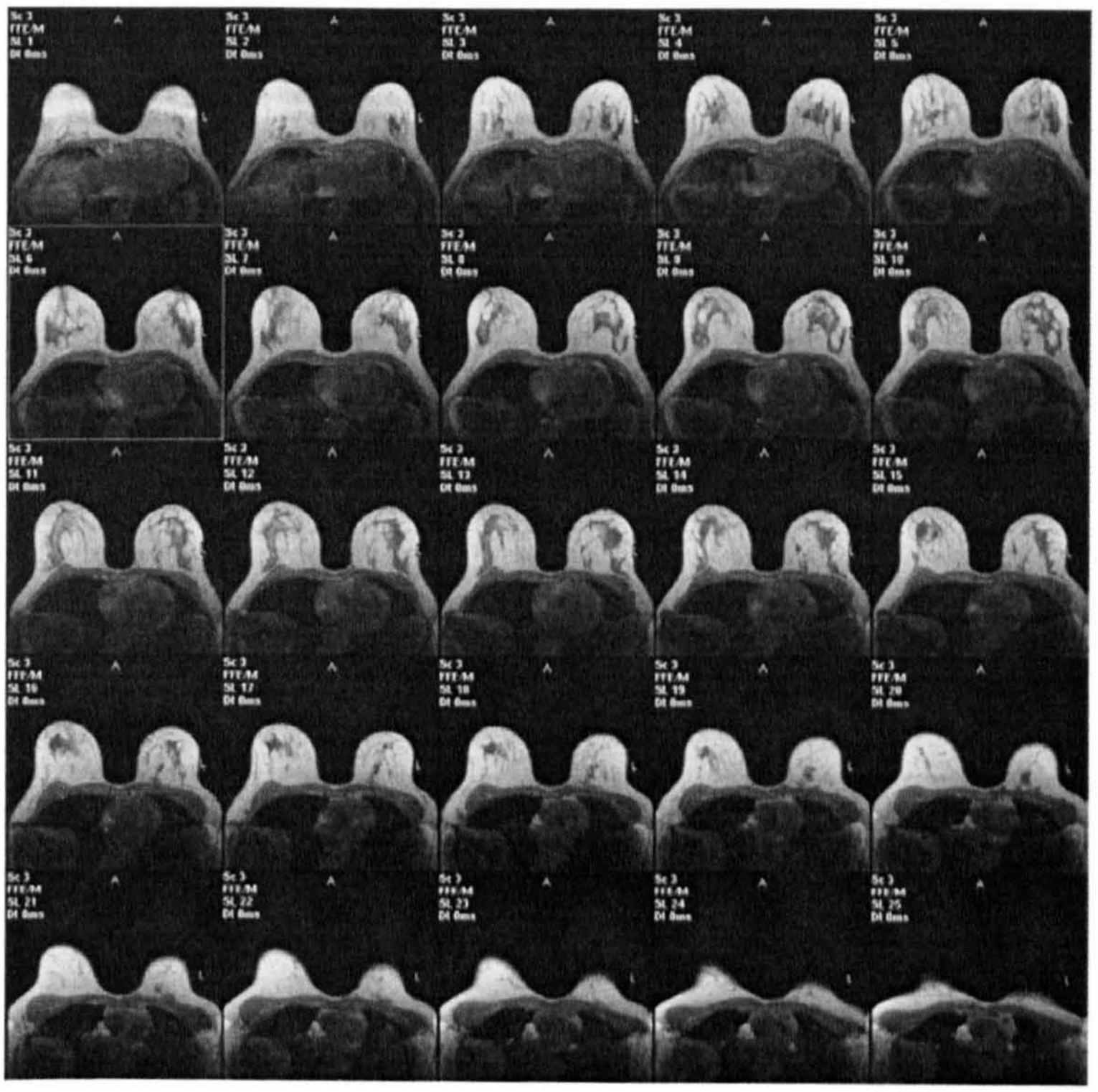

Figure 5-4 Pre-contrast dataset in the Breast Cancer Study

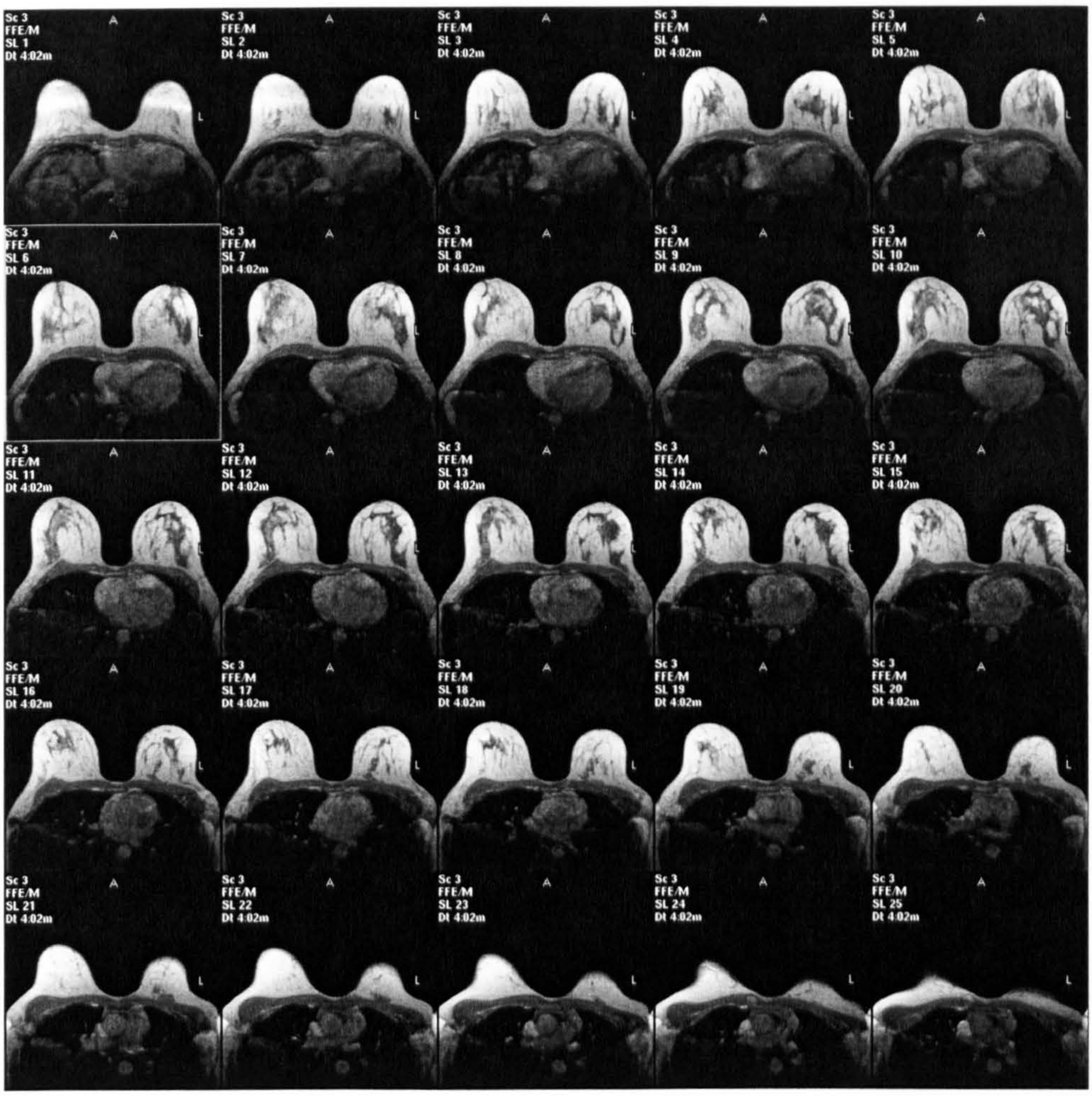

Figure 5-5 Post-contrast dataset in the Breast Cancer Study

These images are normally viewed in a cine-loop, using an MR console. To enable a more efficient identification of the enhancing structures, a set of subtraction images is generated as well (Figure 5-6). A baseline (pre-contrast) image is subtracted on a voxel-by-voxel basis from each subsequent dynamic image. The set of images presented in Figure 5-6 represents the difference between the image set obtained at 4.02 minutes after the acquisition of the baseline and the pre-contrast image.

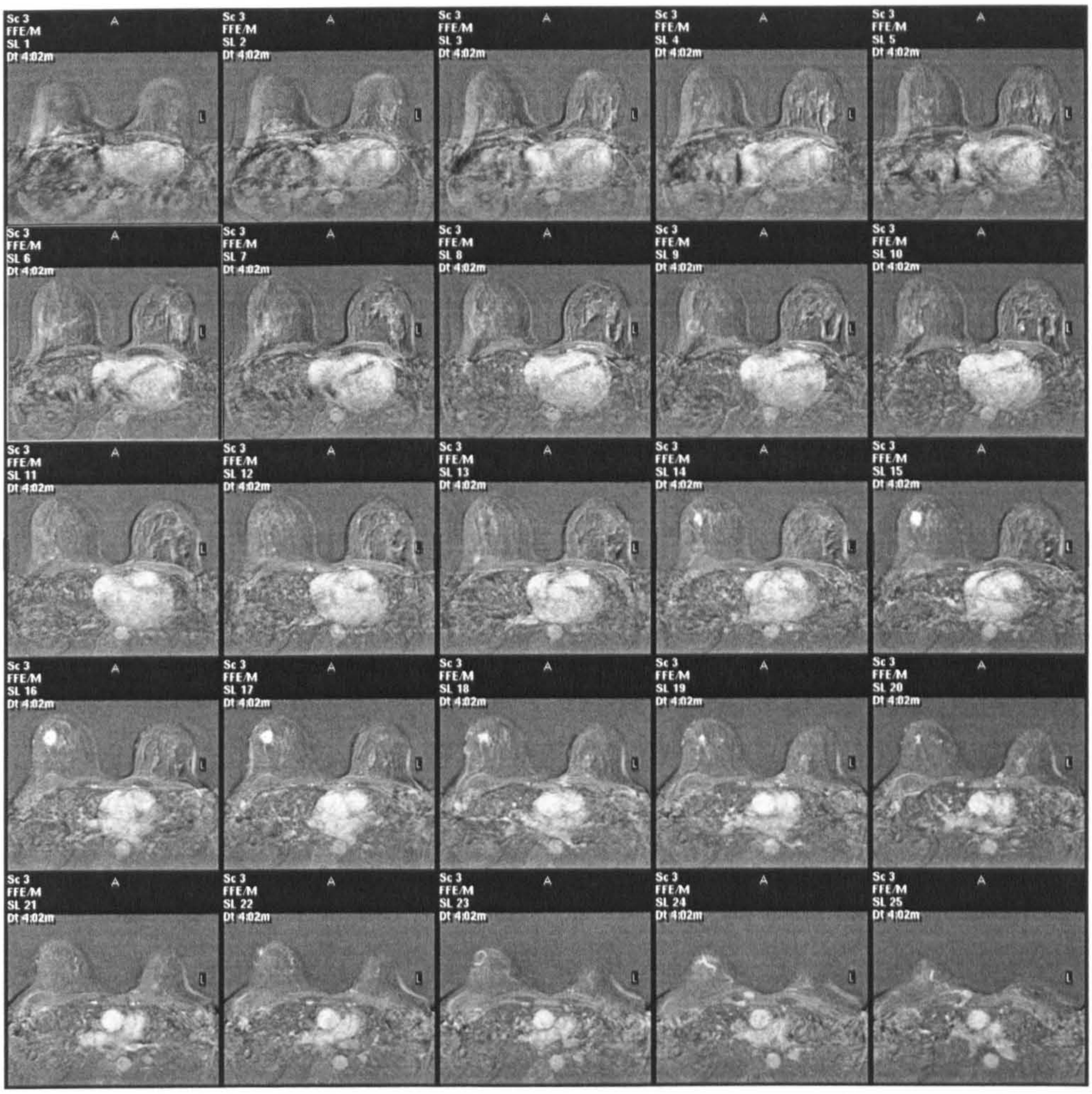

Figure 5-6 Post-pre contrast subtraction dataset in the Breast Cancer Study

A lesion located in the right breast is clearly visible on the subtracted images. Figure 5-7 represents a pair of pre- and post-contrast images and a resulting subtraction image of the transverse slice cutting through the centre of the lesion.

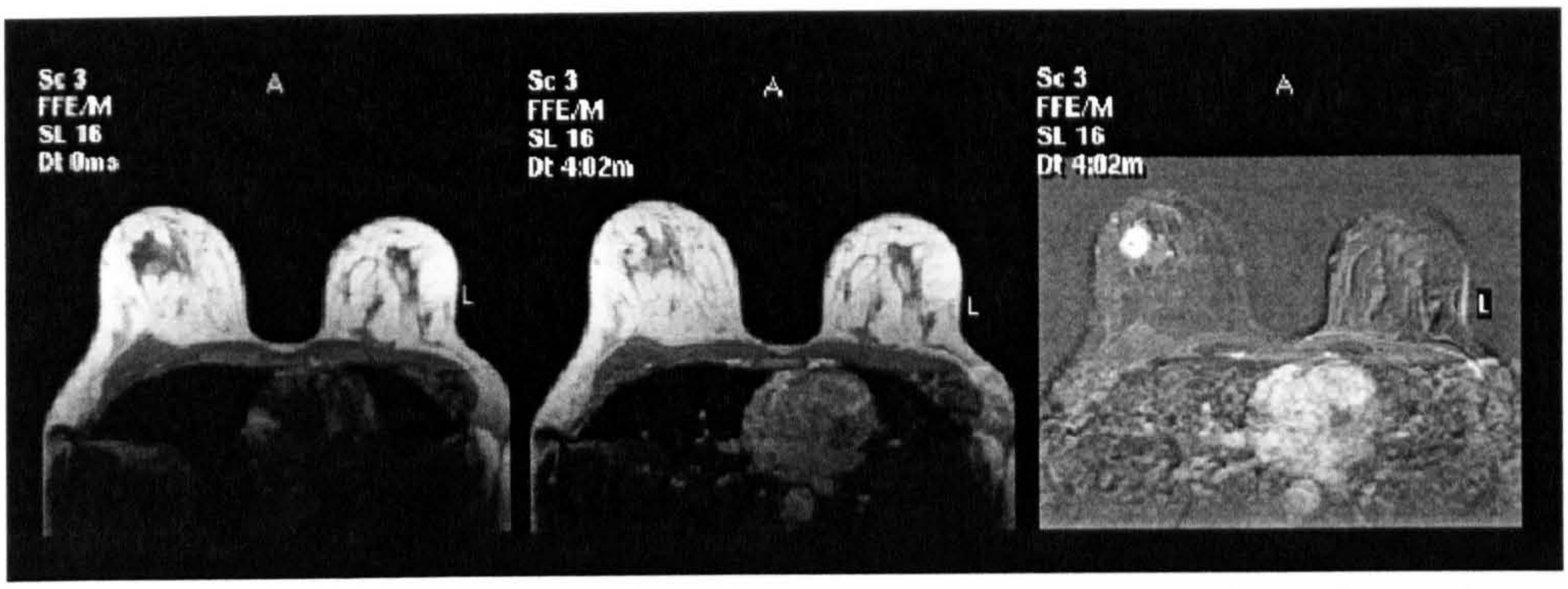

Figure 5-7 Pre-contrast, post-contrast and subtraction image through the centre of the lesion in the Breast Cancer Study

In routine clinical practice, the lesion is evaluated by placing a region of interest (ROI) on a subtraction image and displaying a SI/time curve on a MR console. As illustrated in Figure 5-7, the subtraction method is effective in delineating the extent of the lesion. However, these images are not suitable for the analysis of the internal architecture of the lesion and its relationship to the surrounding parenchyma.

To improve the visualisation of the lesions, parametric maps of BB variables ME, IRE and the wash-out-slope (WOS) were computed on a voxel-by-voxel basis and displayed superimposed on grey-scale anatomical images. These images were generated automatically using a set of programs written in the C programming language, and the resulting colour coded images were linked into an html (hypertext markup language) database. The computation of the BB variables ME and IRE was performed using the method described in Section 4.3. To match the size of the moving windows to the temporal resolution of the DEMRI datasets, a three-point window was used (encompassing temporal segments of 65 seconds). Variable WOS was computed on a voxel-by-voxel basis by measuring the slope of the least-squares straight line through the fixed five-point window encompassing the last 130 seconds of the SI/time curves. All three images (ME, IRE and WOS) could be interrogated simultaneously. This processing step did not involve any user interaction. No segmentation or motion correction was applied and a uniform colour-coding scheme was used in all

studies. Computation of colour-coded parametric maps effectively condensed the information contained in the original DEMRI datasets. The colour-coding scheme used for spatial mapping of BB variables is presented in the Appendix D.

A further data reduction step involved the identification of the anatomical slices which encompassed the individual lesion. Figure 5-8 illustrates a set of parametric maps corresponding to the five transverse slices encompassing a lesion illustrated above in Figure 5-4 to Figure 5-7. In Figure 5-8, the top row contains parametric maps of ME, the middle row represents the maps of IRE, and the WOS maps are presented in the bottom row.

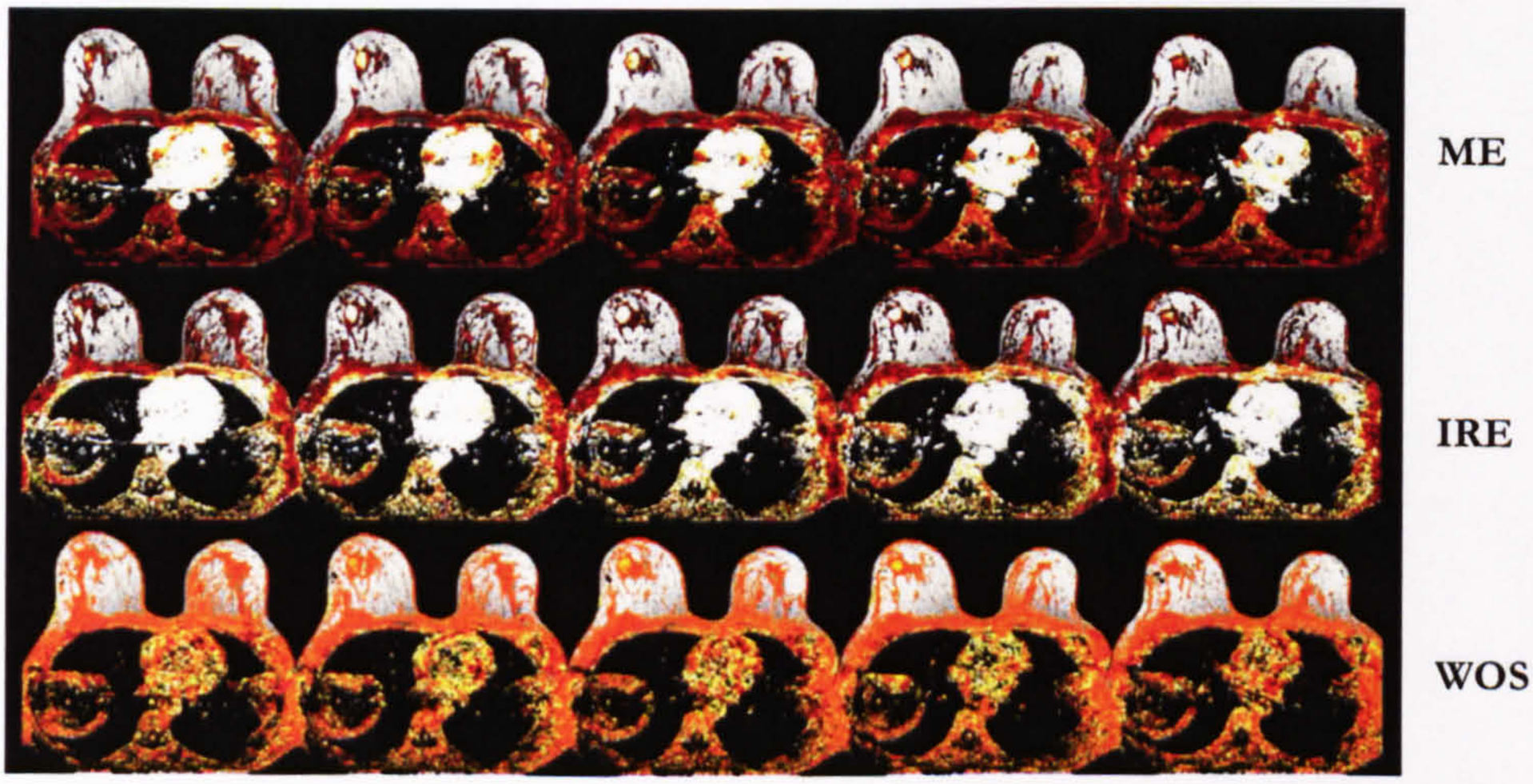

Figure 5-8 Identification of the lesion using colour-coded parametric images

Following the inspection of these maps, the most representative (usually central) cross section was identified by the trained radiologist (Figure 5-9) and a single circular 16-voxel ROI was placed close to the lesion rim and away from the necrotic, central areas (if present). In Figure 5-9 the first (left) image represents a map of ME, the second (central) image represents the map of IRE and WOS map is presented in the third image (right).

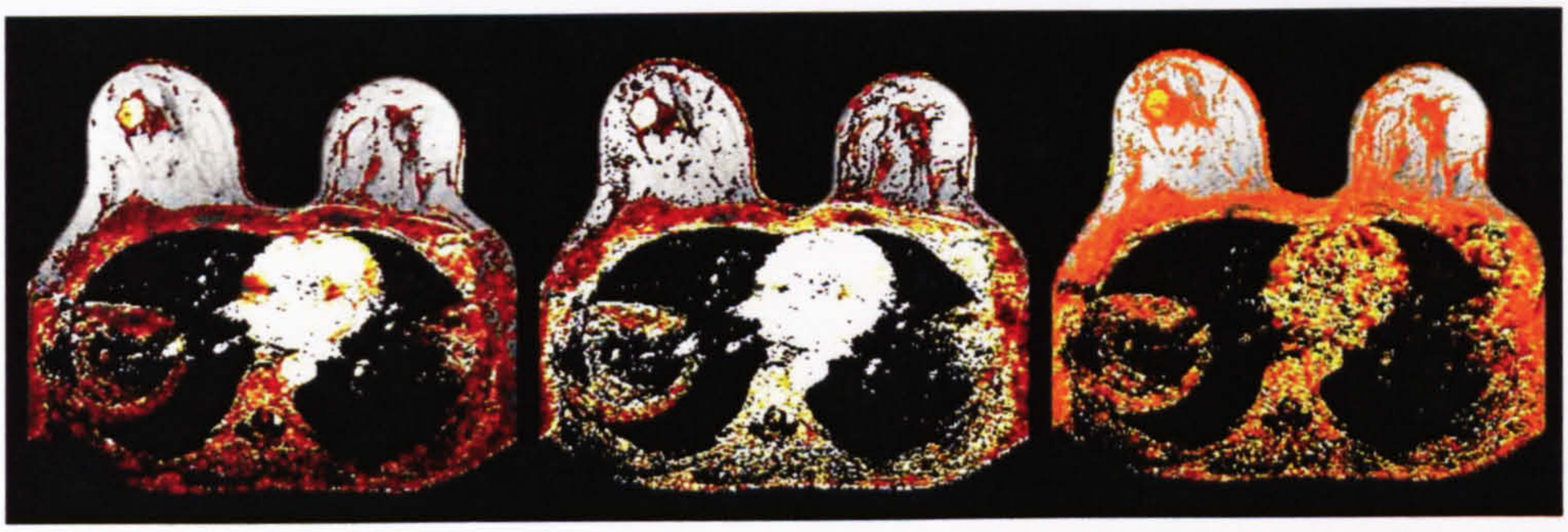

Figure 5-9 Parametric maps of the variables ME, IRE and WOS

ROI selection was restricted to tumour periphery in the light of the evidence that malignant lesions show significantly higher peripheral enhancement than non-malignant lesions [129]. An illustration of the ROI selection procedure is presented in Figure 5-10. A circular ROI (blue circle) was placed inside the lesion and its location was recorded in a separate object file. The ROI illustrated in Figure 5-10 is superimposed onto a colour map of variable IRE. However, ROI selection was based on simultaneous inspection of all three parametric maps (Figure 5-9).

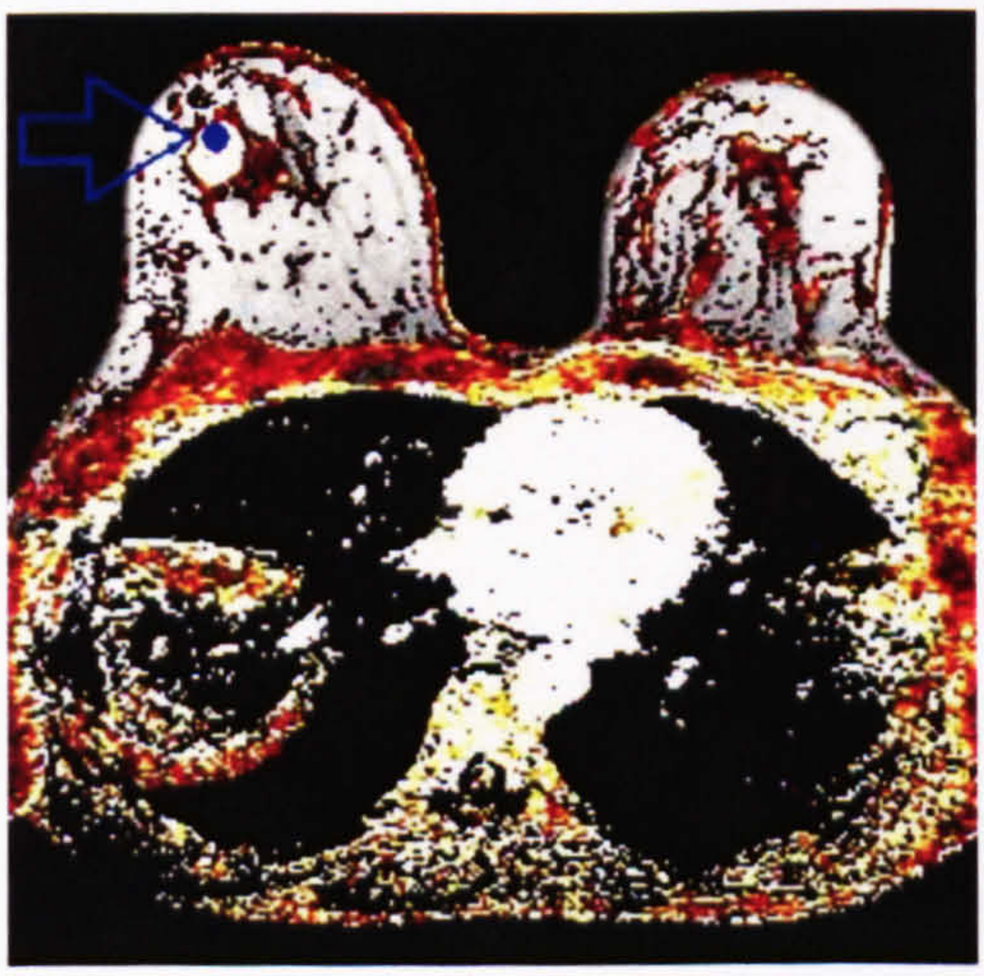

Figure 5-10 ROI selection in the Breast Cancer Study

As a result of this procedure, a single SI/time curve was derived from each identified lesion and analysed using a program written in the C programming language which quantified the

temporal variation of SI change in terms of three black box and three pharmacokinetic variables. In this study, QDEMRI analysis was restricted to the quantification of SI/time curves derived from the 16-voxel ROIs in order to compensate for relatively low temporal resolution (Delta T = 32.5 seconds) by ensuring a high SNR of the sampled curves. The achieved SNR levels in 59 evaluated lesions (estimated as a ratio between the maximal amplitude of enhancement (ME – 1) and the SD of the normalised SI over the temporal window where the maximal enhancement was detected) ranged from 6.5 to 585.4 with a mean of 67.6 ± 101.0 (mean ± SD, n = 59).

5.2.2. RA Studies

The pre-processing of the DEMRI datasets in two RA studies was performed in an identical fashion, apart from the initial segmentation step which was applied only in the Hand RA Study.

The segmentation of DEMRI datasets in the Hand RA study was performed using Analyze™ software (Biomedical Imaging Resource; Mayo Foundation, Rochester, MN). A set of pre-contrast (baseline) images was loaded into the Image Edit module and an interactive region-growing algorithm was applied to segment the MCP joints 2 to 4 and exclude the MCP 1 from further analysis. This step was performed since the imaging volume was designed to encompass joints 2-4 and the position and location of MCP 1 was highly variable and inconsistent. An illustration of this segmentation procedure is given in Figure 5-11. This step was the only part of the processing which involved user intervention.

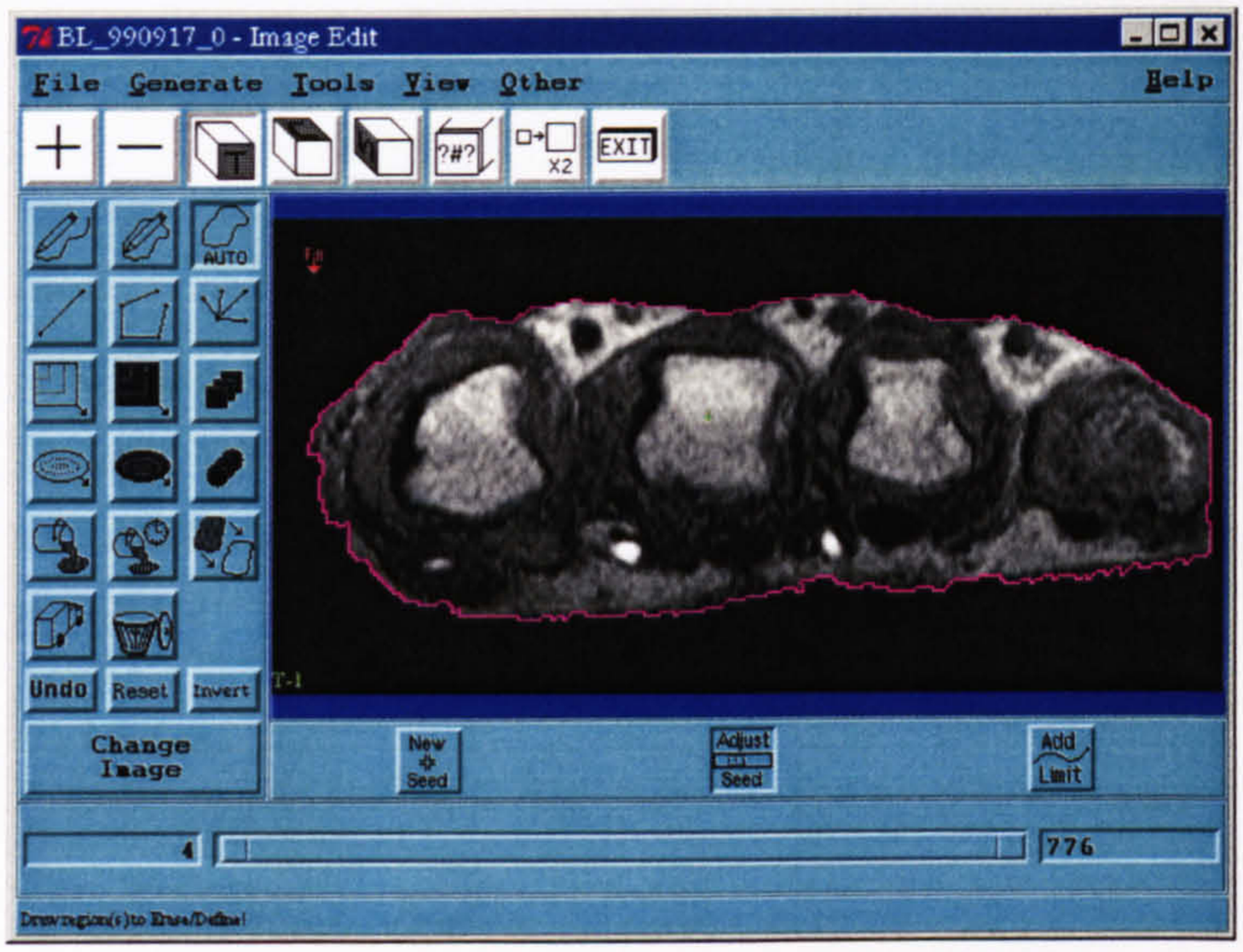

Figure 5-11 Image segmentation module (Analyze™)

The segmented volume was used to create a binary mask, which was applied to each Hand RA DEMRI set prior to further processing.

The preliminary analysis of DEMRI sets involved the computation of parametric maps of ME, in order to define enhancement thresholds and estimate the levels of SNR in the acquired data. The enhancement thresholds were determined by examining a randomly selected set of 5 DEMRI datasets in each study and determining the level of enhancement which allowed the inclusion of the complete enhancing synovial tissue with a minimal inclusion of the voxels from surrounding tissues (i.e. muscle, bone marrow and fat). The selected threshold levels (ME = 1.2 and ME = 1.3) were then applied in all Hand RA and Knee RA datasets, respectively.

The next pre-processing step in the two RA Studies involved the estimation of SNR. SNR was measured on a pixel-by pixel basis as a ratio between the maximal amplitude of enhancement (ME – 1) and the SD of the normalised SI over the window where maximal enhancement was detected. In 106 DEMRI datasets in the Hand RA study, an average SNR was 13.0 ± 1.4 and in 68 studies in the Knee RA Study an average SNR was 11.5 ± 1.5. To

increase the SNR of the measured normalised SI curves prior to the application of non-linear fitting, spatial filtering with a low pass (average) nine-voxel kernel was applied. The filtered SI in each spatial matrix element was computed as an average of the central voxel and the eight neighbouring voxels. The resulting SNR in the two RA studies was 22.3 ± 3.4 and 20.9 ± 3.3, in the Hand RA and Knee RA studies, respectively. Given that the temporal resolution in these two studies was less than 10 seconds and that the application of spatial filtering increased the SNR level (with an average SNR greater than 20), QDEMRI analysis was performed on a voxel-by-voxel basis.

5.3. QDEMRI analysis

5.3.1. Breast Cancer Study

The algorithm for the computation of BB variables in this study was identical to the one used for the computation of parametric maps (Section 5.2.1), i.e. the algorithm described in Section 4.3 was applied with a window size of n = 3 points for the measurement of ME and IRE and an additional measurement of WOS was performed using a fixed five-point window.

In the Breast Study, the acquisition protocol was based on that proposed by Kuhl et al [109] and multi-slice imaging (25 transverse sections) was performed with TR of 213 ms. To examine the effect of non-linearity of normalised SI response to the changing C = Ct(t) with this relatively large TR, the non-linear fitting using both linear and quadratic approximation of normalised SI (S_C / S_0) was performed.

In this analysis, a constant $T1_0$ was assumed in all lesions ($T1_0$ = 876 ms, the mean value of $T1_0$ in invasive breast carcinomas [126]). For an assumed linear response to C = Ct(t), the

expression presented in Eq. 2-20 was used. Next, the measured S_C/S_0 curves were converted to Ct(t) using a quadratic fit of the normalised SI, over the range of concentrations from 0 to 1 mM, thus encompassing the range of Gd-DTPA concentrations in breast lesions reported by den Boer et al [102]. The resulting expression for S_C/S_0 over this range of concentrations is presented in Eq. 5-1. For every measured value of S_C/S_0, the quadratic equation Eq. 5-1 was solved and every normalised SI curve was converted into C = Ct(t).

$$\frac{S_C}{S_0} \approx 1.062 + 3.2222 \cdot C - 1.0940 \cdot C^2 \qquad \text{Eq. 5-1}$$

A quadratic approximation of the normalised SI as a function of Gd-DTPA concentration ($T1_0$ = 876 ms and C < 1 mM)

Three pharmacokinetic variables (k_{21}, A and Ak_{21}) were extracted in 59 lesions and the results were converted to f_{ex} and K^{trans}. With the assumed linear response, the measured k_{21} and f_{ex} were 0.038 ± 0.026 s^{-1} and 0.45 ± 0.13, respectively (with a resulting K^{trans} of 1.00 ± 0.70 min^{-1}). With a quadratic approximation, the measured k_{21} and f_{ex} were 0.036 ± 0.025 s^{-1} and 0.57 ± 0.21, respectively (with a resulting K^{trans} of 1.17 ± 0.84 min^{-1}).

The measurements obtained using these two methods were strongly correlated ($\rho = 0.990$, $\rho = 0.990$ and $\rho = 0.989$ for f_{ex}, k_{21} and K^{trans}, respectively with $p<10^{-6}$) and only the results obtained using a linear approximation were used for the statistical analysis presented in Chapter 6. However, it was noted that the application of the linear approximation leads to the underestimation of f_{ex} (and consequently K^{trans}) if linear approximation is used. The variable k_{21} is only marginally affected by the nature of the assumed relationship between S_C/S_0 and Ct(t), with the mean difference between the k_{21} values obtained using two methods described above being 0.0025 s^{-1} (less than 7% of the mean value) whereas the underestimation of f_{ex} if the linear method is used is 0.13 (i.e. f_{ex} estimated using a linear approximation is 13% lower than that obtained with a quadratic approximation).

Figure 5-12 includes the illustrations of SI/time curves extracted from two different lesions (ROI 1 and ROI 2) and superimposed least squares lines obtained after non-linear fitting of the experimental data to the proposed pharmacokinetic model (Eq. 4-8).

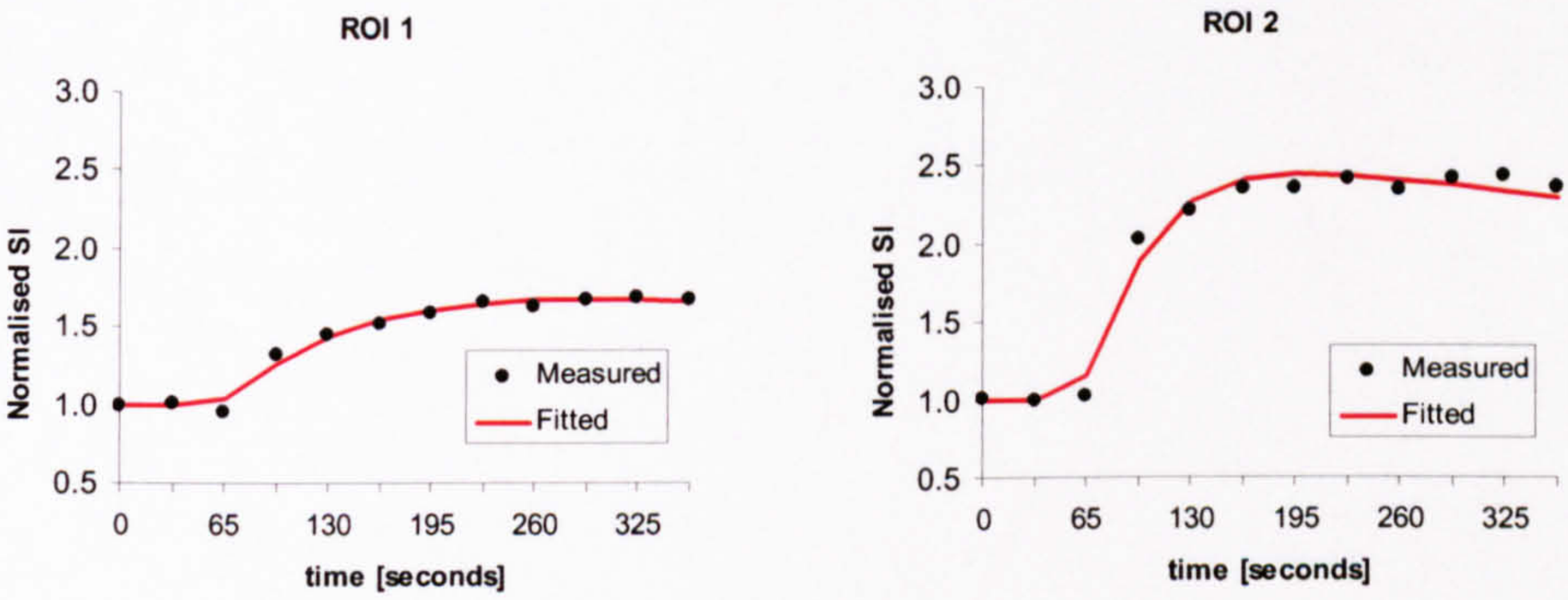

Figure 5-12 Examples of SI/time curves from the Breast Cancer Study

The results of the QDEMRI analysis performed on SI/time curves derived from these two ROIs are presented in Table 5-1. The observed differences in the pattern of Gd-DTPA uptake are reflected in the values of the measured variables.

	ROI 1	ROI 2
ME	1.68E+00	2.39E+00
IRE [s-1]	1.15E-02	3.05E-02
WOS [s-1]	3.32E-04	-1.37E-04
k21 [s-1]	2.58E-02	5.03E-02
A [s-1]	1.18E-02	2.54E-02
Ak21 [s-2]	3.04E-04	1.28E-03

Table 5-1 Example of the results of QDEMRI analysis in the Breast Cancer Study

The samples obtained from individual ROIs were stored in a single text file and the QDEMRI analysis was performed automatically, without any user interaction. In the Breast Cancer Study, experimental data fitted the proposed pharmacokinetic model well, with only one of the 59 ROI-derived SI/time curves generating a relatively large squared residual sum

(exceeding the mean obtained in the entire set by more than two SD), most likely as a result of a significant pure-vascular component. The analysis of the results obtained in this study is presented in Chapter 6.

5.3.2. RA Studies

Following the pre-processing of DEMRI datasets, according to the procedure described in Section 5.2.2, QDEMRI processing in the two RA studies was performed using the QDEMRI method presented in Chapter 4. The processing was performed on a voxel-by-voxel basis and the pattern of Gd-DTPA enhancement in each examined voxel was quantified in terms of two BB variables (ME and IRE) and three PK variables (A, k_{21} and Ak_{21}). The algorithm for voxel-by-voxel processing included several control procedures designed to eliminate from the analysis the voxels with significant vascular and motion artefact components. The total numbers of voxels included in the BB and PK analyses was recorded in each study (N-BB and N-PK, respectively). These numbers correspond to the total volume of the enhancing tissue. Because PK analysis was performed only in voxels where BB variables were measured successfully, N-BB is larger than N-PK, depending on the success rate of the fitting procedure.

An average DEMRI dataset required voxel-by-voxel processing of 29000 and 30500 SI/time curves in the Knee RA and Hand RA studies, respectively. The required processing time was less than 30 seconds per dataset (on a 600MHz, 128Mb PC system). In the two RA studies, pharmacokinetic modelling was successfully performed in 95.5 ± 2.6% and 98.5 ± 0.8% of the voxels (in Hand RA and Knee RA studies, respectively), suggesting that the proposed pharmacokinetic model adequately represents these experimental data. The analysis of the QDEMRI findings in these two studies therefore includes the analysis of seven measured variables: ME, IRE, A, k_{21}, Ak_{21}, N-BB and N-PK.

To illustrate the results of QDEMRI analysis obtained in these two studies, the measured PK variables A and Ak_{21} are converted to f_{ex} and K^{trans}, thus removing a slight influence of the differences in acquisition settings used in the two RA studies. Computed values of variable A can be converted to fractional volume of the EES (f_{ex}) by assuming a constant pre-contrast $T1_0$ value and Cp(0), as described earlier (Eq. 4-16). In the following maps, this conversion was performed with an assumed $T1_0$ of 900 ms and Cp(0) of 0.877 mM. The variable A is converted into f_{ex} (unit-free fraction, i.e. a value of f_{ex} = 0.5 corresponds to the voxels where 50% of the volume is occupied by EES). Likewise, the measured values of the variable Ak_{21}, collected in individual voxels can be transformed into corresponding values of K^{trans} and expressed in min^{-1}, using the same assumed values of $T1_0$ and Cp(0). The same colour-coding scheme was used for spatial mapping of derived values of f_{ex} and K^{trans} in both RA studies (Appendix D).

Examples of the parametric colour-coded maps of PK variables (superimposed on original, pre-contrast anatomical images) obtained in the two RA studies are presented in figures Figure 5-13 to Figure 5-18. The program for the calculation of these images was also written in C programming language. Figure 5-13 demonstrates the distribution of f_{ex} in one of the Hand RA studies. It clearly demonstrates an extensive synovitis in MCPJs 2 and 3, with a lesser involvement of MCPJs 4 and 5. As discussed in Chapter 4, the estimation of f_{ex} is not as vulnerable to random noise fluctuations as the variable k_{21}. The difference in spatial coherence between the maps of f_{ex}, k_{21} and K^{trans} ($K^{trans} \propto Ak_{21}$) further illustrates this point.

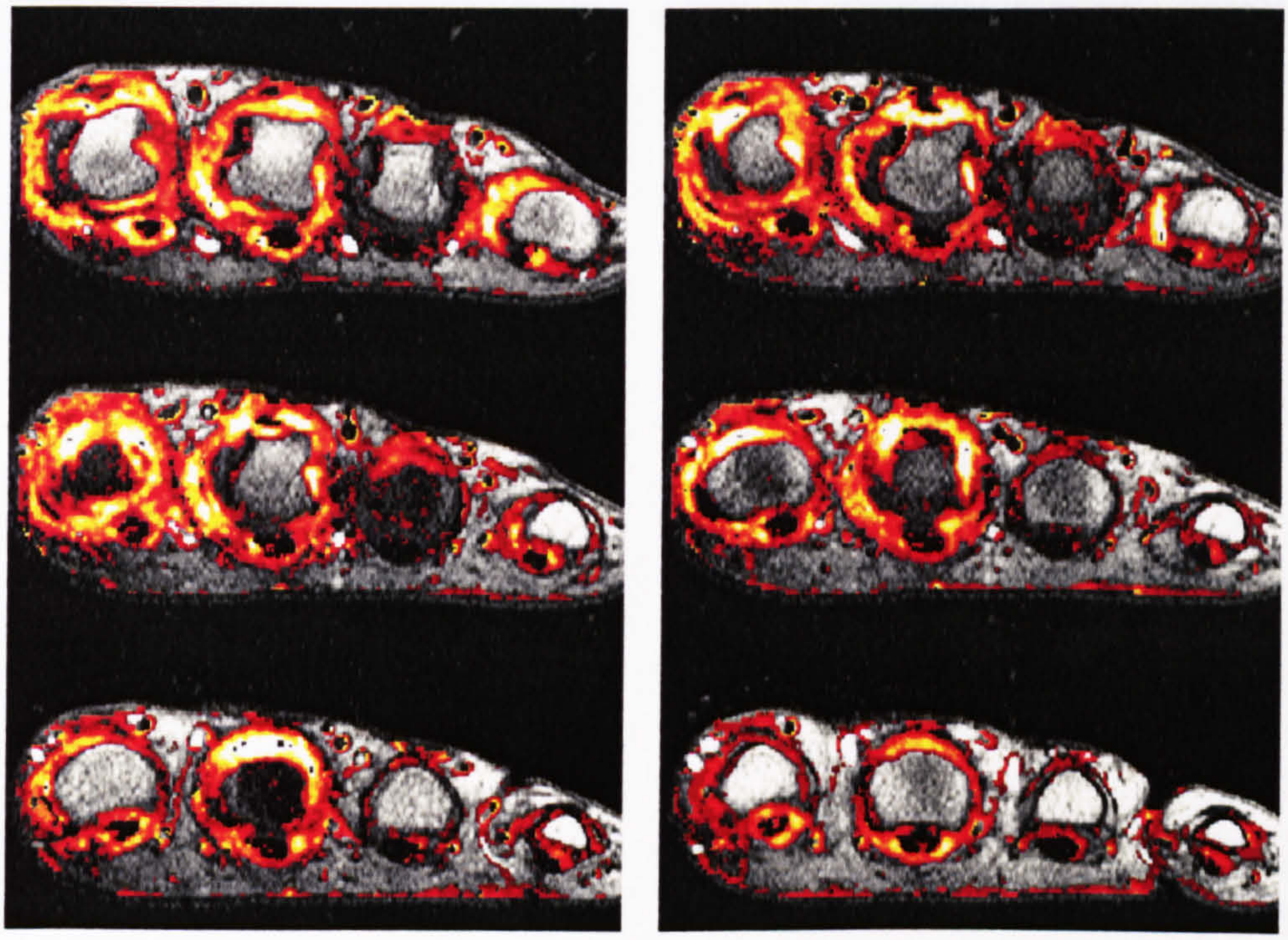

Figure 5-13 Parametric map of f_{ex} in a RA Hand study

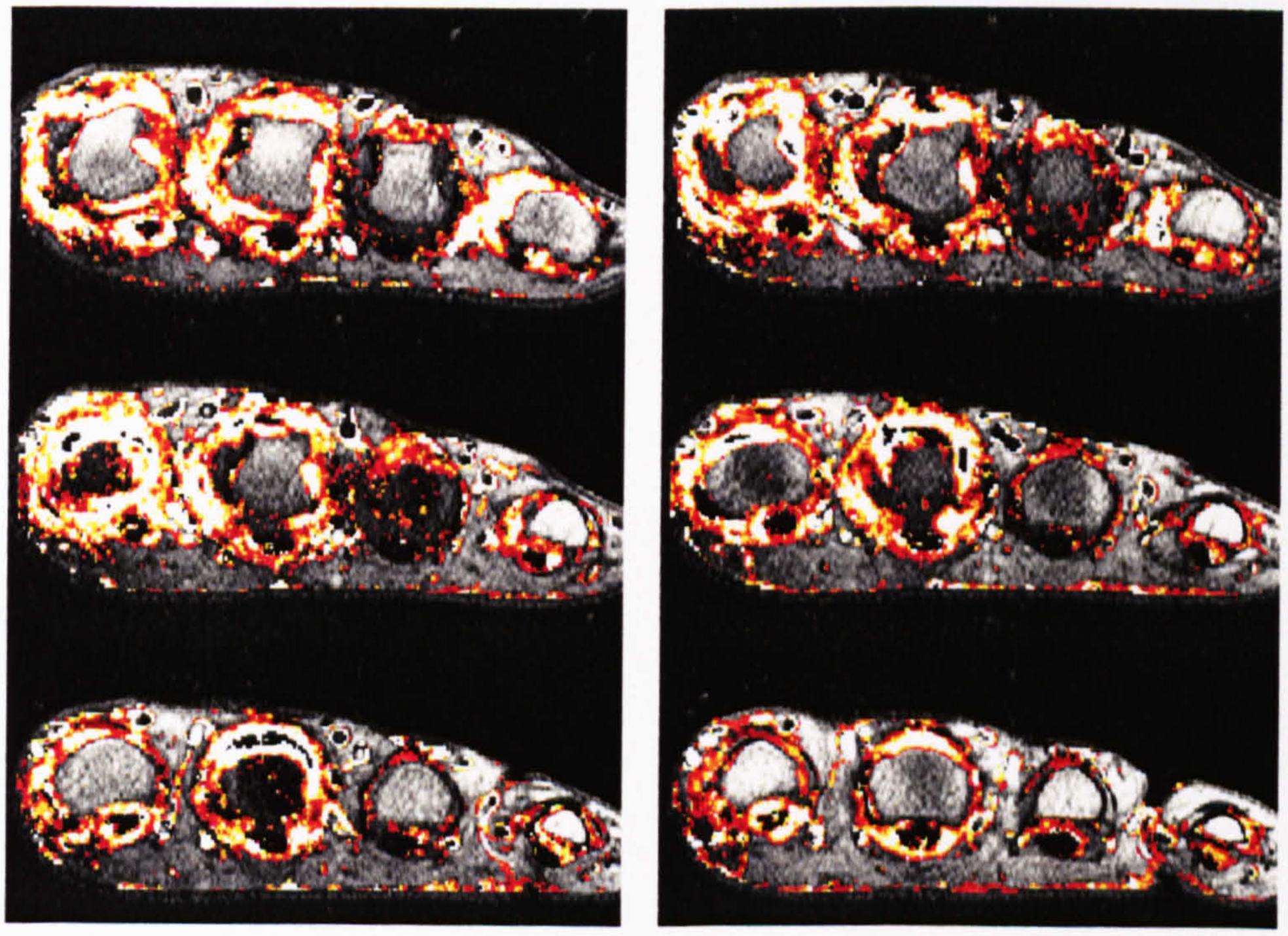

Figure 5-14 Parametric map of K^{trans} in a RA Hand study

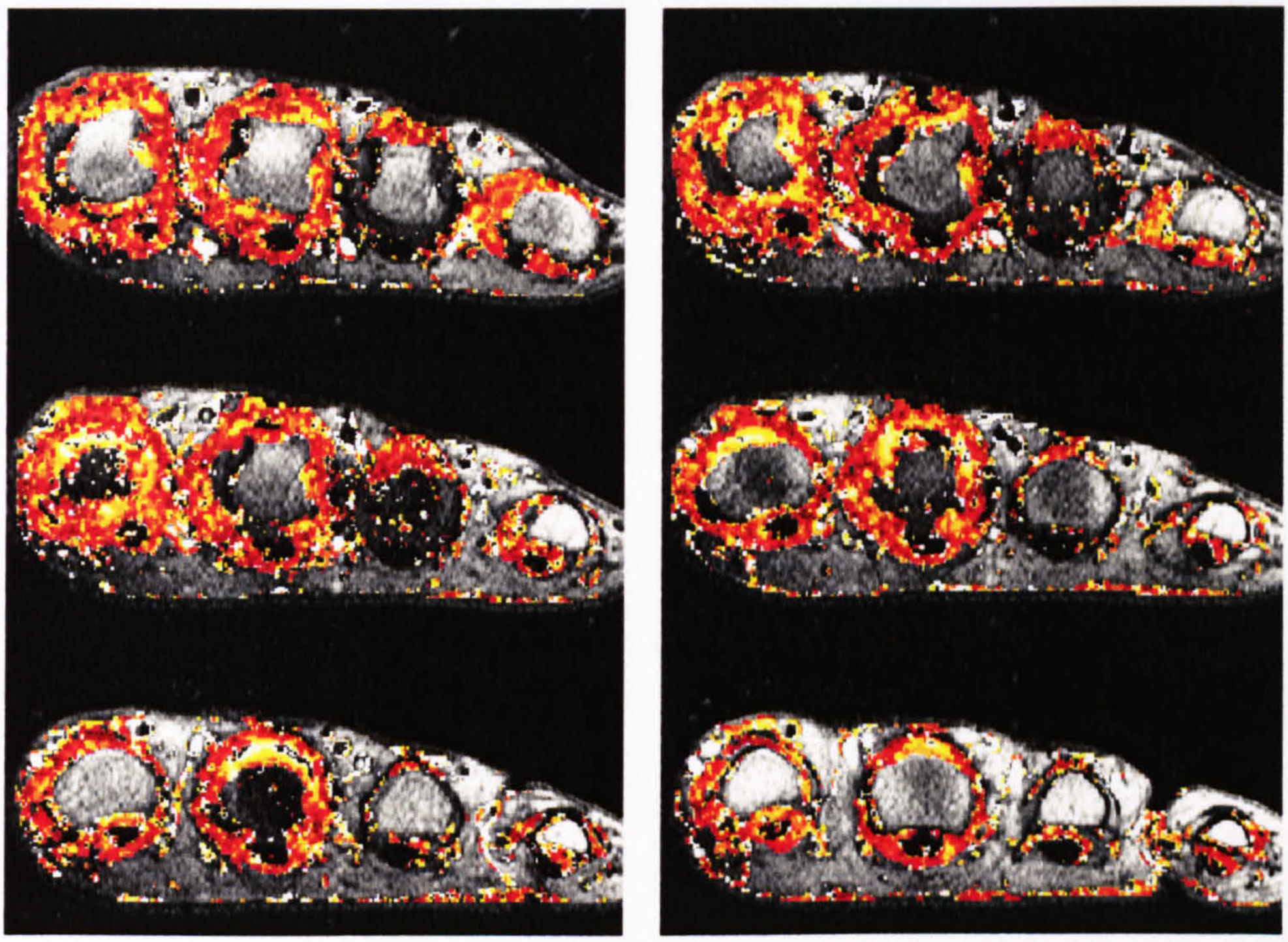

Figure 5-15 Parametric map of k_{21} in a RA Hand study

Parametric maps of PK variables measured in a sample RA Knee study are presented in Figure 5-16 to Figure 5-18. These quantitative maps clearly demonstrate the inflamed pannus in the supra-patellar and tibio-femoral region. It appears that the highest values of PK variables are measured in the central, deep-seated parts of the pannus. However, a degree of contamination by extra-capsular enhancing voxels is also evident (note colour-coded voxels in the skeletal muscle and popliteal vessels in Figure 5-18).

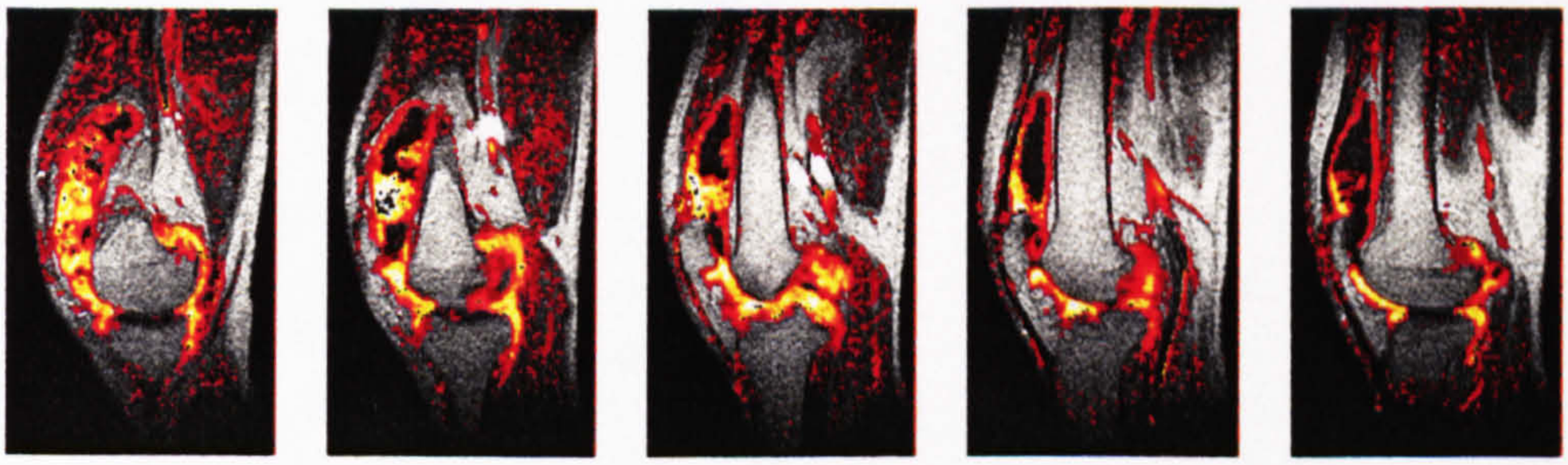

Figure 5-16 Parametric map of f_{ex} in a RA Knee study

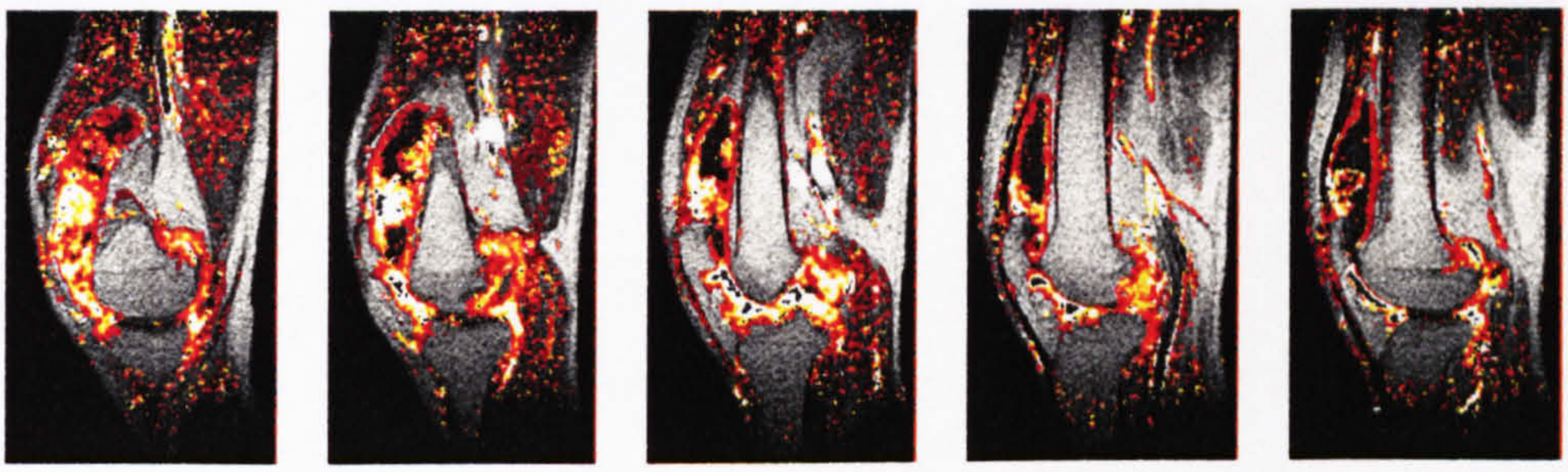

Figure 5-17 Parametric map of K^{trans} in a Knee RA study

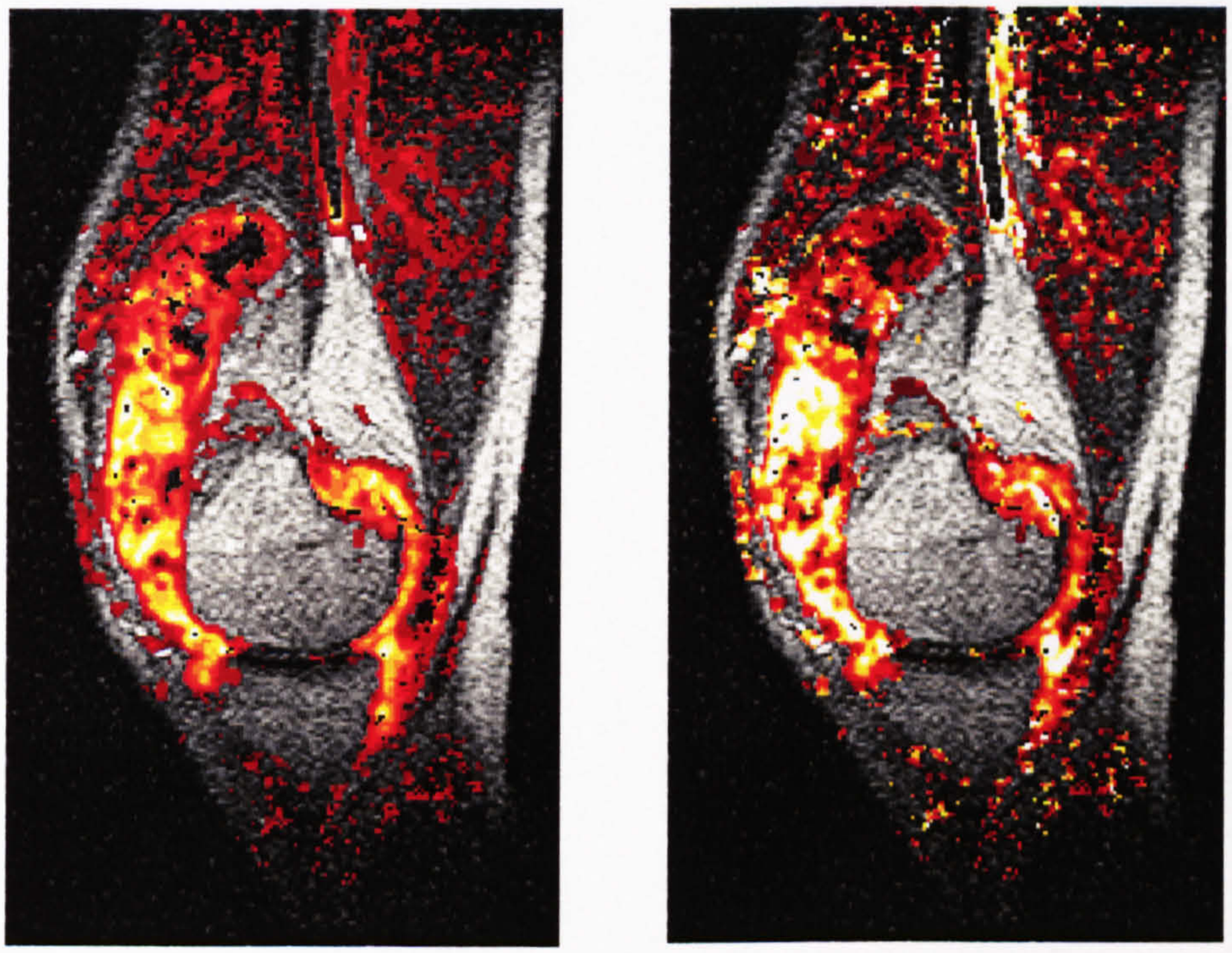

Figure 5-18 Parametric map of f_{ex} (left) and K^{trans} (right) in a Knee RA study (single sagittal slice)

QDEMRI datasets obtained by voxel-to-voxel SI analysis can be presented as histograms. The histograms of variable Ak_{21} obtained in the same patient at three different points during the course of the therapy (Hand RA Study) are illustrated in Figure 5-19.

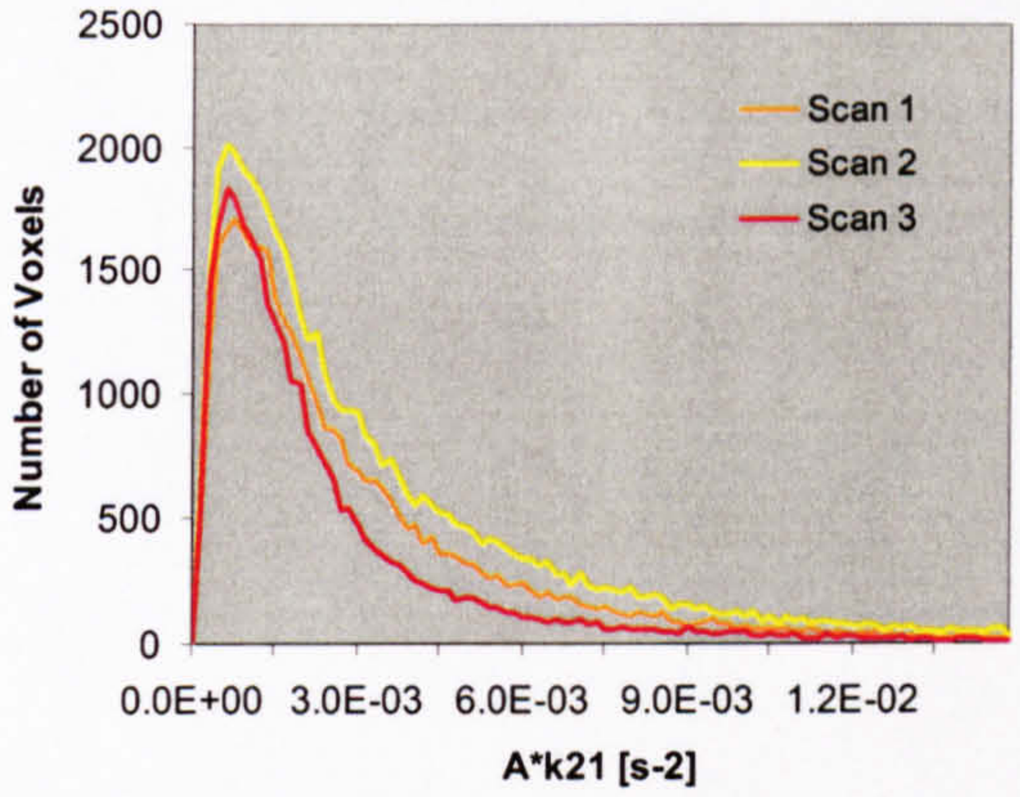

Figure 5-19 Histograms of the variable Ak_{21} measurements in the same patient during the course of the therapy

These histograms are conveying the information about the location and dispersion of measured values inside individual DEMRI sets. Clearly, the mode of all three samples is low, i.e. the largest proportion of measured voxel SI is derived from tissues with low values of Ak_{21} and the histograms are skewed to the right.

For the purposes of analysis of treatment effectiveness, the properties of the calculated parameter populations needed to be quantified even further. The properties of derived parameter populations need to be summarised and expressed as values which enable direct comparison between individual patients and measurements obtained at different points in the treatment cycle. The hypothesis is that all of the measured QDEMRI variables are directly proportional to the physiological variables that reflect the extent and the intensity of the inflammation process and therefore reflect disease activity. At the same time, the extremes of the measured parameter populations are often related to the artefactual enhancement (see Figure 5-18). The decision on how to treat the tail portion of the histograms presented in Figure 5-19 is therefore influenced by the need to preserve the potentially relevant information and at the same time limit the influence of erroneous measurements.

The approach adopted in this thesis was to quantify the measured QDEMRI variables populations in terms of their trimmed means. Percentile limits of the acquired histograms were identified and the values higher than the 90th percentile limit were excluded prior to the computation of the mean. Each DEMRI study was therefore quantified through a set of five QDEMRI variables summarising the location of corresponding QDEMRI variable histograms (ME, IRE, A, k_{21}, Ak_{21}) and two voxel counts (N-BB and N-PK). The results obtained in two clinical trials where these QDEMRI variables were measured at different points during treatment are presented in Chapter 7.

Chapter 6. Application to breast cancer

Since its introduction into clinical practice by Heywang-Kobruner in 1986 [130], DEMRI has almost unequivocally demonstrated high sensitivity for detection of breast cancer [131]. However, an agreement on the optimal scanning, sampling and analysis protocols is still not reached, and a wide variety of methodologies are still being used. The main limitation of DEMRI in the investigation of breast lesions lies in its low specificity and the majority of the studies in this field were centred on the design of methods for improving the distinction between malignant and benign breast lesions. The most basic criterion for the differentiation between benign and malignant lesions (presence or absence of enhancement) yields a specificity of only 37% [132]. Particularly problematic is the differentiation between benign fibroadenomas, ductal carcinoma in situ (DCIS) and some of the less angiogenesis-dependent types of cancer, such as invasive lobular carcinomas [133]. Improvement in DEMRI specificity in breast cancer (to 75-85%) can be achieved by its integration with other diagnostic findings and the formulation of precise inclusion criteria [133, 134].

Previous studies

As discussed in Chapter 3, quantitative analysis of DEMRI allows differentiation between malignant and benign breast lesions and several studies have demonstrated a significant degree of correlation between DEMRI quantifiers and surrogate measures of angiogenesis.

Several animal model studies of breast cancer have demonstrated a strong relationship between tumour grade and capillary permeability using macro-molecular contrast media (MMCM) [135-139]. Turetschek reported a significant correlation between permeability measured using both albumin-$(Gd\text{-}DTPA)_{30}$ [137, 138] and ultra small superparamagnetic iron oxide (USPIO) particles [139], and tumour grade, as well as MVD in chemically induced breast carcinoma in rats. However, experimental studies were unable to demonstrate an increase in permeability to the smaller Gd-DTPA molecule in higher-grade tumours [135, 136]. Daldrup et al reported that permeability to Gd-DTPA did not vary significantly between different tumour grades [136]. Su et al reported that Gd-DTPA can allow differentiation between benign and low-grade tumours, but not between low- and high-grade tumours [135]. One study attempted to compare acquisition and analysis methods according to their capacity to detect differences between different grades of experimental breast cancer [140]. None of the examined acquisition and analysis models yielded a statistically significant differentiation between different tumour grades.

Only a few studies have attempted to directly correlate DEMRI findings with prognostic factors such as tumour grade and nodal status in clinical studies of breast cancer [141-145]. None of these studies included pharmacokinetic analysis of DEMRI. Their results appear to be inconclusive and in part contradictory. Whilst Mussurakis [142] and Bone [144] found a significant correlation between DEMRI and prognostic factors, Fischer [143] and Stomper [141] found no correlation between them. Different acquisition and sampling protocols have been employed in each of these studies, as well as different methods for quantitative analysis of DEMRI. Furthermore, there was a considerable variation in the number of

patients/lesions studied, their histological mix, the method used for grading as well as the choice of prognostic factors that DEMRI was compared with (tumour grade, nodal status, DNA S-phase percentage as well as various immunohistochemical prognostic indicators). The temporal resolution of DEMRI acquisitions used in these studies ranged from 12 seconds [142], to 7 minutes [144]. Tissue coverage ranged from 64 transverse slices encompassing both breasts [144] to 4 targeted sagittal slices [142].

Stomper [141] studied a small series (17 patients) and chose to compare DEMRI with DNA S-phase percentage (a measure of increased cell proliferation). He used a heuristic method proposed by Orel [110] for quantitation of DEMRI. In their acquisition protocol, 5 contiguous slices were scanned with a temporal resolution of 30 seconds and a small ROI (2 mm^2) which gave the highest amplitude of enhancement was selected for analysis. No association between black-box parameters and DNA S-percentage was found in this study. In an earlier study conducted by the same group, a marginal difference in the wash-out rate between low grade (Grade 1 and Grade 2) and high grade (Grade 3) tumours was found [145]. Only 19 invasive carcinomas were available for this comparison. There was no association between DEMRI parameters and nodal status.

In a large study (190 patients) reported by Fischer [143], a semi-dynamic protocol with a low temporal resolution of 1.5 minutes was used. A complete coverage of both breasts was achieved by scanning 32 transverse slices. DEMRI was quantified using an enhancement ratio at 3 minutes post-injection. Small ROIs (2-5 voxels) were selected for analysis. Enhancement ratios were rather crudely grouped into three categories, based on empirically determined percentage thresholds. There was no significant difference between the distributions of enhancement ratios in three histological grade groups and no association with node status was detected. In a sub-set of 40 patients where immunohistochemical staining was performed, no correlation was found between immunohistochemical prognostic factors and ER. However, non-invasive carcinomas had lower ER than invasive carcinomas.

The acquisition protocol used by Bone et al [144] was also semi-dynamic, with only two acquisitions obtained after the baseline pre-contrast scan and the injection of Gd-DTPA, with an extremely low temporal resolution of 7 minutes. The most representative cross section of the lesion was identified from a set of 64 slices and the entire enhancing area used to calculate enhancement ratios (ER) at 7 and 13 minutes post-injection. The lesions were classified in only two groups (high grade and combined low- and intermediate-grade). A significant difference between enhancement ratios in high and low/intermediate grade tumours was found. There was no distinction between node-positive and node-negative tumours.

Mussurakis [142] used a targeted dynamic protocol with temporal resolution of 12 seconds and the coverage of only 4 sagittal sections. In this study, enhancement ratios at 1 and 2 minutes post-injection as well as the maximal enhancement ratio were calculated using SI curves derived from the entire lesion (large manually drawn ROI) and semi-automatically detected 9-voxel ROIs with highest amplitude of uptake. In both sets of ROIs, significantly higher ERs were measured in node-positive than in node-negative tumours. A significant relationship between all ERs extracted from small ROIs and tumour grade was found. Although the selection of ROIs was performed by inspecting parametric maps of pharmacokinetic parameters, their values or possible association with prognostic factors were not reported.

This study

The aim of this Breast Cancer Study was to apply QDEMRI analysis described in Chapters 4 and 5 to histologically confirmed and graded invasive human breast carcinomas and to investigate the capacity of PK measurements of permeability (k_{21} and Ak_{21}) to reflect histological tumour grade and node status. The hypothesis was that given a documented difference in capillary permeability between benign and malignant breast tumours, a

relationship between permeability-related QDEMRI variables and tumour aggressiveness persists within invasive breast carcinomas. Secondly, the capacity of other QDEMRI variables to detect differences between carcinomas of different tumour type and nodal status was investigated.

6.1. Study description

MRI examination of the breasts was performed in patients with breast lesions where conventional triple assessment (X-ray mammography, ultrasound and clinical examination) did not provide conclusive diagnosis and where further information about the extent of a known lesion and/or possible multifocality was being sought.

Of 255 consecutive patients who underwent MRI examination, mastectomy was subsequently performed in 66 cases and a full pathology report, including tumour grade and lymph node status, was available for 53 patients (60 lesions). Tumour grading was performed using the Nottingham Prognostic Index for primary breast cancer [146]. The imaging protocol is described in Chapter 5. Both breasts (25 transverse slices) were scanned for 5 minutes with a temporal resolution of 32.5 seconds. In one examination, quantitative analysis was not possible due to excessive patient motion.

Full QDEMRI analysis was performed retrospectively in 59 lesions (in 52 patients). All patients were female with a median age of 55 (ranging from 32 to 80). The lesions were classified according to their histological grade into three groups. Twelve lesions were found to be Grade 1 tumours, twenty-nine, Grade 2 and eighteen, Grade 3 tumours. Thirty lesions had negative node status and twenty-nine were node positive. Forty-four lesions were classified as invasive ductal carcinomas not otherwise specified (NOS), eleven were invasive lobular carcinomas, two were invasive tubular carcinomas and two were invasive mucinous

carcinomas. Thirty-four out of fifty-nine lesions had a significant in-situ (DCIS) component. Table 6-1 presents a summary of the pathology grading and lymph node status for the set of fifty-nine evaluated lesions.

		Node Status		
		negative	positive	Total
Tumour Grade	Grade 1	10	2	12
	Grade 2	11	18	29
	Grade 3	9	9	18
Total		30	29	59

Table 6-1 Summary of histological status of breast cancer lesions

6.2. Summary of the measurements

All lesions were sampled following a procedure described in Section 5.2.1 and QDEMRI analysis was performed on SI curves derived from representative ROIs. Preliminary computation of parameteric maps used for the selection of ROIs and ROI selection was performed blinded to the results of histopathological analysis. QDEMRI analysis yielded a set of six variables for each evaluated SI curve (three pharmacokinetic variables: A, k_{21} and Ak_{21} and three black-box variables ME, IRE and WOS). A summary of pharmacokinetic QDEMRI variables is presented in Table 6-2. This table lists the mean values and standard deviations in three histological subgroups.

	A [s-1]		k21 [s-1]		Ak21 [s-2]	
	Mean	SD	Mean	SD	Mean	SD
Grade 1 (n = 12)	3.66E-02	1.18E-02	2.70E-02	1.37E-02	9.49E-04	4.32E-04
Grade 2 (n = 29)	4.31E-02	1.35E-02	3.39E-02	2.66E-02	1.43E-03	1.14E-03
Grade 3 (n = 18)	4.31E-02	1.01E-02	5.28E-02	2.69E-02	2.21E-03	1.08E-03

Table 6-2 Pharmacokinetic QDEMRI variables in the Breast Cancer Study

A summary of black-box QDEMRI variables is presented in Table 6-3. Again, the mean values of measured variables and their standard deviations are listed for each of the three subgroups.

	ME		IRE [s-1]		WOS [s-1]	
	Mean	SD	Mean	SD	Mean	SD
Grade 1 (n = 12)	2.04E+00	3.28E-01	2.19E-02	7.40E-03	2.90E-04	1.11E-03
Grade 2 (n = 29)	2.20E+00	3.61E-01	2.50E-02	9.94E-03	-1.18E-04	9.25E-04
Grade 3 (n = 18)	2.26E+00	2.87E-01	2.92E-02	7.98E-03	-5.84E-04	9.26E-04

Table 6-3 Black-box QDEMRI variables in the Breast Cancer Study

Scatter plots of the original measurements and corresponding error-bar plots (representing the mean and two standard error (SE) limits) of measured subgroups of QDEMRI variables are presented in Figure 6-1 to Figure 6-6.

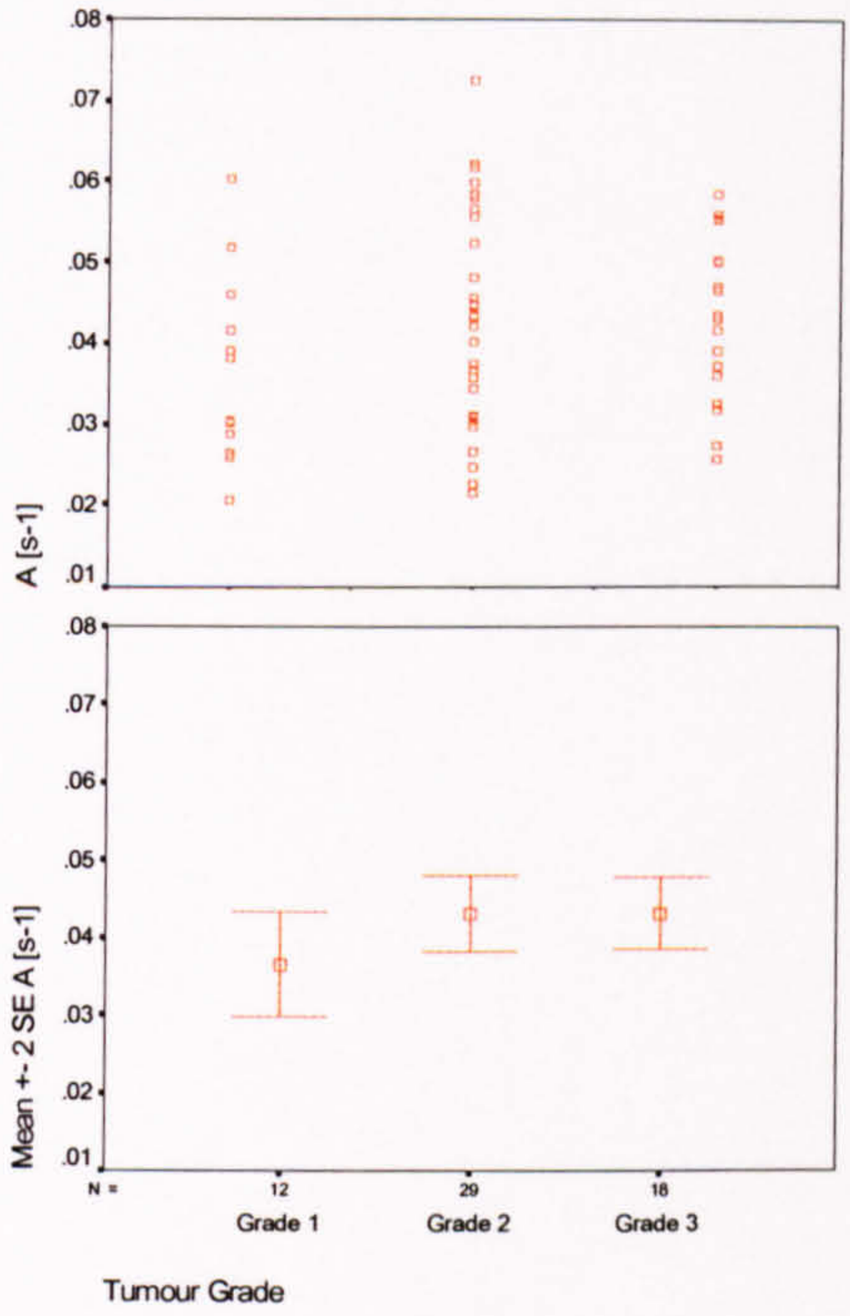

Figure 6-1 Distribution of variable A in the Breast Cancer Study

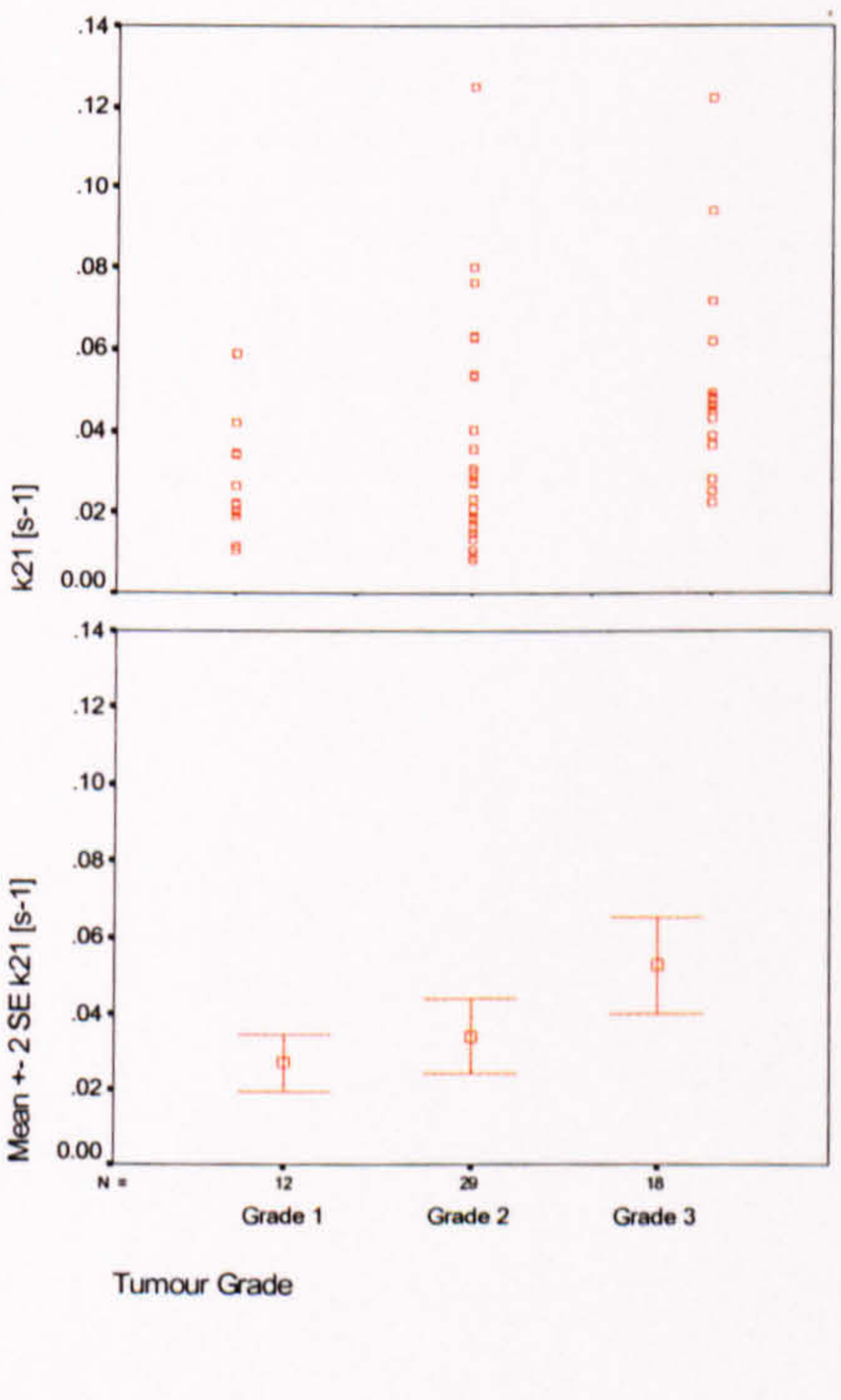

Figure 6-2 Distribution of variable k_{21} in the Breast Cancer Study

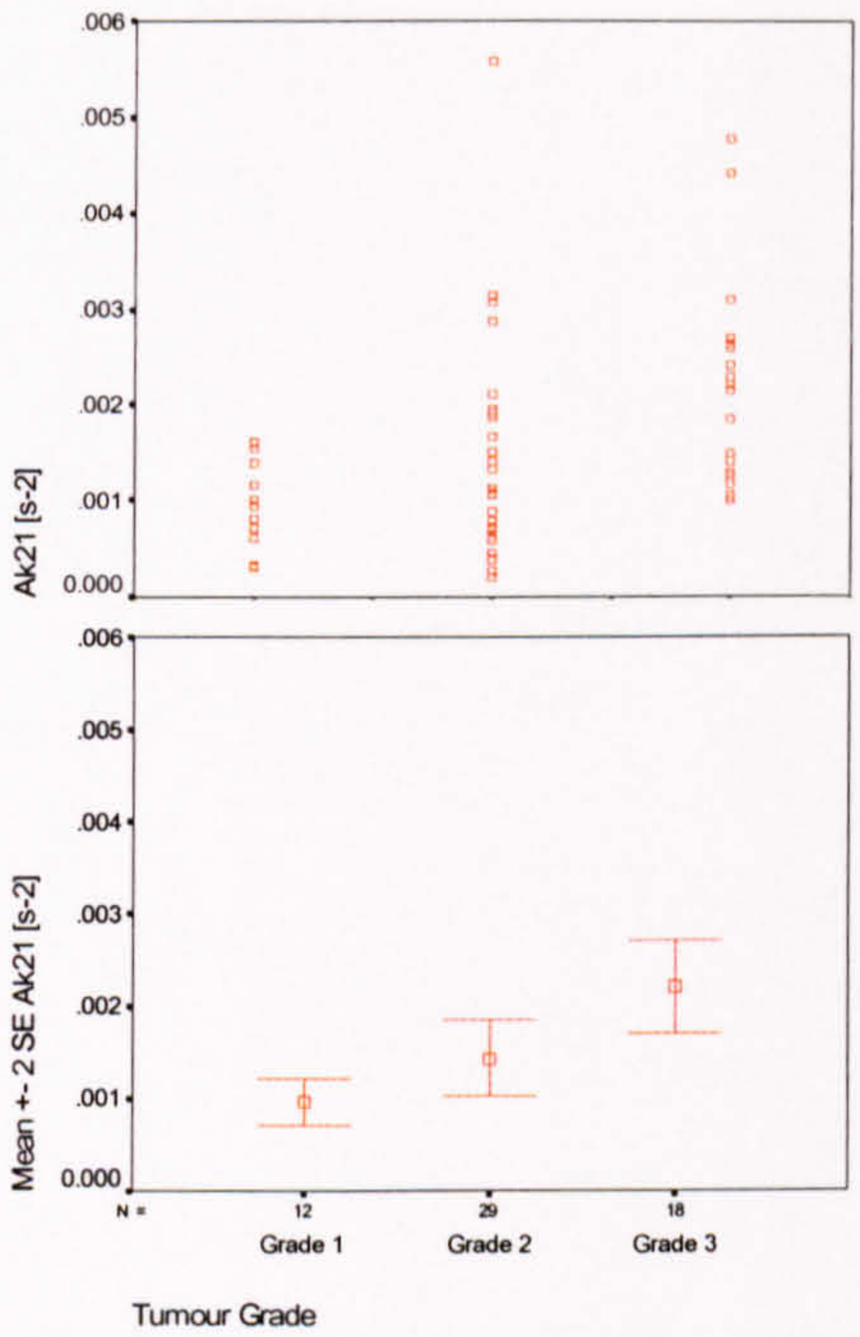

Figure 6-3 Distribution of variable Ak_{21} in the Breast Cancer Study

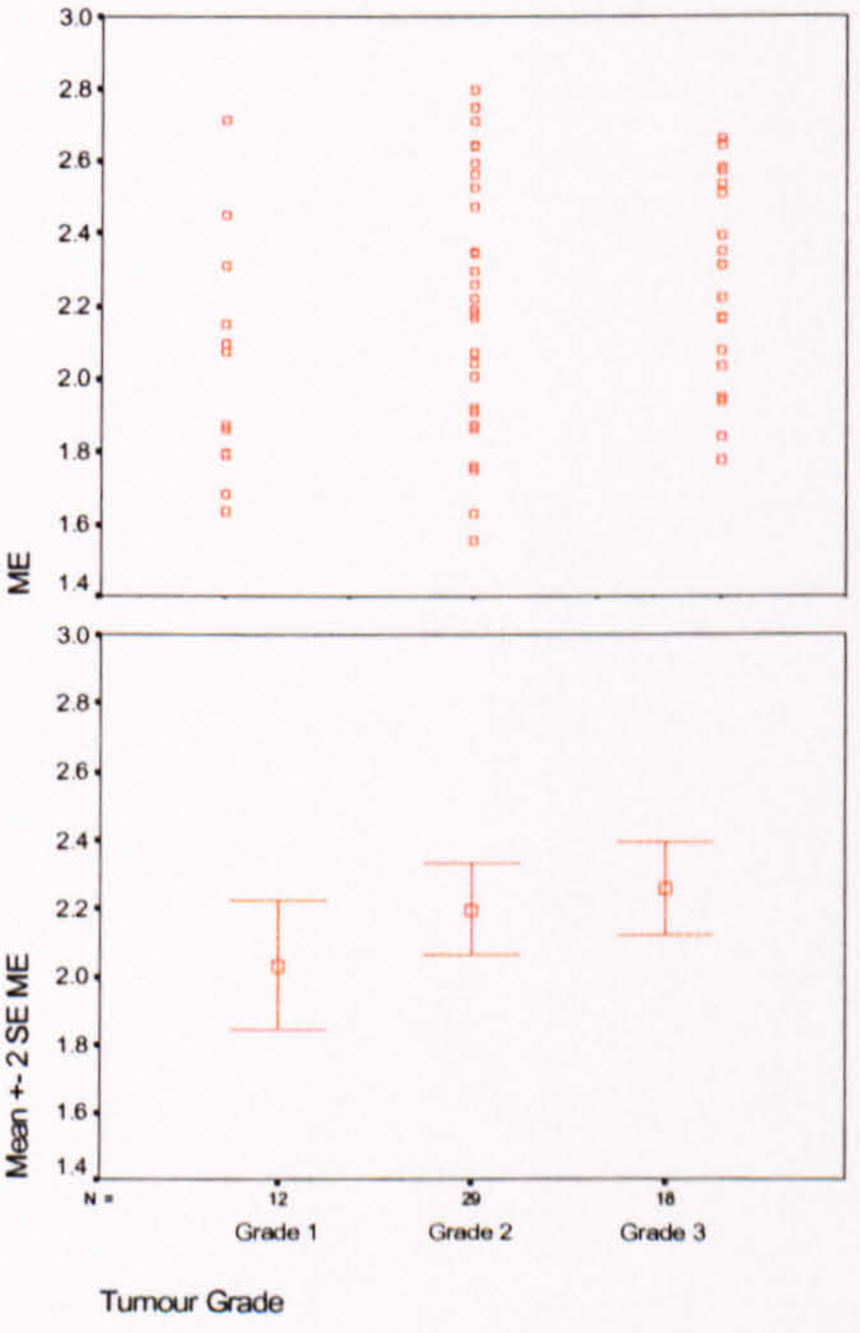

Figure 6-4 Distribution of variable ME in the Breast Cancer Study

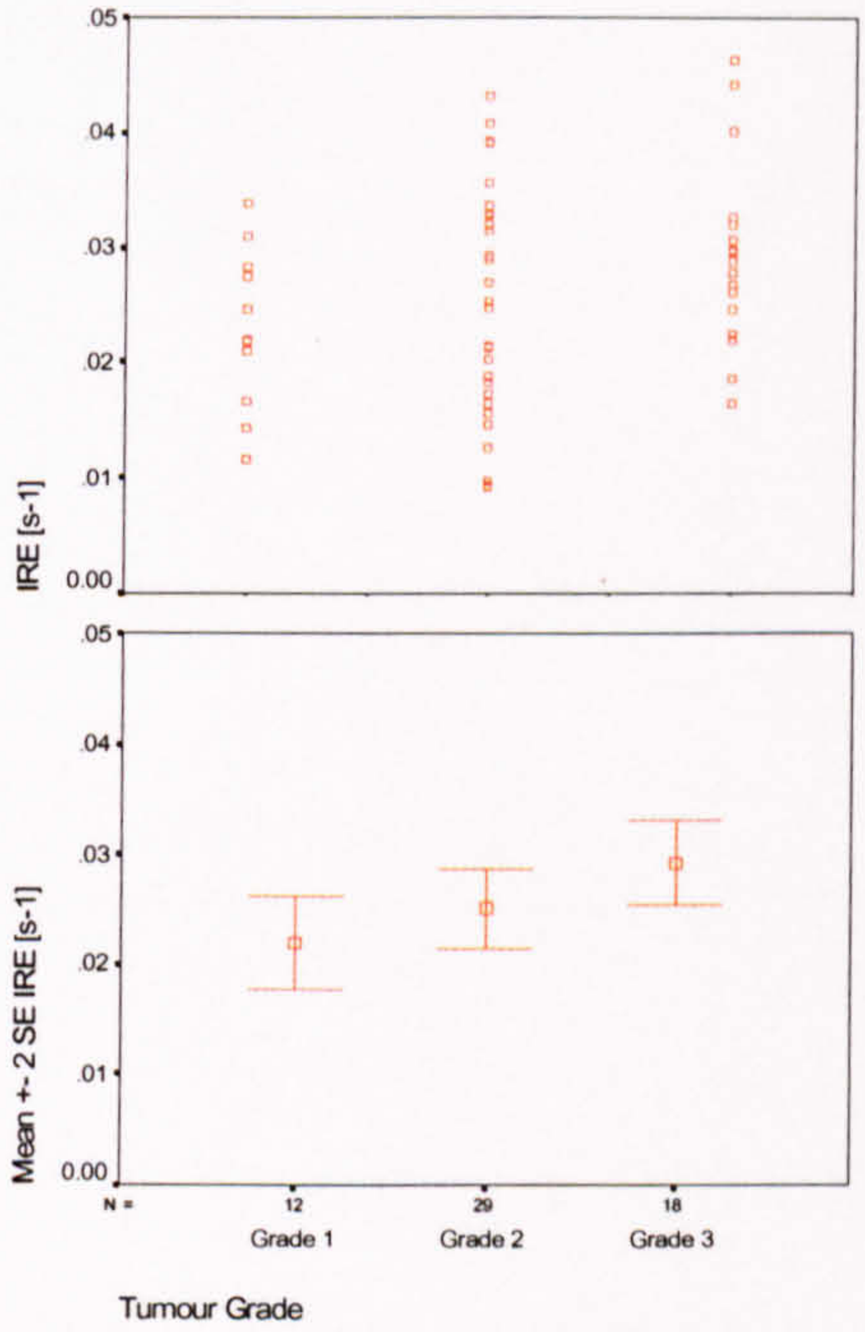

Figure 6-5 Distribution of variable IRE in the Breast Cancer Study

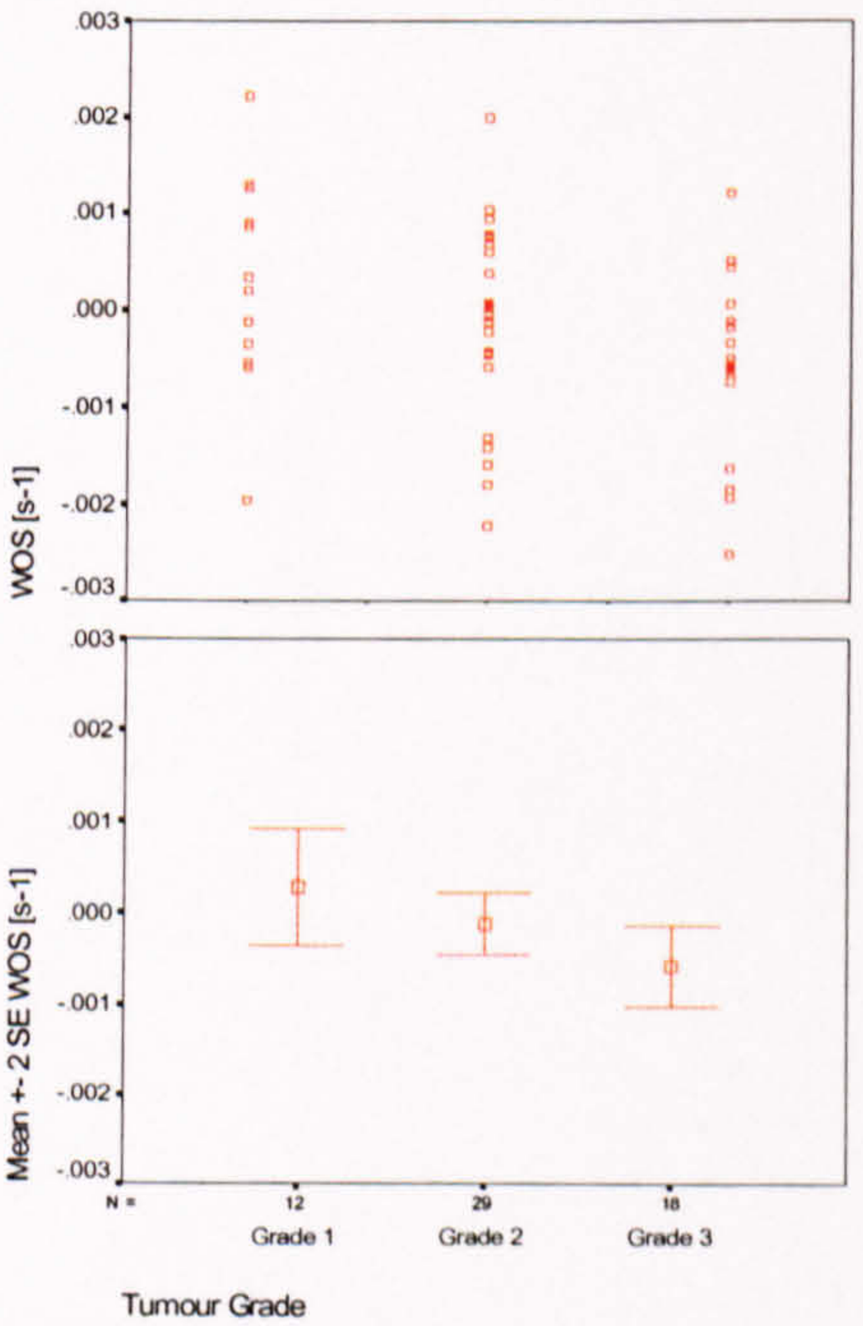

Figure 6-6 Distribution of variable WOS in the Breast Cancer Study

6.3. Statistical analysis

SPSS statistical software package (Version 10.0, SPSS, Chicago, IL) was used for statistical analysis. All statistical tests were performed at $\alpha = 0.05$ confidence level. A preliminary analysis of the distribution of measurements of each of the six QDEMRI variables revealed no significant deviation from normality in three histological subgroups. The results of the Kolmogorov-Smirnov test for normality are listed in Appendix C. This analysis was performed on eighteen sets of measurements (six variables divided into three histological subgroups) with the sample size of n = 12 for Grade 1 lesions, n = 29 for Grade 2 lesions and n = 18 for Grade 3 lesions. Due to the small sample size, further division according to the node status and tumour type was not performed.

Data transformation

Although the Kolmogorov-Smirnov test indicated no significant deviation from normality, the symmetry of the data subgroups was further analysed as symmetry is one of the pre-requisites for reliable calculation of regression coefficients [147]. The symmetry of the data subgroups was quantified through the computation of skewness.

	Tumour Grade		
	Grade 1	Grade 2	Grade 3
A	.689	.253	-.166
k21	1.204	1.819	1.350
Ak21	.036	1.979	1.132
ME	.808	.000	-.146
IRE	-.021	.072	.717
WOS	-.273	-.306	-.357

Table 6-4 Skewness of QDEMRI variable subgroups in the Breast Cancer Study

The values of subgroup skewness values are listed in Table 6-4. In order to increase data symmetry prior to the application of regression analysis, a suitable data transformation was sought for each QDEMRI variable. A maximal absolute value of skewness of 0.5 was accepted as a symmetry target. Transformation coefficients for each of the six QDEMRI variables were determined by an iterative procedure designed to minimise total absolute skewness, whilst ensuring that absolute skewness does not exceed |0.5| in any of the subgroups. With the exception of variable WOS where no further improvement of symmetry could be achieved (and where the original skewness in neither of the three subgroups exceeded |0.5|), natural logarithm transformation yielded adequate reduction of skewness in all data subgroups. A list of transformations is given in Table 6-5.

	Transformation
A	ln (A + 0.0237)
k21	ln (k21 - 0.0046)
Ak21	ln (Ak21 + 0.0005)
ME	ln (ME - 0.7472)
IRE	ln (IRE + 0.0157)

Table 6-5 List of variable transformations

A list of resulting subgroup skewness values is given in Table 6-6. Transformed variables are distinguished from the original measurements by a superscript prime (e.g. original variable A is transformed into A').

	Tumour Grade		
	Grade 1	Grade 2	Grade 3
A'	.360	-.081	-.400
k21'	-.289	-.074	.300
Ak21'	-.497	.460	.388
ME'	.400	-.379	-.389
IRE'	-.297	-.300	.245

Table 6-6 Skewness of the transformed QDEMRI variable subgroups in the Breast Cancer Study

Regression analysis

Following data transformation, linear regression of QDEMRI variables (V') on tumour grade was performed using the following regression model:

$$V' = B_1 + B_2 \cdot G_2 + B_3 \cdot G_3 \qquad \text{Eq. 6-1}$$

where B_1 represents the intercept and B_2 and B_3 represent unstandardised regression coefficients. G_2 and G_3 denote two "dummy variables" used to provide binary coding of tumour grade (independent categorical variable), with $G_2 = 1$ and $G_3 = 0$ for grade 2 tumours, $G_2 = 0$ and $G_3 = 1$ for Grade 3 tumours and $G_2 = G_3 = 0$ for Grade 1 tumours.

The results of the regression analysis are presented in Table 6-7 below. The table lists multiple correlation coefficient R, the coefficient of determination (goodness-of-fit) R^2 and their significance (p-value) for each QDEMRI variable.

	R	R2	p-value
A'	.223	.050	.239
k21'	.432	.187	**.003**
Ak21'	.467	.218	**.001**
ME'	.250	.063	.163
IRE'	.294	.087	.079
WOS	.314	.099	.054

Table 6-7 Regression analysis summary

As can be seen from Table 6-7, there is a significant relationship between tumour grade and PK variables k_{21} and Ak_{21}. The strength of this relationship, however, is modest. This is reflected in relatively low values of R (0.432 and 0.467 for k_{21}' and Ak_{21}', respectively). The strength of association between BB variable WOS and tumour grade reached borderline significance (R = 0.314, p = 0.054). Low values of R^2 (which represents the proportion of variation in the dependent variable explained by the regression model) indicate that a relatively low proportion of the overall variation in the data is attributable to the underlying (histologically determined) tumour grade and reflect a high level of scatter in the data.

The individual unstandardised coefficients B_2 and B_3 with their corresponding 95% confidence intervals (95% CI) and p-values for each of the QDEMRI variables are listed in Table 6-8. Constant B_1 is also included in this summary of the model and its mean and confidence interval describe the location of the intercept (mean value in the Grade 1 group).

			95% CI			
		B	Lower	Upper	p-value	
	B1 (constant)	-2.83E+00	-2.93E+00	-2.72E+00		
A'	B2	1.00E-01	-2.87E-02	2.29E-01	.125	
	B3	1.09E-01	-3.12E-02	2.49E-01	.125	
	B1 (constant)	-3.97E+00	-4.40E+00	-3.55E+00		
k21'	B2	8.61E-02	-4.25E-01	5.97E-01	.737	
	B3	8.11E-01	2.56E-01	1.37E+00	.005	p < 0.005
	B1 (constant)	-6.57E+00	-6.82E+00	-6.31E+00		
Ak21'	B2	1.95E-01	-1.02E-01	4.93E-01	.194	
	B3	5.94E-01	2.71E-01	9.17E-01	.001	p < 0.005
	B1 (constant)	2.25E-01	8.61E-02	3.63E-01		
ME'	B2	1.17E-01	-4.79E-02	2.82E-01	.161	
	B3	1.72E-01	-7.12E-03	3.51E-01	.059	
	B1 (constant)	-3.30E+00	-3.43E+00	-3.17E+00		
IRE'	B2	6.73E-02	-8.55E-02	2.20E-01	.381	
	B3	1.81E-01	1.55E-02	3.47E-01	.033	p < 0.05
	B1 (constant)	2.90E-04	-2.68E-04	8.47E-04		
WOS	B2	-4.07E-04	-1.07E-03	2.55E-04	.223	
	B3	-8.74E-04	-1.59E-03	-1.55E-04	.018	p < 0.05

Table 6-8 Unstandardised regression coefficients in the Breast Cancer Study (contrasts against Grade 1)

The results presented in Table 6-8 indicate that none of the measured variables provided a significant distinction between Grade 1 and Grade 2 tumours since none of the B_2 coefficients were significantly different from zero. However, the separation between Grade 1 and Grade 3 tumours in regression models for k_{21}', Ak_{21}', IRE' and WOS (represented by the regression coefficients B_3), is significant although detected values of B_3 have broad confidence intervals. Furthermore, variables k_{21}' and Ak_{21}' appear to provide a more significant separation between Grade 1 and Grade 3 tumours when compared to BB variables IRE' and WOS.

Whilst Table 6-8 describes contrasts between Grade 2 and Grade 3 tumour measurements against Grade 1, an alternative regression model is used to assess the contrasts between Grade 1 and Grade 3 with respect to Grade 2 measurements. This regression model is described in Eq. 6-2.

$$V' = B_1 \cdot G_1 + B_2 + B_3 \cdot G_3 \qquad \text{Eq. 6-2}$$

In this regression model, B_2 represents the intercept and B_1 and B_3 represent unstandardised regression coefficients. G_1 and G_3 denote two "dummy variables" used to provide binary coding of tumour grade, with $G_1 = 1$ and $G_3 = 0$ for Grade 1 tumours, $G_1 = 0$ and $G_3 = 1$ for Grade 3 tumours and $G_1 = G_3 = 0$ for Grade 2 tumours.

The contrasts between Grade 1 and Grade 3 with respect to Grade 2 measurements are quantified by individual unstandardised regression coefficients B_1 and B_3, their 95% confidence intervals (95% CI) and p-values for each QDEMRI variable (Table 6-9).

			95% CI			
		B	Lower	Upper	p-value	
	B2 (constant)	-2.72E+00	-2.79E+00	-2.65E+00		
A'	B1	-1.00E-01	-2.29E-01	2.87E-02	.125	
	B3	8.54E-03	-1.04E-01	1.21E-01	.880	
	B2 (constant)	-3.89E+00	-4.16E+00	-3.61E+00		
k21'	B1	-8.61E-02	-5.97E-01	4.25E-01	.737	
	B3	7.25E-01	2.78E-01	1.17E+00	.002	**p < 0.005**
	B2 (constant)	-6.37E+00	-6.53E+00	-6.21E+00		
Ak21'	B1	-1.95E-01	-4.93E-01	1.02E-01	.194	
	B3	3.99E-01	1.38E-01	6.59E-01	.003	**p < 0.005**
	B2 (constant)	3.42E-01	2.53E-01	4.31E-01		
ME'	B1	-1.17E-01	-2.82E-01	4.79E-02	.161	
	B3	5.50E-02	-8.92E-02	1.99E-01	.448	
	B2 (constant)	-3.23E+00	-3.31E+00	-3.15E+00		
IRE'	B1	-6.73E-02	-2.20E-01	8.55E-02	.381	
	B3	1.14E-01	-1.95E-02	2.48E-01	.093	
	B2 (constant)	-1.18E-04	-4.76E-04	2.41E-04		
WOS	B1	4.07E-04	-2.55E-04	1.07E-03	.223	
	B3	-4.67E-04	-1.05E-03	1.12E-04	.112	

Table 6-9 Unstandardised regression coefficients in the Breast Cancer Study (contrasts against Grade 2)

Again, constant B_2 is also included in this summary of the model and its mean and confidence interval describe the location of the intercept (mean value in the Grade 2 group).

The results presented in Table 6-9 indicate that the only variables which provide significant distinction between Grade 2 and Grade 3 tumours are k_{21}' and Ak_{21}'. Whilst variables IRE' and WOS are sensitive enough to reflect the differences between Grade 1 and Grade 3 tumours, they do not vary significantly between Grade 2 and Grade 3 tumours (compare regression coefficients in Table 6-8 and Table 6-9).

The confidence intervals of the regression coefficients can be used to estimate the location of the means of transformed variables in each of the tumour grade subgroups. Inverse transformation yields the estimates of the QDEMRI variable means in three tumour grade subgroups, expressed in original units.

			95% CI	
		Mean[a]	Lower	Upper
A	Grade 1	3.56E-02	2.95E-02	4.24E-02
	Grade 2	4.18E-02	3.39E-02	5.09E-02
	Grade 3	4.24E-02	3.37E-02	5.23E-02
k21	Grade 1	2.34E-02	1.68E-02	3.35E-02
	Grade 2	2.51E-02	1.69E-02	3.87E-02
	Grade 3	4.69E-02	2.89E-02	7.82E-02
Ak21	Grade 1	8.88E-04	5.75E-04	1.29E-03
	Grade 2	1.19E-03	7.50E-04	1.79E-03
	Grade 3	2.03E-03	1.33E-03	3.00E-03
ME	Grade 1	2.00E+00	1.84E+00	2.19E+00
	Grade 2	2.15E+00	1.94E+00	2.41E+00
	Grade 3	2.23E+00	1.99E+00	2.53E+00
IRE	Grade 1	2.12E-02	1.68E-02	2.63E-02
	Grade 2	2.38E-02	1.82E-02	3.03E-02
	Grade 3	2.86E-02	2.18E-02	3.66E-02
WOS	Grade 1	2.90E-04	-2.68E-04	8.47E-04
	Grade 2	-1.18E-04	-7.80E-04	5.45E-04
	Grade 3	-5.84E-04	-1.30E-03	1.35E-04

[a] Geometric mean is obtained after inverse logarithmic transformation

Table 6-10 Estimated means of QDEMRI variables in the Breast Cancer Study

These estimated 95% confidence interval limits for mean values of QDEMRI variables are presented graphically in Figure 6-7. The displayed p-values represent the overall regression

model significance (see Table 6-7). Red squares represent lower CI limits, blue squares represent upper CI limits and green squares represent geometric means of each variable (variable WOS, as described earlier, was not subjected to logarithmic transformation).

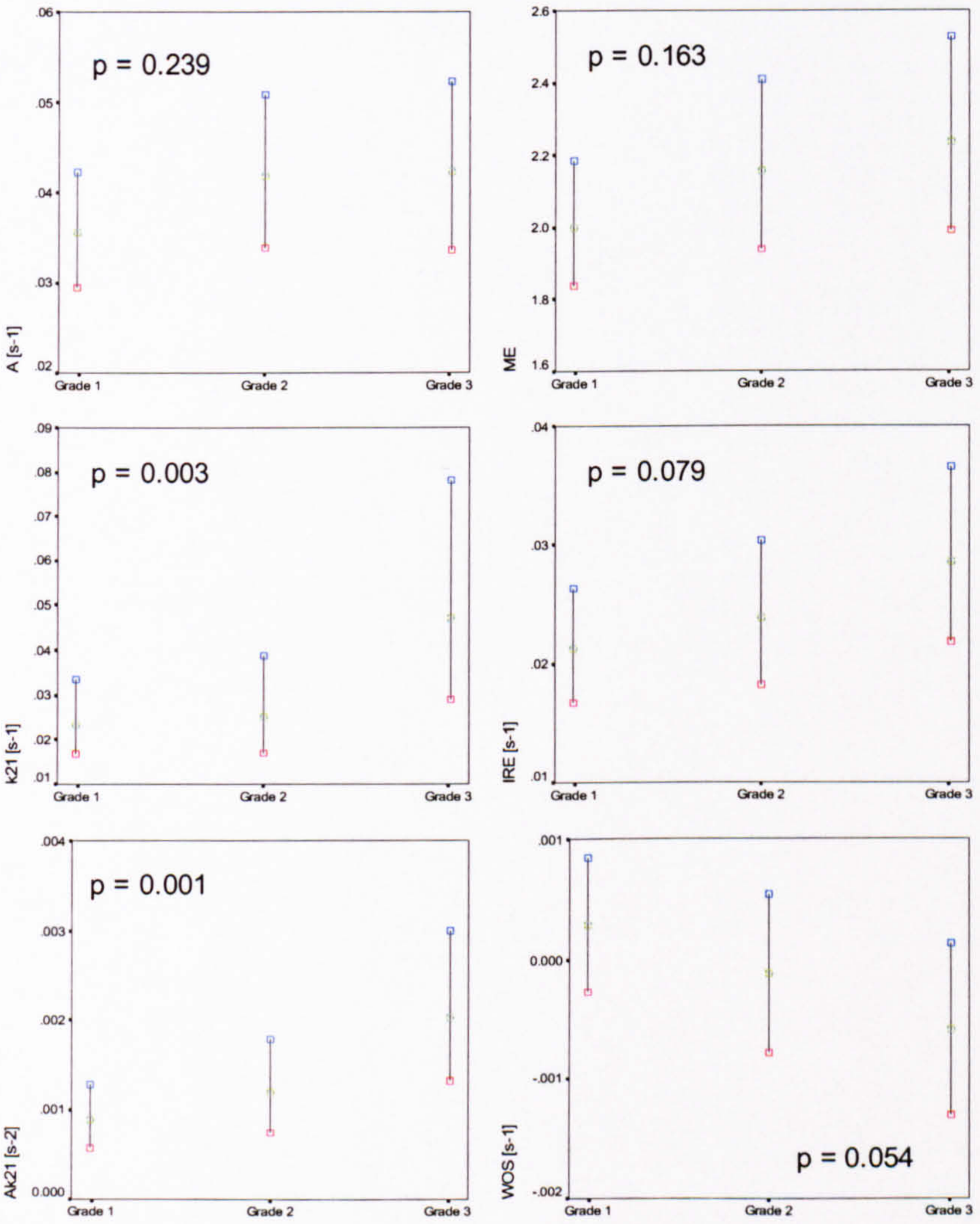

Figure 6-7 Estimated means of QDEMRI variables in the Breast Cancer Study

The results of the regression analysis indicate that there is a slight (non-significant) trend towards higher values of A, ME and IRE with increasing tumour grade. The pattern of distribution of variable A (which is proportional to the fractional volume of the EES, f_{ex}) between tumour groups suggests that Grade 2 and Grade 3 tumours have similar EES

fraction (f_{ex}) whereas permeability-related variables k_{21} and Ak_{21} undergo an abrupt change in the transition between Grade2 and Grade 3 tumours. This change is also reflected in the observed pattern of WOS distribution between different tumour grades, although it is more gradual. High (positive) values of WOS indicate that the uptake of contrast in the lesion continues beyond the end of SI sampling. Low (negative) values of WOS indicate rapid washout of contrast from the lesion.

In the unstandardised regression models (Eq. 6-1 and Eq. 6-2), regression coefficients obtained for different QDEMRI variables have different units and their magnitudes can therefore not be compared directly. A direct comparison between the regression coefficients is possible if the regression analysis is performed on standardised variables. To enable a direct comparison between the strength and the nature of association between measured QDEMRI variables and histologically determined tumour grade all transformed variables were standardised, i.e. expressed as Z scores, using the following expression:

$$Z(V') = \frac{V' - \overline{V'}}{SD(V')} \qquad \text{Eq. 6-3}$$

where $Z(V')$ represents standardised transformed variable, $\overline{V'}$ represents the overall mean of the transformed variable and $SD(V')$ represents the standard deviation of the transformed variable. Standardised regression coefficients (derived from the regression model described in Eq. 6-1, for contrasts against Grade 1 tumours) are presented in Table 6-11. This table includes p-values for individual regression coefficients, which are identical to those presented in Table 6-8.

			95% CI			
		B	Lower	Upper	p-value	
Z(A')	B1 (constant)	-.436	-1.010	.137		
	B2	.530	-.152	1.213	.125	
	B3	.576	-.165	1.316	.125	
Z(k21')	B1 (constant)	-.358	-.889	.173		
	B2	.106	-.525	.737	.737	
	B3	1.002	.317	1.687	.005	**p < 0.005**
Z(Ak21')	B1 (constant)	-.576	-1.097	-.056		
	B2	.406	-.213	1.025	.194	
	B3	1.235	.563	1.907	.001	**p < 0.005**
Z(ME')	B1 (constant)	-.452	-1.021	.118		
	B2	.481	-.197	1.158	.161	
	B3	.706	-.029	1.442	.059	
Z(IRE')	B1 (constant)	-.387	-.949	.175		
	B2	.295	-.374	.963	.381	
	B3	.794	.068	1.520	.033	**p < 0.05**
Z(WOS)	B1 (constant)	.468	-.091	1.027		
	B2	-.408	-1.073	.256	.223	
	B3	-.876	-1.598	-.155	.018	**p < 0.05**

Table 6-11 Standardised regression coefficients in the Breast Cancer Study (contrasts against Grade 1)

The results presented in Table 6-11 in demonstrate the degree of separation between Grade 2 and Grade 3 tumours and the measurements obtained in Grade 1 group, expressed through the standardised regression coefficients and their confidence limits. The estimated mean of variable Ak_{21}' in Grade 3 tumours is displaced from the estimated mean of Grade 1 tumours by 1.235 standard deviations whereas the separation between these two groups measured by variable k_{21}' is 1.002 standard deviations. These standardised regression coefficients can be directly compared to the standardised regression coefficients for BB variables (0.876 and 0.794 SD for WOS and IRE', respectively).

			95% CI			
		B	Lower	Upper	p-value	
Z(A')	B2 (constant)	.094	-.275	.463		
	B1	-.530	-1.213	.152	.125	
	B3	.045	-.551	.641	.880	
Z(k21')	B2 (constant)	-.252	-.593	.090		
	B1	-.106	-.737	.525	.737	
	B3	.895	.344	1.447	.002	**p < 0.005**
Z(Ak21')	B2 (constant)	-.170	-.505	.165		
	B1	-.406	-1.025	.213	.194	
	B3	.829	.287	1.370	.003	**p < 0.005**
Z(ME')	B2 (constant)	.029	-.338	.395		
	B1	-.481	-1.158	.197	.161	
	B3	.226	-.366	.818	.448	
Z(IRE')	B2 (constant)	-.092	-.454	.269		
	B1	-.295	-.963	.374	.381	
	B3	.499	-.085	1.084	.093	
Z(WOS)	B2 (constant)	.060	-.300	.419		
	B1	.408	-.256	1.073	.223	
	B3	-.468	-1.049	.113	.112	

Table 6-12 Standardised regression coefficients in the Breast Cancer Study (contrasts against Grade 2)

The results presented in Table 6-12 demonstrate the degree of separation between Grade 1 and Grade 3 tumours and the measurements obtained in Grade 2 group, expressed through the standardised regression coefficients and their confidence limits. The regression model presented in Eq. 6-2 was applied to standardised variables. The estimated mean of variable Ak_{21}' in Grade 3 tumours is displaced from the estimated mean of Grade 2 tumours by 0.829 standard deviations whereas the separation between these two groups measured by variable k_{21} is 0.895 standard deviations ($p < 0.005$ for both variables). The separation between Grade 2 and Grade 3 tumours based on BB variables, however, is not significant. Regression coefficients have markedly lower amplitudes when compared to PK variables k_{21} and Ak_{21} (0.499 and 0.468 for IRE' and WOS, respectively).

There was no significant association between QDEMRI variables and nodal status ($p>0.05$). Furthermore, groups with and without a significant in-situ component (DCIS) also did not

vary significantly ($p>0.05$). All differences were assessed by applying an independent samples t-test to transformed QDEMRI variable measurements.

Conversion of PK variables into K^{trans} and f_{ex}

If a constant pre-contrast value of $T1_0$ and a constant value of initial plasma concentration Cp(0) are assumed, the measurements of PK variables A and Ak_{21} can be converted into f_{ex} (fractional volume of the extracellular space EES) and K^{trans} (apparent capillary permeability). By assuming $T1_0$ of 876ms in invasive breast tumours (reported by Merchant [126]) and initial plasma concentration of 0.877 mM (after Tofts [69], see Section 3.3), the following values of f_{ex} and K^{trans} are obtained from the measurements of A and Ak_{21} obtained in this study:

	fex		Ktrans [1/min]	
	Mean	SD	Mean	SD
Grade 1 (n = 12)	.389	.126	.606	.276
Grade 2 (n = 29)	.459	.144	.913	.725
Grade 3 (n = 18)	.459	.107	1.409	.689

Table 6-13 Conversion of PK variables into f_{ex} and K^{trans}

These values are in good agreement with f_{ex} and K^{trans} values in invasive breast carcinomas reported by Tofts et al (K^{trans} of 0.1 – 1.2 min^{-1} and f_{ex} of 0.3 –0.8) [84], den Boer et al (K^{trans} of 1.05 ± 0.75 min^{-1} and f_{ex} of 0.47 ± 0.20)[102]. Whereas Tofts did not measure $T1_0$, den Boer included a pre-contrast measurement of $T1_0$ in their pharmacokinetic analysis. Our measurements of K^{trans} are somewhat higher than those obtained by Ikeda [104] (0.52 ± 0.22 min^{-1}) and Hulka [100, 101] (0.45 ± 0.22 min^{-1}) possibly as a result of different Cp(t) models. Both Ikeda and Hulka have modelled Cp(t) as a three-exponential function. Neither of these studies, however, included measurements of f_{ex} and K^{trans} in subgroups of invasive

cancers, defined by histological grade or nodal status. Furthermore, the proportion of high-grade tumours and tumours of different histological type will have influenced the mean values of K^{trans} and f_{ex} measured in all these studies.

6.4. Summary of the findings

In this study a significant correlation between permeability-related pharmacokinetic variables (k_{21} and Ak_{21}) and tumour grade in invasive breast cancer was found. No association was found between any of the QDEMRI variables and tumour nodal status or presence of DCIS.

A comparable measurement of permeability in different histological grades of human breast cancer has not, to our knowledge, been reported in the literature. Our measurements are in broad agreement with permeability-related measurements in invasive breast carcinomas in humans reported elsewhere in studies involving unspecified mix of histological grades and nodal involvement.

None of the measured QDEMRI variables varied significantly between Grade 1 and Grade 2 tumours. Whereas pharmacokinetic variables k_{21} and Ak_{21} varied significantly between Grade 1 and Grade 3 tumours as well as between Grade 2 and Grade 3 tumours, black-box variables IRE and WOS varied significantly only between Grade 1 and Grade 3 tumours and their overall association with tumour grade was not statistically significant. Analysis of standardised regression coefficients indicates that the variable Ak_{21} provides the greatest degree of separation between Grade 1 and Grade 3 tumours, whereas variable k_{21} demonstrated the largest difference between Grade 2 and Grade 3 tumours. Standardised regression coefficients of BB variables were consistently lower than those obtained for PK variables, suggesting the greater sensitivity of PK variables to differences in microcirculation between different tumour grades.

The reported lack of correlation between permeability measurements obtained using Gd-DTPA and tumour grade in experimental breast cancer studies is most probably due to the faster rate of overall circulation in small animal models which requires higher DEMRI temporal resolution in order to resolve extravasation rates of small Gd-DTPA molecule in highly permeable tumours.

Whilst it is not possible to trace all possible sources of discrepancy between the results presented in this study and other clinical studies where the relationship between tumour grade and BB quantifiers of DEMRI was investigated, one probable source of variability lies in the different acquisition sensitivity to underlying T1 changes. To illustrate theoretical T1 sensitivity of acquisition protocols used in this and other studies, normalised SI curves were generated assuming $T1_0$ of 1000 ms and T2* of 100 ms with $\alpha = 4.5$ and $\beta = 5.5$ mM-1 s^{-1} and acquisition parameters (TR/TE/φ) used in each individual study. The most T1 sensitive acquisition sequence was used by Stomper [141, 145] (Figure 6-8). However, their studies included only a small number of subjects and perhaps inadequate ROI selection and analysis, and the imaging volume encompassed only five contiguous slices. Fischer et al [143] conducted a large study but employed a sub-optimal acquisition protocol, with respect to both temporal resolution (1.5 minutes) and T1 sensitivity (Figure 6-8).

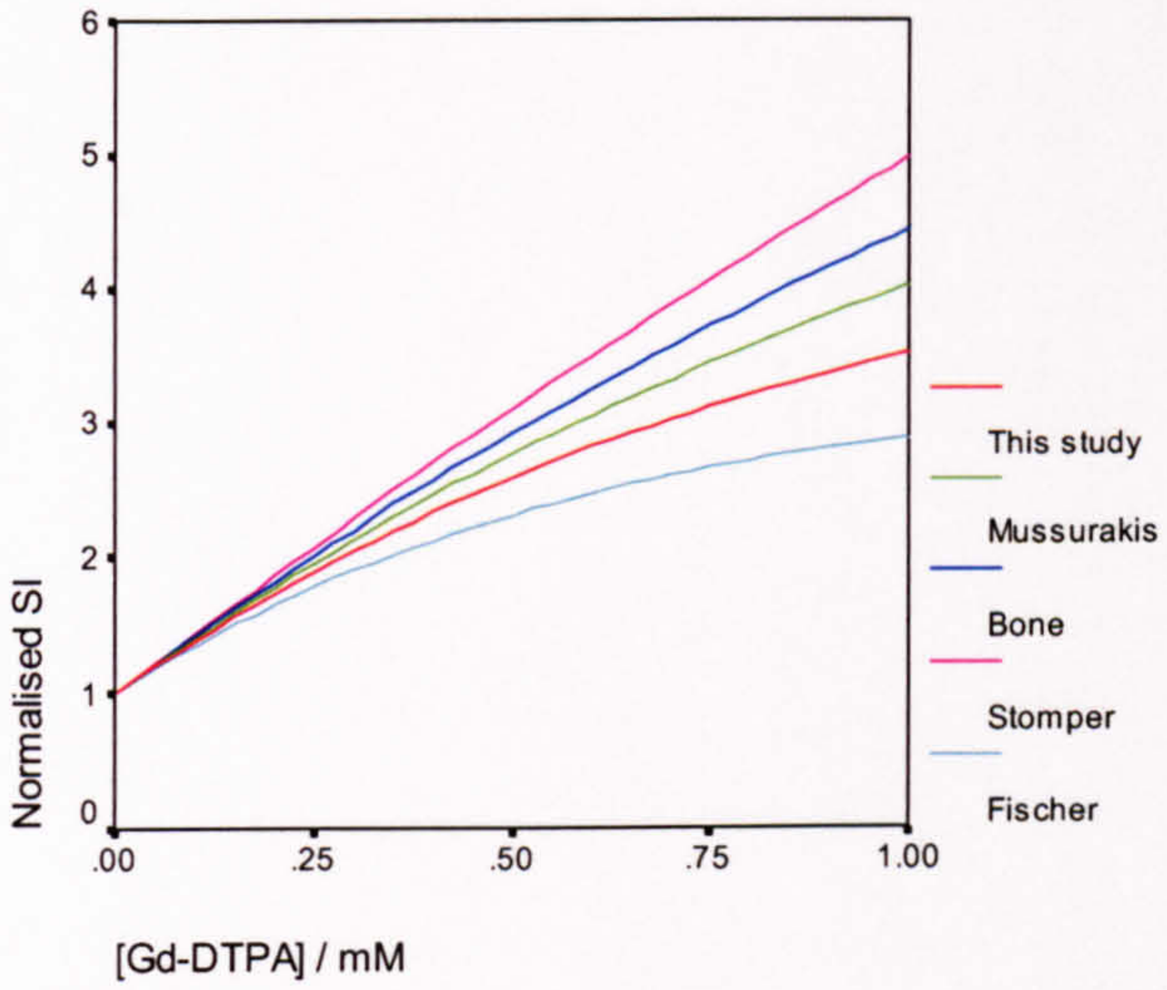

Figure 6-8 Comparison of T1 sensitivity of acquisition sequences

In two studies where simple enhancement ratios displayed significant association with tumour grade [142, 144] and nodal status [142], T1 sensitivity was somewhat higher than that achieved by our acquisition protocol (Figure 6-8). Their superior T1 sensitivity, however, was associated with concomitant loss of spatial coverage [142] and temporal resolution [144].

In summary, this study provided a compromise between the conflicting requirements for high temporal and spatial resolution, tissue coverage and T1 sensitivity all of which are important for determining the utility of breast cancer DEMRI examinations. The results presented in this chapter indicate that permeability-related PK variables obtained using QDEMRI analysis method described in this thesis do differ significantly between different tumour grades, in particular between low-grade (Grade 1 and 2) and high-grade (Grade 3) tumours, whereas simple BB indices do not. None of the measured QDEMRI variables, however, varied significantly between node-positive and node-negative lesions.

Chapter 7. Application to rheumatoid arthritis

Rheumatoid arthritis (RA) is a chronic, systemic, inflammatory disease characterised by the symmetric involvement of the synovial joints. It is brought about by the disruption of the autoimmune system, caused by an, as yet, unidentified mechanism. RA affects approximately 1% of the population [148]. Although the course of RA is variable, long-term follow-up studies have consistently shown that RA is characterised by poor outcome, with progressive structural joint damage and impairment of joint function as well as an increase in premature mortality [149]. RA is therefore no longer regarded as a benign disease and the aim of treatment is not only the control of symptoms but also the reduction of mortality and prevention of structural joint damage and disability. Furthermore, there is mounting evidence that an early, aggressive treatment of the RA can significantly improve the long-term outcome [150].

The pharmacological treatment of RA includes the administration of non-steroidal anti-inflammatory drugs (NSAIDs), disease modifying anti-rheumatic drugs (DMARDs) and possible introduction of low-dose glucocorticoids. The traditional "pyramidal" approach to treatment based on the initial treatment of symptoms (via NSAIDs and glucocorticoids) and gradual introduction of DMARDs has recently been abandoned in favour of more aggressive

treatment with DMARDs in early RA in the light of evidence that early intervention with DMARDs significantly improves the disease outcome [151, 152].

7.1. Angiogenesis in RA

In addition to the recognition of the importance of diagnosing and treating early RA and the mounting evidence that soft tissue inflammatory changes precede and indeed cause subsequent structural joint damage [153], it is now widely acknowledged that RA is an angiogenesis dependant disease as suggested by Folkman and others [1, 17, 154].

The primary sites of RA are diathroidal synovial joints although it is associated with a range of systemic manifestations [148]. Inflammatory soft tissue changes affect primarily the synovial lining of the joint capsule (synovial membrane or synovium, Figure 7-1). However, other peri-capsular structures are often inflamed.

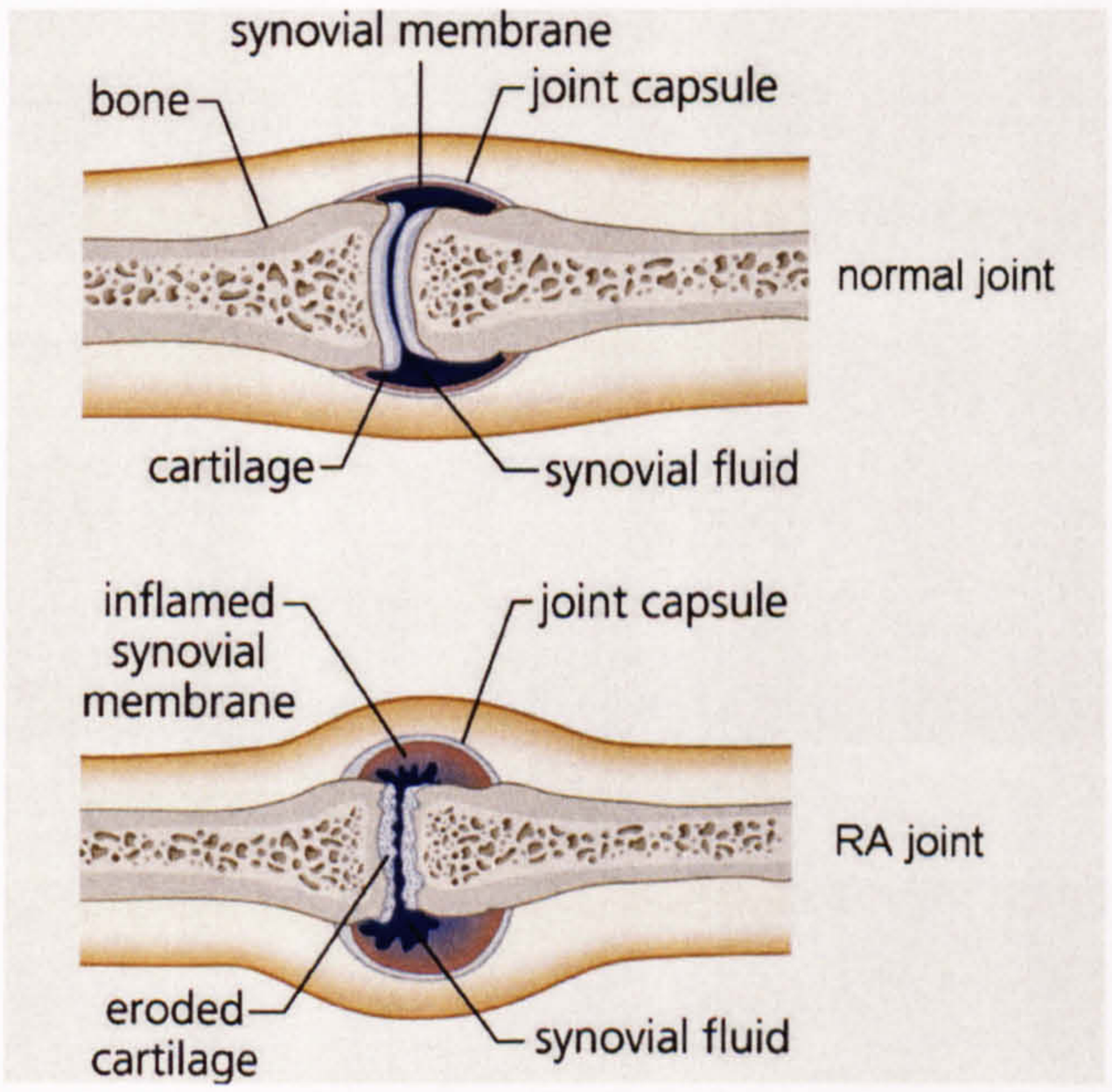

Figure 7-1 Alterations in synovial joints architecture in RA [155]

The joints affected by RA are characterised by the hyperproliferation of the synovium and the formation of hypervascular pathological tissue called pannus. Figure 7-1 illustrates the architectural changes in synovial joints affected by RA. The synovial membrane becomes thickened and inflamed. Hypertrophic synovium, together with a variable degree of joint effusion, contributes to clinical signs of joint swelling.

Pannus formation through angiogenesis is one of the earliest histopathological findings in RA [156]. Angiogenic pannus growth is thought to be central to the initiation of irreversible structural damage to the articular cartilage and subchondral bone in rheumatoid joints [157]. This neovascularisation is thought not only to maintain the chronic architectural changes of the pannus microvasculature but also to play an active role in the inflammation [154]. The alterations in the microvascular architecture resulting from the angiogenesis (including pre-existing vessel dilatation and new blood vessel formation) may facilitate the infiltration of the synovium by the inflammatory cells [158]. The factors specifically promoting angiogenesis in RA have not been identified. However, both synovial tissue and fluid are enriched in angiogenesis-promoting molecules [159, 160].

Many of the available treatments for RA have been shown to possess some degree of antiangiogenic activity [161, 162]. For example, methotrexate induced angiogenesis inhibition was demonstrated by Hirata et al [163]. Furthermore, in patients with active RA treated with glucocorticoid methylprednisolone alterations in pro-angiogenic cytokine TNF-alpha expression in the synovial membrane correlated with clinical response [164].

The recognition of the role of angiogenesis in RA has prompted the research into the formulation of specific anti-angiogenic therapies for RA. The research into the role of pro-angiogenic cytokine TNF-alpha in RA [165] led to the formulation of a new class of anti-rheumatic drugs: biological anticytokine agents. Infliximab and etanercept are anti TNF-alpha antibodies that have been proven to reduce the symptoms of RA in patients with

highly active disease [166, 167]. Both infliximab and etanercept have been shown to arrest structural joint damage in large scale randomised controlled clinical trials [168, 169]. Furthermore, it has been shown that synovial blood vessels from RA patients show increased expression of integrin αvβ3 [170, 171] which is a potent angiogenesis marker [172, 173]. A study of the effect of the intra-articular administration of integrin αvβ3 antagonist in an animal model of arthritis was shown to lead to the inhibition of synovial angiogenesis, as well as a reduction in joint swelling, synovial infiltrate, and pannus formation, in both early and well-established arthritis leading to significant protection against the development of cartilage erosions [174].

These encouraging advances in the field of pharmacological treatment of RA have underlined the need to address the methods used for diagnosis, so that this disease can be treated in its early, potentially reversible stage. A multitude of new therapeutic agents that target synovial microvasculature are being developed and their effective evaluation would benefit from sensitive, objective and quantitative assessment of synovitis in RA, thus shortening the process of pre-clinical testing. Proof-of-concept studies could be carried out using a small number of subjects, over a short time period if an effective tool for measuring sub-clinical changes in synovitis was available. Furthermore, due to the high cost of these emerging therapies, an objective method for pre-treatment assessment of RA may facilitate effective targeted selection of patients who are most likely to benefit from the treatment with particular drugs.

Contrast-enhanced MRI has been put forward as one of the candidates for the fulfilment of this role. Both static and dynamic Gd-DTPA enhanced MRI have been applied for the assessment of disease activity in RA (Section 7.2). MRI applications in RA include characterisation of synovitis (inflammation of the synovial lining of the joints) as well as the assessment of bone damage. There is evidence to suggest that MRI is superior to conventional radiography in demonstrating the extent of bone damage, particularly in early

RA [175]. Furthermore, Gd-DTPA enhanced MRI appears to be superior to clinical assessment in diagnosing early RA [176].

Quantitative analysis of Gd-DTPA uptake in RA has been shown to be feasible and the results presented in the literature suggest a close link between the histological markers of inflammation and Gd-DTPA induced SI changes in MRI. The argument is being put forward that contrast enhanced MRI, due to its sensitivity to pathologic features of RA, as well as its non-invasiveness and favourable spatial and temporal resolution, should be considered as a new gold standard for the assessment of RA [177].

7.2. Quantitative analysis of contrast enhanced MRI in RA

Since the publication of the first images of the human wrist by Hinshaw in 1977 [54], MRI has revolutionised the practice of musculoskeletal radiology [44]. The potential utility of MRI in the assessment of RA has been suggested by Hull [128], Beltran [178] and others [179-181]. The introduction of MRI contrast agents has provided a major impetus for the development of MRI applications in this area. Whereas on conventional non-contrast MRI different joint structures (such as joint effusion, synovitis, intraarticular pannus, subchondral sclerosis, and subchondral pannus) have similar signal intensities, and cannot be reliably differentiated from one another [178, 182], Gd-DTPA enhanced MRI allows the visualisation of hyperthrophic synovium in RA [179, 180, 182], since it selectively enhances only perfused tissues with high capillary permeability and high local distribution volume.

The direct link between the Gd-DTPA-induced MRI signal intensity enhancement and the degree of inflammatory activity stems from the fact that cardinal features of inflammation include increased vascularity, capillary permeability and tissue oedema, all of which have a direct influence on the local pattern of uptake of Gd-DTPA [64].

Different approaches to quantitative measurement of disease activity in RA based on contrast enhanced MRI include static, volumetric assessment of the synovial lining volume through the analysis of subtraction (post-pre contrast) T1-weighted images [183-189] and the analysis of the temporal pattern of enhancement in DEMRI through the computation of enhancement indices derived from manually selected ROIs [179, 183, 184, 190-194].

Whereas quantitative assessment of synovial volumes from static Gd-DTPA enhanced MRI has been studied in the knee [183, 184, 187, 189], wrist [185, 186] and finger joints [188], quantitative analysis of DEMRI has to date been limited to the study of knee joints.

Static contrast enhanced MRI in the assessment of RA

MRI-derived volumes of synovial tissue have been shown to reflect the changes in disease activity following intra-articular treatment with glucocorticoids [183, 184, 195] and radiation synovectomy [187]. The measurement of pannus volume using static Gd-DTPA enhanced MRI in rheumatoid wrists was compared to the findings of F-18 Fluorodeoxyglucose (FDG) Positron Emission Tomography (PET). MRI-derived pannus volume correlated strongly with the FDG uptake, thus confirming that the extent of Gd-DTPA enhancement reflects the metabolic changes in joint inflammation [186]. Østergaard et al have found a significant correlation between the measurements of synovial volume and histological markers of inflammation [189]. However, in their subsequent report, they found that quantitative DEMRI measurements correlated with histology more closely than the measurements obtained from static MRI [193].

Correlation of DEMRI findings with histology in RA

A number of research groups have assessed the correlation between the findings of DEMRI and histological markers of inflammation in RA. König et al [179] demonstrated the link

between the initial rate of Gd-DTPA uptake in rheumatoid knees and the vascularity of synovitis, determined by histological analysis of synovial specimens. They have also demonstrated the capacity of quantitative measures of maximal enhancement and the time of maximal enhancement to distinguish between vascular and fibrous pannus. Tamai et al [194] provided further histological evidence that DEMRI reflects the degree of local disease activity in RA by demonstrating that the degree of enhancement was greater in synovial regions with a higher degree of fibrin exudation, cellular infiltration, villous hypertrophy, vascular proliferation, and granulation formation in synovial specimens from rheumatoid knees. Gaffney et al analysed the relationship between both qualitative [191] and quantitative [190] histological features of synovial samples in RA and the initial rate of enhancement of DEMRI in the acute synovitis of knee joints. They have found that the initial rate of enhancement correlated with qualitative histological score of acute inflammation but not with clinical or laboratory findings [191]. In their subsequent publication, they have reported a significant correlation between the initial rate of enhancement and the blood vessel numerical density as well as the blood vessel fractional area [190]. Østergaard et al also found that initial rate of enhancement was correlated with histological features of active inflammation such as vessel proliferation and mononuclear leukocyte infiltration [193].

DEMRI in the assessment of treatment effectiveness in RA

In addition to the work described above (where DEMRI was used in the RA lesion characterisation), quantification of DEMRI in RA has also been used as a method for the measurement of treatment effectiveness [183, 184, 192]. Østergaard et al have suggested that quantitative analysis of DEMRI in RA may be used to monitor the response to therapy and demonstrated the effect of intra-articular methylprednisolone injection in rheumatoid knees over a period of 180 days [192]. A decrease in measured initial rate of enhancement was detected within a week of the administration of IACS. However, the measured IRE regained

pre-treatment levels at the six months follow-up. Creamer et al [184] reported a significant reduction in the maximal enhancement and the initial rate of enhancement in RA knees treated with intra-articular corticoid triamcinolone hexacetonide as early as one week after treatment. In one study [183], quantitative DEMRI findings (maximal enhancement and time of maximal enhancement) were found to be unrelated to the clinical outcome.

Pharmacokinetic modelling of DEMRI in arthritis and inflammation

Pharmacokinetic analysis of DEMRI in human studies of RA has not been reported to date. However, PK-QDEMRI was applied in animal models of arthritis [196, 197] and inflammation [198]. A macro-molecular blood-pool contrast medium (albumin-(Gd-DTPA)$_{30}$, [199]) was used instead of Gd-DTPA. Van Dijke et al reported a significant difference between the permeability surface area product (PS) in sham-treated and antigen-challenged temporomandibular joints in rabbits, but found no differences between the measurements of plasma volume (PV) [196]. These findings were similar to those obtained by the same research group in a study of knee joint arthritis in rabbits. Again, measurements of PS were correlated with histological score but PV values were found not to be significantly associated with histological assessment of synovitis. Demsar et all [198], who studied a different animal model of inflammation (an intramuscular sterile abscess in Fischer rats) using the same MMCM technique reported a good discrimination between inflamed tissues and surrounding parenchyma based on spatially mapped PS, but not PV values.

7.3. Study description

The studies currently reported in the literature where DEMRI was utilised for the assessment of disease activity and therapeutic response in RA have provided valuable information about the link between DEMRI findings and disease activity in RA. However, the methods used

for quantitative analysis utilised in these studies include a significant degree of subjectivity and are therefore not suitable for objective, user-independent assessment of disease activity in RA. The lack of standardisation in this area has contributed to the fact that, despite initial promise, quantitative analysis of DEMRI is still not effectively used in the assessment of disease activity, response to treatment or the investigation of the aetiology of RA.

Black-box analysis of DEMRI in RA

In all clinical studies published to-date, quantitative analysis of DEMRI in RA was performed using manually selected ROIs and individual SI/time curves were characterised through a range of black-box variables (maximal enhancement, initial rate of enhancement, time to maximal enhancement). The normalisation to pre-contrast SI was performed in some of these studies [183, 192, 193], but not in others [184, 190, 191], thus rendering their findings applicable only within their individual experimental setting. The measurement of the initial rate of enhancement and maximal enhancement was based on visual inspection of individual SI/time curves and no attempt has been made to automate this process and make it insensitive to random fluctuations in SI. The identification of the temporal location of the initial linear phase of enhancement was also made subjectively.

The problems associated with discrete sampling of often highly heterogeneous synovial tissue were highlighted in a study by Østergaard et al [193] and the strongest degree of correlation with histological markers of inflammation was found when the complete DEMRI volume was included in the analysis. Furthermore, this study demonstrated the importance of the measurement of the initial rate of Gd-DTPA uptake in the period between 30 seconds and 1 minute post-injection, since the measurements obtained within this time frame displayed the highest degree of correlation with histological findings. The measurement of the time of maximal enhancement, proposed as an indirect measure of the rate of

enhancement by Clunie et al [183] is limited by the existence of a long plateau of enhancement present in synovial tissues, as demonstrated by Yamatto et al [200].

In this thesis, the measurement of black-box variables ME and IRE was performed using moving-window algorithms described in Section 4.3 and their implementation in RA studies was presented in Chapter 5. These algorithms enable voxel-by-voxel sampling of the normalised SI/time curves throughout the entire enhancing volume in an automated fashion, without the need for user-interaction. The location of the steepest gradient of the normalised SI/time curve (initial rate of enhancement, IRE) is detected automatically, as well as the maximal amplitude of enhancement (ME). This method is thus suitable for an objective, global assessment of disease activity in RA. Parametric colour-coded maps of variables used for quantification of Gd-DTPA enhancement enable the high-resolution analysis of the spatial distribution of the inflamed synovium, whereas quantitative, histogram-based measurements representing the overall measure of disease activity allow the monitoring of treatment effects. An automated method for the measurements of BB variables in rheumatoid knees was reported earlier by our research group [201]. However, the sampling was not performed on a voxel-by-voxel basis. Manually selected ROIs were used for the evaluation of enhancement.

Furthermore, the quantitative analysis of DEMRI in MCP joints has not been reported to-date although these joints are particularly important for the assessment of the early RA since they are often the first joints to be affected by RA [202].

PK analysis of QDEMRI in RA

Macro-molecular contrast media (MMCM) used for the pharmacokinetic analysis of DEMRI in animal models of arthritis [196, 197] and inflammation [198] were not available for clinical applications. It has been argued that MMCM allow a more precise discrimination between

normal and abnormal microvasculature due to the larger size of the MMCM molecules compared to small, extracellular agent such as Gd-DTPA [196-198]. Whilst it seems reasonable to suggest that the measurement of permeability surface area product by MMCM enhanced DEMRI is likely to be more specific [203], it is possible that it may not be sufficiently sensitive to reveal the changes in microcirculation that occur in early RA.

In MMCM enhanced DEMRI, the fractional plasma volume (PV) is measured rather than the fractional volume of the EES (f_{ex}). This presents a major limitation of this approach, because blood plasma volume may not correlate with the degree of inflammation in arthritic lesions in contrast to the volume of the extracellular space [204]. The authors indeed note that their parameter PV does not correlate with the histological features of inflammation and does not provide sufficient discrimination between the lesion and the surrounding parenchyma [196-198]. Furthermore, this method of measuring PS requires long DEMRI acquisitions (30 minutes [196, 197] or even 60 minutes [198]) and simultaneous sampling of Cp(t), making it less suitable for clinical applications.

Pharmacokinetic modelling of Gd-DTPA enhanced MRI in RA has not been reported to date. This work therefore presents the first attempt to apply PK modelling of Gd-DTPA kinetics in clinical studies of RA.

In this thesis, QDEMRI analysis (including both black-box and pharmacokinetic analysis) was applied in two randomised clinical studies where the effectiveness of the treatment with methotrexate was compared to that of methotrexate with concurrent administration of intra-articular steroid (IACS) methylprednisolone (The Hand RA Study) or leflunomide (LEF), in a study of RA of the knee (The Knee RA Study). A summary of the therapies which were assessed by QDEMRI in two RA studies is presented in Table 7-1 below.

	Treatments studied
The Hand RA Study	MTX vs MTX+IACS
The Knee RA Study	MTX vs LEF

Table 7-1 Summary of the investigated treatments in RA studies

The patients treated with methotrexate (MTX), which is the most commonly used conventional DMARD which suppresses cytokine production in RA [205], provided control groups in both trials, because placebo control was ruled out due to ethical considerations.

Whilst these treatments are not specifically targeted to suppress angiogenesis in RA, all of them have been shown to possess a degree of anti-angiogenic effect [163, 164, 206, 207]. The documented difference in the timing of action of these therapies provided the framework for implicit validation of QDEMRI measurements. Whilst MTX is a slow-acting DMARD, intra-articular administration of steroids in rheumatoid knees was shown to result in rapid (within one week) reduction in synovitis [184, 192].

Leflunomide (LEF), is a novel immunomodulatory DMARD (pyrimidine synthesis inhibitor) that has been shown to be effective in treatment of RA [208]. It has been shown to be equivalent to other established DMARDs (methotrexate and sulfasalazine) in terms of its capacity to reduce symptoms of RA and retard disease progression [209-212]. Furthermore, LEF has a somewhat faster onset of action than MTX. In a study of 482 RA patients conducted by Strand et al [209], the onset of effect occurred at a mean of 8.6 weeks in patients treated with LEF compared with 9.5 weeks for those treated with MTX.

The application of this method in a clinical study comparing the effect of fast acting intra-articular injection of steroid and slow acting methotrexate in a study of MCP joints (the Hand RA Study) provided a framework for implicit validation of the findings of PK analysis. In particular, the measurements of variable A, which according to the theoretical

pharmacokinetic model reflects the fractional volume of the EES (f_{ex}), were expected to reflect the changes instituted by the administration of IACS. The results of QDEMRI analysis performed in this study are presented in Section 7.4

A possible differential effect of leflunomide versus methotrexate in rheumatoid knees was investigated in the second randomised clinical study (the Knee RA Study). The results of the BB analysis, performed using an earlier version of the methodology presented in this thesis were presented by our research group [213]. In this thesis, additional measurements of PK variables were performed to compare the findings of BB and PK analysis. The results of QDEMRI analysis performed in this study are presented in Section 7.5.

7.4. Hand RA Study

7.4.1. Study description

This randomised study was designed to examine the effects of two therapies with different times of the onset of action on the degree of synovitis and formation of bone erosions in MCP joints (MCPJs) in patients with early RA. Whereas the primary aim of the work presented in this thesis was the application of QDEMRI analysis for the assessment of synovial Gd-DTPA uptake, the qualitative analysis of synovial enhancement and bone erosions was performed by Conaghan et al [214]. The two therapies under investigation were a slow acting disease modifying drug (DMARD) methotrexate (MTX) and methotrexate with intra-articular injections of corticosteroid methylprednisolone (MTX+IACS), where IACS component of therapy induces rapid reduction in synovitis. The institutional review board provided ethical approval for this study and written informed consent was obtained from all patients.

The MCPJs were studied in forty previously untreated consecutive patients recruited from an early arthritis clinic, all of whom were diagnosed with rheumatoid arthritis according to the revised American Rheumatism Association (ARA) criteria [215]. In the first stage (0-3 months), patients were randomised to receive either methotrexate alone (MTX group) or MTX and intra-articular corticosteroids into all clinically active joints (MTX+IACS group). The MTX group received no further corticosteroids until the second stage (3-12 months) when both groups received standard therapy (with continuing MTX dose escalation and intra-articular and intra-muscular corticosteroid as routinely indicated). DEMRI scans of the dominant hand were performed immediately before the start of treatment (baseline Scan 1) and at three and twelve months after the start of treatment (Scan 2 and Scan 3, respectively) according to the protocol described in Section 5.1.2.

Thirty-seven patients successfully completed the first stage of the study (baseline and three months follow-up). Out of this group of thirty-seven patients, thirty-two completed the second stage of the study (twelve months follow-up). QDEMRI analysis was performed in thirty-seven patients where at least the first follow-up scan was available.

The disease duration varied between 2 and 11 months (median 5.5 months). None of these patients received any DMARDs prior to the enrolment into the study. The median age was 59 years (range: 21 to 83 years). Twenty-one patients were female and sixteen were male. MTX group consisted of 17 patients and MTX + IACS group consisted of 20 patients.

Both patient groups were started on an identical methotrexate treatment regime following the baseline clinical and laboratory assessment and baseline DEMRI scan (Scan 1). They received 7.5mg of methotrexate per week initially rising to 12.5 mg per week for twelve weeks. In addition to this MTX + IACS patients received methylprednisolone injections immediately after the baseline examinations. All clinically active joints were injected, with the dose ranging from 10mg for small joints to 40mg for larger joints. The first follow-up

DEMRI scan was performed at three months (Scan 2). In the second stage of the study (3-12 months) both patient groups received an identical, standard treatment as described above. The second follow-up DEMRI scan (Scan 3) was performed at the end of the stage two (at twelve months after the start of therapy).

7.4.2. Summary of the measurements

All DEMRI scans were analysed on a voxel-by-voxel basis following the procedure described in Chapter 5. The entire DEMRI volume (apart from MCPJ1) was included in the analysis. Seven QDEMRI variables were measured in each DEMRI set including two black-box parameters (IRE and ME) and three pharmacokinetic parameters (A, k_{21}, Ak_{21}) as well as two voxel counts N-BB and N-PK obtained by counting all voxels included in the black-box and pharmacokinetic analyses, respectively. All measurement units are listed in Appendix A. QDEMRI analysis was performed blinded to the treatment allocation and the order of scans. After obtaining the treatment allocation key, the variables were arranged in treatment and visit groups, thus forming six sub-groups. They were labelled as follows:

MTX (1)	baseline scan in the MTX group (n = 17)
MTX (2)	3 months follow-up in the MTX group (n = 17)
MTX (3)	12 months follow-up in the MTX group (n = 16)
MTX+IACS (1)	baseline scan in the MTX+IACS group (n = 20)
MTX+IACS (2)	3 months follow-up in the MTX+IACS group (n = 20)
MTX+IACS (3)	12 months follow-up in the MTX+IACS group (n = 16)

A total of 106 DEMRI studies were analysed. A summary of the measurements is presented in Table 7-2 to Table 7-4 and Figure 7-2 to Figure 7-8. Means and standard deviations of seven measured parameters in each of the six scan groups are presented in Table 7-2 (voxel counts), Table 7-3 (pharmacokinetic parameters) and Table 7-4 (black-box parameters).

	N-PK		N-BB	
	Mean	SD	Mean	SD
MTX (1) (n = 17)	3.66E+04	1.21E+04	3.84E+04	1.21E+04
MTX (2) (n = 17)	3.58E+04	1.42E+04	3.73E+04	1.47E+04
MTX (3) (n = 16)	2.51E+04	9.63E+03	2.61E+04	9.87E+03
MTX+IACS (1) (n = 20)	3.44E+04	1.35E+04	3.57E+04	1.40E+04
MTX+IACS (2) (n = 20)	2.17E+04	1.34E+04	2.26E+04	1.37E+04
MTX+IACS (3) (n = 16)	2.19E+04	9.44E+03	2.30E+04	9.79E+03

Table 7-2 Summary of voxel counts measurements in the Hand RA Study

	A [s-1]		k21 [s-1]		Ak21 [s-2]	
	Mean	SD	Mean	SD	Mean	SD
MTX (1) (n = 17)	7.19E-02	1.68E-02	3.98E-02	5.78E-03	2.19E-03	4.72E-04
MTX (2) (n = 17)	6.90E-02	1.92E-02	3.86E-02	7.08E-03	2.07E-03	5.87E-04
MTX (3) (n = 16)	5.41E-02	1.28E-02	3.73E-02	5.56E-03	1.51E-03	3.92E-04
MTX+IACS (1) (n = 20)	7.22E-02	1.64E-02	3.58E-02	6.28E-03	1.97E-03	4.18E-04
MTX+IACS (2) (n = 20)	5.59E-02	1.84E-02	3.87E-02	8.91E-03	1.60E-03	4.48E-04
MTX+IACS (3) (n = 16)	5.03E-02	1.39E-02	3.87E-02	8.18E-03	1.43E-03	2.33E-04

Table 7-3 Summary of pharmacokinetic parameters measurements in the Hand RA Study

	ME		IRE [s-1]	
	Mean	SD	Mean	SD
MTX (1) (n = 17)	1.93E+00	2.20E-01	3.09E-02	6.61E-03
MTX (2) (n = 17)	1.87E+00	2.28E-01	2.88E-02	7.94E-03
MTX (3) (n = 16)	1.68E+00	1.45E-01	2.24E-02	5.18E-03
MTX+IACS (1) (n = 20)	1.89E+00	1.80E-01	2.77E-02	5.34E-03
MTX+IACS (2) (n = 20)	1.69E+00	1.91E-01	2.23E-02	5.36E-03
MTX+IACS (3) (n = 16)	1.62E+00	1.42E-01	2.07E-02	4.28E-03

Table 7-4 Summary of black-box parameters measurements in the Hand RA Study

To illustrate the distribution of measured QDEMRI variables, the differences between the measurements at different points during the treatment cycle and in different treatment groups, the values of individual measurements are presented in scatter plots and the

corresponding summary error bar plots (Figure 7-2 to Figure 7-8). Error bar plots represent the mean of each individual cluster and two standard error (SE) limits.

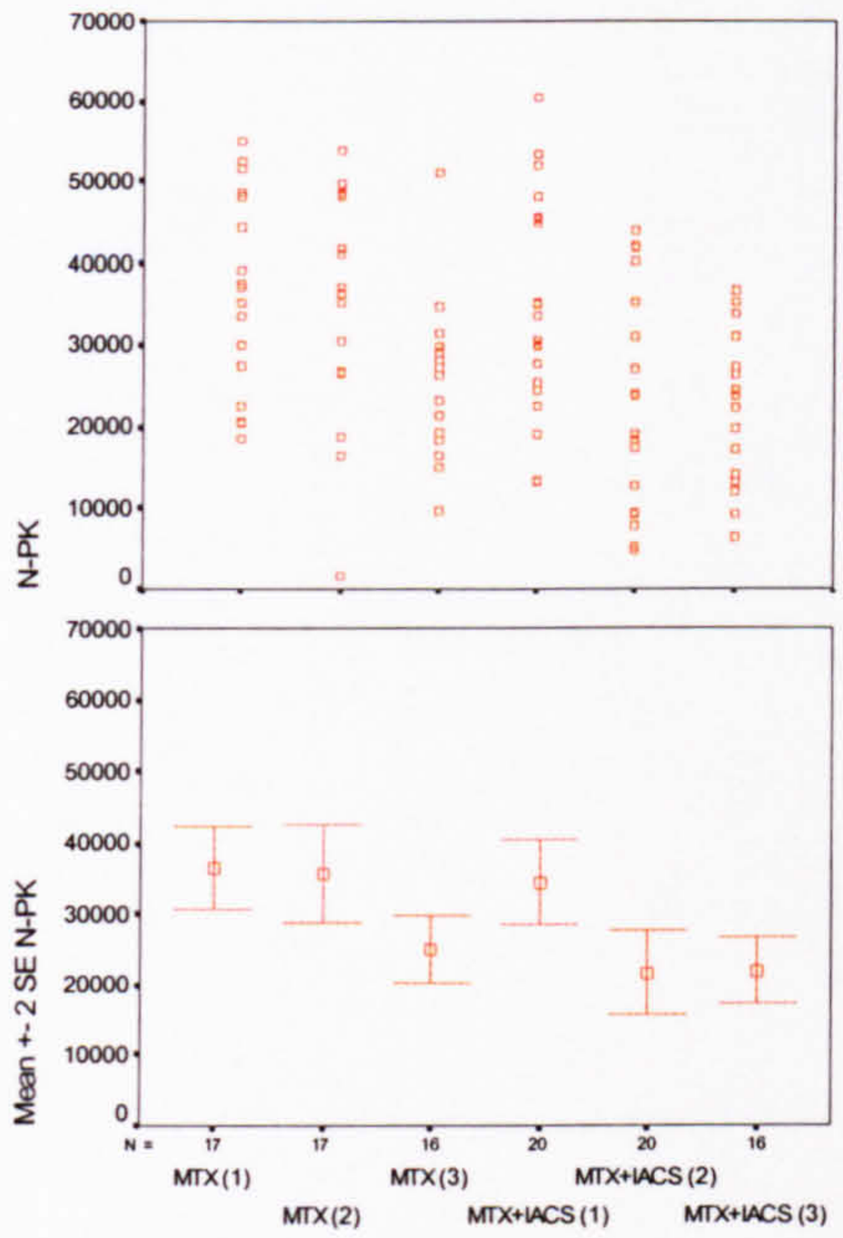

Figure 7-2 Distribution of variable N-PK in the Hand RA Study

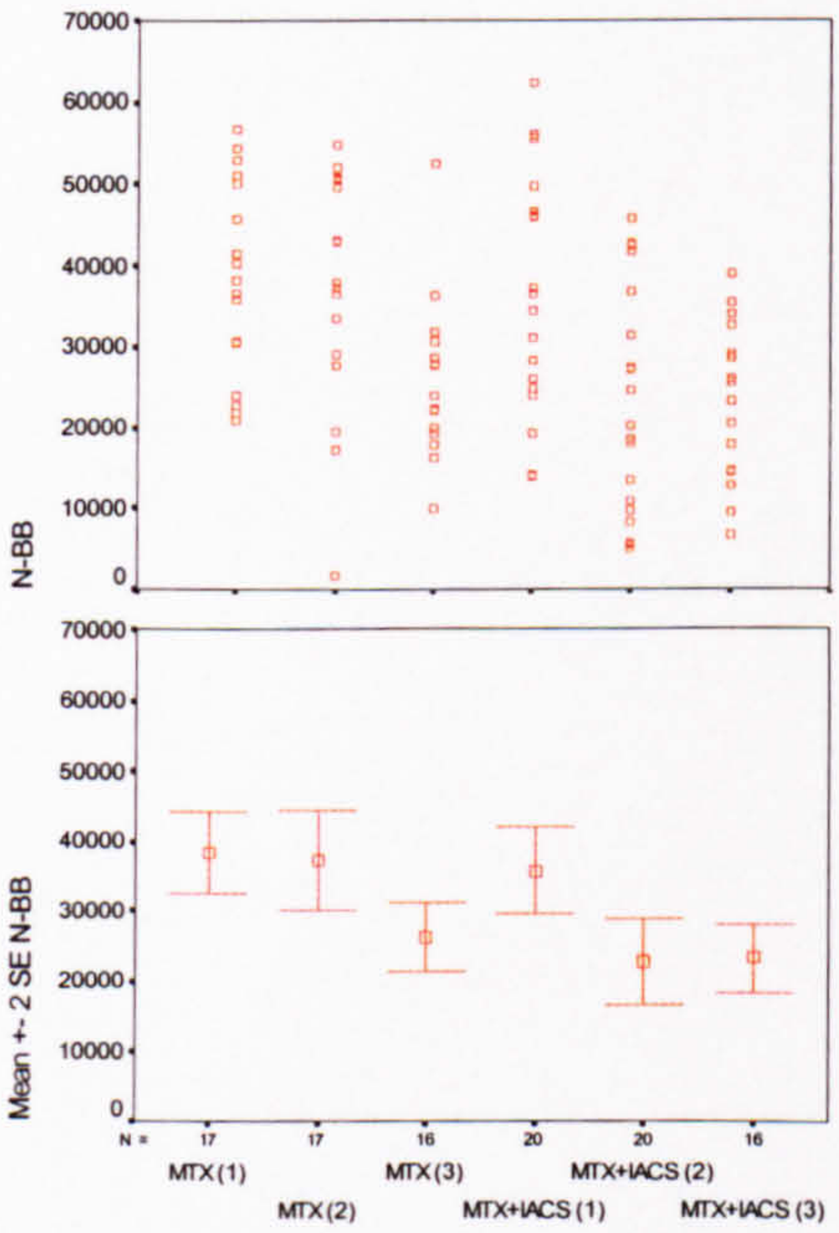

Figure 7-3 Distribution of variable N-BB in the Hand RA Study

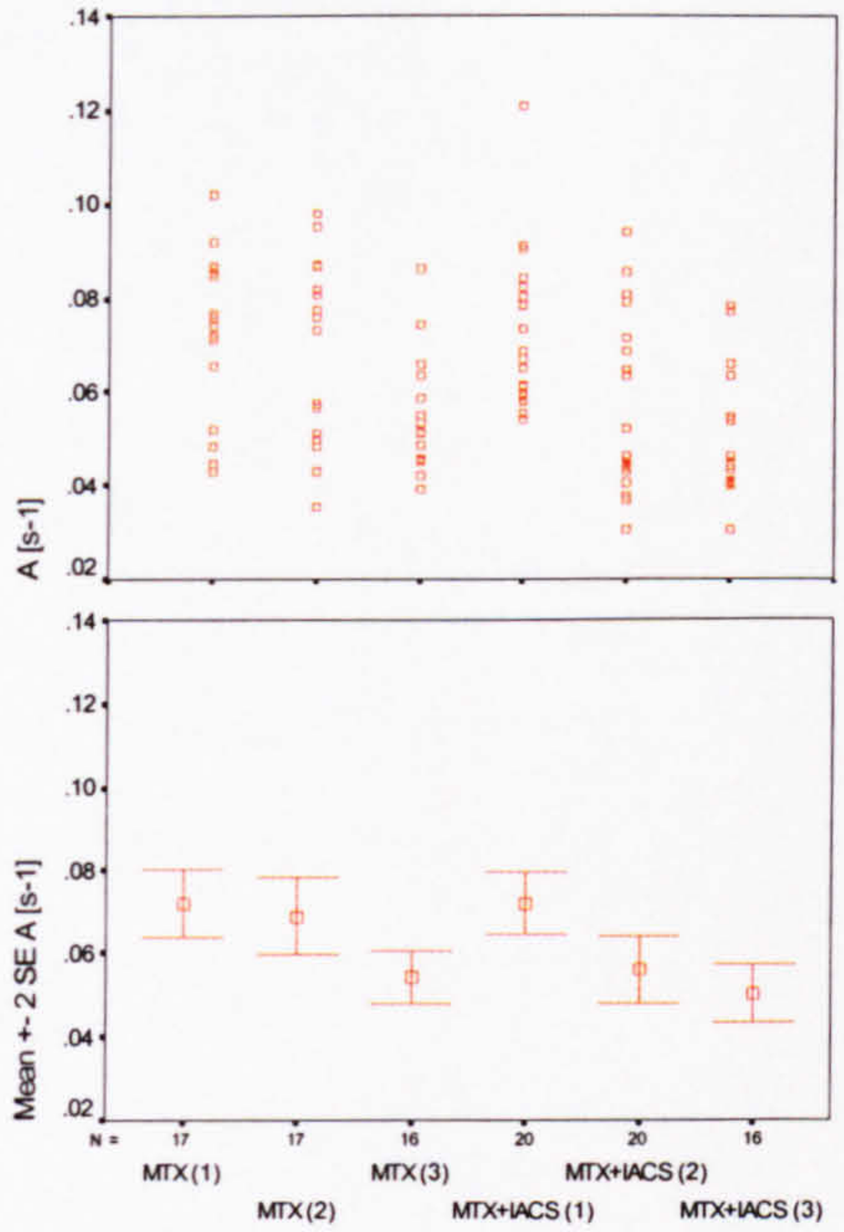

Figure 7-4 Distribution of variable A in the Hand RA Study

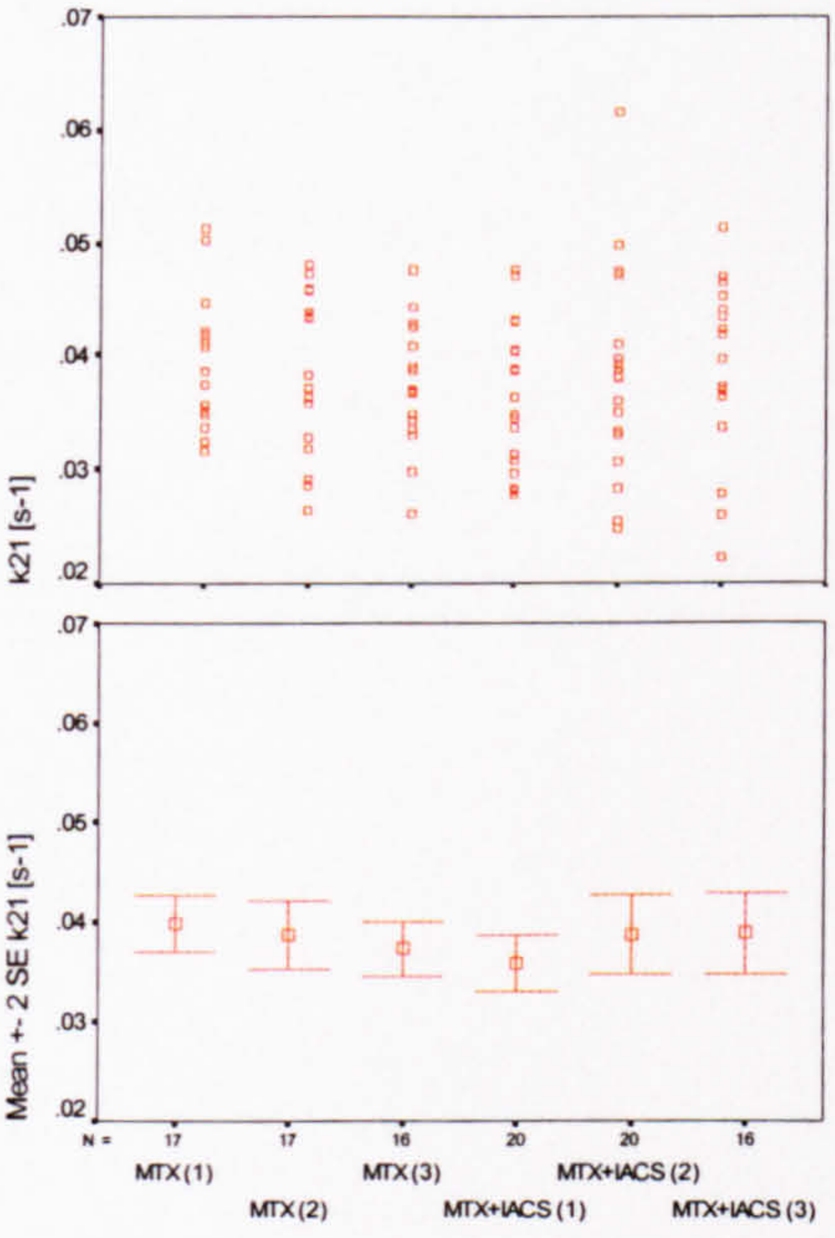

Figure 7-5 Distribution of variable k_{21} in the Hand RA Study

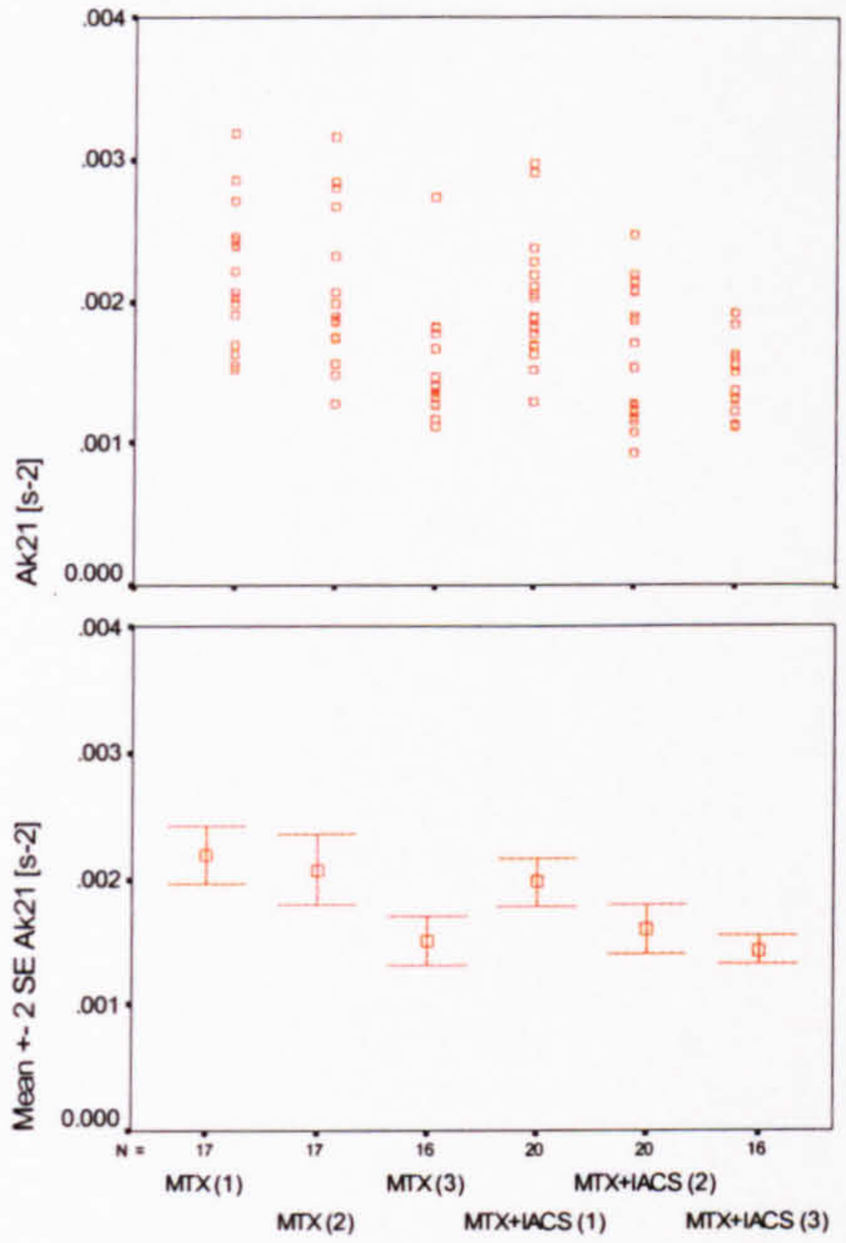

Figure 7-6 Distribution of variable Ak_{21} in the Hand RA Study

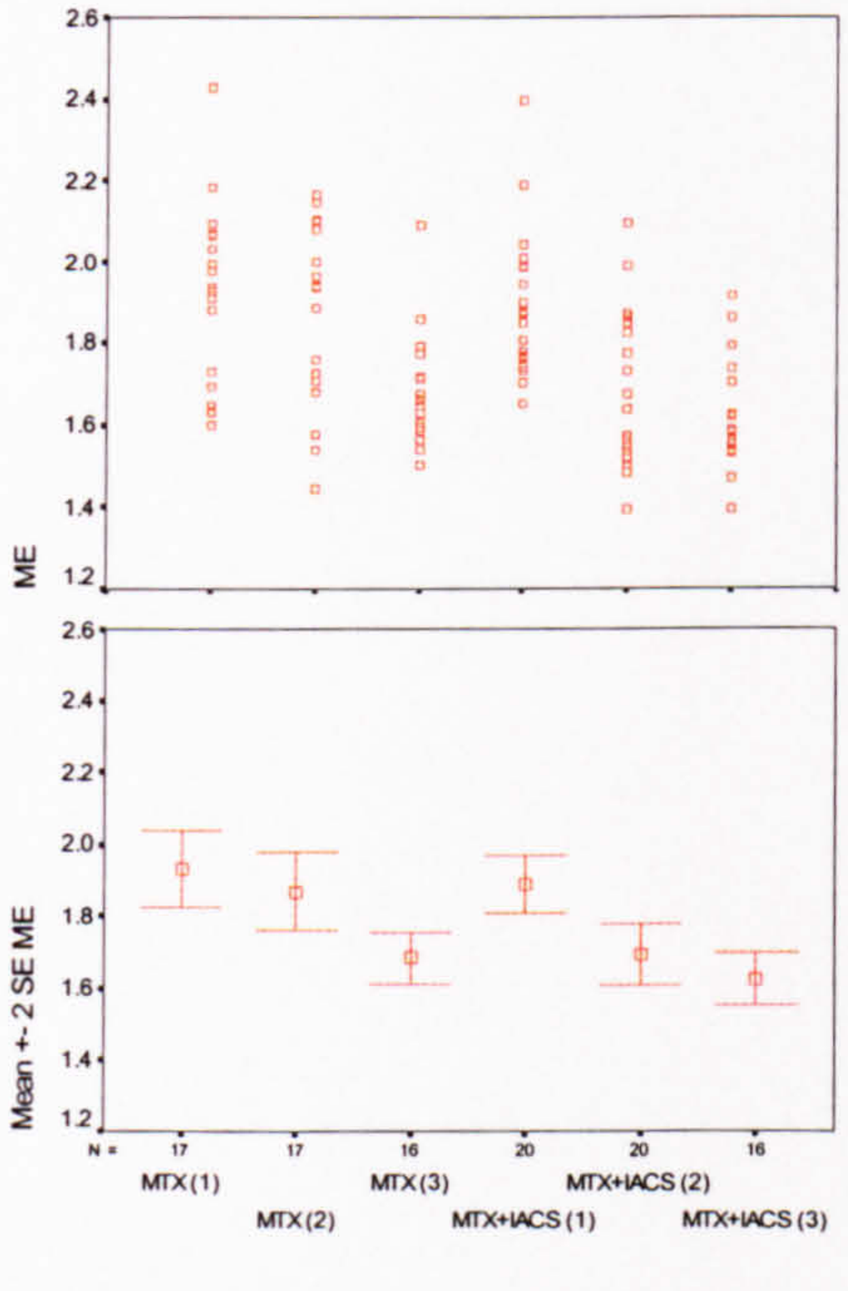

Figure 7-7 Distribution of variable ME in the Hand RA Study

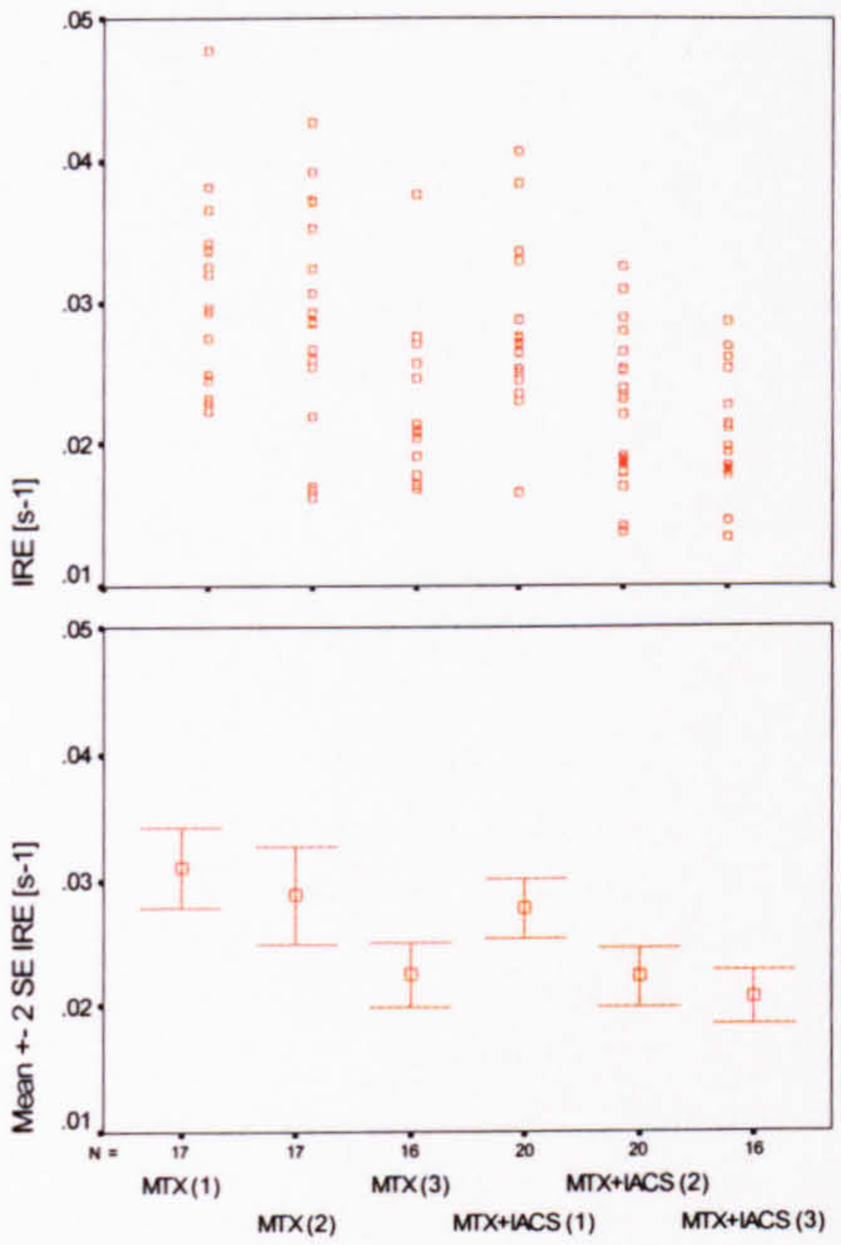

Figure 7-8 Distribution of variable IRE in the Hand RA Study

7.4.3. Statistical analysis

SPSS statistical software package (Version 10.0, SPSS, Chicago, IL) was used for statistical analysis. All statistical tests were performed at $\alpha = 0.05$ confidence level. A preliminary analysis of the distribution of measurements of each of the seven QDEMRI variables revealed no significant deviation from normality in six scan subgroups. This analysis was performed on 42 sets of measurements (seven variables divided into six scan subgroups) with the sample size ranging from 16 to 20. The results of the Kolmogorov-Smirnov test for normality are listed in Appendix C. No significant departure from normality was detected by this test, and the differences between individual QDEMRI variables subgroups were analysed by using tests for normally distributed variables (at $\alpha = 0.05$ confidence level).

Baseline measurements

The analysis of baseline measurements revealed no statistically significant differences between two treatment groups. Parameter k_{21} was, however, marginally elevated in the MTX group (p = 0.051). The results of an independent t-test for the differences in means are presented in Table 7-5.

	t-test for Equality of Means			
			95% Confidence Interval of the Difference	
	p-value	Mean Difference	Lower	Upper
N-PK (1)	.611	2.16E+03	-6.38E+03	1.07E+04
N-BB (1)	.526	2.74E+03	-5.96E+03	1.14E+04
A (1)	.951	-3.38E-04	-1.15E-02	1.08E-02
k21 (1)	.051	4.01E-03	-1.75E-05	8.04E-03
Ak21 (1)	.142	2.22E-04	-7.86E-05	5.23E-04
ME (1)	.530	4.25E-02	-9.38E-02	1.79E-01
IRE (1)	.121	3.19E-03	-8.90E-04	7.27E-03

Table 7-5 Analysis of baseline measurements in the Hand RA Study (MTX vs. MTX+IACS)[1]

Repeated measures ANOVA

Following the analysis of baseline measurements of QDEMRI variables, the analysis of treatment-induced changes was performed by applying repeated measures ANOVA test on the measurements obtained in the two treatment groups at three points during the course of the treatment. The results are summarised in Table 7-6 and Table 7-7 below. The results of this analysis confirm that the observed pattern of changes in QDEMRI variables over the course of treatment is indeed statistically significant for all variables apart from k_{21}.

[1] Mean Difference = Mean (MTX) – Mean (MTX+IACS)

	F	p-value	
N-PK MTX	12.304	.000117	p<0.0005
N-BB MTX	13.298	.000068	p<0.0001
A MTX	15.480	.000022	p<0.00005
k21 MTX	.765	.473974	n.s.
Ak21 MTX	14.695	.000032	p<0.00005
ME MTX	14.278	.000040	p<0.00005
IRE MTX	11.523	.000181	p<0.0005

Table 7-6 Repeated measures ANOVA in the MTX group

	F	p-value	
N-PK MTX+IACS	17.530	.000006	p<0.00001
N-BB MTX+IACS	17.736	.000005	p<0.00001
A MTX+IACS	22.526	.000001	p<0.000005
k21 MTX+IACS	1.165	.324136	n.s.
Ak21 MTX+IACS	11.049	.000201	p<0.0005
ME MTX+IACS	22.528	.000001	p<0.000005
IRE MTX+IACS	13.768	.000042	p<0.00005

Table 7-7 Repeated measures ANOVA in the MTX+IACS group

The results indicate a highly significant change in all QDEMRI variables apart from k_{21} in both treatment groups. The direction and temporal pattern of treatment-induced changes is analysed in more detail in the following section.

Multiple comparisons (post-hoc) analysis

The temporal pattern of treatment-induced changes in the two treatment groups is markedly different as indicated by the measurements presented in Table 7-2 to Table 7-4 and the scatter plots (Figure 7-2 to Figure 7-8). The nature and the magnitude of these differences in individual pairs of measurements were assessed by applying post-hoc tests (multiple comparisons tests) with Least Significant Difference (LSD) correction for multiple testing.

The changes in QDEMRI variables at three months follow-up

At three months follow-up, there were no significant changes in the MTX group (Table 7-8), whereas all variables in the MTX+IACS group (with the exception of k_{21}) were significantly lower when compared to baseline (Table 7-9).

MTX Group	Mean Difference		p-value	95% Confidence Interval	
				Lower Bound	Upper Bound
N-PK	7.90E+02	n.s.	.759	-4.43E+03	6.01E+03
N-BB	1.14E+03	n.s.	.663	-4.15E+03	6.43E+03
A	2.88E-03	n.s.	.431	-4.47E-03	1.02E-02
k21	1.15E-03	n.s.	.451	-1.92E-03	4.23E-03
Ak21	1.20E-04	n.s.	.375	-1.52E-04	3.93E-04
ME	6.15E-02	n.s.	.219	-3.85E-02	1.62E-01
IRE	2.11E-03	n.s.	.262	-1.66E-03	5.87E-03

Table 7-8 Multiple comparisons tests in the MTX group (Scan 1 vs. Scan 2)

MTX+IACS Group	Mean Difference		p-value	95% Confidence Interval	
				Lower Bound	Upper Bound
N-PK	1.27E+04	p<0.00001	.0000061	7.90E+03	1.76E+04
N-BB	1.31E+04	p<0.00001	.0000053	8.14E+03	1.80E+04
A	1.64E-02	p<0.00001	.0000067	1.01E-02	2.26E-02
k21	-2.90E-03	n.s.	.1654564	-7.05E-03	1.26E-03
Ak21	3.70E-04	p<0.005	.0014564	1.53E-04	5.87E-04
ME	1.96E-01	p<0.00001	.0000082	1.20E-01	2.72E-01
IRE	5.47E-03	p<0.0005	.0002110	2.79E-03	8.15E-03

Table 7-9 Multiple comparisons tests in the MTX+IACS group (Scan 1 vs. Scan 2)

The changes in QDEMRI variables at twelve months follow-up

The comparison between baseline measurements and the measurements obtained at twelve months after the start of the treatment indicates a significant reduction in all QDEMRI variables (apart from k_{21}) in both treatment groups (Table 7-10 and Table 7-11).

MTX Group	Mean Difference		p-value	95% Confidence Interval	
				Lower Bound	Upper Bound
N-PK	1.14E+04	p<0.0005	.00012	6.14E+03	1.67E+04
N-BB	1.23E+04	p<0.0001	.00006	6.91E+03	1.77E+04
A	1.78E-02	p<0.00005	.00003	1.04E-02	2.53E-02
k21	2.51E-03	n.s.	.11171	-6.16E-04	5.63E-03
Ak21	6.82E-04	p<0.00005	.00002	4.06E-04	9.59E-04
ME	2.46E-01	p<0.00005	.00003	1.45E-01	3.48E-01
IRE	8.51E-03	p<0.0001	.00008	4.69E-03	1.23E-02

Table 7-10 Multiple comparisons tests in the MTX group (Scan 1 vs. Scan 3)

MTX+IACS Group	Mean Difference		p-value	95% Confidence Interval	
				Lower Bound	Upper Bound
N-PK	1.24E+04	p<0.00005	.0000216	7.31E+03	1.76E+04
N-BB	1.26E+04	p<0.00005	.0000217	7.42E+03	1.79E+04
A	2.19E-02	p<0.0000005	.0000001	1.53E-02	2.85E-02
k21	-2.96E-03	n.s.	.1805830	-7.37E-03	1.44E-03
Ak21	5.37E-04	p<0.00005	.0000370	3.07E-04	7.67E-04
ME	2.63E-01	p<0.0000005	.0000001	1.82E-01	3.43E-01
IRE	7.05E-03	p<0.00005	.0000151	4.21E-03	9.90E-03

Table 7-11 Multiple comparisons tests in the MTX+IACS group (Scan 1 vs. Scan 3)

The differences in treatment effectiveness

Although a significant change in QDEMRI variables was detected at three months in the MTX+IACS group and not in the MTX group, this in itself is not a sufficient evidence of the differences between the treatment effectiveness of these two therapies [147]. Therefore, the magnitude of treatment-induced changes was assessed by applying an independent t-test on the values of differences between measurements obtained in Scan 1 and Scan 2 (e.g. A (1-2), k_{21} (1-2) etc.) as well as differences between measurements in Scan 1 and Scan 3 (e.g. A(1-3), k_{21} (1-3) etc.). All paired measurement differences were tested for normality using the Kolmogorov-Smirnov test and no significant departure from normality was detected. There were no significant differences in responses at twelve months follow-up, whereas the differences in voxel counts, parameter A and ME were significantly higher in the MTX+IACS group at the three months follow up. The differences in voxel counts and A were more pronounced than corresponding changes in ME. Interestingly, the changes in parameter k_{21} displayed opposite trends in two treatment groups. Whereas the values of k_{21} were reduced by 2.51 (10-3 s^{-1}) in the MTX group, they rose by 2.96 (10-3 s^{-1}) in the MTX+IACS group at twelve months post-treatment. This result, however, was not statistically significant ($p = 0.065$).

Independent Samples Test

	t-test for Equality of Means				
				95% Confidence Interval of the Difference	
	p-value	Mean Difference	SE Difference	Lower	Upper
N-PK (1-2)	.0005	-1.20E+04	3.11E+03	-1.83E+04	-5.64E+03
N-BB (1-2)	.0005	-1.19E+04	3.11E+03	-1.82E+04	-5.60E+03
A (1-2)	.0014	-1.35E-02	3.88E-03	-2.14E-02	-5.60E-03
k21 (1-2)	.1380	4.05E-03	2.67E-03	-1.37E-03	9.47E-03
Ak21 (1-2)	.1826	-2.49E-04	1.83E-04	-6.22E-04	1.23E-04
ME (1-2)	.0207	-1.34E-01	5.55E-02	-2.47E-01	-2.18E-02
IRE (1-2)	.1778	-3.36E-03	2.44E-03	-8.34E-03	1.61E-03

Table 7-12 Differences in the magnitude of response in two treatment groups at three months

The results of the independent t-tests performed on the differences between baseline and the three months follow-up measurements are listed in Table 7-12. The changes in variables N-PK, N-BB, A and ME at the three months follow-up were markedly higher in the MTX + IACS group. Differences in the effectiveness of these two treatments at 12 months follow-up were not statistically significant (Table 7-13).

Independent Samples Test

	t-test for Equality of Means				
				95% Confidence Interval of the Difference	
	p-value	Mean Difference	SE Difference	Lower	Upper
N-PK (1-3)	.972	-1.32E+02	3.77E+03	-7.82E+03	7.56E+03
N-BB (1-3)	.906	4.60E+02	3.86E+03	-7.42E+03	8.34E+03
A (1-3)	.851	-1.05E-03	5.56E-03	-1.24E-02	1.03E-02
k21 (1-3)	.065	4.54E-03	2.36E-03	-2.92E-04	9.37E-03
Ak21 (1-3)	.334	1.80E-04	1.83E-04	-1.96E-04	5.55E-04
ME (1-3)	.844	1.43E-02	7.21E-02	-1.34E-01	1.62E-01
IRE (1-3)	.355	2.26E-03	2.40E-03	-2.67E-03	7.19E-03

Table 7-13 Differences in the magnitude of response in two treatment groups at twelve months

Conversion of QDEMRI variables

The voxel counts presented in Table 7-1 can be converted into millilitres of tissue by multiplying them by a voxel volume (0.46 mm^3). Average baseline volume was 16.7 ± 5.5 ml in the MTX group and 15.7 ± 6.2 ml in the MTX+IACS group. At twelve months follow-up the volumes were reduced to 11.5 ± 4.4 ml in the MTX group and 10.0 ± 4.3 ml in the MTX+IACS group. The volumes reported here are based on the total number of voxels included in the pharmacokinetic analysis (N-PK).

	Volume [ml]	
	Mean	SD
MTX (1) (n = 17)	16.7	5.5
MTX (2) (n = 17)	16.4	6.5
MTX (3) (n = 16)	11.5	4.4
MTX+IACS (1) (n = 20)	15.7	6.2
MTX+IACS (2) (n = 20)	9.9	6.1
MTX+IACS (3) (n = 16)	10.0	4.3

Table 7-14 Volumes of the enhancing tissue in the Hand RA Study

If a constant value of T1 is assumed ($T1_0$ = 900 ms) and a uniform Cp(0) in all subjects is assumed to be 0.877 mM, an estimate of physiological variables f_{ex} (v_e, the volume of the EES) and apparent permeability K^{trans} can be obtained from the measurements of A and Ak_{21} presented in Chapter 4, Eq. 4-16.

	fex		Ktrans [min-1]	
	Mean	SD	Mean	SD
MTX (1)	.290	.068	.530	.114
MTX (2)	.278	.077	.501	.142
MTX (3)	.218	.052	.365	.095
MTX+IACS (1)	.291	.066	.476	.101
MTX+IACS (2)	.225	.074	.387	.108
MTX+IACS (3)	.203	.056	.347	.056

Table 7-15 Average values of f_{ex} and K^{trans} in the Hand RA Study

7.4.4. Summary of the findings

The statistical analysis of QDEMRI findings indicated a significant treatment-induced change in both treatment groups over the twelve months course of treatment (Table 7-6 and Table 7-7). The only variable which remained essentially unchanged during this period was k_{21}. Furthermore, QDEMRI analysis demonstrated a significant difference in the time

course of treatment induced changes in two treatment groups. Whereas a significant remission was achieved at three months in the MTX+IACS group (Table 7-9), no changes in QDEMRI variables were detected in the MTX group (Table 7-8). However, at twelve months follow-up, the patients in both treatment groups achieved a comparable degree of remission, suggesting that an early intervention with IACS did not confer a long lasting effect on the microvascular properties of the synovium (Table 7-10 and Table 7-11).

The results obtained at three months follow-up indicate that QDEMRI variable A (which according to the theoretical description of the model reflects the fractional volume f_{ex} of the extracellular extravascular space, EES) was significantly reduced compared to the baseline only in the MTX+IACS group. This is in agreement with the known difference in the timing of action between IACS and MTX. Whereas IACS induce a rapid reduction in tissue oedema, MTX (being a slow acting DMARD) affects the tissue microcirculation more gradually and the achieved reduction in QDEMRI variables (and their physiological counterparts) was not statistically significant at the three months follow-up. Furthermore, the pharmacokinetic variable A exhibited greater sensitivity to the differences in treatment response between two treatment groups at the three months follow-up when compared to the BB variable ME (Table 7-12).

QDEMRI analysis indicates that in addition to the reduction of the volumes of the enhancing tissues, anti-rheumatic therapies have an effect on reducing both the available Gd-DTPA distribution volume (through variable A) and the apparent capillary permeability (K^{trans}) in the residual enhancing volume. They were markedly reduced at twelve months follow-up in both treatment groups. However, the patients in the MTX+IACS group achieved remission at three months after the start of therapy, in contrast to patients treated with MTX only where significant reduction in QDEMRI variables was measured only at twelve months follow-up.

The conversion of the voxel counts into the volumes of the enhancing tissue presented in Table 7-14 can be used to assess the physiological relevance of the detected differences between two therapies at the end of the first stage of the study. After the completion of the first stage of the study, average enhancing tissue volume in the MTX+IACS group was reduced from 15.7 ± 6.2 ml to 9.9 ± 6.1 ml whereas it remained constant in the MTX group (16.7 ± 5.5 at baseline vs. 16.4 ± 6.5 at three months follow-up).

The difference in achieved volume reduction between the MTX and MTX+IACS groups was significant ($p<0.0005$, Table 7-12). Based on the results presented in Table 7-12, the mean difference in achieved volume reduction in two treatment groups is -5.5, with 95% CI limits of (-8.4, -2.6) expressed in ml of enhancing tissue. This means that the achieved reduction in the volume of the enhancing tissue patients treated with MTX+IACS was on average 5.5.ml larger than that measured in the MTX group which represents approximately one third of the average baseline volume and can be interpreted as clinically relevant.

A similar analysis of physiological counterparts of the QDEMRI variable A (Table 7-15) indicates that the average difference between the responses at three months was –1.35 with a 95% confidence interval of (-2.14, -0.56) expressed in 10^{-2} s^{-1}. When converted into f_{ex}, these values correspond to the average difference in f_{ex} change between MTX and MTX+IACS of –0.054 with a 95% CI of (-0.086, -0.023), where f_{ex} is expressed as a unit free fraction. The detected difference in f_{ex} response represents 18.7% of the average baseline f_{ex}.

7.5. Knee RA Study

7.5.1. Study description

Thirty-nine patients were recruited for this prospective two-centre double-blind trial. The study objective was to compare the effectiveness of an established DMARD methotrexate (MTX) with a novel compound, leflunomide (LEF). The institutional review board provided ethical approval for this study and a written informed consent was obtained from all patients. In thirty-four patients both baseline and post-treatment scans (follow-up at four months after the start of treatment) were successfully acquired using a protocol described in Section 5.1.3.

All patients were diagnosed with rheumatoid arthritis according to the revised ARA criteria [215]. Disease duration varied between 3 months and 26 years (median 2 years). None of these patients received any DMARDs for four weeks prior to the enrolment into this study. IACS injections were not allowed during the trial period. The median age was 60.5 years (range: 28 to 77 years). Fifteen patients were male and nineteen were female. This patient group was randomly divided into two treatment groups: MTX only and LEF only. Each group consisted of seventeen patients.

Both patient groups were started on a treatment regime following a baseline clinical and laboratory assessment and a baseline DEMRI scan. The patients received sixteen weeks (four months) of treatment with 20 mg LEF per day with a loading dose of 100 mg/day for three days (LEF group) or 7.5 to 15 mg of MTX per day (MTX group). A follow-up DEMRI scan was performed at four months after the start of the treatment.

7.5.2. Summary of the measurements

All DEMRI scans were analysed on a voxel-by-voxel basis following the procedure described in Chapter 5. The entire DEMRI volume was included in the analysis. Seven QDEMRI variables were measured in each DEMRI set, including two black-box parameters (IRE and ME) and three pharmacokinetic parameters (A, k_{21}, Ak_{21}) as well as two voxel counts N-BB and N-PK obtained by counting all voxels included in the black-box and pharmacokinetic analyses, respectively. All measurement units are listed in Appendix A. QDEMRI analysis was performed blinded to the treatment allocation and the order of scans. After obtaining the treatment allocation key, the variables were arranged in treatment and visit groups, thus forming six sub-groups. They were labelled as follows:

LEF (1)	baseline scan in the LEF group (n = 17)
LEF (2)	follow-up after 4 months in the LEF group (n = 17)
MTX (1)	baseline scan in the MTX group (n = 17)
MTX (2)	follow-up after 4 months in the MTX group (n = 17)

A total of 68 DEMRI studies were analysed. A summary of the measurements is presented in Table 7-16 to Table 7-18 and Figure 7-9 to Figure 7-15. Means and standard deviations of seven measured parameters in each of the six scan subgroups are presented in Table 7-16 (voxel counts), Table 7-17 (pharmacokinetic parameters) and Table 7-18 (black-box parameters).

	N-PK		N-BB	
	Mean	SD	Mean	SD
LEF (1)	2.93E+04	8.74E+03	2.98E+04	8.93E+03
LEF (2)	2.91E+04	8.62E+03	2.95E+04	8.74E+03
MTX (1)	2.77E+04	1.02E+04	2.81E+04	1.04E+04
MTX (2)	2.87E+04	1.11E+04	2.92E+04	1.11E+04

Table 7-16 Summary of voxel counts measurements in the Knee RA Study

	A [s-1]		k21 [s-1]		Ak21 [s-2]	
	Mean	SD	Mean	SD	Mean	SD
LEF (1)	4.19E-02	8.27E-03	2.95E-02	8.86E-03	1.02E-03	4.22E-04
LEF (2)	4.14E-02	7.21E-03	2.13E-02	8.71E-03	7.27E-04	3.55E-04
MTX (1)	4.14E-02	9.05E-03	2.56E-02	7.74E-03	8.44E-04	2.48E-04
MTX (2)	4.06E-02	8.65E-03	2.91E-02	1.29E-02	9.23E-04	3.27E-04

Table 7-17 Summary of pharmacokinetic parameters measurements in the Knee RA Study

	ME		IRE [s-1]	
	Mean	SD	Mean	SD
LEF (1)	1.65E+00	1.32E-01	1.38E-02	2.45E-03
LEF (2)	1.61E+00	1.03E-01	1.24E-02	2.67E-03
MTX (1)	1.63E+00	1.10E-01	1.27E-02	2.52E-03
MTX (2)	1.62E+00	1.03E-01	1.30E-02	2.46E-03

Table 7-18 Summary of black-box parameters measurements in the Knee RA Study

The values of individual measurements are presented in scatter plots and the corresponding summary error bar plots (two SE limits) are presented in Figure 7-9 to Figure 7-15.

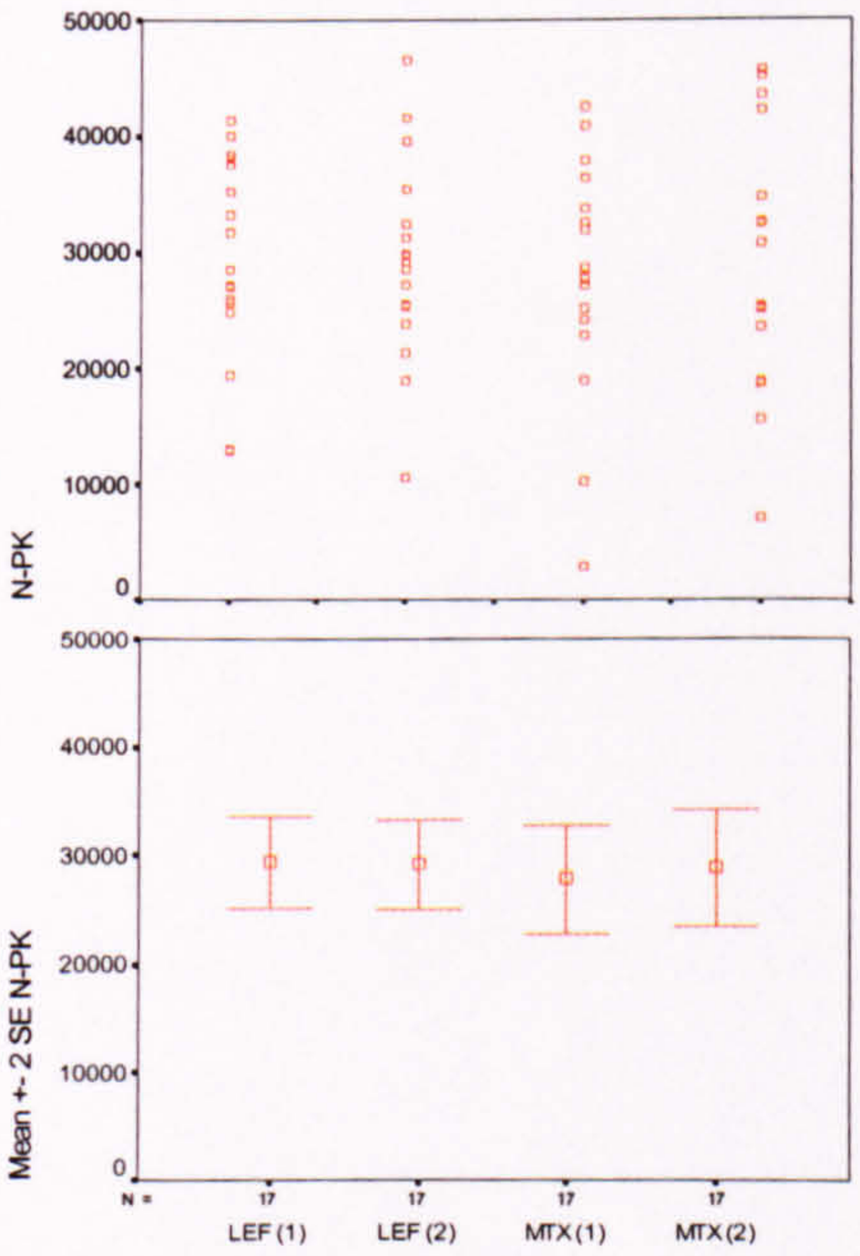

Figure 7-9 Distribution of variable N-PK in the Knee RA Study

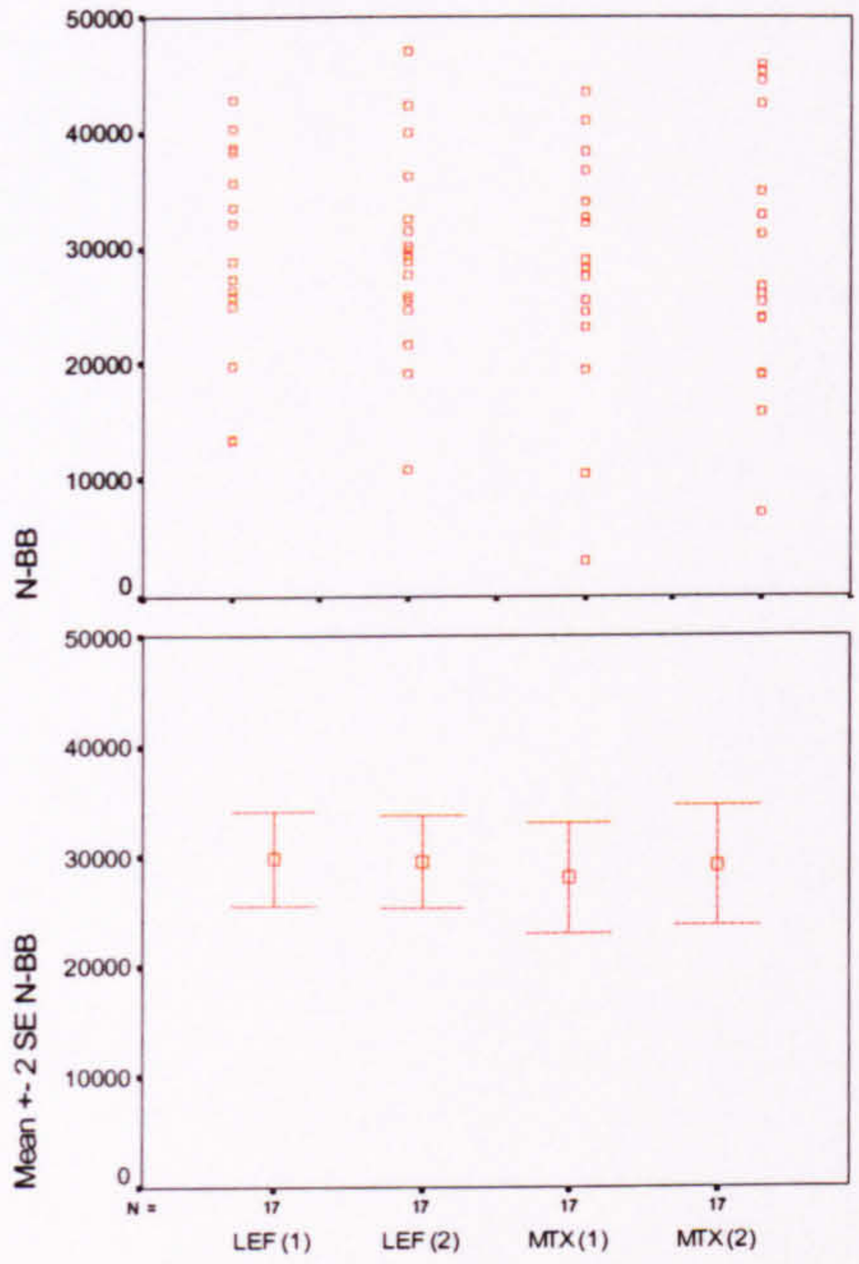

Figure 7-10 Distribution of variable N-BB in the Knee RA Study

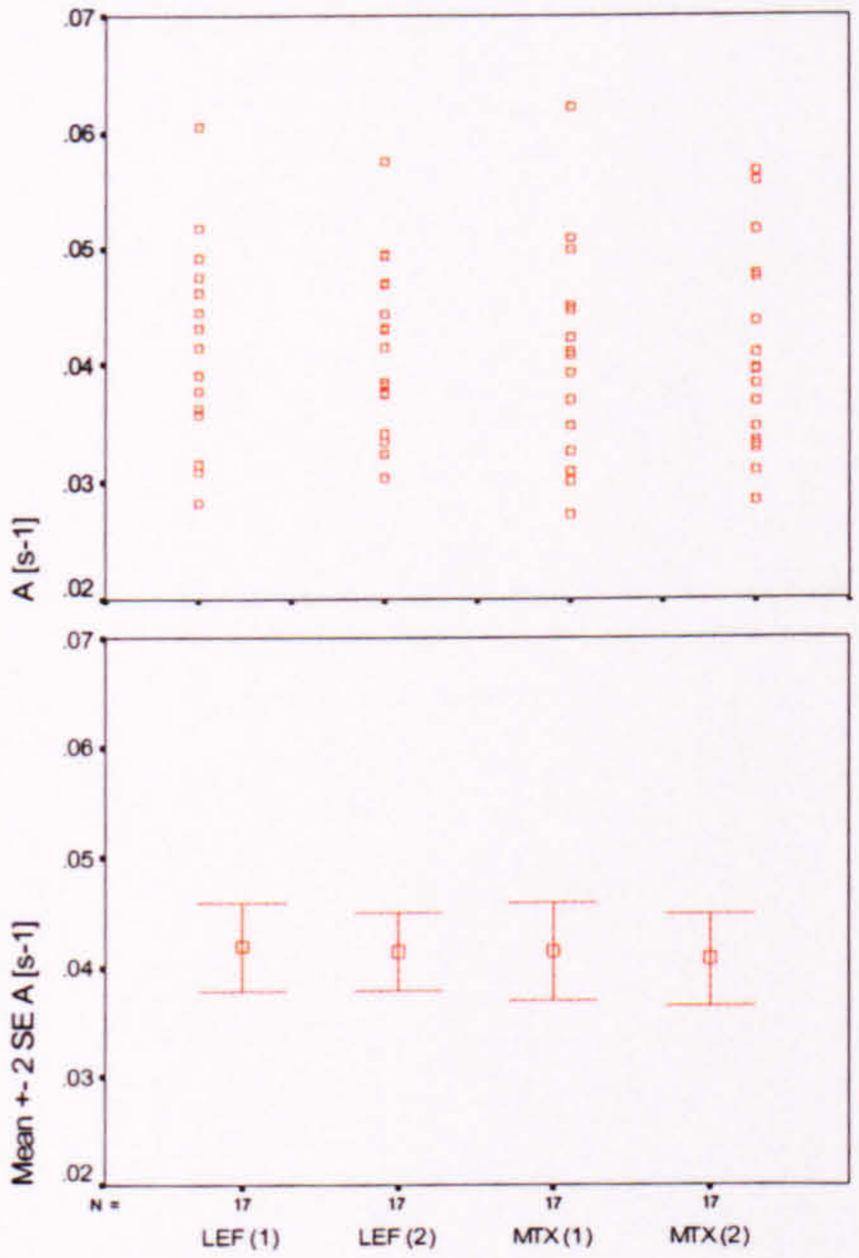

Figure 7-11 Distribution of variable A in the Knee RA Study

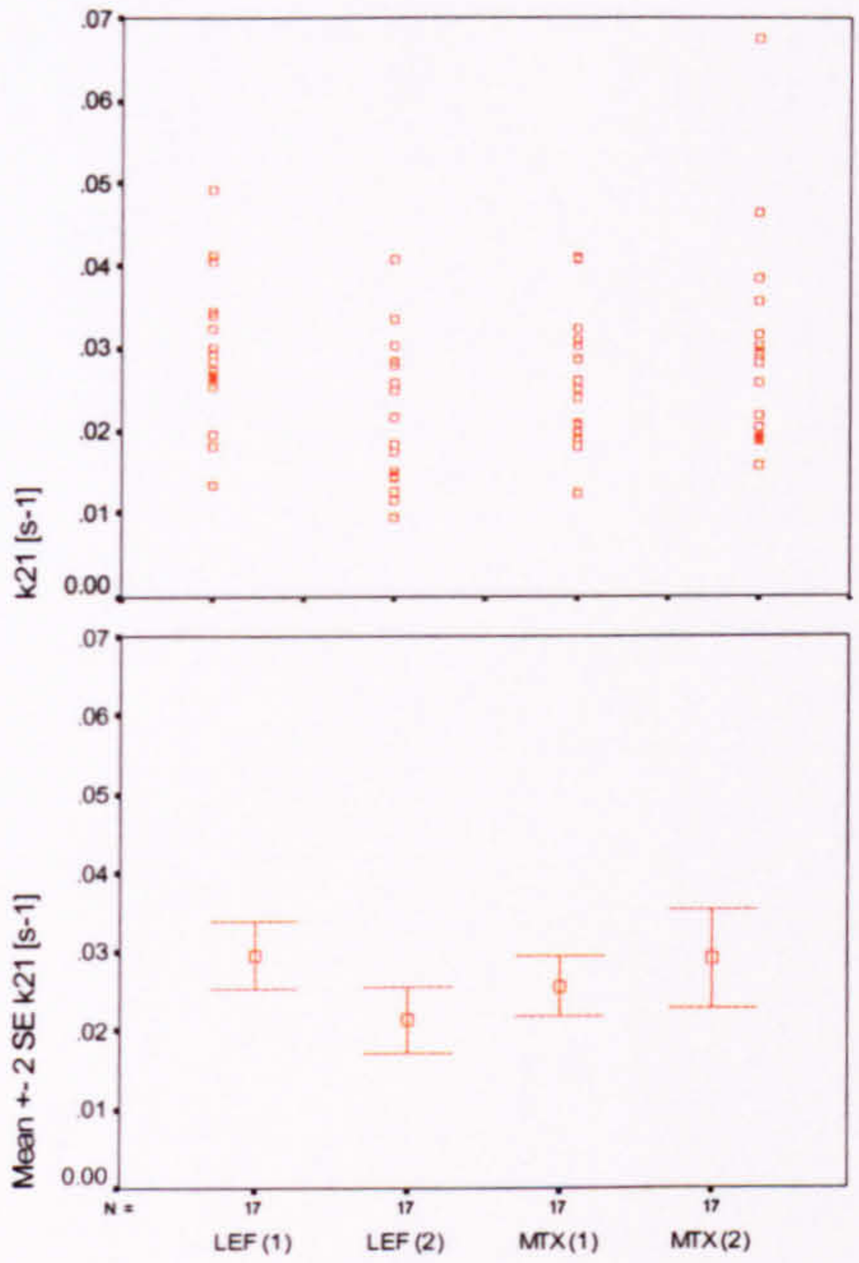

Figure 7-12 Distribution of variable k_{21} in the Knee RA Study

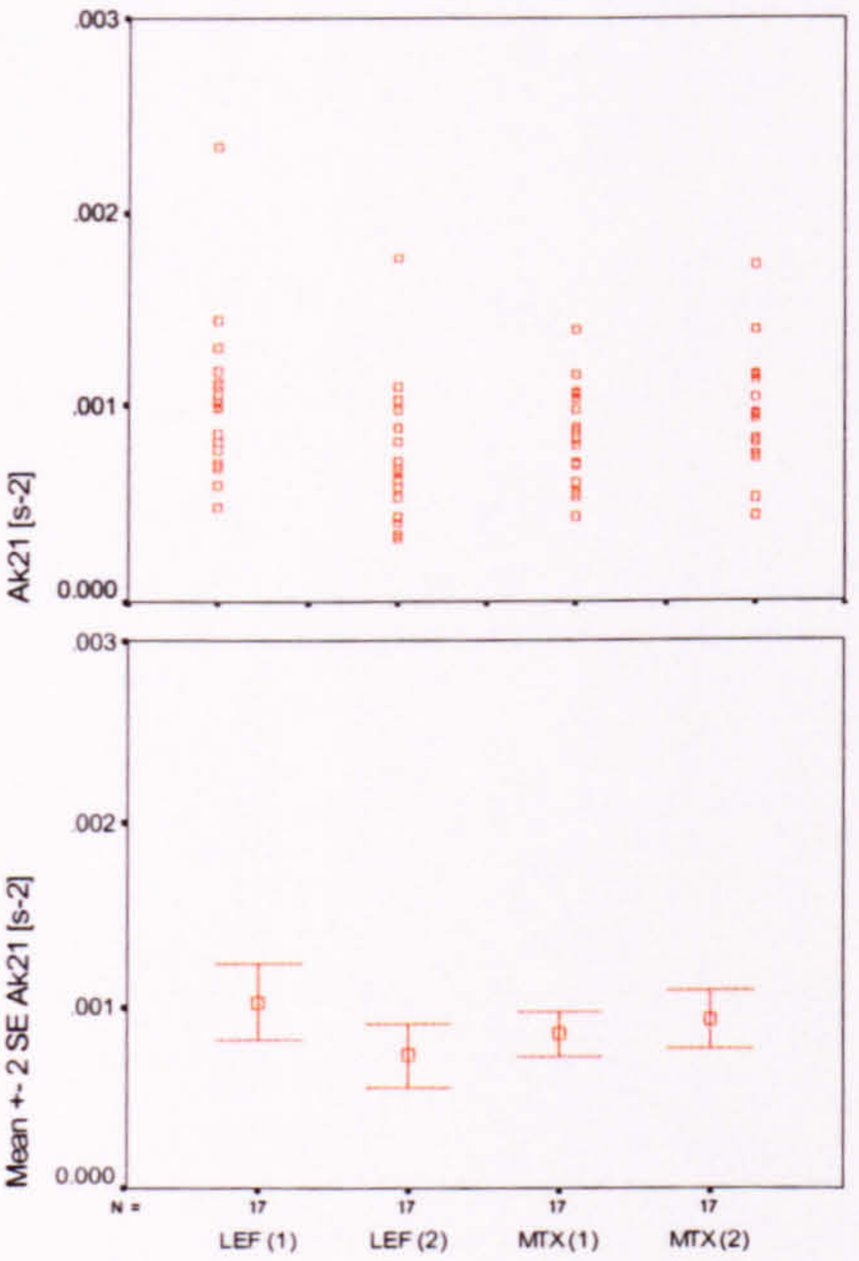

Figure 7-13 Distribution of variable Ak_{21} in the Knee RA Study

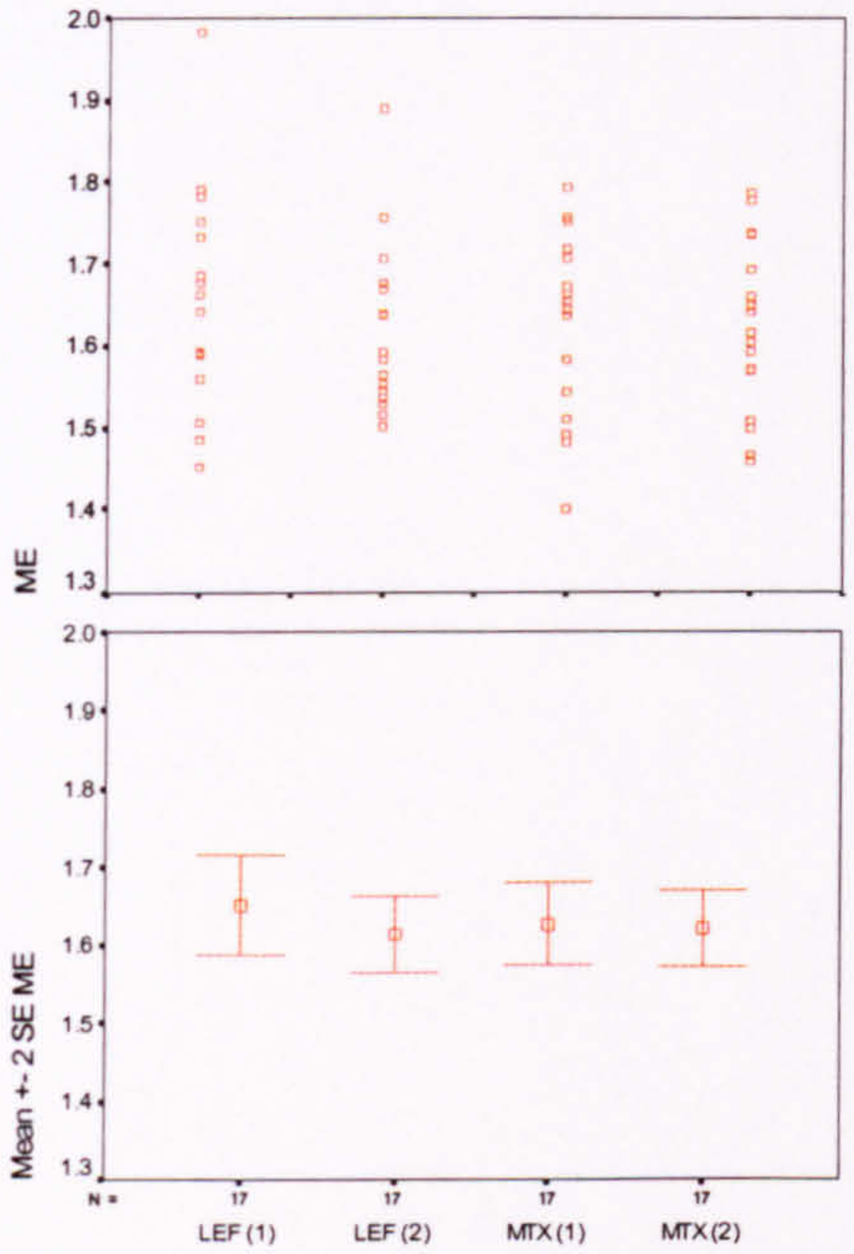

Figure 7-14 Distribution of variable ME in the Knee RA Study

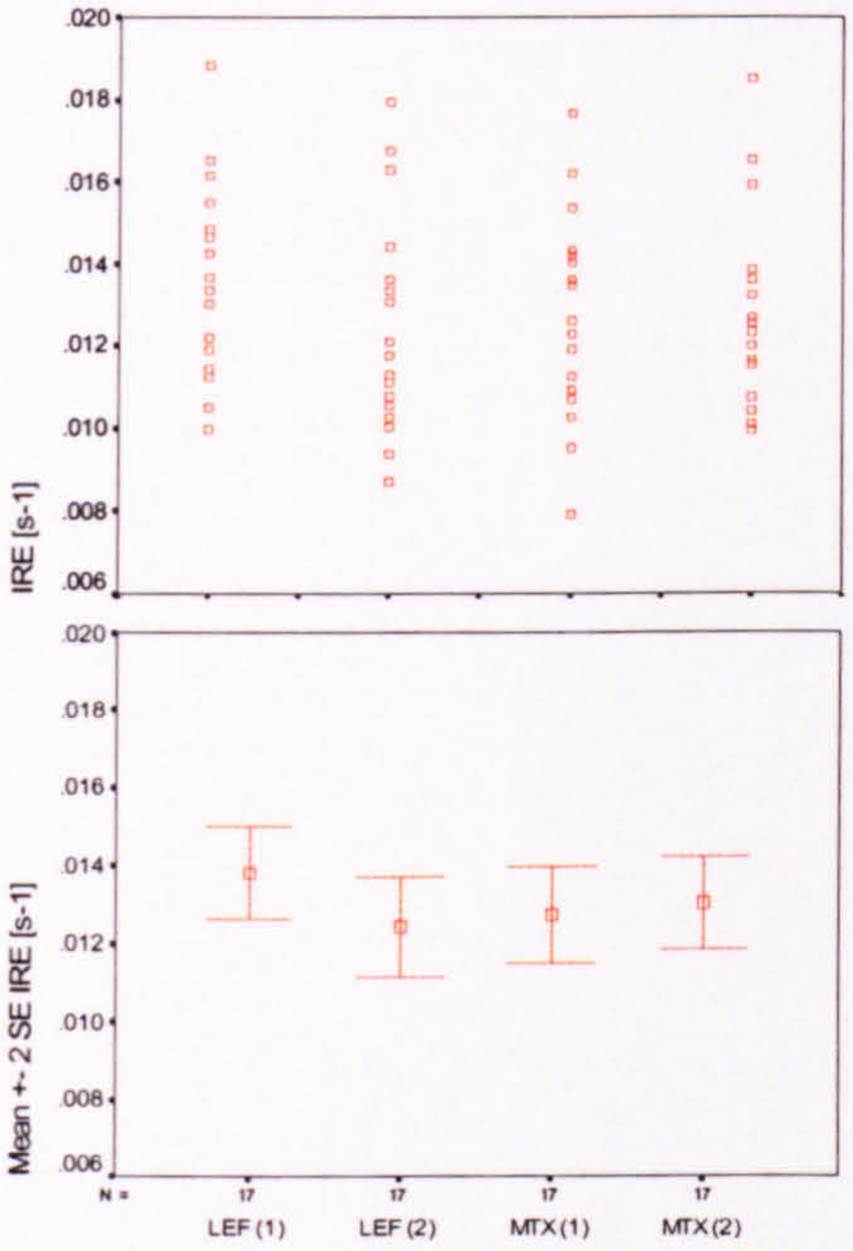

Figure 7-15 Distribution of variable IRE in the Knee RA Study

7.5.3. Statistical analysis

SPSS statistical software package (Version 10.0, SPSS, Chicago, IL) was used for statistical analysis. All statistical tests were performed at $\alpha = 0.05$ confidence level. A preliminary

analysis of the distribution of measurements of each of the seven QDEMRI variables revealed no significant deviation from normality in the four scan subgroups. This analysis was performed on 28 sets of measurements (seven variables divided into the four scan subgroups) with the sample size of 17. The results of the Kolmogorov-Smirnov test for normality are listed in Appendix C. No significant departure from normality was detected by this test, and the differences between individual QDEMRI variables subgroups were analysed by using tests for normally distributed variables (at $\alpha = 0.05$ confidence level).

Baseline measurements

The analysis of baseline measurements in LEF and MTX groups for each of the seven variables revealed no statistically significant differences between the treatment groups. The results of the baseline assessment (an independent t-test for the differences in means) are summarised in Table 7-19.

	t-test for Equality of Means			
			95% Confidence Interval of the Difference	
	p-value	Mean Difference	Lower	Upper
N-PK (1)	.610	1.69E+03	1.69E+03	-4.98E+03
N-BB (1)	.608	1.72E+03	1.72E+03	-5.04E+03
A (1)	.878	4.61E-04	4.61E-04	-5.60E-03
k21 (1)	.181	3.90E-03	3.90E-03	-1.91E-03
Ak21 (1)	.147	1.77E-04	1.77E-04	-6.65E-05
ME (1)	.557	2.47E-02	2.47E-02	-6.02E-02
IRE (1)	.216	1.08E-03	1.08E-03	-6.60E-04

Table 7-19 Analysis of the baseline measurements in the Knee RA Study[2]

[2] Mean Difference = Mean (LEF) – Mean (MTX)

Paired samples t-tests

The changes in QDEMRI variables between baseline and four months follow-up were assessed by applying a paired samples t-test. The results of the statistical analysis of paired measurements at baseline (1) and at the four months follow-up (2) in the two treatment groups are presented in Table 7-20 (LEF group) and Table 7-21 (MTX group).

Paired Samples Test [a]

	Paired Differences				
			95% Confidence Interval of the Difference		
	Mean	SD	Lower	Upper	p-value
N-PK (1) - N-PK (2)	2.24E+02	8.64E+03	-4.22E+03	4.67E+03	.916
N-BB (1) - N-BB (2)	2.54E+02	8.84E+03	-4.29E+03	4.80E+03	.907
A (1) - A (2)	4.90E-04	5.27E-03	-2.22E-03	3.20E-03	.707
k21 (1) - k21 (2)	8.17E-03	1.03E-02	2.89E-03	1.34E-02	.005
Ak21 (1) - Ak21 (2)	2.95E-04	3.24E-04	1.28E-04	4.61E-04	.002
ME (1) - ME (2)	3.83E-02	6.65E-02	4.14E-03	7.25E-02	.030
IRE (1) - IRE (2)	1.36E-03	2.07E-03	2.96E-04	2.43E-03	.016

[a]. Treatment = LEF, (n = 17)

Table 7-20 QDEMRI variables changes in the LEF group

Paired Samples Test [a]

	Paired Differences				
			95% Confidence Interval of the Difference		
	Mean	SD	Lower	Upper	p-value
N-PK (1) - N-PK (2)	-1.06E+03	1.27E+04	-7.57E+03	5.44E+03	.733
N-BB (1) - N-BB (2)	-1.11E+03	1.27E+04	-7.63E+03	5.41E+03	.723
A (1) - A (2)	7.93E-04	4.96E-03	-1.76E-03	3.34E-03	.519
k21 (1) - k21 (2)	-3.52E-03	1.46E-02	-1.10E-02	4.00E-03	.336
Ak21 (1) - Ak21 (2)	-7.90E-05	3.94E-04	-2.82E-04	1.24E-04	.420
ME (1) - ME (2)	5.26E-03	6.36E-02	-2.75E-02	3.80E-02	.738
IRE (1) - IRE (2)	-3.03E-04	2.47E-03	-1.57E-03	9.65E-04	.619

[a]. Treatment = MTX, (n = 17)

Table 7-21 QDEMRI variables changes in the MTX group

A significant reduction in variables k_{21}, Ak_{21}, ME and IRE was detected in the LEF group (Table 7-20) whereas all variables remained constant at four months follow-up in the MTX group (Table 7-21).

The differences in treatment effectiveness

The magnitude of the treatment-induced changes (see section 7.4.3) was assessed by applying an independent t-test on the values of differences between measurements obtained in Scan 1 and Scan 2 (e.g. A (1-2), k_{21} (1-2) etc.). All paired measurement differences were tested for normality using the Kolmogorov-Smirnov test and no significant departure from normality was detected. The results are presented in Table 7-22.

Independent Samples Test

	t-test for Equality of Means				
				95% Confidence Interval of the Difference	
	p-value	Mean Difference	SE Difference	Lower	Upper
N-PK (1-2)	.731	1.29E+03	3.72E+03	-6.32E+03	8.90E+03
N-BB (1-2)	.719	1.36E+03	3.75E+03	-6.31E+03	9.03E+03
A (1-2)	.864	-3.03E-04	1.76E-03	-3.88E-03	3.27E-03
k21 (1-2)	.012	1.17E-02	4.33E-03	2.82E-03	2.06E-02
Ak21 (1-2)	.005	3.74E-04	1.24E-04	1.21E-04	6.26E-04
ME (1-2)	.148	3.31E-02	2.23E-02	-1.24E-02	7.85E-02
IRE (1-2)	.041	1.67E-03	7.82E-04	7.12E-05	3.26E-03

Table 7-22 Difference in treatment response magnitude between two treatment groups

Parameters k_{21}, Ak_{21} and IRE exhibited significantly different degree of change at the four months post treatment in LEF and MTX group.

Conversion of QDEMRI variables

The voxel counts presented in Table 7-1 can be converted into millilitres of tissue by multiplying them by the voxel volume (4.77 mm3). The average baseline volume was 139.9 ± 41.7 ml in the LEF group and 131.9 ± 48.9 ml in the MTX group.

These volumes remained constant at the four months follow-up (138.8 ± 41.1 ml in the LEF group and 136.9 ± 52.7 ml in the MTX group). The volumes reported here are based on the total number of voxels included in the pharmacokinetic analysis (N-PK). They include not only the enhancing synovium but also the enhancing extra-capsular structures.

	Volume [ml]	
	Mean	SD
LEF (1)	139.9	41.7
LEF (2)	138.8	41.1
MTX (1)	131.9	48.9
MTX (2)	136.9	52.7

Table 7-23 Volumes of the enhancing tissue in the Knee RA Study

If a constant value of T1 is assumed ($T1_0$ = 900 ms) and a uniform Cp(0) in all subjects is assumed to be 0.877 mM, an estimate of physiological variables f_{ex} (v_e, the volume of the EES) and the apparent permeability K^{trans} can be obtained from the measurements of A and Ak_{21} presented in Chapter 4, Eq. 4-16.

	fex		Ktrans [min-1]	
	Mean	SD	Mean	SD
LEF (1)	.190	.038	.278	.115
LEF (2)	.188	.033	.198	.097
MTX (1)	.188	.041	.230	.068
MTX (2)	.184	.039	.251	.089

Table 7-24 Average values of f_{ex} and K^{trans} in the Knee RA Study

Correlation with clinical and laboratory findings

The clinical and laboratory data collected concurrently with the DEMRI data was not available for point-to point statistical comparison with the results presented in this study. However, the results that have been reported using the data collected in this study indicate that there was no statistically significant difference in the responses measured in the MTX and LEF groups using clinical and laboratory assessment. It was reported, though, that patients in the LEF group exhibited greater improvement in tender joint count, duration of morning stiffness, visual analogue scale (VAS) pain intensity, Modified Health Assessment Questionnaire (M-HAQ) score, C-reactive protein (CRP) level, and rheumatoid factor (RF) titer [213]. The patients in the MTX group showed greater improvement in erythrocyte sedimentation rate (ESR) compared with the baseline.

Table 1. Summary of changes from baseline in clinical outcome assessments after 4 months of treatment*

Parameter	Treatment: Leflunomide (n = 18)	Treatment: Methotrexate (n = 21)	*P*
Tender joint count†	−9.9 ± 9.0	−5.9 ± 6.4	0.1738
Swollen joint count†	−4.6 ± 7.1	−4.6 ± 7.0	0.9628
Patient global assessment‡	−0.9 ± 0.9	−1.0 ± 1.1	0.9604
Physician global assessment‡	−0.9 ± 0.8	−0.8 ± 1.0	0.5293
Morning stiffness, minutes	−120 ± 318	−76.2 ± 165	0.9218
Pain intensity‡	−16.2 ± 25.8	−10.1 ± 17.7	0.4072
M-HAQ score, 0–24	−6.44 ± 8.89	−4.1 ± 7.82	0.3042
ESR, mm/hour	−3.3 ± 18.3	−11.6 ± 22.1	0.2445
CRP level, mg/dl	−17.1 ± 33.8	−14.1 ± 27.0	0.6464
RF, units/ml	−65.7 ± 104.6	−40.3 ± 105.1	0.8477
ACR 20% responders, %	50	47.6	1.000

* Except where otherwise indicated, values are the mean ± SD. M-HAQ = modified Health Assessment Questionnaire; ESR = erythrocyte sedimentation rate; CRP = C-reactive protein; RF = rheumatoid factor; ACR = American College of Rheumatology.
† Twenty-eight–joint assessment.
‡ 0–100-mm visual analog scale (VAS).

Table 7-25 Summary of clinical and laboratory findings in the Knee RA Study (reproduced from [213])

As can be seen from Table 7-25, an improvement in clinical and laboratory findings was detected at four months after the start of therapy in both treatment groups with no

statistically significant changes between LEF and MTX treated patients. Similar clinical and laboratory outcomes were reported in two further studies performed on the subsets of the patients included in the QDEMRI analysis presented in this thesis [216, 217] with no significant differences between treatment groups.

The immunohistochemical analysis of synovial samples revealed that the expression of vascular cell adhesion molecule 1 (VCAM-1), which is a marker for endothelial cell activation and injury, was reduced in both groups [216], but this difference was significant only in the leflunomide-treated patients ($p<0.05$). Arthroscopic samples cellularity (CD68+ macrophages and T cells) was also significantly reduced in LEF patients and remained constant in the MTX group ($p<0.05$). In a separate report [217], a rapid reduction in neutrophil migration was detected in the period between 3 and 14 days post-treatment in both treatment groups ($p<0.001$). However, this effect was not detected at four months after the start of treatment.

7.5.4. Summary of the findings

In this study, the results of QDEMRI analysis demonstrated significant reduction in PK variables related to capillary permeability (k_{21} and Ak_{21} and black-box variables (ME and IRE) in patients treated with leflunomide and no change in patients treated with methotrexate at four months after the start of treatment. Total volumes of enhancing tissue remained constant in both treatment groups as well as the measurements of PK variable A, which reflects the fractional volume of the extracellular space (f_{ex}). The changes in BB variables detected over this time period were less pronounced and the highest degree of discrimination between two treatment groups was demonstrated through the measurements of variable Ak_{21}, which according to the pharmacokinetic model definition reflects capillary permeability surface area product (K^{trans}).

The findings reported by Kraan et al [216], which report a significant reduction in the expression of vascular cell adhesion molecule 1 (VCAM-1) in patients from this study treated with leflunomide but not the ones treated with methotrexate, suggest that leflunomide acts as a more potent angiogenesis inhibitor since VCAM-1 was shown to induce angiogenesis in-vivo by Koch et al [218]. Although only a tentative link between the findings presented in this thesis and those reported by Kraan et al can be made at present due to the lack of direct point-to-point statistical comparison, the apparent agreement between the measured reduction in QDEMRI variables Ak_{21} and VCAM-1 is encouraging and adds weight to the notion that QDEMRI variables, and Ak_{21} in particular, can indeed detect the changes in angiogenic activity in RA.

Chapter 8. Discussion

In this project, a method for quantitative analysis of dynamic Gd-DTPA enhanced MRI was developed and the feasibility of its application for the analysis of DEMRI studies acquired within a clinical setting was demonstrated.

The project structure provided the framework for evaluating the proposed methodology in an already widely studied application (breast cancer), translating it to a novel application (rheumatoid arthritis) where established therapies were examined in a randomised study design (the Hand RA Study). Finally, it was implemented in a study where an established therapeutic agent was compared to a novel anti-rheumatic drug (the Knee RA Study).

The pharmacokinetic model which forms the part of the method for QDEMRI analysis described in this thesis has evolved from the existing approaches to modelling Gd-DTPA kinetics as described in Chapter 3. The most comprehensive method, as described by Larsson [71], could not be applied within the project's experimental setting. A measurement of truly quantitative physiological variables is possible only if the $T1_0$ values are sampled in individual lesions and the concentration of Gd-DTPA in plasma is measured in each patient and incorporated into the calculation of pharmacokinetic variables. The model presented

here, therefore, incorporates a theoretical representation of Cp(t) based on data provided by Weinmann [64] in a fashion similar to that employed by Tofts [69], with a distinction that a) mono-exponential plasma clearance model is used instead of the bi-exponential one and b) input function was represented by a constant rate infusion rather than an idealised delta function.

It was noted that the accurate estimation of k_{el} (fractional elimination rate, which is primarily related to the systemic Gd-DTPA washout following intravenous administration) is impeded by the short duration of DEMRI acquisitions. This parameter is allowed to vary freely in the Brix's implementation [68], although the authors note that it is not of diagnostic value and often assumes negative (physiologically uninterpretable) values. Furthermore, the formulation of the mathematical representation of residual tissue concentration is symmetrical with respect to k_{21} and k_{el}, which may lead to the erroneous estimation of k_{21} [122]. Therefore, in the proposed model k_{el} is fixed to the mean value reported by Weinmann and the non-linear fitting algorithm is constrained with respect to the relationship between k_{21} and k_{el} which leads to the suppression of k_{21} values which are lower than $2k_{el}$.

The input function was modelled as a constant rate infusion (as in Brix's model [68] and in contrast to Tofts' implementation) in an attempt to allow for a more realistic representation of characteristic sigmoid-shape SI changes observed in lesions distal from major blood vessels. Although this modification leads to the increased complexity of the derived function for normalised SI, the model behaved well in a range of pathologies in all three clinical studies.

In Brix's implementation (and other models derived from Brix's, such as that used by Buckley [121]), variable A was not explicitly linked to the fractional volume of the extracellular space (f_{ex}). Subject to the same set of assumptions used in Tofts' model, it was

shown that this variable could be used to obtain an estimate f_{ex} as described in Section 4.3. In this thesis, estimates of f_{ex} were obtained using assumed constant values of $T1_0$ representative of the tissues studied and a uniform value of initial Cp(0), which are in good agreement with literature values. Furthermore, in the Breast Cancer Study, a conversion of variable Ak_{21}, which was theoretically linked to a standardised measure of apparent permeability K^{trans}, yielded estimates which are in broad agreement with K^{trans} measured in invasive breast cancers reported by other workers.

Although the precise measurement of individual values of f_{ex} and K^{trans} was not possible in this project, due to the unavailability of individual measurements of $T1_0$ and concomitant measurements of representative Cp(t), the described conversion of measured pharmacokinetic variables A and Ak_{21} into their counterparts (f_{ex} and K^{trans}, respectively) may allow a direct comparison of measurements obtained using different acquisition protocols. The remaining pharmacokinetic variable k_{21} is by definition independent of acquisition settings.

The proposed method was applied for the analysis of DEMRI datasets acquired using conventional, commercial MRI hardware and all processing was performed on a standard personal computer workstation. A degree of user interaction was necessary in the Breast Cancer Study (ROI selection based on calculated parametric images) and the removal of MCPJ1 by segmentation in the Hand RA study. The processing of the DEMRI datasets in the Knee RA Study required no user interaction. The selection of the enhancement thresholds for QDEMRI analysis in the two RA studies was performed following the inspection of parametric enhancement maps in a randomly selected subset of DEMRI datasets.

In all three studies, both pharmacokinetic and black-box variables were extracted in parallel with the aim of performing a direct comparison between their measurements. A theoretical

link between pharmacokinetic and black-box variables was also explored during the development of QDEMRI algorithms (Section 4.3).

The pre-processing procedures were performed using commercially available software (Analyze™) whilst all computations of pharmacokinetic and black-box variables were performed using software written for this thesis in the C programming language. Following the selection of ROIs in the Breast Cancer Study and the enhancement thresholds in the two RA Studies, QDEMRI analysis of SI/time curves (derived from ROIs or individual voxels) was performed in a fully automated fashion, requiring no user interaction. Dynamic allocation of initial solutions for the non-linear least-squares fitting of the measured SI/time curves to the proposed model (required for the extraction of pharmacokinetic variables) ensured a robust performance of the computational algorithm and enabled automated batch processing of the DEMRI datasets. In the two RA studies, where voxel-by-voxel processing was performed, a complete analysis of individual DEMRI datasets required less than 30 seconds, allowing uninterrupted analysis of 120 DEMRI datasets in only one hour (on a 600 MHz, 128Mb PC system).

In all three clinical studies, experimental data fitted the proposed pharmacokinetic model well, with only one out of fifty-nine examined SI/time curves in the Breast Cancer Study generating an excessive residual Chi Square value (χ^2) and with the success rate of voxel-by-voxel processing higher than 95% in the two RA studies.

The measurement of black-box variables was performed using moving-window algorithms which circumvented the need for user interaction, such as the visual inspection of individual SI/time curves, subjective identification of the onset of enhancement and maximal enhancement or the measurement of enhancement ratios at discrete time points. The objectivity and robustness of this approach thus compares favourably to that employed for the measurement of black-box variables in similarly designed DEMRI studies in breast

cancer [141-144] and RA [183, 184, 192]. Furthermore, these automated algorithms were found to be particularly well suited to the voxel-by-voxel computation of QDEMRI variables and allowed the creation of quantitative parametric maps of individual variables. Similar parametric maps of rheumatoid synovium have not been utilised by other research groups to date. These maps are used as an additional tool in the identification of suspect lesions in the clinical evaluation of breast DEMRI studies at our institution. In RA they provided a tool for the analysis of the morphology of the inflamed synovium and have recently been used to demonstrate radial predilection of synovitis in MCPJs [220]. A histogram-based method for the measurement of the overall disease activity in RA was also proposed in this thesis as a tool for objective monitoring of treatment-induced changes.

A conventional 'explicit' validation of the measurements which are obtained by the described model for QDEMRI analysis would involve their direct comparison with gold standard measurements of relevant physiological variables. In the absence of a suitable non-invasive in-vivo gold standard method for the measurement of these variables, several research groups have attempted to correlate the findings of quantitative analysis of DEMRI with surrogate markers of angiogenesis, such as MVD and VEGF.

In this work, an alternative 'implicit' functional validation of the QDEMRI measurements was performed. This approach is based on the notion that a functional assessment of microcirculation should not be compared to the isolated morphological or chemical surrogate markers of angiogenic activity, but that a suitable functional model should be used to assess the capacity of QDEMRI to provide an objective measure of disease activity. Implicit functional validation involved the application of the QDEMRI method in clinical studies that were chosen as exemplars in which specific changes in physiological variables are expected to occur.

This approach is reasonable given the large variability of correlation coefficients between MVD and QDEMRI parameters reported in the literature (see Section 3.5) suggesting that perhaps the structural information obtained by immunohistochemical staining does not reflect fully the functional status of the microvasculature. A dense network of capillaries can be utilised only partially, with effective transport across the capillary walls in a sample occurring in a fraction of the available network. Similarly, a relatively sparse capillary network can be formed by highly permeable vessels, allowing easy transport between plasma and extracellular space. The metabolic activity of the tissues which is directly related to metastatic potential of cancers or severity of inflammation will be reflected by the rate of transport across capillary walls and not necessarily by the density of the available capillary network.

It is the *function,* and not the morphology alone, that determines the pathological status of the tissues. QDEMRI can (under optimal scanning conditions) quantify the *function* and it is therefore not surprising that it does not correlate unequivocally with a morphological measurement, such as MVD.

The most vociferous proponents of the anti-angiogenic cancer therapy, including Folkman who is credited with the major discoveries in this area [9], have increasingly criticised the use of MVD and VEGF as independent measures of treatment efficacy. They argue that although MVD and VEGF were shown to be useful prognostic indicators in cancer, they may not be a suitable for the detection of treatment induced changes [18]. Morphological assessment of histology specimens may not reflect a true functional MVD. This is indicated by the results in the study of xenografts where as few as 20% and not more than 85% of tumour microvessels were perfused at any given time [219]. In anti-angiogenic treatment cancer, the primary objective is the impairment of the nutrient delivery to the cancer cells through a direct action on capillary endothelium. If the treatment is successful, and results in the reduction of the number of cancer cells, a paradoxical increase of MVD can occur as a result of the reduction of intercapillary distance. Furthermore, isolated measurements of

VEGF (or any other angiogenic factor) may not adequately represent the effect of anti-angiogenic treatment. This is because an overall angiogenic activity depends on a multitude of pro- and anti-angiogenic factors that arise from both tumour [15] and host [16] cells.

The implicit functional validation of QDEMRI measurements obtained in the Breast Cancer Study was therefore carried out by their direct comparison with the prognostic factors: histologically determined tumour grade and nodal status. The capacity of the proposed model to measure apparent permeability in this study was judged by the degree of correlation between permeability-related pharmacokinetic variables and tumour grade in the invasive breast cancer.

The most important finding of this study is that there was a statistically significant correlation between permeability-related pharmacokinetic variables (k_{21} and Ak_{21}) and tumour grade in invasive breast cancer. However, no association was found between any of the QDEMRI variables and tumour nodal status. Whereas the measurements of k_{21} and Ak_{21} did not vary significantly between low grade tumours (Grade 1 and Grade 2) they differed significantly between low grade and high grade (Grade 3) tumours. Whilst black-box variables ME, IRE and WOS did exhibit a degree of variation with tumour grade, none of them reached statistical significance for the overall association with tumour grade.

These findings confirm the hypothesis that the relationship between permeability-related QDEMRI variables and tumour aggressiveness persists within invasive breast carcinomas. The strength of this relationship, however, is relatively weak due to the large amount of scatter in the measurements obtained in different tumour grade groups and in particular between Grade 1 and Grade 2 lesions.

These results are in agreement with the results of animal studies reported by Turetschek et al who found a significant correlation between permeability measured using both albumin-(Gd-

DTPA)$_{30}$ [137, 138] and ultrasmall superparamagnetic iron oxide (USPIO) particles [139], and tumour grade in chemically induced breast carcinoma in rats. However, animal studies where Gd-DTPA was used as a contrast agent [135, 136, 140] found no correlation between the tumour grade and the permeability. A study reported by Heiblich [140] was designed to compare different acquisition and analysis strategies using a controlled, chemically induced animal model of breast cancer. None of the examined methods provided a significant quantitative association with histological tumour grade. A T2* based method proposed by Kuhl [221], reached borderline significance for the discrimination between the tumour grades. It is unclear, though, if these findings [135, 136, 140] can be directly applicable to human studies due to the faster rate of systemic circulation in small animal models which requires higher DEMRI temporal resolution in order to resolve extravasation rates of small Gd-DTPA molecules in highly permeable tumours.

None of the four published clinical studies where a similar comparison between the quantitative findings of Gd-DTPA enhanced dynamic MRI were compared to prognostic indices in breast cancer [141-144] included the extraction of pharmacokinetic permeability-related variables. Their results (based on the measurements of descriptive black-box indices) are contradictory. A significant correlation between histological tumour grades and lymph-node status and DEMRI findings in breast cancer was reported in two studies [142, 144] but in two remaining studies [141, 143], no such relationship was found. It is difficult to perform a direct comparison between the results obtained in these studies and the results presented in this thesis due to the differences in the data acquisition, methods employed for quantitative analysis as well as the size and histological composition of examined lesions. The possible influence of different DEMRI acquisition sensitivity to T1 is illustrated in Section 6.4.

There is a broad agreement between the results obtained in this Breast Cancer Study and those of Fischer and Stomper [141, 143], in that no significant changes in IRE and ME with tumour grade and nodal status were found in either study. It is unclear, however, if

pharmacokinetic modelling of their data using the model proposed in this work would confirm the finding that a significant difference in PK variables can exist even if the BB variables extracted from the same DEMRI datasets remain constant.

In the two studies where a significant correlation between histological tumour grades and lymph-node status and DEMRI findings in breast cancer was reported [142, 144], the parameters used for the quantification of DEMRI were black-box enhancement ratios, similar to the BB QDEMRI variables described in this study (ME and IRE). Early enhancement ratios at fixed time points following the administration of the contrast are related to IRE, whereas maximal enhancement ratio corresponds to the variable ME. These results are in contradiction with the findings of the Breast Cancer Study presented in this thesis where no significant association of similar BB parameters (IRE and ME) with tumour grade and nodal status was found.

Buckley and Mussurakis have compared tumour grade (and other histopathological findings) to the enhancement ratios, but not to PK variables [142]. In their earlier work, PK variables were shown to differ significantly between benign and malignant lesions [222], but did not correlate with MVD measurements [118]. An apparent contradiction between the findings obtained in this study and those reported by Mussurakis' group could perhaps be investigated by performing both analysis methods (the one used in this thesis and the method used in [142]) on DEMRI datasets acquired in these two studies.

The capacity of this method to provide a measure of fractional volume of EES (f_{ex}) was similarly assessed by performing an implicit functional validation in the Hand RA Study. Tissue oedema is a primary target for intra-articular steroid therapy in RA, with consequently predictable rapid reduction in f_{ex}. QDEMRI analysis was performed in a randomised study design at three time points during the course of therapy in early RA. The validity of the

measurements of f_{ex}-related PK variable (A) was assessed by its capacity to measure f_{ex} reduction at three months after the start of therapy with IACS.

The main finding of the Hand RA Study was that the post-hoc analysis of changes of QDEMRI variables at three months after the initiation of treatment revealed a significant reduction in EES related variable A (which is directly proportional to f_{ex}) only in the MTX+IACS group. This is in accordance with the expected action of the intra-articular steroids on the reduction of tissue oedema in inflammatory disorders. A slow acting MTX group served as a control at the first follow-up (three months after the initiation of treatment). No significant change in variable A was detected in this control group at the first follow-up due to the slower and more gradual onset of MTX induced effects.

The results of the Hand RA Study also demonstrate a significant reduction of the total volume of the inflamed synovium in the MTX+IACS group at first follow-up. This is consistent with the findings of other MRI studies where the volume of the enhanced synovium was used as a primary MRI endpoint in assessing the effect of steroid treatment in RA [183, 184, 195]. The results obtained in this study, however, indicate that the average fractional volume of the EES within the residual synovium also decreases following therapy.

Pharmacokinetic modelling of Gd-DTPA enhanced MRI in RA has not been reported to date and consequently no similar measurements of f_{ex} in synovial tissues were available for comparison with the results obtained in this work. As discussed in Section 7.2, pharmacokinetic modelling of dynamic MRI with the application of macro-molecular contrast media in animal models of arthritis [196, 197] and inflammation [198] does not allow the measurement of f_{ex}. These methods allow the measurement of the fractional plasma volume (PV) but the authors note that PV does not correlate with histological assessment of synovitis nor does it allow the discrimination between the inflamed tissue and the surrounding parenchyma. Furthermore, MMCM-based methods require prohibitively

long DEMRI acquisitions (in excess of 30 minutes) as well as simultaneous sampling of Cp(t), making it less suitable for clinical applications.

In the Hand RA Study, a significant treatment-induced change in all examined BB and PK variables (with the exception of fractional transfer rate k_{21}) was measured in both treatment groups. In the second part of this study, both patient groups received identical treatment and at the second follow-up (twelve months after baseline assessment), no significant differences between the two treatment groups were detected. This suggests that the administration of IACS did not confer any additional long-term therapeutic benefit. In this study, BB variables IRE and ME provide an equivalent estimate of the treatment effectiveness, due to the fact that they are primarily influenced by the variable A. A significant change in A is therefore translated into a significant change in IRE and ME, if the value of k_{21} remains constant.

A comparison between the measurements of BB and PK variables indicates that the level of agreement between these two groups of variables depends on the nature and the magnitude of differences in the underlying microcirculatory characteristics of the examined tissues. Whereas in the Breast Cancer Study a significant association between tumour grades and QDEMRI variables was found only in the PK variables subset, in the two RA studies both sets of variables demonstrated a similar pattern of change during the course of treatment.

A more pronounced relationship between PK variables and histological tumour grade in the Breast Cancer Study and marginally higher sensitivity to treatment induced changes in two RA studies could be attributed to the fact that PK analysis utilises measured DEMRI curves in their entirety whereas individual BB variables are extracted from limited subsets of the acquired data.

Although the described method for QDEMRI analysis yielded promising results in three different clinical applications, several problems were identified during the model

development and practical implementation. A large amount of scatter in the measurements obtained in the Breast Cancer Study and the lack of correlation between QDEMRI findings (the permeability-related variables, in particular) and the lymph node status suggest the importance of covariates which were not accounted for in this method. The most important covariates include pre-contrast T1 value of the individual lesions and the properties of individual, subject-specific description of Gd-DTPA concentration in blood plasma, Cp(t). Due to the lack of these measurements, PK variables extracted in this study could not be converted to absolute individual values of f_{ex} and K^{trans}. If these covariates are not accounted for, this method will be of limited value in the assessment of individual lesions and tissue characterisation. Due to the fact that most of the sources of uncertainty that severely impair the capacity of this method to characterise individual lesions are essentially randomly distributed, the randomised controlled studies, such as two RA studies presented in this report, are less likely to be adversely influenced by the lack of individual $T1_0$ and Cp(t) measurements and other sources of error. Therefore, this QDEMRI method can be used in the assessment of treatment effectiveness in its present form. It is nevertheless possible that the inclusion of $T1_0$ and Cp(t) measurements may increase the sensitivity of the method and allow the measurement of smaller treatment-induced changes in RA.

The strength of the arguments for the introduction of the proposed changes to the pharmacokinetic model could have been examined formally by replicating the methods applied by other research groups and performing full analysis of the data collected in the three clinical studies using multiple model formulations. This also applies to the measurement of BB variables. The true value of the proposed moving-window algorithms could have been tested by performing a direct comparison with the measurement of BB variables used in similarly designed clinical studies. Furthermore, the influence of acquisition and sampling strategies on the performance of the QDEMRI method could have been investigated in more detail by extending the scope of Monte Carlo simulations presented in Chapter 4 to include factors such as T1 sensitivity.

Throughout the development of the proposed QDEMRI method, the need to increase the robustness and objectivity of the measurements compared to the existing approaches was one of the most important aims. Although the set of decisions taken to meet this aim can certainly be justified theoretically, they have not been tested on experimental data collected in this project. For example, the reproducibility of pre-processing stages of QDEMRI analysis was not assessed formally. The assessment of reproducibility from the point of acquisition could have been used as one of the criteria for the comparison of different sampling and analysis methods in addition to the capacity of derived variables to reflect expected functional differences in microcirculation. An important measure of in-vivo precision of this method could be obtained by performing scan-rescan reproducibility measurements. Serial measurements of synovial tissues in patients with RA could also be used to quantify the degree of spontaneous fluctuations of disease activity, unrelated to the effect of specific therapies.

The statistical analysis of the measurements obtained in this project was limited to the analysis of individual QDEMRI variables and their isolated performance within the chosen models used for implicit functional validation. It is possible that the application of more sophisticated multivariate statistical methods and the inclusion of clinical and laboratory findings may increase the amount of information gained from QDEMRI analysis.

A continual evaluation of new DEMRI acquisition strategies and emerging MRI contrast agents should be undertaken in order to increase the capability of the QDEMRI analysis to provide a more specific measure of truly quantitative physiological variables that characterise tissue microcirculation. The method described here can be used for investigation of other soft tissue tumours and other joints affected by RA. The theoretical evaluation of new acquisition protocols should be performed initially by applying Monte Carlo simulations by extending the method illustrated in Chapter 4. This method could identify a limited number of the most promising acquisition strategies suited to the investigation of particular

pathology (with respect to their location and size). These can then be further tested by performing phantom measurements and finally, limited pilot studies can be used to evaluate the performance of the chosen acquisition strategy in a clinical setting.

The work presented in this thesis demonstrated the feasibility of quantitative analysis of dynamic Gd-DTPA enhanced MRI acquired within a clinical setting, using standard imaging hardware. Fast and robust image processing and computational algorithms, requiring minimal user interaction, were developed and implemented on a readily available PC platform. The capacity of this method to extract measurements related to important physiological variables (capillary permeability and the fractional volume of the extracellular space) was demonstrated through its application in two different angiogenesis-dependent diseases. Whereas the results obtained in this thesis indicate that the utility of this approach in routine clinical evaluation of individual lesions is limited at present, they confirm its potential role as a non-invasive, objective method for measurement of treatment-induced changes in RA, even in its current form.

Perhaps the most significant recent development in the study of angiogenesis, which is directly related to the work presented in this thesis, is the widespread acceptance of the notion that angiogenesis plays a central role in the evolution of RA. This development led to the introduction of novel specific anti-angiogenic therapies for RA, such as biological anticytokine agents infliximab and etanercept [166, 167]. With further development of similar therapeutic agents, the need for serial, non-invasive and objective assessment of the treatment effects on abnormal synovial microcirculation is likely to increase in the coming years [177]. The method for QDEMRI analysis described in this thesis has a potential to fulfil this role as demonstrated by the results obtained in two clinical RA studies presented in Chapter 7. It incorporates pharmacokinetic modelling of dynamic Gd-DTPA enhanced MRI which has been utilised in the assessment of angiogenesis in cancer but not yet applied in the

clinical evaluation of RA. This work, therefore, presents the first attempt to apply pharmacokinetic modelling of Gd-DTPA kinetics in clinical studies of RA.

This method may be of particular value in the pharmaceutical research. "Proof-of-concept" studies of anti-angiogenic therapeutic agents could be performed on relatively small numbers of patients. An indication of a potential drug effect can possibly be obtained earlier, due to the fact that this method can reveal subclinical changes which are in the direct pathway of the angiogenic treatment. Possible applications of this method include not only the monitoring of therapies in RA but also the evaluation of neo-adjuvant chemotherapy in soft tissue tumours.

With further advances in MRI acquisition techniques and the formulation of novel MRI contrast agents, the present limitations of QDEMRI analysis will continue to be addressed and this method will gain a more prominent role in the clinical evaluation of angiogenesis-dependent diseases. The work presented in this thesis hopefully presents a step towards its introduction into clinical practice.

Appendices

Appendix A.

QDEMRI variables: symbols and units

Variable	Units	Description
A	s^{-1}	PK variable (proportional to the volume of the extracellular fluid)
k_{21}	s^{-1}	PK variable (proportional to the capillary permeability)
Ak_{21}	s^{-2}	PK variable (proportional to the capillary permeability and the volume of the extracellular space)
ME	a.u.	BB variable, maximal enhancement, with 100*(ME-1) representing % SI increase over baseline
IRE	s^{-1}	BB variable, initial rate of enhancement, with 100*IRE representing % SI increase per second
WOS	s^{-1}	BB variable, the rate of washout with 100*WOS representing % SI change per second (Breast Cancer Study only)
N-BB	count	a total number of voxels included in BB analysis (proportional to the volume of the enhancing tissue (not included in Breast Cancer Study)
N-PK	count	a total number of voxels included in PK analysis (proportional to the volume of the enhancing tissue (not included in Breast Cancer Study)

Appendix B.

Derivation of the expression for normalised SI in spoiled GE sequence following the administration of Gd-DTPA

S_0 Pre-contrast (baseline) SI

S_C Post-contrast SI

The ratio between post-contrast and baseline SI is given by:

$$\frac{S_C}{S_0} = \frac{k\rho \dfrac{1-e^{-\frac{TR}{T1_c}}}{1-\cos\varphi \cdot e^{-\frac{TR}{T1_c}}} \cdot e^{-\frac{TE}{T2^*_c}} \cdot \sin\varphi}{k\rho \dfrac{1-e^{-\frac{TR}{T1_0}}}{1-\cos\varphi \cdot e^{-\frac{TR}{T1_0}}} \cdot e^{-\frac{TE}{T2^*_0}} \cdot \sin\varphi} \qquad \text{Eq. B - 1}$$

After substituting post-contrast relaxation times with expressions Eq. 2-14 and Eq. 2-16, the following expression is obtained:

$$\frac{S_C}{S_0} = \frac{\dfrac{1-e^{-TR\left(\frac{1}{T1_0}+\alpha C\right)}}{1-\cos\varphi \cdot e^{-TR\left(\frac{1}{T1_0}+\alpha C\right)}} \cdot e^{-TE\left(\frac{1}{T2^*_0}+\beta' C\right)}}{\dfrac{1-e^{-\frac{TR}{T1_0}}}{1-\cos\varphi \cdot e^{-\frac{TR}{T1_0}}} \cdot e^{-\frac{TE}{T2^*_0}}} \qquad \text{Eq. B - 2}$$

The following substitution is made for ease of notation:

$$e^{-\frac{TR}{T1_0}} = x \qquad \text{Eq. B - 3}$$

Furthermore, for low concentrations and short repetition times TR:

$$TR\alpha C \ll 1$$

$$e^{-TR\alpha C} \approx 1 - TR\alpha C \qquad \text{Eq. B - 4}$$

Also, for very short TE and low concentrations

$$e^{-TE\beta' C} \approx 1 \qquad \text{Eq. B - 5}$$

Normalised SI is then given by:

$$\frac{S_C}{S_0} = \frac{\dfrac{1 - x \cdot (1 - TR\alpha C)}{1 - \cos\varphi \cdot x \cdot (1 - TR\alpha C)}}{\dfrac{1 - x}{1 - \cos\varphi \cdot x}} =$$

$$= \frac{1 - x + x \cdot TR\alpha C}{1 - x} \cdot \frac{1 - \cos\varphi \cdot x}{1 - \cos\varphi \cdot x + \cos\varphi \cdot x \cdot TR\alpha C} =$$

$$= \left(1 + \frac{x}{1 - x} \cdot TR\alpha C\right) \cdot \frac{1}{1 + \dfrac{\cos\varphi \cdot x \cdot TR\alpha C}{1 - \cos\varphi \cdot x}} \approx \qquad \text{Eq. B - 6}$$

$$\approx 1 + \frac{x}{1 - x} \cdot TR\alpha C = 1 + \frac{e^{-\frac{TR}{T1_0}}}{1 - e^{-\frac{TR}{T1_0}}} \cdot TR\alpha C$$

Assuming that:

$$\frac{1}{1 + \dfrac{\cos\varphi \cdot x \cdot TR\alpha C}{1 - \cos\varphi \cdot x}} \approx 1$$

$$\cos\varphi \cdot x \cdot TR\alpha C \ll 1 - \cos\varphi \cdot x \qquad \text{Eq. B - 7}$$

$$C \ll \frac{1 - \cos\varphi \cdot x}{\cos\varphi \cdot x \cdot TR\alpha}$$

Normalised SI can be approximated by:

$$\frac{S_C}{S_0} \approx 1 + \frac{x}{1-x} \cdot TR\alpha C = 1 + \frac{e^{-\frac{TR}{Tl_0}}}{1-e^{-\frac{TR}{Tl_0}}} \cdot TR\alpha C \qquad \text{Eq. B - 8}$$

Finally:

$$\frac{S_C}{S_0} \approx 1 + a \cdot C \qquad \text{Eq. B - 9}$$

where:

$$a = \frac{e^{-\frac{TR}{Tl_0}}}{1-e^{-\frac{TR}{Tl_0}}} \cdot TR\alpha \qquad \text{Eq. B - 10}$$

Appendix C.

Results of the Kolomogorov-Smirnov tests

Tumour Grade	A	k21	Ak21	ME	IRE	WOS
Grade 1	.707	.689	.997	.759	.999	.989
Grade 2	.948	.083	.449	.966	.968	.707
Grade 3	.989	.138	.738	.888	.700	.414

Table C - 1 Asymptotic 2-tail significance of the Kolomogorov-Smirnov test in the Breast Cancer Study

Scan Group	N-PK	N-BB	A	k21	Ak21	ME	IRE
MTX (1)	.962	.944	.625	.972	.965	.979	.898
MTX (2)	.783	.815	.722	.439	.793	.869	.989
MTX (3)	.936	.843	.787	.999	.325	.815	.218
MTX+IACS (1)	.894	.912	.758	.636	.552	.868	.259
MTX+IACS (2)	.872	.928	.151	.755	.270	.504	.598
MTX+IACS (3)	.991	.977	.279	.889	.587	.609	.892

Table C - 2 Asymptotic 2-tail significance of the Kolomogorov-Smirnov test in the Hand RA Study

Scan Group	N-PK	N-BB	A	k21	Ak21	ME	IRE
LEF (1)	.963	.952	1.000	.897	.620	.860	.995
LEF (2)	.955	.929	.945	.729	.755	.695	.899
MTX (1)	.896	.886	.982	.883	1.000	.602	.999
MTX (2)	.829	.958	.911	.569	.955	.996	.900

Table C - 3 Asymptotic 2-tail significance of the Kolomogorov-Smirnov test in the Knee RA Study

Appendix D.

Colour-coding schemes for parametric images

ME	**IRE** [s^{-1}]	**WOS** [s^{-1}]
1.1 to 1.2	0.001 to 0.002	> 0.004
1.2 to 1.4	0.002 to 0.003	0.002 to 0.003
1.4 to 1.6	0.003 to 0.004	0.001 to 0.002
1.6 to 1.8	0.004 to 0.005	-0.001 to 0.001
1.8 to 2.0	0.005 to 0.006	-0.002 to -0.001
2.0 to 2.2	0.006 to 0.007	-0.003 to -0.002
2.2 to 2.4	0.007 to 0.008	-0.004 to -0.003
> 2.4	> 0.008	-0.005 to -0.004

Figure D - 1 Colour-coding scheme in parametric images of ME, IRE and WOS in the Breast Cancer Study

ME [%] and **IRE** [%/min]	f_{ex} [fraction]	K^{trans} [min^{-1}]
0 to 35	0 to 0.1	0 to 0.1
35 to 70	0.1 to 0.2	0.1 to 0.2
70 to 105	0.2 to 0.3	0.2 to 0.3
105 to 140	0.3 to 0.4	0.3 to 0.4
140 to 175	0.4 to 0.5	0.4 to 0.5
175 to 210	0.5 to 0.6	0.5 to 0.6
210 to 245	0.6 to 0.7	0.6 to 0.7
245 to 280	0.7 to 0.8	0.7 to 0.8
280 to 315	0.8 to 0.9	0.8 to 0.9
> 315	> 0.9	> 0.9

Figure D - 2 Colour-coding scheme in parametric images of ME, IRE and f_{ex} and K^{trans} in the two RA Studies

Appendix E.

A sample source code: Monte Carlo Simulation

```
1  /*************************************************************************
2   Application:   Monte Carlo Simulation
3   Platform:      Microsoft DOS/Windows
4   Author:        Aleksandra Radjenovic (inlcudes routines adopted from
5                  Numerical Recipes by Press, W. H. et al, 1994)
6   Date:          June 2000
7
8  *************************************************************************/
9
10 #include    <stdio.h>
11 #include    <stdlib.h>
12 #include    <string.h>
13 #include    <math.h>
14 #include    "nr.h"
15 #include    "nrutil.h"
16 #include    "simulate.h"
17
18 /*************************************************************************
19  FUNCTION:      main()
20 *************************************************************************/
21 void main(void)
22 {
23     int     i, j, k, l;
24     OutFile = fopen("MC_dump.txt", "wt");
25     if (OutFile == NULL)
26     {
27         printf("fopen ERROR!\n");
28         exit(1);
29     }
30     M_in = Dose * BW;
31     fprintf(OutFile, "Simulation\tMC_No\tk21\tfex\tfit_k21\tfit_fex\t"\
32                      "fit_chi2\tno_iterations\n");
33     for (i=0; i<1; i++)
34     {
35         Initialise();
36         Fill_Simulation_Parameters(i);
37         for (j=0; j<NO_POINTS; j++)
38         {
39             Time[j] = Time[j] = j * TimeStep;
40
41             if (Time[j] <= SimParams[i].mTINF)
42                 Tau[j] = Time[j];
43             else
44                 Tau[j] = SimParams[i].mTINF;
45         }// j loop: concentrations time
46         Fill_Sample_Data(i);
47         Look_Up(i);
48         for (l = 0; l<MATRIX_DIM; l++)
49         {
50             for(k=0; k<MATRIX_DIM; k++)
51             {
52                 TINF = TINFSet;
53
54                 Fill_Simulation_Parameters(i);
55                 Fill_Sample_Data(i);
56                 Success     = NO_MONTE_CARLO;
57                 SuccessFit  = NO_MONTE_CARLO;
```

```
58
59                  Calculate_ME_IRE_From_My_Function(k, l, i);
60                  // Start Monte Carlo Here
61                  Do_Monte_Carlo(i, k, l);
62                  Fill_Sample_Data(i);
63                  Perform_Calculations(i, k, l);
64              }// l loop
65          }// k loop
66      }// simulation loop i
67      NumOfSims = i;
68      for (i=0; i<NumOfSims; i++)
69      {
70          Print_Simulation_Summary(i);
71          //accuracy of fex
72  #define PS(fld, lab)    Print_Summary(i, OffsetOf(TSimResult, fld), lab)
73          PS(mFit_fex_Accuracy, "\nAccuracy of fex");
74          PS(mFit_fex_Std_over_Mean, "Precision of fex");
75          PS(mFit_k21_Accuracy, "\nAccuracy of k21");
76          PS(mFit_k21_Std_over_Mean, "Precision of k21");
77          PS(mFit_fex_Accuracy_Trim, "\nAccuracy of fex trimmed");
78          PS(mFit_fex_Std_over_Mean_Trim, "Precision of fex trimmed");
79          PS(mFit_k21_Accuracy_Trim, "\nAccuracy of k21 trimmed");
80          PS(mFit_k21_Std_over_Mean_Trim, "Precision of k21 trimmed");
81  #undef PS
82          Print_All(i);
83      }
84      fclose(OutFile);
85
86  }
87
88  /*****************************************************************************
89   FUNCTION:      Do_Monte_Carlo()
90  *****************************************************************************/
91  void Do_Monte_Carlo
92  (
93      int i,
94      int k,
95      int l
96  )
97  {
98      int n;
99
100     struct TSimulationParameters *pSP = &SimParams[i];
101     struct TSimBlock *pSB = &SimBlock[k][l];
102     struct TRunningSums *pRS = &RunningSums[k][l];
103     struct TPlateau *pPD = &PlateauData[k][l];
104     struct TNonLin *pNL = &NonlinData[k][l];
105     struct TSlope *pSD = &SlopeData[k][l];
106     memset(&RunningSums[k][l], 0, sizeof(struct TRunningSums));
107     for (n=0; n<NO_MONTE_CARLO; n++)
108     {
109
110         Create_Concentration_Curves(
111             pSP->mV1_1, pSP->mV1_2, pSP->mTINF, pSP->mkel_1,
112             pSP->mkel_2, pSP->ma1_Tofts,  pSP->ma2_Tofts,
113             pSP->mk1_Tofts,  pSP->mk2_Tofts,
114             pSB->mSB_k21, pSB->mSB_u_1, pSB->mSB_v_1,
115             pSB->mSB_u_2, pSB->mSB_v_2);
116         A = pSP->mA * pSB->mSB_fex;
117         Create_Noiseless_Signal(A);
118
119         Create_Noisy_Curves(pSP->mNoiseFactor);
120         Select_Sparse_Sample(
121             pSP->mStart, pSP->mNumber_to_sample_int,
122             pSP->mSamplingInterval);
123         Get_Plateau(S1_WithNoiseSample, k, l, i);
124         Get_Slope(S1_WithNoiseSample, k, l, i);
125
126         pRS->mPlateau += pPD->mVal;
127         pRS->mPlateau2 += pPD->mVal * pPD->mVal;
128         pRS->mSlope += pSD->mMaxSlope;
129         pRS->mSlope2 += pSD->mMaxSlope * pSD->mMaxSlope;
130         pRS->mStartIRE += pSD->mMaxSlopeInterval;
131         pRS->mStartIRE2 += pSD->mMaxSlopeInterval *
```

```
                    pSD->mMaxSlopeInterval;
        pRS->mRatio += pSD->mTheRatio;
        pRS->mRatio2 += pSD->mTheRatio * pSD->mTheRatio;
        NumOfFuncCalls = 0;
        // revert now to the pre-set assumed values
        KEL = pSP->mkel_2;
        TDASH = pSP->mTINF;
        Get_Init_Est_k21(k, l);
        Get_Init_Est_A(k, l, i);
        status = Calculate_Fit(S1_WithNoiseSample, k, l, i);

        MC_k21[n] = pNL->mNL_fitk21;
        MC_fex[n] = pNL->mNL_fit_fex;
        pRS->mk21 += pNL->mNL_fitk21;
        pRS->mk21_2 += pNL->mNL_fitk21*pNL->mNL_fitk21;
        pRS->mfex += pNL->mNL_fit_fex;
        pRS->mfex_2 += pNL->mNL_fit_fex*pNL->mNL_fit_fex;
        pRS->mchi2 += pNL->mNL_fitChi2;
        pRS->mchi2_2 += pNL->mNL_fitChi2*pNL->mNL_fitChi2;
        pRS->mno_its += (double)pNL->mNL_number_of_iterations;
        pRS->mno_its_2 += (double)pNL->mNL_number_of_iterations *
                          pNL->mNL_number_of_iterations;
    }// n loop monte-carlo
}

/*****************************************************************************
 FUNCTION:      Perform_Calculations()
*****************************************************************************/
void Perform_Calculations
(
    int i,
    int k,
    int l
)
{
    struct TSimulationParameters *pSP = &SimParams[i];
    struct TSimBlock *pSB = &SimBlock[k][l];
    struct TRunningSums *pRS = &RunningSums[k][l];
    struct TPlateau *pPD = &PlateauData[k][l];
    struct TNonLin *pNL = &NonlinData[k][l];
    struct TSlope *pSD = &SlopeData[k][l];
    struct TSimResult *pSR = &SimResult[k][l][i];

    Summary_Trimmed(MC_k21, k, l, SuccessFit);

    pSR->mFit_k21_Mean_Trim              = MC_Mean;
    pSR->mFit_k21_Std_Trim               = MC_SD;
    pSR->mFit_k21_Std_over_Mean_Trim     = MC_SDOverMean;

    pSR->mFit_k21_Accuracy_Trim = 100 * (MC_Mean - pSB->mSB_k21 ) /
                                  pSB->mSB_k21;

    Summary_Trimmed(MC_fex, k, l, SuccessFit);

    pSR->mFit_fex_Mean_Trim              = MC_Mean;
    pSR->mFit_fex_Std_Trim               = MC_SD;
    pSR->mFit_fex_Std_over_Mean_Trim     = MC_SDOverMean;

    pSR->mFit_fex_Accuracy_Trim = 100 * (MC_Mean - pSB->mSB_fex) /
                                  pSB->mSB_fex;

    // calculate plateau results
    Summary_Monte_Carlo(pRS->mPlateau, pRS->mPlateau2, Success);

    pSR->mPlateau_Mean          = MC_Mean;
    pSR->mPlateau_Std           = MC_SD;
    pSR->mPlateau_Std_over_Mean = MC_SDOverMean;

    // calculate slope results
    Summary_Monte_Carlo(pRS->mSlope, pRS->mSlope2, Success);

    pSR->mSlope_Mean            = MC_Mean;
    pSR->mSlope_Std             = MC_SD;
    pSR->mSlope_Std_over_Mean   = MC_SDOverMean;
```

```
206
207     // calculate Start
208     Summary_Monte_Carlo(pRS->mStartIRE, pRS->mStartIRE2, Success);
209
210     pSR->mStartIRE_Mean              = MC_Mean;
211     pSR->mStartIRE_Std               = MC_SD;
212     pSR->mStartIRE_Std_over_Mean     = MC_SDOverMean;
213
214     // calculate Ratio
215     Summary_Monte_Carlo(pRS->mRatio, pRS->mRatio2, Success);
216
217     pSR->mMeasured_Ratio_Mean            = MC_Mean;
218     pSR->mMeasured_Ratio_Std             = MC_SD;
219     pSR->mMeasured_Ratio_Std_over_Mean   = MC_SDOverMean;
220
221
222     // calculate k21
223     Summary_Monte_Carlo(pRS->mk21, pRS->mk21_2, SuccessFit);
224
225     pSR->mFit_k21_Mean           = MC_Mean;
226     pSR->mFit_k21_Std            = MC_SD;
227     pSR->mFit_k21_Std_over_Mean = MC_SDOverMean;
228
229     pSR->mFit_k21_Accuracy = 100 * (MC_Mean - pSB->mSB_k21) /
230                              pSB->mSB_k21;
231
232     // calculate fex
233     Summary_Monte_Carlo(pRS->mfex, pRS->mfex_2, SuccessFit);
234
235     pSR->mFit_fex_Mean           = MC_Mean;
236     pSR->mFit_fex_Std            = MC_SD;
237     pSR->mFit_fex_Std_over_Mean = MC_SDOverMean;
238
239     pSR->mFit_fex_Accuracy = 100 * (MC_Mean - pSB->mSB_fex) /
240                              pSB->mSB_fex;
241
242     // calculate chi2
243     Summary_Monte_Carlo(pRS->mchi2, pRS->mchi2_2, SuccessFit);
244
245     pSR->mFit_chi2_Mean              = MC_Mean;
246     pSR->mFit_chi2_Std               = MC_SD;
247     pSR->mFit_chi2_Std_over_Mean     = MC_SDOverMean;
248
249     // calculate no iterations
250     Summary_Monte_Carlo(pRS->mno_its, pRS->mno_its_2, SuccessFit);
251
252     pSR->mFit_NoIts_Mean             = MC_Mean;
253     pSR->mFit_NoIts_Std              = MC_SD;
254     pSR->mFit_NoIts_Std_over_Mean    = MC_SDOverMean;
255
256     pSR->mSuccess = SuccessFit;
257 }
258
259 /*****************************************************************************
260  FUNCTION:      Initialise()
261 *****************************************************************************/
262 void Initialise
263 (
264     void
265 )
266 {
267     SamplingInterval = 10;
268     Start = 0;
269
270     NumberToSample       = ((NO_POINTS + NO_BASELINE - 1) - Start) /
271                             (SamplingInterval) + 1;
272     NumberToSampleInt    = (int) NumberToSample;
273
274
275     TINFAssumed          = 1;
276     TINFPointsAssumed    = (int)(TINFAssumed / TimeStep);
277
278     TINFSet              = 20;
279
```

```
280     TINFPointsSet       = (int)(TINFSet / TimeStep);
281
282     TINF                = TINFSet;
283     TINFPoints = (int)(TINF / TimeStep);
284
285     a1_Tofts = 0.399;
286     a2_Tofts = 0.478;
287     k1_Tofts = 0.0019;
288     k2_Tofts = 0.000185;
289
290     kel_1       = 0.080000000001;
291     kel_2_set   = 0.0009627;
292     kel_2       = kel_2_set;
293
294     T10_set     = 900;
295     T10         = T10_set;
296     Alpha       = 4.5;
297     TR          = 13;
298
299     NoiseFactor = 0.1;
300
301     NPT         = 5;
302     BLOCK       = 5;
303 }
304
305 /*****************************************************************************
306  FUNCTION:      Print_Summary()
307 *****************************************************************************/
308 void Print_Summary
309 (
310     int sim,
311     int offset,
312     char *label
313 )
314 {
315     int k, l;
316     struct TSimResult *p;
317     double val;
318
319     NumInMatrix = MATRIX_DIM * MATRIX_DIM;
320     TempSum     = 0;
321     TempSum2    = 0;
322     TempSummary = 0;
323     for (k=0; k<MATRIX_DIM; k++)
324     {
325         for (l=0; l<MATRIX_DIM; l++)
326         {
327             p = &SimResult[k][l][sim];
328             val = *((double *)((int)p + offset));
329             if (val > 100000)
330             {
331                 NumInMatrix = NumInMatrix - 1;
332                 continue;
333             }
334             TempSum  += val;
335             TempSum2 += (val * val);
336         }
337     }
338     TempSummary = TempSum / NumInMatrix;
339     printf("%s (mean and SD)\t%e\t", label, TempSummary);
340     TempSummary = TempSum2 * NumInMatrix - TempSum * TempSum;
341     TempSummary = TempSummary / NumInMatrix;
342     TempSummary = TempSummary / (NumInMatrix-1);
343     TempSummary = sqrt(TempSummary);
344     printf("%e\n", TempSummary);
345 }
346
347 /*****************************************************************************
348  FUNCTION:      PrintSingle()
349 *****************************************************************************/
350 void Print_Single
351 (
352     int sim,
353     int offset,
```

```
354         char *label
355     )
356     {
357         int k, l;
358         struct TSimResult *p;
359         for (k=0; k<MATRIX_DIM; k++)
360         {
361             for(l=0; l<MATRIX_DIM; l++)
362             {
363                 p = &SimResult[k][l][sim];
364                 OneToPrintBuffer[k][l] = *((double *)(((int)p) + offset));
365             }
366         }
367         Print_Summary_Results(label);
368     }
369
370     /*****************************************************************************
371      FUNCTION:       PrintAll()
372     *****************************************************************************/
373     void Print_All
374     (
375         int sim
376     )
377     {
378     #define PS(fld, lab)    Print_Single(sim, OffsetOf(TSimResult, fld), lab)
379         int k, l;
380         PS(mCalc_IRE, "Calculated IRE");
381         PS(mCalc_ME, "Calculated ME");
382         PS(mCalc_Ratio, "Calculated Ratio");
383         PS(mCalc_TMAX, "Calculated TMAX");
384         PS(mCalc_True_Start, "Calculated True Start");
385         PS(mFit_fex_Mean_Trim, "Calculated Mean Fitted fex_Trim");
386         PS(mFit_fex_Accuracy_Trim, "Calculated Accuracy of Fitted fex_Trim");
387         PS(mFit_fex_Std_Trim, "Calculated SD of Fitted fex_Trim");
388         PS(mFit_fex_Std_over_Mean_Trim, "100*SD/Mean of Fitted fex_Trim");
389         PS(mFit_fex_Mean, "Calculated Mean Fitted fex");
390         PS(mFit_fex_Std, "Calculated SD of Fitted fex");
391         PS(mFit_fex_Std_over_Mean, "100*SD/Mean of Fitted fex");
392         PS(mFit_fex_Accuracy, "Accuracy fex 100*(fitted_fex - set_fex)/set_fex");
393         PS(mFit_k21_Mean_Trim, "Calculated Mean Fitted k21_Trim");
394         PS(mFit_k21_Accuracy_Trim, "Calculated Accuracy of Fitted k21_Trim");
395         PS(mFit_k21_Std_over_Mean_Trim, "100*SD/Mean of Fitted k21_Trim");
396         PS(mFit_k21_Mean, "Calculated Mean Fitted k21");
397         PS(mFit_k21_Std, "Calculated SD of Fitted k21");
398         PS(mFit_k21_Std_over_Mean, "100*SD/Mean of Fitted k21");
399         PS(mFit_k21_Accuracy, "Accuracy k21 = 100*(k21 fit - k21 set)/k21 fit");
400         PS(mFit_chi2_Mean, "Calculated Mean Fitted Chi2");
401         PS(mFit_chi2_Std, "Calculated SD of Fitted Chi2");
402         PS(mFit_chi2_Std_over_Mean, "100*SD/Mean of Fitted Chi2");
403         PS(mFit_NoIts_Mean, "Calculated Mean Fitted No Iterations");
404         PS(mFit_NoIts_Std, "Calculated SD of Fitted No Iterations");
405         PS(mFit_NoIts_Std_over_Mean, "100*SD/Mean of Fitted No Iterations");
406         PS(mPlateau_Mean, "Calculated Mean Measured ME");
407         PS(mPlateau_Std, "Calculated SD of Measured ME");
408         PS(mPlateau_Std_over_Mean, "100*SD/Mean of Measured ME");
409         PS(mSlope_Mean, "Calculated Mean Measured IRE");
410         PS(mSlope_Std, "Calculated SD of Measured IRE");
411         PS(mSlope_Std_over_Mean, "100*SD/Mean of Measured IRE");
412         PS(mMeasured_Ratio_Mean, "Calculated Mean Measured Ratio");
413         PS(mMeasured_Ratio_Std, "Calculated SD of Measured Ratio");
414         PS(mMeasured_Ratio_Std_over_Mean, "100*SD/Mean of Measured Ratio");
415         PS(mStartIRE_Mean, "Calculated Mean Measured Start");
416         PS(mStartIRE_Std, "Calculated SD of Measured Start");
417         PS(mStartIRE_Std_over_Mean, "100*SD/Mean of Measured Start");
418         for (k=0; k<MATRIX_DIM; k++)
419         {
420             for (l=0; l<MATRIX_DIM; l++)
421                 OneToPrintBuffer[k][l] = SimResult[k][l][sim].mSuccess;
422         }
423         Print_Summary_Results("Success of MC runs");
424
425     #undef  PS
426     }
427
```

```
/*****************************************************************************
 FUNCTION:      Create_Concentration_Curves()
*****************************************************************************/
void Create_Concentration_Curves
(
    double V1_1,
    double V1_2,
    double TINF,
    double kel_1,
    double kel_2,
    double a1_Tofts,
    double a2_Tofts,
    double k1_Tofts,
    double k2_Tofts,
    double k21,
    double u_1,
    double v_1,
    double u_2,
    double v_2
)
{
    int     i;
    for (i=0; i<NO_POINTS; i++)
    {
        C1_1[i] = M_in / V1_1 / TINF / kel_1 *
                  (exp(kel_1 * Tau[i]) - 1) * exp(-kel_1 * Time[i]);

        C1_2[i] = M_in / V1_2 / TINF / kel_2 *
                  (exp(kel_2 * Tau[i]) - 1) * exp(-kel_2 * Time[i]);
        C1[i] = C1_1[i] + C1_2[i];
        C2_1[i] = M_in / V1_1 / TINF *
                  (
                     u_1 * (exp(kel_1 * Tau[i]) - 1) * exp(-kel_1 * Time[i]) -
                     v_1 * (exp(k21 * Tau[i]) - 1) * exp(-k21 * Time[i])
                  );
        C2_2[i] = M_in / V1_2 / TINF *
                  (
                     u_2 * (exp(kel_2 * Tau[i]) - 1) * exp(-kel_2 * Time[i]) -
                     v_2 * (exp(k21 * Tau[i]) - 1) * exp(-k21 * Time[i])
                  );
        C2[i] = C2_1[i] + C2_2[i];
        C1_Tofts[i] = a1_Tofts * exp(-k1_Tofts * Time[i]) +
                      a2_Tofts * exp(-k2_Tofts * Time[i]);

        C2_Tofts[i] = a1_Tofts * k21 / (k21 - k1_Tofts) *
                     ( exp(-k1_Tofts * Time[i]) - exp(-k21 * Time[i]) ) +
                      a2_Tofts * k21 / (k21 - k2_Tofts) *
                     ( exp(-k2_Tofts * Time[i]) - exp(-k21 * Time[i]));
    }
}

/*****************************************************************************
 FUNCTION:      Create_Noiseless_Signal()
*****************************************************************************/
void Create_Noiseless_Signal
(
    double A
)
{
    int     i;
    for (i= 0; i<NO_BASELINE; i++)
    {
        S1[i] = 1.0;
        S2[i] = 1.0;
        S3[i] = 1.0;
    }
    for (i= NO_BASELINE; i<NO_POINTS+NO_BASELINE; i++)
    {
        S1[i] = 1 + A * C2_2[i-NO_BASELINE];
        S2[i] = 1 + A * C2[i-NO_BASELINE];
        S3[i] = 1 + A * C2_Tofts[i-NO_BASELINE];
    }
}

```

```
/*****************************************************************************
 FUNCTION:      Create_Noisy_Curves
*****************************************************************************/
void Create_Noisy_Curves
(
    double NoiseFactor
)
{
    int     i;
    for (i=0; i<(NO_POINTS + NO_BASELINE); i++)
    {
        SampleTime[i] = i * TimeStep;
        S1_WithNoise[i] = S1[i] * (1 + NoiseFactor * gasdev(&Idum));
        S2_WithNoise[i] = S2[i] * (1 + NoiseFactor * gasdev(&Idum));
        S3_WithNoise[i] = S3[i] * (1 + NoiseFactor * gasdev(&Idum));
    }
}

/*****************************************************************************
 FUNCTION:      Select_Sparse_Sample()
*****************************************************************************/
void Select_Sparse_Sample
(
    int Start,
    int NumberToSampleInt,
    int SamplingInterval
)
{
    int     i;
    for(i=0; i<NumberToSampleInt; i++)
    {
        S1_WithNoiseSample[i] = S1_WithNoise[Start + i * SamplingInterval];
        S2_WithNoiseSample[i] = S2_WithNoise[Start + i * SamplingInterval];
        S3_WithNoiseSample[i] = S3_WithNoise[Start + i * SamplingInterval];

        S1_WithoutNoiseSample[i] = S1[Start + i * SamplingInterval];
        S2_WithoutNoiseSample[i] = S2[Start + i * SamplingInterval];
        S3_WithoutNoiseSample[i] = S3[Start + i * SamplingInterval];
    }

}

/*****************************************************************************
 FUNCTION:      Fill_Sample_Data()
*****************************************************************************/
void Fill_Sample_Data
(
    int index
)
{
    int     i, j;
    struct TSimBlock *pSB;
    for (j=0; j<MATRIX_DIM; j++)
    {
        for(i = 0; i<MATRIX_DIM; i++)
        {
            pSB = &SimBlock[i][j];

            pSB->mSB_fex    = 0.1 + j * 0.1;        // for 5 0.1 + j*0.2
            pSB->mSB_k21    = 0.01 + i * 0.01;      // for 5: 0.01 + i*0.02
            pSB->mSB_kel_1 = SimParams[index].mkel_1;
            pSB->mSB_kel_2 = SimParams[index].mkel_2;

            pSB->mSB_v_1 = 1 / (pSB->mSB_k21 - pSB->mSB_kel_1);
            pSB->mSB_u_1 = pSB->mSB_k21 / pSB->mSB_kel_1 * pSB->mSB_v_1;
            pSB->mSB_v_2 = 1 / (pSB->mSB_k21 - pSB->mSB_kel_2);
            pSB->mSB_u_2 = pSB->mSB_k21 / pSB->mSB_kel_2 * pSB->mSB_v_2;
        }
    }
}

/*****************************************************************************
 FUNCTION:      Fill_Sample_Data_With_Noise
*****************************************************************************/
```

```
576  void Fill_Sample_Data_With_Noise
577  (
578      int index
579  )
580  {
581      int     i, j;
582      struct TSimBlock *pSB;
583      for ( j=0; j<MATRIX_DIM; j++ )
584      {
585          for(i = 0; i<MATRIX_DIM; i++)
586          {
587              pSB = &SimBlock[i][j];
588
589              pSB->mSB_fex    = 0.1 + j * 0.1;    // for 5 0.1 + j*0.2
590              pSB->mSB_k21    = 0.01 + i*0.01;    // for 5: 0.01 + i*0.02
591              pSB->mSB_fex    = pSB->mSB_fex + 0.1 * gasdev(&Idum);
592              pSB->mSB_k21    = pSB->mSB_k21 + 0.01 * gasdev(&Idum);
593              while (pSB->mSB_fex < 0)
594              {
595                  pSB->mSB_fex = 0.1 + j * 0.1;
596                  pSB->mSB_fex = pSB->mSB_fex + 0.1 * gasdev(&Idum);
597              }
598              while (pSB->mSB_k21 < 2 * SimParams[index].mkel_2)
599              {
600                  pSB->mSB_k21 = 0.01 + i * 0.01;
601                  pSB->mSB_k21 = pSB->mSB_k21 + 0.01 * gasdev(&Idum);
602              }
603
604              pSB->mSB_kel_1  = SimParams[index].mkel_1;
605              pSB->mSB_kel_2  = SimParams[index].mkel_2;
606
607              pSB->mSB_v_1 = 1 / (pSB->mSB_k21 - pSB->mSB_kel_1);
608              pSB->mSB_u_1 = pSB->mSB_k21 / pSB->mSB_kel_1 * pSB->mSB_v_1;
609              pSB->mSB_v_2 = 1 / (pSB->mSB_k21 - pSB->mSB_kel_2);
610              pSB->mSB_u_2 = pSB->mSB_k21 / pSB->mSB_kel_2 * pSB->mSB_v_2;
611          }//i
612      }//j
613  }
614
615  /*****************************************************************************
616   FUNCTION:      Fill_Simulation_Parameters()
617  *****************************************************************************/
618  void Fill_Simulation_Parameters
619  (
620      int i
621  )
622  {
623      struct TSimulationParameters *pSP = &SimParams[i];
624
625      pSP->mNumber_to_sample_int  = NumberToSampleInt;
626      pSP->mSamplingInterval      = SamplingInterval;
627      pSP->mStart                 = Start;
628      pSP->mTINF                  = TINF;
629      pSP->mTINFPoints            = TINFPoints;
630      pSP->mTINFAssumed           = TINFAssumed;
631      pSP->mTINFPointsAssumed     = TINFPointsAssumed;
632      pSP->mBW                    = BW;
633      pSP->mDose                  = Dose;
634      pSP->mM_in                  = Dose * BW;
635      pSP->ma1_Tofts              = a1_Tofts;
636      pSP->ma2_Tofts              = a2_Tofts;
637      pSP->mk1_Tofts              = k1_Tofts;
638      pSP->mk2_Tofts              = k2_Tofts;
639      pSP->mkel_1                 = kel_1 * 10.0 / TINF;
640      pSP->mkel_2                 = kel_2;
641      pSP->mV1_Fraction1          = V1_Fraction1;
642      pSP->mV1_Fraction2          = V1_Fraction2;
643      pSP->mV1_1                  = BW * V1_Fraction1 * TINF / 10.0;
644      pSP->mV1_2                  = BW * V1_Fraction2;
645      pSP->mT10                   = T10;
646      pSP->mT10_set               = T10_set;
647      pSP->mAlpha                 = Alpha;
648      pSP->mTR                    = TR;
649      pSP->mA                     = TR / 1000 * Alpha * exp(-TR / T10) /
```

```
650                                         (1 - exp(-TR / T10));
651         pSP->mA_set                   = TR / 1000 * Alpha * exp(-TR / T10_set) /
652                                         (1 - exp(-TR / T10_set));
653         pSP->mNoiseFactor             = NoiseFactor;
654         pSP->mNPT                     = NPT;
655         pSP->mBLOCK                   = BLOCK;
656     }
657
658     /*****************************************************************************
659      FUNCTION:       My_Compare
660     *****************************************************************************/
661     int  My_Compare
662     (
663         const void *p1,
664         const void *p2
665     )
666     {
667         double  d1,d2;
668
669         d1 = ( (struct TTempSort *)p1 )->mValue;
670         d2 = ( (struct TTempSort *)p2 )->mValue;
671
672         if (d1 < d2)
673             return -1;
674         if (d1 == d2)
675             return 0;
676         return 1;
677     }
678
679     /*****************************************************************************
680      FUNCTION:       Get_Plateau()
681     *****************************************************************************/
682     void Get_Plateau
683     (
684         double *column,
685         int x,
686         int y,
687         int sim_index
688     )
689     {
690         int     i, k;
691         double  sum_std, plateau;
692         int     BLOCK = SimParams[sim_index].mBLOCK;
693         int     ZZ = SimParams[sim_index].mNumber_to_sample_int;
694         double  DELTA = SimParams[sim_index].mSamplingInterval * TimeStep;
695         struct TTempSort    *pTS;
696         struct TPlateau     *pPD;
697         for ( k = 0; k<=ZZ-BLOCK; k++)
698         {
699             sum_std = 0;
700             plateau = 0;
701
702             for (i = 0; i<BLOCK; i++)
703             {
704                 plateau += column[k+i];
705             }
706             //*************************************************************************
707             //  store the values for sorting in the temp structure
708             //*************************************************************************
709
710             TempSort[k].mValue = plateau / BLOCK;
711             for (i = 0; i<BLOCK; i++)
712             {
713                 sum_std += ( (plateau / BLOCK-column[k+i]) *
714                              (plateau / BLOCK-column[k+i]) );
715             }
716             if (BLOCK !=1)
717                 TempSort[k].mStdDev = (double) sqrt(sum_std / (BLOCK - 1));
718             else
719                 TempSort[k].mStdDev = 0;
720             TempSort[k].mIndex = k;
721         }
722         qsort (TempSort, ZZ-BLOCK+1, sizeof (struct TTempSort), My_Compare);
723         pPD = &PlateauData[x][y];
```

```
724         pTS = &TempSort[ZZ - BLOCK];
725         pPD->mVal    = pTS->mValue;
726         pPD->mStd    = pTS->mStdDev;
727         pPD->mTime   = (double) ( (pTS->mIndex + BLOCK / 2) * DELTA );
728         pPD->mMin    = TempSort[0].mValue;
729         if (pPD->mVal < 1)
730             pPD->mVal = 1;
731         if (pPD->mStd)
732             pPD->mVal_Std = (pPD->mVal-1) / pPD->mStd;
733         else
734             pPD->mVal_Std = 0;
735     }
736
737     /*****************************************************************************
738      FUNCTION:      Get_Slope()
739     *****************************************************************************/
740     void Get_Slope
741     (
742         double *column,
743         int pix_x,
744         int pix_y,
745         int sim_index
746     )
747     {
748         int     j,
749                 index,
750                 mwt;
751         int     NPT     = SimParams[sim_index].mNPT;
752         int     START   = 0;
753         int     STOP    = SimParams[sim_index].mNumber_to_sample_int - NPT;
754         double  DELTA   = SimParams[sim_index].mSamplingInterval * TimeStep;
755         double  a[NO_POINTS+NO_BASELINE], b[NO_POINTS+NO_BASELINE],
756                 siga[NO_POINTS+NO_BASELINE], sigb[NO_POINTS+NO_BASELINE],
757                 chi2[NO_POINTS+NO_BASELINE], q[NO_POINTS+NO_BASELINE];
758         double  x[NO_POINTS+NO_BASELINE], y[NO_POINTS+NO_BASELINE],
759                 sig[NO_POINTS+NO_BASELINE];
760         struct TSlope       *pSD;
761         struct TTempSort    *pTS;
762         struct TPlateau     *pPD;
763         mwt = 0;          // No STD weighting
764         START = (int) (
765                         NO_BASELINE / SimParams[sim_index].mSamplingInterval -
766                         2 * SimParams[sim_index].mTINF /
767                         SimParams[sim_index].mSamplingInterval
768                       );
769         STOP  = (int) (
770                         NO_BASELINE / SimParams[sim_index].mSamplingInterval +
771                         2 * SimParams[sim_index].mTINF /
772                         SimParams[sim_index].mSamplingInterval
773                       );
774
775         for ( index=START;  index <= STOP; index++ )
776         {
777
778
779             for ( j=0; j<NPT; j++ )
780             {
781                 x[j+1]      = (index + j) * DELTA;
782                 y[j+1]      = (double) column[index+j];
783                 sig[j+1]    = 1.0;
784             }
785
786             fit (x, y, NPT, sig, mwt, &a[index], &b[index], &siga[index],
787                  &sigb[index], &chi2[index], &q[index]);
788
789
790             TempSort[index-START].mIndex    = index;
791             TempSort[index-START].mValue    = b[index];
792             TempSort[index-START].mStdDev   = sigb[index];
793         }
794         qsort (TempSort, STOP-START+1, sizeof (struct TTempSort), My_Compare);
795         pSD = &SlopeData[pix_x][pix_y];
796         pTS = &TempSort[STOP-START];
797
```

```
798     pSD->mMaxSlope              = (double)pTS->mValue;
799     pSD->mMaxSlopeSig           = (double)sigb[pTS->mIndex];
800     pSD->mMaxSlopeIntercept     = (double)a[pTS->mIndex];
801     pSD->mMaxSlopeInterceptSig  = (double)siga[pTS->mIndex];
802     pSD->mMaxSlopeChi2          = (double)chi2[pTS->mIndex];
803
804     pSD->mMaxSlopeInterval  = (pTS->mIndex) * DELTA;
805     pSD->mMinSlope          = (double)TempSort[0].mValue;
806     pPD = &PlateauData[pix_x][pix_y];
807
808     pSD->mTheRatio  = (pPD->mVal != 1) ?
809                       (pSD->mMaxSlope / (pPD->mVal - 1)) :
810                       (0);
811     pSD->mOnset     = (pSD->mMaxSlope != 0) ?
812                       ((1 - pSD->mMaxSlopeIntercept) / pSD->mMaxSlope) :
813                       (0);
814 }
815
816 /*****************************************************************************
817  FUNCTION:      Calculate_ME_IRE_From_My_Function()
818 *****************************************************************************/
819 void Calculate_ME_IRE_From_My_Function
820 (
821     int pix_x,
822     int pix_y,
823     int sim_index
824 )
825 {
826     struct TSimBlock *pSB = &SimBlock[pix_x][pix_y];
827     struct TSimulationParameters *pSP = &SimParams[sim_index];
828     struct TSimResult *pSR = &SimResult[pix_x][pix_y][sim_index];
829     double  t_max, c_max;
830     double  k21 = pSB->mSB_k21;
831     double  u   = pSB->mSB_u_2;
832     double  v   = pSB->mSB_v_2;
833     double  kel = pSB->mSB_kel_2;
834     double  T   = pSP->mTINF;
835     double  A   = pSP->mA * pSB->mSB_fex *
836                   pSP->mM_in / pSP->mV1_2 /
837                   pSP->mTINF;
838     t_max = 1 / (k21-kel) * log( (exp(k21 * T) - 1) / (exp(kel * T) - 1) );
839
840     c_max = u * (exp(kel * T) - 1) * exp(-kel * t_max) -
841             v * (exp(k21 * T) - 1) * exp(-k21 * t_max);
842     pSR->mCalc_ME           = 1 + A * c_max;
843     pSR->mCalc_IRE          = A * k21 * v * (exp(-kel * T) - exp(-k21 * T));
844     pSR->mCalc_TMAX         = t_max;
845     pSR->mCalc_True_Start   = TimeStep * NO_BASELINE;
846     pSR->mCalc_Ratio        = k21 * v * (exp(-kel*T) - exp(-k21*T)) / c_max;
847 }
848
849 /*****************************************************************************
850  FUNCTION:      Xmrqmin()
851 *****************************************************************************/
852 int Xmrqmin
853 (
854     double *Column,
855     int px,
856     int py,
857     int sim_index,
858     double *Result
859 )
860 {
861     struct TSimulationParameters *pSP = &SimParams[sim_index];
862     struct TSimBlock *pSB = &SimBlock[px][py];
863     int     Start = (int) (SlopeData[px][py].mMaxSlopeInterval /
864             (TimeStep * pSP->mSamplingInterval))-1;
865     int     ZZ = pSP->mNumber_to_sample_int;
866     int     NPT = ZZ - Start;
867     double  DELTA = pSP->mSamplingInterval * TimeStep;
868     double  Guess_A =   pSP->mA * pSB->mSB_fex * pSP->mM_in /
869                         pSP->mV1_2 / pSP->mTINF;
870     double  Guess_k21 = pSB->mSB_k21;
871     int     True_start;
```

```
872     int     i,*ia,itst,k,mfit=MA;
873     double  alamda,chisq,ochisq,*x,*y,*yt,*sig,**covar,**Alpha;
874     static double   a[MA+1]     = {0.0, 1.0, 2.0};
875     static double   gues[MA+1]  = {0.0, 0.001, 0.001};
876     ia      = ivector(1,MA);
877     x       = vector(1,NPT_MAX);
878     y       = vector(1,NPT_MAX);
879     yt      = vector(1,NPT_MAX);
880     sig     = vector(1,NPT_MAX);
881     covar   = matrix(1,MA,1,MA);
882     Alpha   = matrix(1,MA,1,MA);
883
884     True_start  = (int)NO_BASELINE/pSP->mSamplingInterval;
885     Start       = True_start;
886     NPT = ZZ - Start;
887     for (i=1; i<=NPT; i++)
888     {
889         x[i]    = (double) DELTA*(i-1);
890         sig[i]  = 1.0;
891         y[i]    = (double) Column[Start+i-1];
892     }
893     gues[1] = Guess_A;
894     gues[2] = Guess_k21;
895     for (i=1; i<=mfit; i++)
896         ia[i]=1;
897
898     for (i=1; i<=MA; i++)
899         a[i]=gues[i];
900     alamda = -1;
901     status = mrqmin(x,y,sig,NPT,a,ia,MA,covar,Alpha,&chisq,My_Func,&alamda);
902     k=1;
903     itst = 0;
904     for (;;)
905     {
906         k++;
907         ochisq = chisq;
908         status = mrqmin( x, y, sig, NPT, a, ia, MA, covar, Alpha, &chisq,
909                          My_Func, &alamda);
910
911         if (chisq > ochisq)
912         {
913             itst=0;
914         }
915         else if ( fabs(ochisq-chisq) < CHI_TOLERANCE )
916         {
917             itst++;
918         }
919         if (itst < 4)
920             continue;
921         alamda = 0.0;
922         status = mrqmin( x, y, sig, NPT, a, ia, MA, covar, Alpha, &chisq,
923                          My_Func, &alamda);
924         break;
925     }
926     //---------------------------------------------------------
927     // Gaussj returns 0 when OK. This is then passed on to mrqmin
928     // 1 and 2 mean singular matrix errors
929     //---------------------------------------------------------
930     // Everything is fine!
931     if ( !status )
932     {
933         Result[0] = a[1];
934         // convert to fex
935         Result[1] = a[2];
936         Result[2] = covar[1][1];
937         Result[3] = covar[2][1];
938         Result[4] = chisq;
939         free_matrix(Alpha, 1, MA, 1, MA);
940         free_matrix(covar, 1, MA, 1, MA);
941         free_vector(sig, 1, NPT_MAX);
942         free_vector(yt, 1, NPT_MAX);
943         free_vector(y, 1, NPT_MAX);
944         free_vector(x, 1, NPT_MAX);
945         free_ivector(ia, 1, MA);
```

```
946
947         return 1;
948     }
949     else
950     {
951         free_matrix(Alpha, 1, MA, 1, MA);
952         free_matrix(covar, 1, MA, 1, MA);
953         free_vector(sig, 1, NPT_MAX);
954         free_vector(yt, 1, NPT_MAX);
955         free_vector(y, 1, NPT_MAX);
956         free_vector(x, 1, NPT_MAX);
957         free_ivector(ia, 1, MA);
958         return 0;
959     }
960 }
961
962 /*****************************************************************************
963  FUNCTION:       My_Func()
964 *****************************************************************************/
965 void My_Func
966 (
967     double t,
968     double a[],
969     double *y,
970     double dyda[],
971     int na
972 )
973 {
974     double  z, v, conc, dydc;
975     NumOfFuncCalls += 1;
976
977     if ( a[2] < (2 * KEL) )
978     {
979         dyda[2] = -dyda[2];
980         return;
981     }
982
983     if ( a[1] < 0 )
984     {
985         dyda[1] = -dyda[1];
986         return;
987     }
988
989     if ( a[2] > 0.125 )
990     {
991         dyda[2] = -dyda[2];
992         return;
993     }
994
995     if ( a[2] > KEL )
996         z = 1 / ( a[2] - KEL );
997     else
998     {
999         return;
1000    }
1001
1002    v = z / KEL;
1003    if ( t <= TDASH )
1004        conc = a[2] * v * ( 1 - exp(-KEL * t) ) - z * ( 1 - exp(-a[2] * t) );
1005    else
1006        conc = a[2] * v * ( exp(-KEL * (t - TDASH)) - exp(-KEL * t) ) -
1007                z * ( exp(-a[2] * (t - TDASH)) - exp(-a[2] * t) );
1008    *y = (1 + a[1] * conc);
1009    dydc = a[1];
1010    dyda[1] = conc;
1011    if ( t <= TDASH )
1012    {
1013        dyda[2] = dydc * (
1014                    z * z * ( exp(-KEL * t) - exp(-a[2] * t) ) -
1015                    z * t * exp(-a[2] * t)
1016                );
1017    }
1018    else
1019    {
```

```
1020            dyda[2] = dydc * (
1021                        z * z * ( exp(-KEL * t) - exp(-KEL * (t - TDASH)) ) -
1022                        z * z * ( exp(-a[2] * t) - exp(-a[2] * (t - TDASH)) ) -
1023                        z * (
1024                              t * exp(-a[2] *t ) -
1025                              (t - TDASH) * exp(-a[2] * (t - TDASH))
1026                            )
1027                      );
1028        }
1029    }
1030
1031    /*****************************************************************************
1032     FUNCTION:       Calculate_Fit()
1033    *****************************************************************************/
1034    int Calculate_Fit
1035    (
1036        double *Column,
1037        int px,
1038        int py,
1039        int sim_index
1040    )
1041    {
1042        int                 status = 0;
1043        double              results[6];
1044        struct TSimBlock    *pSB = &SimBlock[px][py];
1045        struct TNonLin      *pNLD = &NonlinData[px][py];
1046        struct TSimulationParameters *pSP = &SimParams[sim_index];
1047        double  kel = pSB->mSB_kel_2;
1048        status = Xmrqmin(Column, px, py, sim_index, results);
1049        pNLD->mNL_fitA      = results[0];
1050        pNLD->mNL_fit_fex   = (pNLD->mNL_fitA / pSP->mA_set / pSP->mM_in) *
1051                              (pSP->mV1_2 * pSP->mTINF);
1052        pNLD->mNL_fitk21    = results[1];
1053        if ( pNLD->mNL_fitk21>0.3 )
1054        {
1055            status = Xmrqmin(Column, px, py, sim_index, results);
1056        }
1057        pNLD->mNL_fitChi2                 = results[4];
1058        pNLD->mNL_number_of_iterations    = NumOfFuncCalls;
1059        pNLD->mNL_fitAk21                 = pNLD->mNL_fitA * pNLD->mNL_fitk21;
1060        if (pNLD->mNL_fitk21 > 0.1)
1061            status = 0;
1062        if (pNLD->mNL_fitA <= 0)
1063            status = 0;
1064
1065        return status;              // 1 if OK
1066    }
1067
1068    /*****************************************************************************
1069     FUNCTION:       Summary_Monte_Carlo()
1070    *****************************************************************************/
1071    void Summary_Monte_Carlo
1072    (
1073        double Sum,
1074        double Sum2,
1075        long int No
1076    )
1077    {
1078        double  a_, b, d, e;
1079        if ( No < 2 )
1080        {
1081            MC_SD           = 1000000;
1082            MC_Mean         = 1000000;
1083            MC_SDOverMean   = 1000000;
1084
1085            return;
1086        }
1087
1088        MC_Mean = Sum / No;
1089        a_ = No * Sum2;
1090        b = Sum * Sum;
1091        d = a_ - b;
1092        e = d / No;
1093        e = e / (No - 1);
```

```
1094        MC_SD             = sqrt(e);
1095        MC_SDOverMean     = 100 * MC_SD / MC_Mean;
1096    }
1097
1098    /*****************************************************************************
1099     FUNCTION:       Print_Simulation_Summary()
1100    *****************************************************************************/
1101    void Print_Simulation_Summary
1102    (
1103        int i
1104    )
1105    {
1106        struct TSimulationParameters     *sp = &SimParams[i];
1107
1108        printf("\n\nSimulation no\t%d\n\n", i);
1109        printf("a\t%e\n",                 sp->mA);
1110        printf("a1_Tofts\t%e\n",          sp->ma1_Tofts);
1111        printf("a2_Tofts\t%e\n",          sp->ma2_Tofts);
1112        printf("a_set\t%e\n",             sp->mA_set);
1113        printf("Alpha\t%e\n",             sp->mAlpha);
1114        printf("BLOCK\t%d\n",             sp->mBLOCK);
1115        printf("BW\t%e\n",                sp->mBW);
1116        printf("Dose\t%e\n",              sp->mDose);
1117        printf("k1_Tofts\t%e\n",          sp->mk1_Tofts);
1118        printf("k2_Tofts\t%e\n",          sp->mk2_Tofts);
1119        printf("kel_1\t%e\n",             sp->mkel_1);
1120        printf("kel_2\t%e\n",             sp->mkel_2);
1121        printf("M_in\t%e\n",              sp->mM_in);
1122        printf("NoiseFactor\t%e\n",       sp->mNoiseFactor);
1123        printf("NPT\t%d\n",               sp->mNPT);
1124        printf("NumberToSampleInt\t%d\n", sp->mNumber_to_sample_int);
1125        printf("SamplingInterval\t%d\n",  sp->mSamplingInterval);
1126        printf("Start\t%d\n",             sp->mStart);
1127        printf("T10\t%e\n",               sp->mT10);
1128        printf("T10_set\t%e\n",           sp->mT10_set);
1129        printf("TINF\t%e\n",              sp->mTINF);
1130        printf("TINFPoints\t%d\n",        sp->mTINFPoints);
1131        printf("TINFAssumed\t%e\n",       sp->mTINFAssumed);
1132        printf("TINFAssumed_points\t%d\n", sp->mTINFPointsAssumed);
1133        printf("TR\t%e\n",                sp->mTR);
1134        printf("V1_1\t%e\n",              sp->mV1_1);
1135        printf("V1_2\t%e\n",              sp->mV1_2);
1136        printf("V1_Fraction1\t%e\n",      sp->mV1_Fraction1);
1137        printf("V1_Fraction2\t%e\n",      sp->mV1_Fraction2);
1138    }
1139
1140    /*****************************************************************************
1141     FUNCTION:       Print_Summary_Results()
1142    *****************************************************************************/
1143    void Print_Summary_Results
1144    (
1145        char label[]
1146    )
1147    {
1148        int     l, k;
1149        printf("\n\t\t\t\t%s\n", label);
1150        printf("\n\t\t\t\t");
1151        for (l=0; l<MATRIX_DIM; l++)
1152        {
1153            printf("fex = %.2e\t", SimBlock[0][l].mSB_fex);
1154        }
1155        printf("\n");
1156        for (k=0; k<MATRIX_DIM; k++)
1157        {
1158            printf("\t\t\tk21 = %.2e\t", SimBlock[k][0].mSB_k21);
1159            for(l=0; l<MATRIX_DIM; l++)
1160            {
1161                printf("%e\t",  OneToPrintBuffer[k][l]);
1162            }
1163            printf("\n");
1164        }
1165    }
1166
1167    /*****************************************************************************
```

```
 FUNCTION:      Look_Up()
*****************************************************************************/
void Look_Up
(
    int i
)
{
    double  k21_delta    = 0.00001;
    double  T            = SimParams[i].mTINF;
    double  kel          = SimParams[i].mkel_2;
    double  K21, up, down, TMAX;
    int     step;

    for (step = 0; step < MAXLOOKUPS; step++)
    {
        K21 = 0.001 + k21_delta * step;
        TMAX = 1 / (K21 - kel) * log((exp(K21 * T) - 1) / (exp(kel * T) -
1));
    up = K21 * ( exp(-kel * T) - exp(-K21 * T) );
    down = K21 / kel * (exp(kel * T) - 1) * exp(-kel * TMAX) -
           (exp(K21 * T) - 1) * exp(-K21 * TMAX);
    LookUps[step][1] = up / down;
    LookUps[step][0] = K21;
    }
}

/*****************************************************************************
 FUNCTION:      Get_Init_Est_k21()
*****************************************************************************/
void Get_Init_Est_k21
(
    int px,
    int py
)
{
    double      Ratio;
    long int    i = 0;
    Ratio = SlopeData[px][py].mTheRatio;
    if ( Ratio < LookUps[0][1] )
        NonlinData[px][py].mNL_estk21 = LookUps[0][0];
    else if ( Ratio > LookUps[MAXLOOKUPS-1][1] )
        NonlinData[px][py].mNL_estk21 = LookUps[MAXLOOKUPS-1][0];
    else
    {
        while(Ratio>LookUps[i][1])
            i++;
        NonlinData[px][py].mNL_estk21 = LookUps[i][0];
    }
}

/*****************************************************************************
 FUNCTION:      Get_Init_Est_A()
*****************************************************************************/
void Get_Init_Est_A
(
    int px,
    int py,
    int i
)
{
    double  k21, u, v;
    double  Max, c_max, t_max;
    double  T = SimParams[i].mTINF;
    double  kel = SimParams[i].mkel_2;
    k21 = NonlinData[px][py].mNL_estk21;
    Max = (double)PlateauData[px][py].mVal;
    u = k21 / ( kel * (k21 - kel) );
    v = 1 / (k21-kel);
    t_max = 1 / (k21 - kel) * log( (exp(k21 * T) - 1) / (exp(kel * T) - 1) );
    c_max = u * (exp(kel * T) - 1) * exp(-kel * t_max) -
            v * (exp(k21 * T) - 1) * exp(-k21 * t_max);

    NonlinData[px][py].mNL_estA = (Max - 1) / c_max;
}
```

```
1242
1243 /*****************************************************************************
1244  FUNCTION:       Summary_Trimmed()
1245 *****************************************************************************/
1246 void Summary_Trimmed
1247 (
1248     double *MC_column,
1249     int x,
1250     int y,
1251     int No_MC
1252 )
1253 {
1254     int                 i, j, Step;
1255     struct TTempSort    Cell[NO_MONTE_CARLO];
1256     double              Perc[NO_MONTE_CARLO], Score, Score2, a, b, d, e,
1257                         Mean, Std;
1258     Score = 0;
1259     Score2 = 0;
1260     for(i=0; i<No_MC; i++)
1261     {
1262         Cell[i].mValue = MC_column[i];
1263         Cell[i].mIndex = i;
1264     }
1265     qsort(Cell, No_MC, sizeof (struct TTempSort), My_Compare);
1266     Step = No_MC / NO_DIVISIONS;
1267     for (j=0; j<NO_DIVISIONS; j++)
1268     {
1269         Perc[j] = Cell[j  * Step].mValue;
1270     }
1271
1272     Perc[NO_DIVISIONS] = Cell[No_MC - 1].mValue;
1273     j = 0;
1274     for(i = 0; i < (NO_DIVISIONS-1) * Step; i++)
1275     {
1276         Score += Cell[i].mValue;
1277         Score2 += Cell[i].mValue * Cell[i].mValue;
1278         j++;
1279     }
1280
1281     Mean = (float) Score / j;
1282     a = j * Score2;
1283     b = Score * Score;
1284     d = a - b;
1285     e = d / j;
1286     e = e / (j - 1);
1287     Std = sqrt(e);
1288
1289     MC_Mean = Mean;
1290     MC_SD =Std;
1291     MC_SDOverMean = 100 * Std / Mean;
1292 }
```

References

1. Folkman, J., *Angiogenesis in cancer, vascular, rheumatoid and other disease.* Nature Medicine, 1995. 1(1): p. 27-31.
2. Tofts, P.S. et al, *Estimating kinetic parameters from dynamic contrast-enhanced T1-weighted MRI of a diffusable tracer: Standardized quantities and symbols.* Journal of Magnetic Resonance Imaging, 1999. 10(3): p. 223-232.
3. Fanelli, M. et al, *Assessment of tumor vascularization: Immunohistochemical and non-invasive methods.* International Journal of Biological Markers, 1999. 14(4): p. 218-31.
4. Risau, W., *Embryonic angiogenesis factors.* Pharmacology and Therapeutics, 1991. 51(3): p. 371-376.
5. Zagzag, D., *Angiogenic growth factors in neural embryogenesis and neoplasia.* American Journal of Pathology, 1995. 146(2): p. 293-309.
6. Arnold, F. and D.C. West, *Angiogenesis in wound healing.* Pharmacology and Therapeutics, 1991. 52(3): p. 407-422.
7. Reynolds, L.P., S.D. Killilea, and D.A. Redmer, *Angiogenesis in the female reproductive system.* FASEB Journal, 1992. 6(3): p. 886-892.
8. Hanahan, D. and J. Folkman, *Patterns and emerging mechanisms of the angiogenic switch during tumorigenesis.* Cell, 1996. 86(3): p. 353-364.
9. Folkman, J., *Tumor angiogenesis.* Advances in Cancer Research, 1985. 43: p. 175-203.
10. Sebag, J. and J.W. McMeel, *Diabetic-retinopathy - Pathogenesis and the role of retina-derived growth factor in angiogenesis.* Survey of Ophthalmology, 1986. 30(6): p. 377-384.
11. Aiello, L.P. et al, *Vascular endothelial growth factor in ocular fluid of patients with diabetic retinopathy and other retinal disorders.* New England Journal of Medicine, 1994. 331(22): p. 1480-1487.
12. Taraboletti, G. et al, *Inhibition of angiogenesis and murine hemangioma growth by batimastat, a synthetic inhibitor of matrix metalloproteinases.* Journal of the National Cancer Institute, 1995. 87(4): p. 293-298.
13. Szekanecz, Z., G. Szegedi, and A.E. Koch, *Angiogenesis in rheumatoid arthritis: Pathogenic and clinical significance.* Journal of Investigative Medicine, 1998. 46(2): p. 27-41.
14. Ware, J.A. and M. Simons, *Angiogenesis in ischemic heart disease.* Nature Medicine, 1997. 3(2): p. 158-164.

15. Hahnfeldt, P. et al, *Tumor development under angiogenic signaling: A dynamical theory of tumor growth, treatment response, and postvascular dormancy.* Cancer Research, 1999. **59**(19): p. 4770-4775.

16. Hlatky, L. et al, *Mammary fibroblasts may influence breast-tumor angiogenesis via hypoxia-induced vascular endothelial growth factor up-regulation and protein expression.* Cancer Research, 1994. **54**(23): p. 6083-6086.

17. Paleolog, E.M. and R.A. Fava, *Angiogenesis in rheumatoid arthritis: Implications for future therapeutic strategies.* Springer Seminars in Immunopathology, 1998. **20**(1-2): p. 73-94.

18. Hlatky, L., P. Hahnfeldt, and J. Folkman, *Clinical application of antiangiogenic therapy: Microvessel density, what it does and doesn't tell us.* Journal of the National Cancer Institute, 2002. **94**(12): p. 883-893.

19. Klagsbrun, M., *Regulators of angiogenesis.* Annual Review of Physiology, 1991. **53**: p. 217-239.

20. Folkman, J. and M. Klagsbrun, *Angiogenic factors.* Science, 1987. **235**(4787): p. 442-447.

21. Molls, M. and P. Vaupel, eds. *Blood Perfusion and Microenvironment of Human Tumors: Implications for Clinical Radiooncology.* ed. L.W. Brady, H.P. Heilmann, and M. Molls. 2000, Springer Verlag: Berlin Heilderberg.

22. Guyton, A.C., *Textbook of Medical Physiology.* 8th ed. 1991, Philadelphia; London: Saunders.

23. Peterson, H.I., *Vascular and extravscular spaces in tumors: tumor vascular permeability*, in *Tumor Blood Circulation. Angiogenesis, Vascular Morphology and Blood Flow of Experimental and Human Tumors*, H.I. Peterson, Editor. 1979, CRC Press Inc: Boca Raton, Florida, USA. p. 77-85.

24. Hirano, A. and T. Matsui, *Vascular structures in brain tumors.* Human Pathology, 1975. **6**(5): p. 611-21.

25. Waggener, J.D. and J.L. Beggs, *Vasculature of neural neoplasms.* Advances in Neurology, 1976. **15**: p. 27-49.

26. Appelgren, L., H.I. Peterson, and B. Rosengren, *Vascular and extravascular spaces in two transplantable tumors of the rat.* Bibliotheca Anatomica, 1973. **12**: p. 504-10.

27. Jain, R.K., *Vascular and interstitial barriers to delivery of therapeutic agents in tumors.* Cancer and Metastasis Reviews, 1990. **9**(3): p. 253-266.

28. Yuan, F. et al, *Vascular permeability and microcirculation of gliomas and mammary carcinomas transplanted in rat and mouse cranial windows.* Cancer Research, 1994. **54**(17): p. 4564-4568.

29. Yuan, F. et al, *Vascular permeability in a human tumor xenograft - Molecular-size dependence and cutoff size.* Cancer Research, 1995. **55**(17): p. 3752-3756.
30. Weidner, N. et al, *Tumor angiogenesis and metastasis - Correlation in invasive breast carcinoma.* New England Journal of Medicine, 1991. **324**(1): p. 1-8.
31. Gasparini, G., *Clinical significance of determination of surrogate markers of angiogenesis in breast cancer.* Critical Reviews in Oncology Hematology, 2001. **37**(2): p. 97-114.
32. Weidner, N. et al, *Tumor angiogenesis correlates with metastasis in invasive prostate carcinoma.* American Journal of Pathology, 1993. **143**(2): p. 401-409.
33. West, C.M.L. et al, *Tumor vascularity: A histological measure of angiogenesis and hypoxia.* Cancer Research, 2001. **61**(7): p. 2907-2910.
34. Ferrara, N. and T. DavisSmyth, *The biology of vascular endothelial growth factor.* Endocrine Reviews, 1997. **18**(1): p. 4-25.
35. Grunstein, J. et al, *Tumor-derived expression of vascular endothelial growth factor is a critical factor in tumor expansion and vascular function.* Cancer Research, 1999. **59**(7): p. 1592-1598.
36. Brekken, R.A. et al, *Vascular endothelial growth factor as a marker of tumor endothelium.* Cancer Research, 1998. **58**(9): p. 1952-1959.
37. Yuan, F. et al, *Time-dependent vascular regression and permeability changes in established human tumor xenografts induced by an anti-vascular endothelial growth factor vascular permeability factor antibody.* Proceedings of the National Academy of Sciences of the United States of America, 1996. **93**(25): p. 14765-14770.
38. Senger, D.R. et al, *Vascular permeability factor (VPF, VEGF) in tumor biology.* Cancer and Metastasis Reviews, 1993. **12**(3-4): p. 303-324.
39. Senger, D.R. et al, *Tumor cells secrete a vascular permeability factor that promotes accumulation of ascites fluid.* Science, 1983. **219**(4587): p. 983-985.
40. Obermair, A. et al, *Vascular endothelial growth factor (VEGF) in human breast cancer: Correlation with disease-free survival.* International Journal of Cancer, 1997. **74**(4): p. 455-458.
41. Dirix, L.Y. et al, *Elevated levels of the angiogenic cytokines basic fibroblast growth factor and vascular endothelial growth factor in sera of cancer patients.* British Journal of Cancer, 1997. **76**(2): p. 238-243.
42. Abragam, A., *Principles of Nuclear Magentism.* International Series of Monographs on Physics, ed. J. Birman. 1999, New York: Oxford University Press.
43. Haacke, E.M. et al, *Magnetic Resonance Imaging: Physical Principles and Sequence Design.* 1999: John Wiley & Sons, Inc.
44. Stark, D.D. and W.G. Bradley, *Magnetic Resonance Imaging.* 3rd ed. 1999: Mosby, Inc.

45. Bradley, W.G. and G.M. Bydder, *Advanced MRI Imaging Techniques.* 1st ed. 1997, London: Martin Dunitz.

46. Bloch, F., W.W. Hanson, and M.E. Packard, *Nuclear induction.* Phys. Rev., 1946. **69**: p. 127.

47. Purcell, E.M., H.C. Torrey, and R.V. Pound, *Resonance absorption by nuclear magnetic moments in solid.* The Physical Review, 1946. **69**: p. 37.

48. Kangarlu, A. and P.M.L. Robitaille, *Biological effects and health implications in magnetic resonance imaging.* Concepts in Magnetic Resonance, 2000. **12**(5): p. 321-359.

49. Gadian, D.G., *Nuclear Magnetic Resonance and its Applications to Living Systems.* 1982: Oxford Clarendon Press.

50. Bottomley, P.A. et al, *A review of normal tissue hydrogen NMR relaxation times and relaxation mechanisms from 1-100 MHz: Dependence on tissue type, NMR frequency, temperature, species, excision, and age.* Medical Physics, 1984. **11**(4): p. 425-48.

51. Damadian, R., *Tumor detection by nuclear magnetic resonance.* Science, 1971. **171**(976): p. 1151-3.

52. Lauterbur, P.C., *Image formation by induced local interactions: Examples of employing nuclear magnetic resonance.* Nature, 1973. **242**: p. 190.

53. Damadian, R., M. Goldsmith, and L. Minkoff, *NMR in cancer: XVI. FONAR image of the live human body.* Physiological Chemistry and Physics, 1977. **9**(1): p. 97-100, 108.

54. Hinshaw, W.S., P.A. Bottomley, and G.N. Holland, *Radiographic thin-section image of the human wrist by nuclear magnetic resonance.* Nature, 1977. **270**(5639): p. 722-3.

55. Kumar, A., D. Welti, and R.R. Ernst, *NMR Fourier zeugmatography.* Journal of Magnetic Resonance, 1975. **18**: p. 69-83.

56. Edelstein, W.A. et al, *Spin warp NMR imaging and applications to human whole-body imaging.* Physics in Medicine and Biology, 1980. **25**(4): p. 751-6.

57. Mansfield, P., *Multi-planar image formation using NMR spin echoes.* Journal of Physics C: Solid State Physics, 1977. **10**: p. L55-L58.

58. Matwiyoff, N.A. and W.M. Brooks, *Instrumentation*, in *Magnetic Resonance Imaging*, D.D. Stark and W.G. Bradley, Editors. 1999, Mosby, Inc. p. 15-32.

59. Haase, A. et al, *FLASH imaging - Rapid NMR imaging using low flip-angle pulses.* Journal of Magnetic Resonance, 1986. **67**(2): p. 258-266.

60. Hennig, J., A. Nauerth, and H. Friedburg, *RARE imaging - a fast imaging method for clinical MR.* Magnetic Resonance in Medicine, 1986. **3**(6): p. 823-833.

61. Carr, D.H. et al, *Intravenous chelated gadolinium as a contrast agent in NMR imaging of cerebral tumours.* Lancet, 1984. **1**(8375): p. 484-6.

62. Laniado, M. et al, *First use of Gd-DTPA/dimeglumine in man.* Physiological Chemistry and Physics and Medical NMR, 1984. **16**(2): p. 157-65.

63. Lauffer, R.B., *Paramagnetic metal complexes as water proton relaxation agents for NMR imaging - Theory and design.* Chemical Reviews, 1987. **87**(5): p. 901-927.

64. Weinmann, H.J., M. Laniado, and W. Mutzel, *Pharmacokinetics of Gd-DTPA dimeglumine after intravenous injection into healthy volunteers.* Physiological Chemistry and Physics and Medical NMR, 1984. **16**(2): p. 167-172.

65. Taylor, J.S. et al, *MR imaging of tumor microcirculation: Promise for the new millenium.* Journal of Magnetic Resonance Imaging, 1999. **10**(6): p. 903-907.

66. Hollis, D.P. et al, *Nuclear magnetic resonance studies of cancer. VI. Relationship among spin-lattice relaxation times, growth rate, and water content of Morris hepatomas.* Journal of the National Cancer Institute, 1975. **54**(6): p. 1469-72.

67. Eggleston, J.C., L.A. Saryan, and D.P. Hollis, *Nuclear magnetic resonance investigations of human neoplastic and abnormal nonneoplastic tissues.* Cancer Research, 1975. **35**(5): p. 1326-32.

68. Brix, G. et al, *Pharmacokinetic parameters in CNS Gd-DTPA enhanced MR imaging.* Journal of Computer Assisted Tomography, 1991. **15**(4): p. 621-628.

69. Tofts, P.S. and A.G. Kermode, *Measurement of the blood-brain-barrier permeability and leakage space using dynamic MR imaging .1. Fundamental-concepts.* Magnetic Resonance in Medicine, 1991. **17**(2): p. 357-367.

70. Tofts, P.S., *Modeling tracer kinetics in dynamic Gd-DTPA MR imaging.* Journal of Magnetic Resonance Imaging, 1997. **7**(1): p. 91-101.

71. Larsson, H.B.W. et al, *Quantitation of blood brain barrier defect by magnetic resonance imaging and gadolinium-DTPA in patients with multiple sclerosis and brain tumors.* Magnetic Resonance in Medicine, 1990. **16**(1): p. 117-131.

72. Wagner, J.G., *Pharmacokinetics for the Pharmaceutical Scientist.* 1993: Technomic Publishing Company, Inc.

73. Solomon, I., *Relaxation processes in a system of two spins.* The Physical Review, 1955. **99**: p. 559-565.

74. Bloembergen, N., *Proton relaxation times in paramagnetic solutions.* Journal of Chemical Physics, 1957. **27**(2): p. 572-573.

75. Oksendal, A.N. and P.A. Hals, *Biodistribution and toxicity of MR imaging contrast media.* Journal of Magnetic Resonance Imaging, 1993. **3**(1): p. 157-165.

76. Strich, G. et al, *Tissue distribution and magnetic resonance spin-lattice relaxation effects of Gadolinium-DTPA.* Radiology, 1985. **154**(3): p. 723-726.

77. Gadian, D.G. et al, *Gadolinium-DTPA as a contrast agent in MR imaging - Theoretical projections and practical observations.* Journal of Computer Assisted Tomography, 1985. **9**(2): p. 242-251.

78. Tofts, P.S., B. Shuter, and J.M. Pope, *Ni-DTPA doped agarose gel - A phantom material for Gd-DTPA enhancement measurements.* Magnetic Resonance Imaging, 1993. **11**(1): p. 125-133.

79. Hendrick, R.E. and E.M. Haacke, *Basic physics of MR contrast agents and maximization of image contrast.* Journal of Magnetic Resonance Imaging, 1993. **3**(1): p. 137-148.

80. Andersen, C. et al, *Approximation of arterial input curve data in MRI estimation of cerebral blood-tumor-barrier leakage: Comparison between Gd- DTPA and Tc-99m-DTPA input curves.* Magnetic Resonance Imaging, 1996. **14**(3): p. 235-241.

81. Godfrey, K., *Compartmental Models and Their Application.* 1983, London, UK: Academic Press Inc.

82. Buckley, D.L., *Uncertainty in the analysis of tracer kinetics using dynamic contrast-enhanced T-1-weighted MRI.* Magnetic Resonance in Medicine, 2002. **47**(3): p. 601-606.

83. Hoffmann, U. et al, *Pharmacokinetic mapping of the breast - A new method for dynamic MR mammography.* Magnetic Resonance in Medicine, 1995. **33**(4): p. 506-514.

84. Tofts, P.S., B. Berkowitz, and M.D. Schnall, *Quantitative analysis of dynamic Gd-DTPA enhancement in breast tumors using a permeability model.* Magnetic Resonance in Medicine, 1995. **33**(4): p. 564-568.

85. Port, R.E. et al, *Multicompartment analysis of gadolinium chelate kinetics: Blood-tissue exchange in mammary tumors as monitored by dynamic MR imaging.* Journal of Magnetic Resonance Imaging, 1999. **10**(3): p. 233-241.

86. Hawighorst, H. et al, *Angiogenesis of uterine cervical carcinoma: Characterization by pharmacokinetic magnetic resonance parameters and histological microvessel density with correlation to lymphatic involvement.* Cancer Research, 1997. **57**(21): p. 4777-4786.

87. Müller-Schimpfle, M. et al, *Recurrent rectal cancer - Diagnosis with dynamic MR-imaging.* Radiology, 1993. **189**(3): p. 881-889.

88. Fritz-Hansen, T. et al, *Measurement of the arterial concentration of Gd-DTPA using MRI: A step toward quantitative perfusion imaging.* Magnetic Resonance in Medicine, 1996. **36**(2): p. 225-231.

89. Larsson, H.B.W. et al, *In vivo quantification of the unidirectional influx constant for Gd-DTPA diffusion across the myocardial capillaries with MR imaging.* Journal of Magnetic Resonance Imaging, 1994. **4**(3): p. 433-440.

90. Larsson, H.B.W. et al, *Myocardial perfusion modeling using MRI.* Magnetic Resonance in Medicine, 1996. **35**(5): p. 716-726.

91. Stanisz, G.J. and R.M. Henkelman, *Gd-DTPA relaxivity depends on macromolecular content.* Magnetic Resonance in Medicine, 2000. **44**(5): p. 665-667.

92. Donahue, K.M., R.M. Weisskoff, and D. Burstein, *Water diffusion and exchange as they influence contrast enhancement.* Journal of Magnetic Resonance Imaging, 1997. **7**(1): p. 102-110.

93. Kety, S.S., *The theory and applications of the exchange of inert gas at the lungs and tissues.* Pharmacol Rev, 1951. **3**: p. 1-41.

94. Henderson, E., B.K. Rutt, and T.Y. Lee, *Temporal sampling requirements for the tracer kinetics modeling of breast disease.* Magnetic Resonance Imaging, 1998. **16**(9): p. 1057-1073.

95. Tofts, P.S. and B.A. Berkowitz, *Measurement of capillary permeability from the Gd enhancement curve - A comparison of bolus and constant infusion injection methods.* Magnetic Resonance Imaging, 1994. **12**(1): p. 81-91.

96. Berkowitz, B.A. et al, *Accurate and precise measurement of blood-retinal barrier breakdown using dynamic Gd-DTPA MRI.* Investigative Ophthalmology and Visual Science, 1992. **33**(13): p. 3500-3506.

97. Larsson, H.B.W. and P.S. Tofts, *Measurement of blood brain barrier permeability using dynamic Gd-DTPA scanning - A comparison of methods.* Magnetic Resonance in Medicine, 1992. **24**(1): p. 174-176.

98. Mussurakis, S. et al, *Dynamic MR imaging of the breast combined with analysis of contrast agent kinetics in the differentiation of primary breast tumours.* Clinical Radiology, 1997. **52**(7): p. 516-526.

99. Knopp, M.V. et al, *Pathophysiologic basis of contrast enhancement in breast tumors.* Journal of Magnetic Resonance Imaging, 1999. **10**(3): p. 260-6.

100. Hulka, C.A. et al, *Dynamic echo-planar imaging of the breast: Experience in diagnosing breast carcinoma and correlation with tumor angiogenesis.* Radiology, 1997. **205**(3): p. 837-842.

101. Hulka, C.A. et al, *Benign and malignant breast lesions - Differentiation with echo-planar MR imaging.* Radiology, 1995. **197**(1): p. 33-38.

102. den Boer, J.A. et al, *Pharmacokinetic analysis of Gd-DTPA enhancement in dynamic three-dimensional MRI of breast lesions.* Journal of Magnetic Resonance Imaging, 1997. **7**(4): p. 702-15.

103. Daniel, B.L. et al, *Breast disease: Dynamic spiral MR imaging.* Radiology, 1998. **209**(2): p. 499-509.

104. Ikeda, O., Y. Yamashita, and M. Takahashi, *Gd-enhanced dynamic magnetic resonance imaging of breast masses.* Topics in Magnetic Resonance Imaging, 1999. **10**(2): p. 143-51.

105. Heywang, S.H. et al, *MR imaging of the breast with Gd-DTPA: Use and limitations.* Radiology, 1989. **171**(1): p. 95-103.

106. Kaiser, W.A. and E. Zeitler, *MR imaging of the breast - Fast imaging sequences with and without Gd-DTPA - Preliminary observations.* Radiology, 1989. **170**(3): p. 681-686.

107. Gilles, R. et al, *Nonpalpable breast tumors - Diagnosis with contrast-enhanced subtraction dynamic MR imaging.* Radiology, 1994. **191**(3): p. 625-631.

108. Boetes, C. et al, *MR characterization of suspicious breast lesions with a gadolinium-enhanced turboFLASH subtraction technique.* Radiology, 1994. **193**(3): p. 777-781.

109. Kuhl, C.K. et al, *Dynamic breast MR imaging: Are signal intensity time course data useful for differential diagnosis of enhancing lesions?* Radiology, 1999. **211**(1): p. 101-110.

110. Orel, S.G. et al, *Suspicious breast lesions - MR imaging with radiologic pathological correlation.* Radiology, 1994. **190**(2): p. 485-493.

111. Müller-Schimpfle, M. et al, *Dynamic 3D-MR mammography: Is there a benefit of sophisticated evaluation for enhancement curves for clinical routine?* Journal of Magnetic Resonance Imaging, 1997. **7**(1): p. 236-240.

112. Weidner, N. et al, *Tumor angiogenesis - A new significant and independent prognostic indicator in early-stage breast carcinoma.* Journal of the National Cancer Institute, 1992. 84(24): p. 1875-1887.

113. Hawighorst, H. et al, *Uterine cervical carcinoma: Comparison of standard and pharmacokinetic analysis of time-intensity curves for assessment of tumor angiogenesis and patient survival.* Cancer Research, 1998. 58(16): p. 3598-3602.

114. George, M.L. et al, *Non-invasive methods of assessing angiogenesis and their value in predicting response to treatment in colorectal cancer.* British Journal of Surgery, 2001. 88(12): p. 1628-1636.

115. Mayr, N.A. et al, *MR microcirculation assessment in cervical cancer: Correlations with histomorphological tumor markers and clinical outcome.* Journal of Magnetic Resonance Imaging, 1999. 10(3): p. 267-276.

116. Stomper, P.C. et al, *Angiogenesis and dynamic MR imaging gadolinium enhancement of malignant and benign breast lesions.* Breast Cancer Research and Treatment, 1997. 45(1): p. 39-46.

117. Buadu, L.D. et al, *Breast lesions: Correlation of contrast medium enhancement patterns on MR images with histopathologic findings and tumor angiogenesis.* Radiology, 1996. 200(3): p. 639-49.

118. Buckley, D.L. et al, *Microvessel density in invasive breast cancer assessed by dynamic Gd-DTPA enhanced MRI.* Journal of Magnetic Resonance Imaging, 1997. 7(3): p. 461-464.

119. Tietz, N.W., ed. *Clinical Guide to Laboratory Tests.* 2nd ed. 1990, Saunders: Philadelphia, London.

120. Tortora, G.J. and S. Reynolds Grabowski, *Principles of Anatomy and Physiology.* 7th ed. 1993: Harper Collins.

121. Buckley, D.L. et al, *Quantitative analysis of multislice Gd-Dtpa enhanced dynamic MR images using an automated simplex minimization procedure.* Magnetic Resonance in Medicine, 1994. **32**(5): p. 646-651.

122. Buckley, D.L. et al, *Quantitative-Analysis of Multislice Gd-Dtpa Enhanced Dynamic Mr-Images Using an Automated Simplex Minimization Procedure (Vol 32, Pg 646, 1994).* Magnetic Resonance in Medicine, 1995. **33**(2): p. 282-282.

123. Press, W.H. et al, *Numerical Recipes in C.* 2nd ed. 1994: Cambridge University Press.

124. Doucet, A., N. de Freitas, and N. Gordon, eds. *Sequential Monte Carlo Methods in Practice.* Statistics for Engineering and Information Science. 2001, Springer Verlag: New York.

125. Park, S.K. and K.W. Miller, *Random number generators - Good ones are hard to find.* Communications of the ACM, 1988. **31**(10): p. 1192-1201.

126. Merchant, T.E. et al, *Application of a mixed imaging sequence for MR-imaging characterization of human breast disease.* Acta Radiologica, 1993. **34**(4): p. 356-361.

127. Bottomley, P.A. et al, *A review of 1H nuclear magnetic resonance relaxation in pathology: Are T1 and T2 diagnostic?* Medical Physics, 1987. **14**(1): p. 1-37.

128. Hull, R.G. et al, *Nuclear magnetic resonance (NMR) tomographic imaging for popliteal cysts in rheumatoid arthritis.* Annals of the Rheumatic Diseases, 1984. **43**(1): p. 56-9.

129. Mussurakis, S., P. Gibbs, and A. Horsman, *Peripheral enhancement and spatial contrast uptake heterogeneity of primary breast tumours: Quantitative assessment with dynamic MRI.* Journal of Computer Assisted Tomography, 1998. **22**(1): p. 35-46.

130. Heywang, S.H. et al, *MR imaging of the breast using gadolinium-DTPA.* Journal of Computer Assisted Tomography, 1986. **10**(2): p. 199-204.

131. Kuhl, C.K. and H.H. Schild, *Dynamic image interpretation of MRI of the breast.* Journal of Magnetic Resonance Imaging, 2000. **12**(6): p. 965-974.

132. Harms, S.E. et al, *MR imaging of the breast with rotating delivery of excitation off resonance - Clinical experience with pathological correlation.* Radiology, 1993. **187**(2): p. 493-501.

133. Kuhl, C.K., *MRI of breast tumors.* European Radiology, 2000. **10**(1): p. 46-58.

134. Heywang-Köbrunner, S.H. et al, *Contrast-enhanced MRI of the breast: Accuracy, value, controversies, solutions.* European Journal of Radiology, 1997. **24**(2): p. 94-108.

135. Su, M.Y. et al, *Characterization of N-ethyl-N-nitrosourea-induced malignant and benign breast tumors in rats by using three MR contrast agents.* Journal of Magnetic Resonance Imaging, 1999. 9(2): p. 177-86.

136. Daldrup, H. et al, *Correlation of dynamic contrast-enhanced MR imaging with histologic tumor grade: Comparison of macromolecular and small-molecular contrast media.* American Journal of Roentgenology, 1998. **171**(4): p. 941-9.

137. Turetschek, K. et al, *MRI assessment of microvascular characteristics in experimental breast tumors using a new blood pool contrast agent (MS-325) with correlations to histopathology.* Journal of Magnetic Resonance Imaging, 2001. **14**(3): p. 237-42.

138. Turetschek, K. et al, *Assessment of a rapid clearance blood pool MR contrast medium (P792) for assays of microvascular characteristics in experimental breast tumors with correlations to histopathology.* Magnetic Resonance in Medicine, 2001. **45**(5): p. 880-6.

139. Turetschek, K. et al, *MR imaging characterization of microvessels in experimental breast tumors by using a particulate contrast agent with histopathologic correlation.* Radiology, 2001. **218**(2): p. 562-9.

140. Helbich, T.H. et al, *Quantitative gadopentetate-enhanced MRI of breast tumors: Testing of different analytic methods.* Magnetic Resonance in Medicine, 2000. 44(6): p. 915-24.

141. Stomper, P.C. et al, *Invasive breast carcinoma - Analysis of dynamic magnetic resonance imaging enhancement features and cell proliferative activity determined by DNA S-phase percentage.* Cancer, 1996. **77**(9): p. 1844-1849.

142. Mussurakis, S., D.L. Buckley, and A. Horsman, *Dynamic MR imaging of invasive breast cancer: Correlation with tumour grade and other histological factors.* British Journal of Radiology, 1997. 70(833): p. 446-451.

143. Fischer, U. et al, *Prognostic value of contrast-enhanced MR mammography in patients with breast cancer.* European Radiology, 1997. 7(7): p. 1002-5.

144. Bone, B. et al, *Contrast-enhanced MR imaging as a prognostic indicator of breast cancer.* Acta Radiologica, 1998. **39**(3): p. 279-84.

145. Stomper, P.C. et al, *Suspect breast lesions - Findings at dynamic gadolinium enhanced MR imaging correlated with mammographic and pathological features.* Radiology, 1995. **197**(2): p. 387-395.

146. Galea, M.H. et al, *The Nottingham prognostic index in primary breast cancer.* Breast Cancer Research and Treatment, 1992. **22**(3): p. 207-219.

147. Altman, D.G., *Practical Statistics for Medical Research.* 1999: Chapman & Hall, CRC.

148. MacGregor, A.J. and A.J. Silman, *Rheumatoid arthritis: classification and epidemiology*, in *Rheumatology*, J.H. Klippel and P.A. Dieppe, Editors. 1998, Mosby: London. p. 1-6.

149. Pincus, T. et al, *Severe functional declines, work disability, and increased mortality in 75 rheumatoid arthritis patients studied over 9 years.* Arthritis and Rheumatism, 1984. **27**(8): p. 864-872.

150. van der Heide, A. et al, *The effectiveness of early treatment with "second-line" antirheumatic drugs - A randomized, controlled trial.* Annals of Internal Medicine, 1996. **124**(8): p. 699-&.

151. Tsakonas, E. et al, *Consequences of delayed therapy with second-line agents in rheumatoid arthritis: A 3 year follow-up on the hydroxychloroquine in early rheumatoid arthritis (HERA) study.* Journal of Rheumatology, 2000. **27**(3): p. 623-629.

152. Fries, J.F. et al, *Reduction in long-term disability in patients with rheumatoid arthritis by disease-modifying antirheumatic drug-based treatment strategies.* Arthritis and Rheumatism, 1996. **39**(4): p. 616-622.

153. McGonagle, D. et al, *The relationship between synovitis and bone changes in early untreated rheumatoid arthritis - A controlled magnetic resonance imaging study.* Arthritis and Rheumatism, 1999. **42**(8): p. 1706-1711.

154. Colville-Nash, P.R. and D.L. Scott, *Angiogenesis and rheumatoid arthritis - Pathogenic and therapeutic implications.* Annals of the Rheumatic Diseases, 1992. **51**(7): p. 919-925.

155. *Copyright © 2000 by Houghton Mifflin Company. Reproduced by permission from The American Heritage Dictionary of the English Language, Fourth Edition.* 2000.

156. Kimball, E.S. and J.L. Gross, *Angiogenesis in pannus formation.* Agents and Actions, 1991. **34**(3-4): p. 329-331.

157. Zvaifler, N.J. and G.S. Firestein, *Pannus and pannocytes - Alternative models of joint destruction in rheumatoid arthritis.* Arthritis and Rheumatism, 1994. **37**(6): p. 783-789.

158. Paleolog, E., *Target effector role of vascular endothelium in the inflammatory response: Insights from the clinical trial of anti-TNF alpha antibody in rheumatoid arthritis.* Journal of Clinical Pathology-Molecular Pathology, 1997. **50**(5): p. 225-233.

159. Qu, Z.H. et al, *Expression of basic fibroblast growth-factor in synovial tissue from patients with rheumatoid arthritis and degenerative joint disease.* Laboratory Investigation, 1995. **73**(3): p. 339-346.

160. Koch, A.E., *Review: Angiogenesis: Implications for rheumatoid arthritis.* Arthritis and Rheumatism, 1998. **41**(6): p. 951-62.

161. Matsubara, T. and M. Ziff, *Inhibition of human endothelial cell proliferation by gold compounds.* Journal of Clinical Investigation, 1987. **79**(5): p. 1440-1446.

162. Potvin, F. et al, *Mechanisms of action of antimalarials in inflammation - Induction of apoptosis in human endothelial cells.* Journal of Immunology, 1997. **158**(4): p. 1872-1879.

163. Hirata, S. et al, *Inhibition of in vitro vascular endothelial cell proliferation and in vivo neovascularization by low-dose methotrexate.* Arthritis and Rheumatism, 1989. **32**(9): p. 1065-1073.

164. Youssef, P.P. et al, *Effects of pulse methylprednisolone on inflammatory mediators in peripheral blood, synovial. Fluid, and synovial membrane in rheumatoid arthritis.* Arthritis and Rheumatism, 1997. **40**(8): p. 1400-1408.

165. Elliott, M.J. et al, *Repeated therapy with monoclonal antibody to tumor necrosis factor (CA 2) in patients with rheumatoid arthritis.* Lancet, 1994. **344**(8930): p. 1125-1127.

166. Maini, R. et al, *Infliximab (chimeric anti-tumour necrosis factor alpha monoclonal antibody) versus placebo in rheumatoid arthritis patients receiving concomitant methotrexate: A randomised phase III trial.* Lancet, 1999. **354**(9194): p. 1932-1939.

167. Weinblatt, M.E. et al, *A trial of etanercept, a recombinant tumor necrosis factor receptor : Fc fusion protein, in patients with rheumatoid arthritis receiving methotrexate.* New England Journal of Medicine, 1999. **340**(4): p. 253-259.

168. Genovese, M.C. et al, *Etanercept versus methotrexate in patients with early rheumatoid arthritis - Two-year radiographic and clinical outcomes.* Arthritis and Rheumatism, 2002. **46**(6): p. 1443-1450.

169. Lipsky, P.E. et al, *Infliximab and methotrexate in the treatment of rheumatoid arthritis.* New England Journal of Medicine, 2000. **343**(22): p. 1594-1602.

170. Johnson, B.A. et al, *Adhesion molecule expression in human synovial tissue.* Arthritis and Rheumatism, 1993. **36**(2): p. 137-146.

171. Walsh, D.A. et al, *Focally regulated endothelial proliferation and cell death in human synovium.* American Journal of Pathology, 1998. **152**(3): p. 691-702.

172. Brooks, P.C. et al, *Integrin alpha V beta 3 antagonists promote tumor regression by inducing apoptosis of angiogenic blood vessels.* Cell, 1994. **79**(7): p. 1157-1164.

173. Brooks, P.C., R.A.F. Clark, and D.A. Cheresh, *Requirement of Vascular Integrin Alpha(V)Beta(3) for Angiogenesis.* Science, 1994. **264**(5158): p. 569-571.

174. Storgard, C.M. et al, *Decreased angiogenesis and arthritic disease in rabbits treated with an alpha v beta 3 antagonist.* Journal of Clinical Investigation, 1999. **103**(1): p. 47-54.

175. McQueen, F.M. et al, *Magnetic resonance imaging of the wrist in early rheumatoid arthritis reveals a high prevalence of erosions at four months after symptom onset.* Annals of the Rheumatic Diseases, 1998. **57**(6): p. 350-356.

176. Sugimoto, H., A. Takeda, and K. Hyodoh, *Early stage rheumatoid arthritis: Prospective study of the effectiveness of MR imaging for diagnosis.* Radiology, 2000. **216**(2): p. 569-575.

177. Østergaard, M. and M. Szkudlarek, *Imaging in rheumatoid arthritis - Why MRI and ultrasonography can no longer be ignored.* Scandinavian Journal of Rheumatology, 2003. **32**(2): p. 63-73.

178. Beltran, J. et al, *Rheumatoid arthritis - MR imaging manifestations.* Radiology, 1987. **165**(1): p. 153-157.

179. König, H., J. Sieper, and K.J. Wolf, *Rheumatoid arthritis - Evaluation of hypervascular and fibrous pannus with dynamic MR imaging enhanced with Gd-DTPA.* Radiology, 1990. **176**(2): p. 473-477.

180. Kursunoglu Brahme, S. et al, *Rheumatoid knee - Role of gadopentetate-enhanced MR imaging.* Radiology, 1990. **176**(3): p. 831-835.

181. Reiser, M.F. et al, *Gadolinium-DTPA in rheumatoid arthritis and related diseases - First results with dynamic magnetic resonance imaging.* Skeletal Radiology, 1989. **18**(8): p. 591-597.

182. Adam, G. et al, *Rheumatoid arthritis of the knee - Value of gadopentetate dimeglumine enhanced MR imaging.* American Journal of Roentgenology, 1991. **156**(1): p. 125-129.

183. Clunie, G. et al, *Measurement of synovial lining volume by magnetic resonance imaging of the knee in chronic synovitis.* Annals of the Rheumatic Diseases, 1997. **56**(9): p. 526-534.

184. Creamer, P. et al, *Quantitative magnetic resonance imaging of the knee: A method of measuring response to intra-articular treatments.* Annals of the Rheumatic Diseases, 1997. **56**(6): p. 378-381.

185. Østergaard, M. et al, *Quantitative assessment of the synovial membrane in the rheumatoid wrist: An easily obtained MRI score reflects the synovial volume.* British Journal of Rheumatology, 1996. **35**(10): p. 965-971.

186. Palmer, W.E. et al, *Quantification of inflammation in the wrist with gadolinium-enhanced MR imaging and PET with 2-[F-18]-fluoro-2-deoxy-D-glucose.* Radiology, 1995. **196**(3): p. 647-655.

187. Clunie, G.P.R. et al, *Changes in articular synovial lining volume measured by magnetic resonance in a randomized, double-blind, controlled trial of intra-articular samarium-153 particulate hydroxyapatite for chronic knee synovitis.* Rheumatology, 1999. **38**(2): p. 113-117.

188. Klarlund, M., M. Østergaard, and I. Lorenzen, *Finger joint synovitis in rheumatoid arthritis: Quantitative assessment by magnetic resonance imaging.* Rheumatology, 1999. **38**(1): p. 66-72.

189. Østergaard, M. et al, *Magnetic resonance imaging-determined synovial membrane and joint effusion volumes in rheumatoid arthritis and osteoarthritis - Comparison with the macroscopic and microscopic appearance of the synovium.* Arthritis and Rheumatism, 1997. **40**(10): p. 1856-1867.

190. Gaffney, K. et al, *Quantitative assessment of the rheumatoid synovial microvascular bed by gadolinium-DTPA enhanced magnetic resonance imaging.* Annals of the Rheumatic Diseases, 1998. **57**(3): p. 152-157.

191. Gaffney, K. et al, *Quantification of rheumatoid synovitis by magnetic resonance imaging.* Arthritis and Rheumatism, 1995. **38**(11): p. 1610-7.

192. Østergaard, M. et al, *Quantitative assessment of synovial inflammation by dynamic gadolinium-enhanced magnetic resonance imaging. A study of the effect of intra-articular methylprednisolone on the rate of early synovial enhancement.* British Journal of Rheumatology, 1996. **35**(1): p. 50-59.

193. Østergaard, M. et al, *Quantification of synovitis by MRI: Correlation between dynamic and static gadolinium-enhanced magnetic resonance imaging and microscopic and macroscopic signs of synovial inflammation.* Magnetic Resonance Imaging, 1998. **16**(7): p. 743-754.

194. Tamai, K. et al, *Dynamic magnetic resonance imaging for the evaluation of synovitis in patients with rheumatoid arthritis.* Arthritis and Rheumatism, 1994. **37**(8): p. 1151-1157.

195. Østergaard, M. et al, *Changes in synovial membrane and joint effusion volumes after intraarticular methylprednisolone. Quantitative assessment of inflammatory and destructive changes in arthritis by MRI.* Journal of Rheumatology, 1996. **23**(7): p. 1151-1161.

196. van Dijke, C.F. et al, *Arthritic temporomandibular joint: Correlation of macromolecular contrast-enhanced MR imaging parameters and histopathologic findings.* Radiology, 1997. **204**(3): p. 825-832.

197. van Dijke, C.F. et al, *MR imaging of the arthritic rabbit knee joint using albumin (Gd-DTPA)(30) with correlation to histopathology.* Magnetic Resonance Imaging, 1999. **17**(2): p. 237-245.

198. Demsar, F. et al, *Mapping abnormal synovial vascular permeability in temporomandibular joint arthritis in the rabbit using MRI.* British Journal of Rheumatology, 1996. **35**(S3): p. 23-25.

199. Ogan, M.D. et al, *Albumin labeled with Gd-DTPA - An Intravascular contrast-enhancing agent for magnetic resonance blood pool imaging - Preparation and characterization.* Investigative Radiology, 1987. **22**(8): p. 665-671.

200. Yamato, M. et al, *MRI of the knee in rheumatoid arthritis - Gd-DTPA perfusion dynamics.* Journal of Computer Assisted Tomography, 1993. **17**(5): p. 781-785.

201. Veale, D.J. et al, *Intra-articular primatised anti-CD4: Efficacy in resistant rheumatoid knees. A study of combined arthroscopy, magnetic resonance imaging, and histology.* Annals of the Rheumatic Diseases, 1999. **58**(6): p. 342-349.

202. Fleming, A. et al, *Early rheumatoid disease. II. Patterns of joint involvement.* Annals of the Rheumatic Diseases, 1976. **35**(4): p. 361-4.

203. Simkin, P.A., *Synovial permeability in rheumatoid arthritis.* Arthritis and Rheumatism, 1979. **22**(7): p. 689-96.

204. Stevens, C.R. et al, *A comparative study by morphometry of the microvasculature in normal and rheumatoid synovium.* Arthritis and Rheumatism, 1991. **34**(12): p. 1508-13.

205. Cronstein, B.N., *Molecular therapeutics - Methotrexate and its mechanism of action.* Arthritis and Rheumatism, 1996. **39**(12): p. 1951-1960.

206. Waldman, W.J. et al, *Inhibition of angiogenesis-related endothelial activity by the experimental immunosuppressive agent leflunomide.* Transplantation, 2001. **72**(9): p. 1578-82.

207. Manna, S.K., A. Mukhopadhyay, and B.B. Aggarwal, *Leflunomide suppresses TNF-induced cellular responses: effects on NF-kappa B, activator protein-1, c-Jun N-terminal protein kinase, and apoptosis.* Journal of Immunology, 2000. **165**(10): p. 5962-9.

208. Mladenovic, V. et al, *Safety and effectiveness of leflunomide in the treatment of patients with active rheumatoid arthritis - Results of a randomized, placebo-controlled, phase-II study.* Arthritis and Rheumatism, 1995. **38**(11): p. 1595-1603.

209. Strand, V. et al, *Treatment of active rheumatoid arthritis with leflunomide compared with placebo and methotrexate.* Archives of Internal Medicine, 1999. **159**(21): p. 2542-2550.

210. Sharp, J.T. et al, *Treatment with leflunomide slows radiographic progression of rheumatoid arthritis - Results from three randomized controlled trials of leflunomide in patients with active rheumatoid arthritis.* Arthritis and Rheumatism, 2000. **43**(3): p. 495-505.

211. Emery, P. et al, *A comparison of the efficacy and safety of leflunomide and methotrexate for the treatment of rheumatoid arthritis.* Rheumatology, 2000. **39**(6): p. 655-665.

212. Cohen, S. et al, *Two-year, blinded, randomized, controlled trial of treatment of active rheumatoid arthritis with leflunomide compared with methotrexate.* Arthritis and Rheumatism, 2001. **44**(9): p. 1984-1992.

213. Reece, R.J. et al, *Comparative assessment of leflunomide and methotrexate for the treatment of rheumatoid arthritis, by dynamic enhanced magnetic resonance imaging.* Arthritis and Rheumatism, 2002. **46**(2): p. 366-72.

214. Conaghan, P.G. et al, *Elucidation of the relationship between synovitis and bone damage - A randomized magnetic resonance imaging study of individual joints in patients with early rheumatoid arthritis.* Arthritis and Rheumatism, 2003. **48**(1): p. 64-71.

215. Arnett, F.C., S.M. Edworthy, and D.A.e.a. Bloch, *The American Rheumatism Association 1987 revised criteria for the classification of rheumatoid arthritis.* Arthritis and Rheumatism, 1988. **31**: p. 315-24.

216. Kraan, M.C. et al, *Modulation of inflammation and metalloproteinase expression in synovial tissue by leflunomide and methotrexate in patients with active rheumatoid arthritis. Findings in a*

prospective, randomized, double-blind, parallel-design clinical trial in thirty-nine patients at two centers. Arthritis and Rheumatism, 2000. **43**(8): p. 1820-30.

217. Kraan, M.C. et al, *Inhibition of neutrophil migration soon after initiation of treatment with leflunomide or methotrexate in patients with rheumatoid arthritis: Findings in a prospective, randomized, double-blind clinical trial in fifteen patients.* Arthritis and Rheumatism, 2000. **43**(7): p. 1488-95.

218. Koch, A.E. et al, *Angiogenesis mediated by soluble forms of E-selectin and vascular cell-adhesion molecule-1.* Nature, 1995. **376**(6540): p. 517-519.

219. Endrich, B. and P. Vaupel, *The role of microcirculation in the treatment of malignant tumours: facts and fiction*, in *Blood Perfusion and Microenvironment of Human Tumors: Implications for Clinical Radiooncology*, M. Molls and P. Vaupel, Editors. 2000, Springer Verlag: Berlin Heilderberg. p. 19-39.

220. Tan, A.L. et al, *Role of metacarpophalangeal joint anatomic factors in the distribution of synovitis and bone erosion in early rheumatoid arthritis.* Arthritis and Rheumatism, 2003. **48**(5): p. 1214-1222.

221. Kuhl, C.K. et al, *Breast neoplasms: T2* susceptibility-contrast, first-pass perfusion MR imaging.* Radiology, 1997. **202**(1): p. 87-95.

222. Mussurakis, S. et al, *Dynamic contrast-enhanced magnetic resonance imaging of the breast combined with pharmacokinetic analysis of gadolinium- DTPA uptake in the diagnosis of local recurrence of early stage breast carcinoma.* Investigative Radiology, 1995. **30**(11): p. 650-662.